THE METAL-DEPENDENT FUNCTION OF C2α:

A CONDITIONAL MEMBRANE DOMAIN FROM PROTEIN KINASE Cα

A Dissertation

by

KRYSTAL A. MORALES-RIVERA

Submitted to the Office of Graduate and Professional Studies of
Texas A&M University
in partial fulfillment of the requirements for the degree of

DOCTOR OF PHILOSOPHY

Chair of Committee,	Tatyana I. Igumenova
Committee Members,	Andreas Holzenburg
	Hays Rye
	Ryland Young
Head of Department,	Gregory D. Reinhart

December 2013

Major Subject: Biochemistry

ABSTRACT

Protein Kinase C (PKC) isoforms function in signaling pathways responsible for controlling cell proliferation, survival and apoptosis. Up or down-regulation of PKCs has been implicated in cancer progression, cardiovascular dysfunction, and neurological disorders. Moreover, the conventional Protein Kinase Cα (PKCα) has also been identified as an important molecular target in Pb^{2+} poisoning. Two out of three Pb^{2+} sites in full-length PKCα were mapped onto its C2 domain (C2α), which associates with anionic membranes in response to binding Ca^{2+} ions in the first step of activation. The objective of this work was to determine the specific role of divalent metal ions on the modulation of C2α structure, function, and interactions with other PKCα domains.

Nuclear magnetic resonance (NMR) and Förster resonance energy transfer were used to characterize the specific role of divalent metal ions in C2α membrane-interactions. Pb^{2+} and Cd^{2+} ions bind C2α with high affinity. Pb^{2+} drives C2α association with lipid-membranes, whereas Cd^{2+} does not support membrane-binding. This work provides direct evidence for the specific role of divalent metal ions in mediating protein-membrane interactions and illustrates the opposite responses produced by toxic metal ions in a single molecular target.

The structures of metal-free (1.9 Å) and Pb^{2+}-bound (1.5 Å) C2α were determined using X-ray crystallography. These revealed a remarkable coexistence of hemi- and holo-directed coordinated geometries for the two Pb^{2+} ions that are bound to the Ca^{2+} binding loops (CBLs). The overall backbone conformation does not change

upon metal-binding. However, elevated B-factors were observed in the CBLs of metal-free C2α, suggesting that this region is dynamic. NMR techniques were used to identify the dynamic regions and to quantify the timescales of C2α motions in different states of metal ligation. Metal-binding quenches the microsecond-timescale motions of the CBLs but results in elevated millisecond-timescale dynamics of the N- and C-terminal regions. These regions are implicated in the interactions of C2 with other regulatory domains of PKC. Our data suggest that the changes in protein dynamics is a mechanism by which the information about the metal-binding event propagates to other regions of the protein.

We then extended our structural and dynamical studies to the two-domain construct of PKCα comprising two regulatory domains, C1B-C2. NMR chemical shift perturbation and dynamic studies showed that these domains do not behave as independent modules in solution. The linker region connecting the functional modules shows significant chemical shifts and conformational dynamic changes induced by Ca^{2+}-binding. These results support our hypothesis that Ca^{2+}-binding triggers the rearrangement of the C1B and C2 domains. The strategy of using paramagnetic relaxation enhancement experiments to refine the C1B-C2 structure is presented.

A prevailing view in the PKC field is that the function of metal ion is to alter the electrostatic potential of the C2 domain and thereby facilitate the protein insertion into the negatively charged membranes. The results of our work support the multi-faceted role of metal ions, which includes the formation of specific coordination bonds with lipid head groups, as well as the modulation of protein dynamics and inter-domain orientation.

ACKNOWLEDGEMENTS

I would like to thank my principal investigator, Dr. Tatyana I. Igumenova, and the members of my graduate committee: Dr. Andreas Holzenburg, Dr. Hays Rye, and Dr. Ryland Young, for their guidance, time, and helpful discussions throughout these years.

I would also like to give a special thanks to my collaborators at Texas A&M University: Dr. Pingwei Li, Dr. Joseph Mire, and Dr. James Sacchettini for their expertise in crystallography that led to solving the structures of C2 and C1B-C2. I want to thank Dr. Mauricio Lasagna and Dr. Gregory D. Reinhart for the training and time usage of the fluorometer. For performing Isothermal Titration Calorimetry experiments, I would like to extend my gratitude to Alexey V. Gribenko and James C. Lee in the Department of Biochemistry and Molecular Biology at The University of Texas Medical Branch at Galveston. Thanks to Youngdae Yoon and Wonhwa Cho in the University of Illinois at Chicago for conducting Surface Plasmon Resonance experiments. Lastly, thanks to Alexander B. Taylor and P. John Hart in the Department of Biochemistry and the X-ray Crystallography Core Laboratory at the University of Texas Health Science Center at San Antonio for C2 structure refinement assistance.

Special thanks to the amazing faculty and staff of the Department of Biochemistry and Biophysics for their support and guidance throughout these years. I would also like to extend my gratitude to the National Institute of Health Training Grant for providing funding through the chemical biology interface training program during the 2010-2011 school year.

Thanks to the present and former members of the Igumenova laboratory for their support, scientific input, and for creating an amazing working atmosphere.

Finally, thanks to my family and friends for their unconditional love and support.

TABLE OF CONTENTS

LIST OF FIGURES

Page

LIST OF TABLES

CHAPTER I

INTRODUCTION

Motivations and goals

Protein Kinase C function

Protein Kinase C (PKC) isoforms are multi-modular lipid-responsive enzymes that belong to the AGC (PKA, PKG, and PKC) family of serine/threonine kinases. They function as central signal transducers in lipid-generating pathways responsible for controlling cellular processes including proliferation, survival, apoptosis, and differentiation.[1-3] Over 30 years ago, PKCs became noteworthy in cancer research after they were discovered to be a target of tumor-promoting phorbol esters (PE), which are plant-extracted compounds that were found to promote skin tumors in mice.[4-6] In addition, exposure of the environmental toxins, Pb^{2+} and Cd^{2+}, were also identified to modulate PKC activity for decades.[7-11]

Despite the well-established involvement of PKC isoforms malfunction in the development and progression of numerous diseases including cancer,[12-14] diabetes,[15,16] cardiovascular dysfunction,[13,17,18] and mental illnesses such as Alzheimer's,[15,19,20] Parkinson's,[21] and bipolar disorders[22,23], the unique mechanisms that activate and regulate these closely related kinases are not fully understood. This has led to pharmacological challenges when designing isoform-specific modulators.[2,12,20,24-26] Furthermore, heavy metal ions dominate the top 10 list of most toxic substances according to the Center for Disease Control and Prevention,[27] and while their detrimental effects have no safe minimum exposure, the molecular mechanism of toxicity also remain poorly understood.[11]

PKC isoforms can be modulated by three general mechanisms: (1) autoinhibitory interactions within the N-terminal regulatory region, (2) phosphorylation state of the catalytic domain, and (3) association with specific adaptor proteins at particular cellular locations (*vide infra*). The stimuli for the work presented in this dissertation lie in understanding the role of metal binding that controls the first step in conventional PKC (cPKC) activation, accompanied by disruption of intra-molecular autoinhibitory interactions and membrane translocation. This work provides insights into both the function of metal-binding in PKC activation and the mechanism by which its normal function is disrupted by heavy metal ions.

The following sections are dedicated to the introduction of PKC family isoforms and the functional differences between the lipid-binding modules that regulate the enzyme. The emphasis is on reviewing the metal-binding, metal-dependent membrane association, and intra-domain interactions carried out by the C2 domain of the conventional PKCα (C2α). This metal-dependence is the basis for the work carried out in this dissertation.

Structural and functional constituents of PKC family

There are at least 10 mammalian PKC isoforms that are classified in three classes, based on the sequence variation and multi-modular architecture of their N-terminal regulatory region: conventional, cPKC (α, βI/βII, γ), novel, nPKC (ε, δ, θ, η), and atypical, aPKC (ζ, ι/λ). They can be divided in two main segments: the conserved C-terminal domain and the variable N-terminal regulatory domain (Figure 1).

The N-terminal region contains the lipid-binding domains that dictate the isoform-specific second messengers required for activation, whereas, the C-terminal domain contains the catalytic domain and phosphorylation sites essential for the newly synthesized enzyme to become stable and catalytically competent (Figure 1).

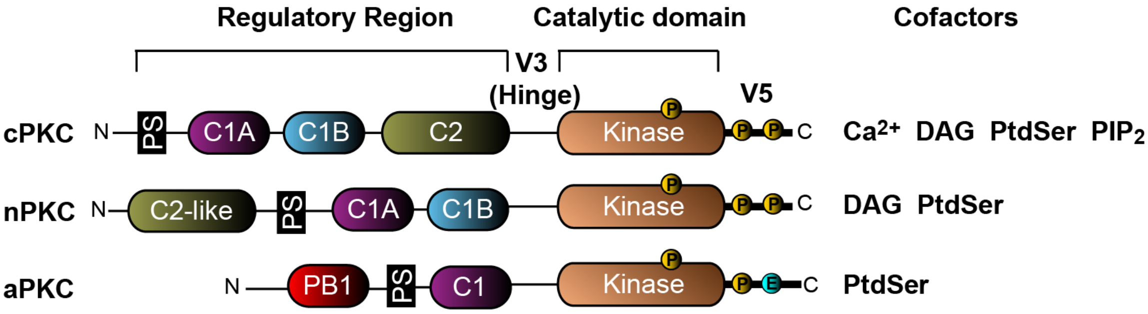

Figure 1. Functional components of PKC isoforms. Phosphorylation sites are shown in yellow spheres. The conserved homology domains are numbered C1A, C1B and C2. The variable (V) regions are numbered accordingly. The cofactors that bind the regulatory region and are required for activation are listed on the right. PS, PtdSer, DAG, and PIP_2 stand for pseudo-substrate, phosphatidylserine, diacylglycerol, and phosphatidylinositol, respectively. The N- and C-terminal regions are identified. There are three sequential maturation phosphorylation sites located at the C-terminal region: the activation loop in the catalytic domain and two at the hydrophobic and turn motifs of the V5 region. Atypical isoforms contain a glutamate in the position of the turn motif phosphorylation site.

The regulatory and catalytic segments are connected by the variable region 3 (V3). The V3 region is a flexible and proteolytically susceptible segment targeted by caspases (cysteine-aspartic proteases actively involved in apoptosis).[2] Cleavage within this region results in physical disconnection of the catalytic and regulatory region, releasing a constitutively active kinase. This was the state in which PKC was originally discovered and named protein kinase M (PKM), for magnesium (Mg^{2+}), which was observed to be required for activation.[28,29] It was later found that PKM was the result of a proteolytic cleavage, and that the full-length enzyme was regulated by second messengers Ca^{2+} and diacylglycerol (DAG), which constitute the two required activators for the cPKC isoforms.[30]

The N-terminal regulatory region

The N-terminal segment consists of a multi-modular architecture, containing the independently folded conserved homology-1A, -1B, and -2 (C1A, C1B and C2) domains. Within this region all PKC isoforms have in common an auto-inhibitory pseudosubstrate (PS) that mimics a PKC substrate and that is bound to the substrate cavity in the autoinhibited state. This long-range association constitutes the main autoinhibitory interaction. However, it is not the only interaction identified to stabilize the inactive cytosolic enzyme.[31]

In cPKCs, the pseudo-substrate segment is followed by the C1A and C1B tandem repeat and C2 domain lipid-binding modules (Figure 1). These isoforms require the binding of two second messengers; Ca^{2+} (C2 domain) and DAG (C1 domains) for the membrane translocation event that results in full enzyme activation.[2] The C1 domains target DAG and PtdSer in the membrane, whereas the C2 domain binds anionic phospholipid membranes in a Ca^{2+}-dependent manner, with selectivity for phosphatidylserine (PtdSer) and phosphoinositides (PIs). The C2 domain from PKCα (C2α) displayed a preference for phosphatidylinositol 4,5-bisphosphate (PIP_2). Together these modules preferentially target cPKC isoforms to the inner leaflet of the plasma membrane when DAG is present and where PtdSer and PIP_2 are enriched.[2,32]

The nPKC isoforms contain an altered order of regulatory domains that begins with a Ca^{2+}-independent C2-like domain that lacks the acidic residues critical for Ca^{2+}-coordination.[2] Consequently, these isoforms are only sensitive to DAG. Interestingly, these isoforms compensate for the lack of one lipid-binding module (C2 domain) by having an affinity for DAG approximately two orders of magnitude higher than cPKCs. This has implications for the subcellular location of nPKCs, in view of the basal enrichment of DAG in the Golgi, endoplasmic reticulum, and nuclear membranes.[33]

Lastly, aPKC are insensitive to both, Ca^{2+} and DAG due to the absence of a C2 domain and the presence of a DAG-binding incompetent C1 domain. Instead, these are primarily regulated trough protein-protein interactions via their PB1 (Phox and Bem 1) domain. Due to the high degree of similarity among catalytic domains, the variations within this N-terminal region represent the most promising selective pharmacological targets.[26]

Conventional PKC activation

The current model for cPKC activation relies on information gathered on the cPKCα isoform, where the mature enzyme is found in the cytosol of resting cells under the acute control of intra-molecular interactions.[2] The cPKC activation model also relies on transient association with membranes in the absence of second messengers, Ca^{2+} and DAG. Agonist stimulation of the PLC-dependent hydrolysis of PIP_2, produces membrane anchored DAG and inositol triphosphate (IP_3). IP_3 binds to specific IP_3-receptors in the endoplasmic reticulum (ER), inducing Ca^{2+} release from this compartment into the cytosol.[2]

Several studies seeking to inhibit the activation cPKC have focused on the initial trigger that induces the conformational change required for membrane translocation and enzyme activation. It is now well known that the first step of activation involves Ca^{2+}-binding to C2, which targets this domain to the plasma membrane where it recognizes PtdSer and PIP_2.[34-38] Noteworthy, is the dual function of PIP_2 in the activation of cPKC. While PIP_2 hydrolysis produces second messengers DAG and Ca^{2+}, a direct and specific interaction site has also been identified for C2α.[39] The initial binding of C2 to the plasma membrane, specifically PtdSer recognition, has been proposed to be the trigger that induces dissociation of intra-domain interactions between C2 and the upstream C1A domain that subsequently allows the C1 domains to search laterally for DAG and sustain full cPKC residency at the plasma membrane (Figure 2).[40] In effect, phorbol esters malignancy comes from hyperactivation of PKC and its downstream targets by increasing its residence time in the membrane. It has been hypothesized that the binding energy that results from the binding of C1 and C2 domains to the membrane provides the energy to pull the pseudosubstrate out of the active site.[38]

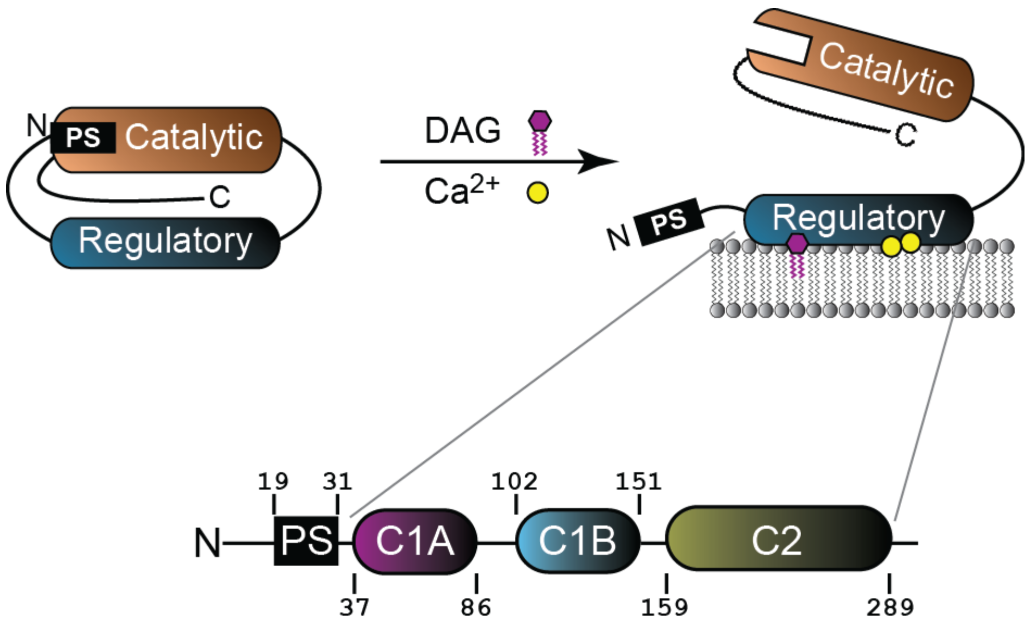

Figure 2. Current model for cPKC activation. The N- and C-terminal regions of the enzyme are identified. In the expansion of the regulatory domain, the modular structure of the conserved homology domains C1A, C1B and C2 as well as the pseudosubstrate (PS) are shown. Abbreviations as defined in Figure 1.

PKC lipid-binding regulatory modules

The intracellular membrane compartments are central sites for signaling and trafficking. The asymmetry of lipid composition within these compartments plays a critical role in the recruitment of specific lipid-binding domains to particular regions within the cell that serve as platforms of signaling cascades complexes. As indicated above, the trademark of cPKC activation has been the membrane translocation and association with DAG and the acidic phospholipids PtdSer and PIP$_2$. This regulation is conveyed by two markedly distinct lipid-binding domains (C1 and C2), located at the N-terminal regulatory region of the enzyme. However, these independently folded domains are also ubiquitously found as membrane-anchoring modules in many other proteins.

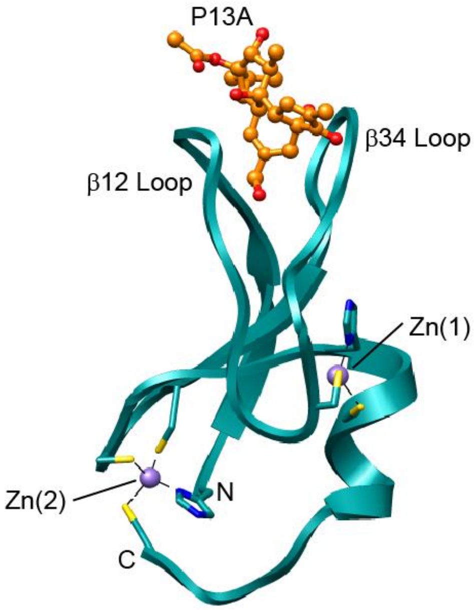

Figure 3. C1 domain structure. X-ray structure of the C1 domain from PKCδ bound to the PE, phorbol-13-acetate (P13A) (PDB ID: 1PTR).[42] The N- and C-terminal ends, ligand binding loops, and Zn^{2+} coordination sites are identified.

C1 domains

C1 domains are small independently folded domains of approximately 50 amino acids. They were first identified in PKC isoforms as the DAG second messenger receptors in PKC and attracted more attention after they were shown to bind tumor-promoting phorbolesters. They are zinc-finger domains, containing 6 conserved cysteines and two histidines required for zinc coordination and structural scaffold.[41]

Figure 3 shows the common features seen for all known C1 structures: a β-sheet core with a C-terminal α-helix. The tip of the protein is a highly hydrophobic region containing the two ligand binding loops, designated β12L and β34L.

C2 domains

C2 domains are independently folded modules (~ 130 aa) found in over 120 different proteins.[43,44] This lipid-binding module was first discovered as part of the N-terminal regulatory region of the Ca^{2+}-dependent cPKC isoforms[45] and they currently constitute the second most abundant lipid-binding module after pleckstrin homology (PH) domains.

Proteins with C2 domains

C2 domains are generally found in proteins that are involved in signal transduction and membrane trafficking. Examples of these include the cytosolic phospholipase A_2 ($cPLA_2$), phosphoinositide-specific phospholipase Cδ (PLCδ), Rabphilin-3A (Rab-3A), synaptotagmin (Syt), phosphatidylinositide 3-kinase (PI3K), GTPase-activator protein for Ras-like GTPases (Ras-GAP), Rab3-interacting molecules (RIMs), and the mammalian uncoordinated-13 (Munc13) proteins.[43]

Unlike C1 domains, C2 domains have a low sequence conservation, constituting the most variable domain of the N-terminal regulatory region between cPKC and nPKC.[44] This variability manifests in the occurrence of C2 domains with differential Ca^{2+} affinities (in cases with abolished Ca^{2+}-binding) and lipid selectivity. These contribute to changes in subcellular location and also produce very distinct membrane binding mechanisms. In addition, proteins such as Syn and Rab-3A contain more than one C2 domain in tandem, and they denote additional structural and functional elements with regulatory capabilities.[43]

Ca^{2+}-independent C2 domains

Novel C2 domains and other Ca^{2+}-independent C2 domains, lack the acidic residues located in the interconnected loops that are critical for Ca^{2+} coordination. Although membrane-association has been observed in Ca^{2+}-independent isolated C2 domains,[43] the interaction was not relevant under physiological conditions and did not contribute to the full-length enzyme membrane association. For example, studies carried in the isolated C2 domain from PKCε (C2ε) detected binding with membranes containing DAG and phosphatidic acid. However, deletion of C2ε does not affect the membrane targeting of the full length PKCε enzyme.[46] Similarly, the isolated C2 domain from PKCδ (C2δ) does not bind membranes, and a deletion of the C2δ domain has no effect on the membrane targeting of the full length PKCδ.[47] Accordingly, Ca^{2+}-independent C2 domains have been shown to play a structural role in intra-domains interactions as well as specific interactions with scaffold proteins that influence the subcellular localization of the host enzyme.[2]

C2 domains structure

The high sequence variation not only hampered the identification of C2 domains in other proteins but also caused the C2 region to be classified as one of the variable regions within PKC isoforms. It was not until structural information became available that their characteristic and conserved three-dimensional fold could be delineated (Figure 4). As shown for the C2 domain from PKCα (C2α) in Figure 5, this fold is characterized by eight β-strands that fold into a canonical β-sandwich, interconnected by three loops at the tip of the protein, and designated as the Calcium Binding Loops (CBLs), 1, 2, and 3, in Ca^{2+}-dependent C2 domains.

In conventional C2 domains, the CBLs are involved in the binding of two or three Ca^{2+} ions in addition to PtdSer head group recognition (Figure 6A). The second lipid-recognition motif is the β3-β4 groove or "lysine-rich cluster" region involved in interactions with PIP_2 (Figure 6B). The last structural feature is the C-terminal helix 3 (H3), which has been recently identified as a potential site for intra-domain interaction with the upstream C1A domain. This site along with two other sites on the CBL3 vicinity were identified by C1A and C2 surface docking.[40] This was confirmed by mutagenesis studies to be involved in intra-domain interactions that sustain the inactive state of the enzyme (residues highlighted in yellow in Figure 6C).

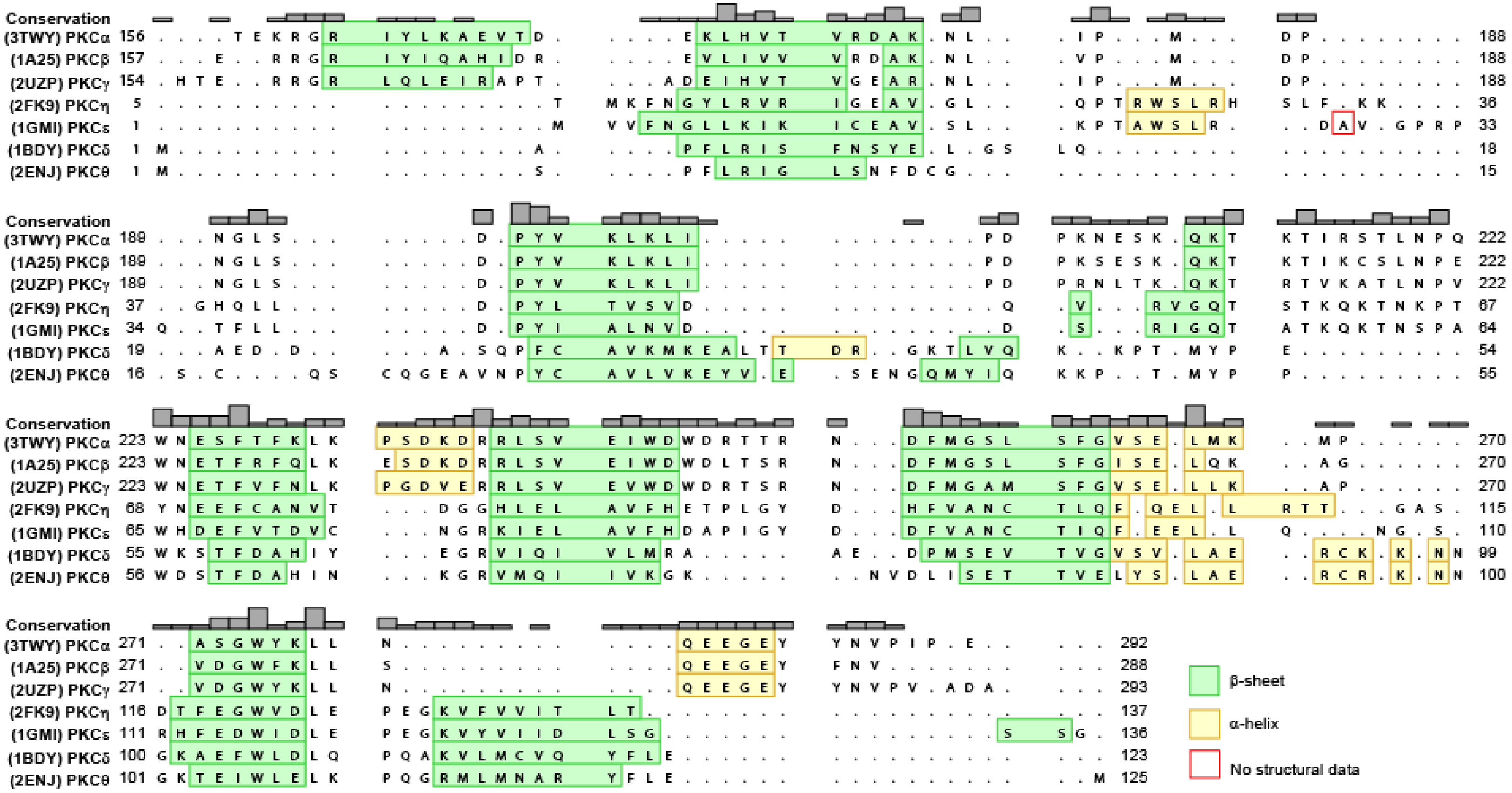

Figure 4. Structural alignment of conventional and novel C2 domains from PKC isoforms The PDB files used for the structural alignment are specified. Grey bars correspond to the amino acid conservation.

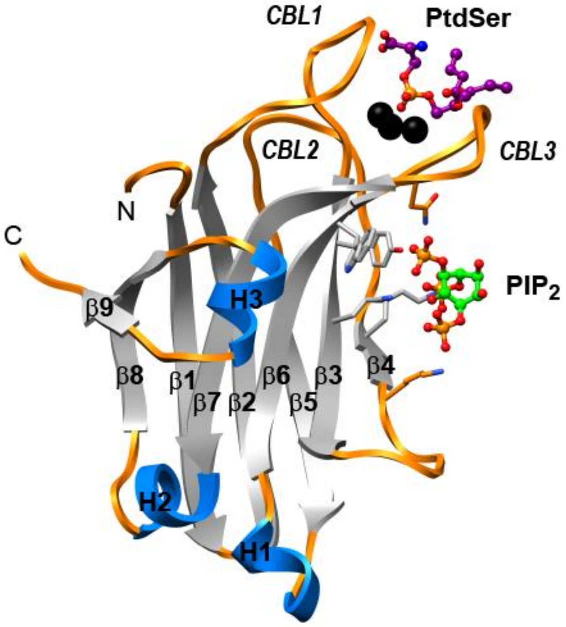

Figure 5. Structure of C2α complex with Ca^{2+} and PIP_2. C2α crystal structure in complex with PIP_2 and Ca^{2+} (PDB ID: 3GPE). The 1,2-dicaproyl-sn-phosphatidyl-L-serine (PSF) coordinates from PDB ID, 1DSY were added for better illustration of all lipid interaction sites. Secondary structure elements are identified and colored gray, blue and orange for β-strands, α-helices, and coils, respectively.

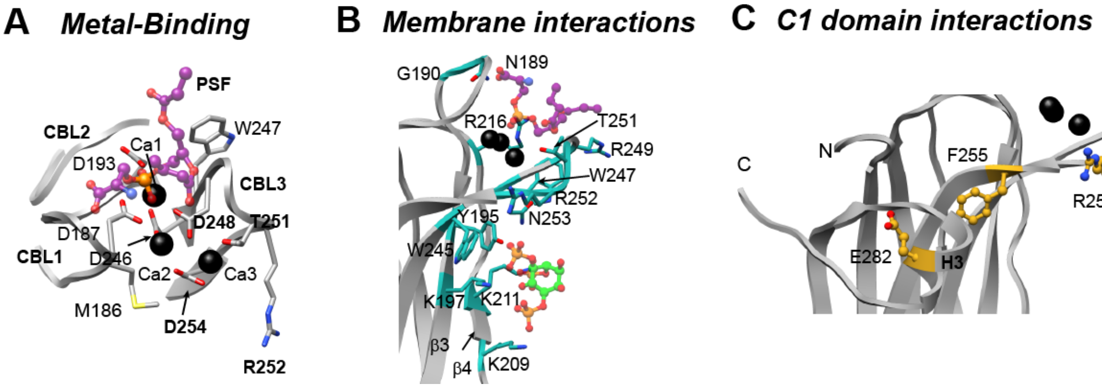

Figure 6. Detailed view of C2α structural features essential for function. Crystal structures of C2α in complex with PIP_2 and Ca^{2+} (PDB ID: 3GPE), illustrate the regions involved in metal, membrane, and intra-domain interactions. (A) Top-view expansion of CBL1, 2 and 3 and PtdSer binding regions. (B) Side-view illustrating PIP_2 ("lysine rich cluster") and PtdSer (CBLs) binding regions. (C) Side-view expansion illustrates the three residues implicated by surface docking and mutagenesis in intra-domain interactions with the C1A domain. PSF added as in Figure 5.

Structural differences are found in the interconnection of the strands, which led to the classification of C2 domains in two different topologies — Topology I (i.e. Syt I C2A domain) and Topology II (i.e. PLA_2 C2 domain), which places the N- and C-termini of the domain in opposite directions (Figure 7). Interestingly, Topology I exists for cPKC C2 domains, and Topology II exists for novel PKC. While no clear functionality has been established, this is an interesting structural arrangement, which along with the C1 and C2 domains swap in nPKCs, might play an important role in the context of multi-domain protein intra-domain interactions and relative orientation.

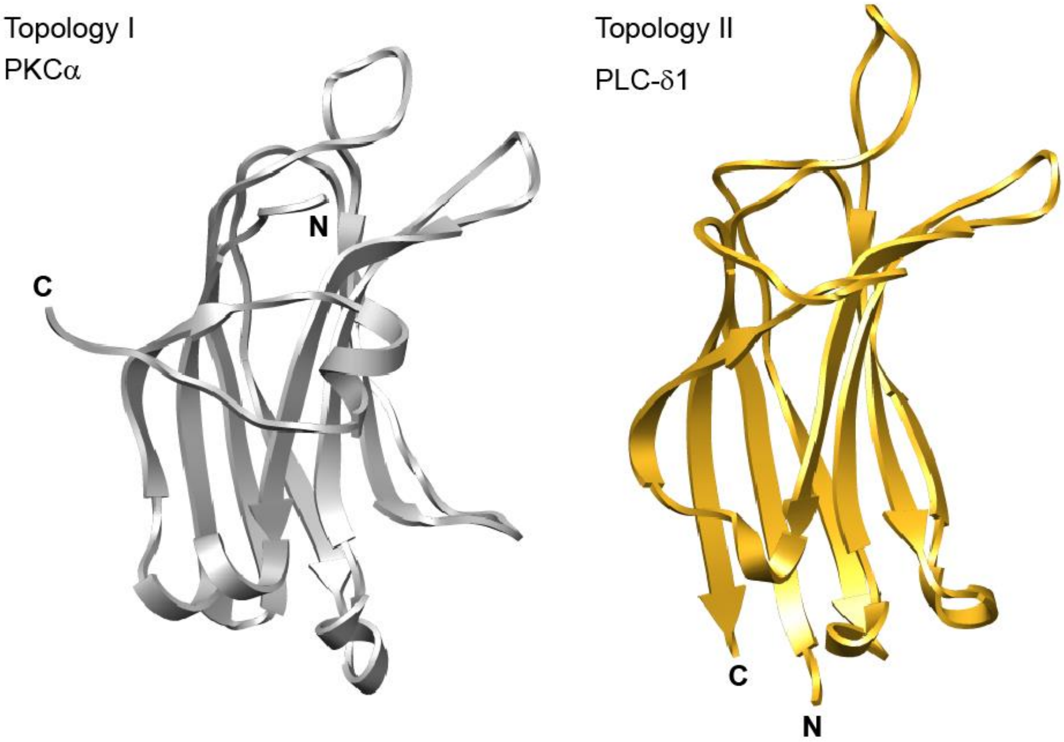

Figure 7. C2 domains existing topologies. Ribbon diagram of PKCα (PDB ID: 3RDJ)[48] and PLC-δ1 (PDB ID: 1DJX)[49] illustrate the different topologies adopted in C2 domains. The N- and C-terminal ends are identified.

The role of C2 domain in PKC signaling

C2 metal-binding

Ca^{2+} binding is exclusively required for the initial activation of cPKCs. The C2 domain serves as the Ca^{2+} sensor, which together with together with the production of DAG in the membrane, conveys the spatiotemporal specificity for these isoforms. During cPKC activation, Ca^{2+}-binding generates a change in electrostatic potential of the C2 CBLs and allows its association with the anionic components, PtdSer and PIP_2, of the plasma membrane. This initial C2-Ca^{2+} membrane association event is thought to disrupt intra-molecular interactions between C1 and C2 domains, which then allows the C1 domain search for DAG in the membrane. This membrane engagement of all lipid-binding modules is thought to provide the energy required for expelling the pseudo-substrate from the kinase domain (Figure 2).[38] This mechanism is supported by functional mutagenesis and kinetic studies carried out in the full-length PKC as well as the isolated domains. First, replacing the conserved aspartic acid residues with asparagine, which renders the C2 domain incompetent to bind Ca^{2+} ions, show that the membrane penetration and activity is abolished.[34,35] Simultaneously, *in vivo* kinetic studies show that Ca^{2+}-induced PKC translocation occurs much faster than DAG-stimulated translocation, suggesting an occlusion of the DAG binding site.[37] Lastly, C1 domain mutagenesis studies demonstrated that PKC Ca^{2+}- and PtdSer-dependent membrane binding is comparable to the wild type enzyme.[36]

Accordingly, the role of Ca^{2+}-binding during cPKC activation has been proposed to have at least three modes. First, Ca^{2+} has been shown to modulate C2 electrostatic potential.[50] This is proposed to act as an electrostatic switch that allows the domain to associate with anionic membranes. However, the Ca^{2+}-binding of C2 does not constitute merely non-specific charge neutralization. This is supported by mutagenic studies carried out on full-length PKCβ, showing that replacement of two negative charges with two positive charges in C2β CBLs does not result in an increase of the affinity for acidic membranes in the absence of Ca^{2+}.[51]

Second, Ca^{2+} has been proposed to serve as a bridge between the C2 domain and the membrane phospholipid headgroup. This mechanism is supported by C2α structure in complex with Ca^{2+} and a PtdSer short chain mimic, in which Ca^{2+} ions were directly coordinating the lipid headgroup.[52]

Furthermore, C2α was hypothesized to be the target of two out of three Pb^{2+} binding sites proposed in the full-length PKCα.[10] A major objective of the work presented in this dissertation deals with the use of C2α as a paradigm to study both the direct role of the metal-dependent function in C2 domains and mechanisms by which heavy metal ions poison the function of CBPs. Chapters II-IV provide evidence for the role of metal ions in C2α functionality and, at the same time, these chapters illustrate how heavy metal ions can generate opposite responses within a single target.

Lastly, Ca^{2+} is proposed to trigger a global conformational change that prepares the enzyme for membrane translocation by altering intra-domain interactions.[34,36,37,40] At least two auto-inhibitory interactions directly involving C2 have been proposed to be disrupted during activation. One involves the C-terminal variable region 5 (V5), which is variable in length and sequence (Figure 1). The phosphorylation state and interactions with the C2α were shown to be critical in the stabilization of the PKCα autoinhibited (DAG insensitive) state.[53] These interactions are thought to be disrupted upon Ca^{2+}-binding and subsequent membrane translocation of PKC during activation.

The DAG-insensitive state is proposed to be sustained by interactions between C2α and the upstream C1Aα domain.[40,54] C1Aα is the strongest contributor to DAG-binding with respect to the full-length enzyme.[36,55] Thereby, masking its DAG-binding conveys PKCα spatiotemporal activation, but only under conditions where DAG production is accompanied by increase of the concentration of cytosolic Ca^{2+}.

As discussed, Ca^{2+}-binding to C2 has been associated with a large-scale conformational change of the full-length enzyme.[34,36,37,40] While this was initially thought to be induced by large conformational changes within the C2 domain,[56] as has been observed for other Ca^{2+} binding proteins (CBPs), NMR and X-ray structures did not reveal significant structural changes within C2. The NMR structure determination of the C2A domain form SytI, also revealed that the loops are highly dynamic and indicated that a stabilization effect was induced by Ca^{2+}-binding, rather than large conformational changes in the average structure.[57] In fact, Ca^{2+}-binding has been shown to stabilize the C2α domain β-sandwich structure.[58] The lack of significant structural changes within C2α observed in Chapter II prompted in-depth characterization of conformational dynamics, which is presented in Chapter V. Along with these studies, Chapter VI investigates the origins and domain rearrangements induced by Ca^{2+}-binding, in the context of the C1B-C2 construct. Together, these studies contribute to the Ca^{2+} signal transduction field, provide a mechanism for Ca^{2+}-sensors in which a defined conformational change is not observed, and also gives a better understanding of the Ca^{2+}-induced arrangement in cPKC.

C2α membrane interactions

There are two distinct lipid recognition motifs within C2 domains. The CBLs region that recognizes PtdSer and a cationic patch, alternatively called the "lysine-rich cluster" or "β-groove", that forms a concave pocket involved in phosphoinositide binding.[43] The inherent sequence variability among C2 domains, in particular hydrophilic versus hydrophobic variation in the CBLs region, plays an important role in determining the intrinsic affinity for Ca^{2+} and membrane-binding driving forces.[44] In addition, the lysine-rich cluster region also varies in sequence and pocket size, adding another level of regulation and lipid recognition selectivity conferred by C2 domains.[43]

Crystal structures (Figure 5),[52,59] and spin-labeling[56] studies provide insights into lipid-binding sites and membrane insertion mechanisms of C2 domains. According to these data, C2α is oriented almost parallel to the membrane surface.[56] While electrostatic interactions have been identified as the main driving force of C2α membrane binding,[60-62] according to a recent kinetics study, hydrophobic interactions appear to be more critical for the initial membrane association. In contrast, electrostatic interactions play an important role in stabilizing the residence time of complex at the membrane.[62]

In addition, a well-known synergism also exists between C2α Ca^{2+}-binding and anionic lipid components in membranes. Ca^{2+} enhances the affinity of the C2α domain for anionic membranes.[61] Likewise, the presence of acidic phospholipids enhances C2α affinity for Ca^{2+}.[44,63,64] This sensing mechanism allows C2α to bind Ca^{2+} ions in solution and associate weakly with the membrane. This membrane bound state can then pick up Ca^{2+} ions with a higher affinity while strengthening the membrane interaction.[61] Of particular importance is PIP_2 binding to the lysine-rich cluster of C2α. While this region binds PIP_2 in a Ca^{2+}-independent manner,[65] albeit with very low affinity, the presence of PIP_2 and Ca^{2+} act synergistically to enhance each other's affinity to C2α. In addition, the binding of PIP_2 has been shown to induce a change in the domain geometry with respect to the membrane plane. In the presence of PtdSer the domain lies almost parallel to the membrane and the binding of PIP_2 to the "lysine rich cluster" induces a ~ 40 degree tilt that yields a more perpendicular orientation.[66,67] PIP_2 is the most abundant phosphoinositide at the plasma membrane[32,68] (where PKCα translocates during activation). While the hydrolysis of PIP_2 acts as a precursor of both of the second messengers that are required for cPKC activation (Ca^{2+} and DAG), *in vivo* and *in vitro* studies have shown the importance of C2α-PIP_2 interactions in the subcellular localization of full-length PKCα.[39,64,68] PIP_2 binding to this region is important for C2α, assisting in: (i) responsiveness to cytosolic concentrations of Ca^{2+} reached during a signaling event,[39,64,68] (ii) subcellular localization of full-length PKCα to the inner leaflet of the plasma membrane,[39,64,68] and (iii) prolonging the membrane residence of the domain.[63,64] These effects, induced by the presence of metal and anionic phospholipids, and their implications in heavy metal ion toxicity are studied in depth in Chapter III.[69]

The complexity of PKC multi-modular structure and regulation

There are several aspects of PKC biology and structural architecture that contribute to the prevailing obstacles when designing isoform-specific modulators. First, PKC isoforms are highly homologous (predominantly within the catalytic domain) and are, therefore, stimulated by the same activating lipid-derived signals. Therefore, the acute control of the amplitude and duration of the second messengers, combined with subcellular localization, plays a critical role in controlling their specialized functions.[47,70] While some isoforms display tissue-specific expression, the majority of isoforms is ubiquitously expressed in many cell types. In addition, isoform expression changes associated with disease progression have been observed. However, these changes are difficult to interpret and in most cases obscure the identification of the isoform(s) directly involved, since they can reflect an active isoform-specific role or the end result from pathway compensatory effects induced by the disease.[70]

Studies have also shown that isoforms simultaneous expression can sometimes result in equal and/or entirely opposite roles. The best illustration of this behavior has been described for the PKCε and PKCδ isoforms during cardiac ischemic preconditioning.[47] The same stimuli (ischemic preconditioning) result in the activation of both; however, PKCε isoform is involved in protection from ischemic-damage whereas PKCδ isoform is involved in the ischemic-induced damage. On the other hand, the activation of both causes non-pathological cardiac hypertrophy.[47] The isoform(s) actively involved were highly debated. However, this was ultimately resolved for this isoforms pair with the use of a structurally guided peptide design.[70]

From the biophysical standpoint the large size (80 kDa) and multi-modular nature of these enzymes represent challenges for the study of the full-length enzyme using conventional biophysical and structural biology techniques. Currently, the only information about the intact enzyme comes from an electron microscopy reconstruction of the PKCδ isoform[71] and a recent X-ray structure of the full PKCβII isoform. However, the latter was captured in an intermediate activated state, as it was crystallized in the presence of cofactors (Ca^{2+}) and defined density was not observed for all the domains in the enzyme.[72]

The enzyme goes through a series of maturation phosphorylation events and cofactor-induced structural reorganization that are required for the plasma membrane translocation during activation.[73] This adds another level of complexity for biophysical studies that must be considered to guide a rational drug-design which can take into consideration the changes that occur upon phosphorylation and second messenger-induced membrane association.

The translocation to internal membrane compartments has been the hallmark of PKC activation. In the cPKC and nPKC isoforms, this is carried out by the C1 and C2 regulatory domains. These domains display different affinity for membranes, and are also ubiquitously found in a wide variety of proteins. Currently, approximately 54 out of 518 human kinases contain at least one or more known lipid-binding domains.[74] Therefore, the study of the isoform-specific mechanisms controlled by C1 and C2 domains will also impact: (1) the approaches that are currently used to identify the isoform(s) directly involved in the aforementioned diseases, (2) our understanding of the regulation of other lipid-dependent kinases,[75] and (3) the regulation of other C1- and C2-containing proteins.

CHAPTER II

PB(II) AS A CA(II) SURROGATE IN C2 DOMAINS MEMBRANE INTERACTIONS[*]

Background

Early studies of the effect of Pb^{2+} on the activity of full-length PKCα led to a hypothesis that at least two of the Pb^{2+}-binding sites reside on the C2 domain.[10] In this chapter, we describe the experiments designed to probe (i) the affinity of C2α to Pb^{2+}, (ii) the influence of Pb^{2+} on the structure of C2α and its mode of interaction with lipid bilayers; (iii) the coordination geometry of Pb^{2+} in complex with C2α; (iv) the ability of Pb^{2+} to compete for protein and membrane-binding sites.

The objective of this work was to understand the effect of Pb^{2+} on the structure and membrane-binding properties of the C2α. Specifically, establish if Pb^{2+} binds to the same sites on the protein as Ca^{2+}; measure the relative binding affinities of Ca^{2+} and Pb^{2+} to C2α; determine if the replacement of Ca^{2+} with Pb^{2+} has any influence on the structure of C2α and conformation of the Ca^{2+}-binding loops (CBLs); compare the coordination geometries of protein-bound Ca^{2+} and Pb^{2+}; and finally understand how the change in the chemical environment of C2α brought about by Pb^{2+} binding affects the downstream reaction, which is the association of C2α with lipid membranes. In addition to reporting

---

[*] Reproduced with permission from: Krystal A. Morales, Mauricio Lasagna, Alexey V. Gribenko, Youngdae Yoon, Gregory D. Reinhart, James C. Lee, Wonhwa Cho, Pingwei Li, and Tatyana I. Igumenova. *Journal of the American Chemical Society* 2011, 133, 10599. Copyright 2011 © by the American Chemical Society.

on the Pb^{2+}-dependent activity of the parent enzyme, C2α can serve as a paradigm for the Ca^{2+}-dependent C2 domains that are found in other molecular targets of Pb^{2+}, such as synaptotagmin I and phospholipase C.[11]

The activation of PKC partially purified from rat brain by picomolar concentrations of Pb^{2+} was first reported in 1988.[76] The effect was shown to be specific to Pb^{2+}, as none of the other ten heavy metals that were tested activated PKC to the same extent as Pb^{2+} at picomolar concentrations. The evidence for multi-site interactions of Pb^{2+} with PKC was subsequently obtained by both in vivo and in vitro studies.[9,10,77] Micromolar concentrations of Pb^{2+} inhibited the constitutive kinase activity of both Ca^{2+}- dependent and -independent PKCs, suggesting the presence of a low-affinity Pb^{2+} site in the catalytic domain. Partial activation of PKC at picomolar to nanomolar Pb^{2+} concentrations was attributed to the presence of the high-affinity Pb^{2+}-binding site in the C2 domain. The second Pb^{2+}-binding site having a lower affinity than the first was suggested to have an inhibitory effect on PKC.[10] These experiments established the central role of the C2 domain in the Pb^{2+}-dependent modulation of PKC activity.

Current understanding of how divalent lead interacts with proteins has been shaped by the structural work on the Pb^{2+}-protein and -peptide complexes, mostly having thiolate-rich coordination sites. For example, the best-studied molecular target of Pb^{2+} is the Zn^{2+}-dependent 5-aminolevulinic acid dehydratase (ALAD), also known as porphobilinogen synthase.[78] Structural characterization of the Pb^{2+}-complexed yeast ALAD,[79] ab initio studies of the Pb^{2+} coordination geometry in the human enzyme,[80] and biochemical characterization of Pb^{2+}/Zn^{2+} substitution[81] revealed the central role of the stereochemically active $6s^2$ pair of Pb^{2+} in altering the geometry of the metal-binding site. The work of Godwin's laboratory on Pb^{2+} complexation of cysteine-containing peptides[82] showed that Pb^{2+} adopts a tri-coordinate geometry when replacing structural Zn^{2+} ions with tetrahedral coordination[83] and is thus unable to facilitate proper folding of zinc finger domains. Using the designed cysteine-rich peptides and ^{207}Pb NMR detection, Pecoraro's group developed sensitive methods for probing the coordination environment of Pb^{2+} in biological molecules.[84]

Interactions of Pb^{2+} with oxygen-rich coordination environment found in CBPs are not as well characterized as those with sulfur-rich sites. The only high-resolution structure of a Ca^{2+}- binding protein in complex with Pb^{2+} is that of calmodulin (CaM),[85] for which the non-EF hand Pb^{2+} binding sites were hypothesized to be responsible for CaM's lack of activation at high Pb^{2+} concentrations.[86]

In this work, C2α is used as a paradigm for the Ca^{2+}-dependent C2 domains to understand how Pb^{2+} affects their structure and membrane-binding properties. To our knowledge, this was the first time the interactions within the ternary system comprising a peripheral membrane domain, Pb^{2+} ions, and lipid bilayers were investigated at the molecular level. Using solution NMR methods and ITC, we established that Pb^{2+} binds to C2α with high affinity. We report high-resolution structures of apo and Pb^{2+}-complexed C2α, which makes C2α only the second protein after CaM with apo, Ca^{2+}-bound, and Pb^{2+}- bound structures available. Despite being only 4.1 Å apart in the structure, two Pb^{2+} ions adopt different coordination geometries due to the effect of the stereochemically active $6s^2$ electron pair. We used FRET spectroscopy to conduct Ca^{2+}-

and Pb^{2+}-driven C2α membrane-binding experiments, which revealed that Pb^{2+} is able to displace Ca^{2+} from C2α in the presence of PtdSer-containing membranes. In aggregate, our data demonstrate that Pb^{2+} can potentially act as a concentration-dependent modulator of the C2α-membrane interactions by competing with Ca^{2+} for the protein metal-binding sites and with C2α for the PtdSer membrane sites.

Experimental procedures

Materials

1-palmitoyl-2-oleoyl-sn-glycero-3-phosphocholine (POPC), 1-palmitoyl-2-oleoyl-sn-glycero-3- phospho-L-serine (POPS), and 1,2-dioleoyl-sn-glycero-3-phosphoethanolamine-N-(5-dimethylamino-1- naphthalenesulfonyl) (dansyl-PE) were obtained from Avanti Polar Lipids (Alabaster, AL).

Over-expression and purification of C2α

The C2α construct comprising residues 155-293 of PKCα (*Rattus norvegicus*) was cloned into a pET-SUMO vector (Invitrogen).[87] Over-expression was carried out in *E. coli* BL21(DE3) cells. Cell cultures were grown to an OD_{600} of 0.6 and induced with 0.5 mM IPTG for 4 hours at 37 °C for all natural abundance preparations. Isotopically enriched protein was over-expressed according to the method of Marley et al.,[88] with overnight induction at 15 °C. The M9 minimal media was supplemented with 1 g/L of $^{15}NH_4Cl$ and 3 g/L of $[^{13}C\text{-}6]$-D-glucose (or natural abundance D-glucose) as sole nitrogen and carbon sources, respectively. Fractionally deuterated protein sample was produced using M9 minimal media containing 75% ^2H_2O, 3 g/L of [^{13}C-6]-D-glucose, and 1 g/L of $^{15}NH_4Cl$.

The histidine-tagged SUMO-C2α fusion protein was purified using a HisTrap™ HP Ni affinity column (GE Healthcare Life Sciences). The fractions containing fusion protein were desalted on a HiPrep 26/10 column (GE Healthcare Life Sciences). Isolated C2α domain was obtained by cleaving the fusion protein for 30 minutes with histidine-tagged SUMO protease at room temperature, followed by another Ni affinity purification step to remove the histidine-tagged SUMO and SUMO protease. The final purification step was cation-exchange chromatography on a Source 15S column (GE Healthcare Life Sciences), carried out in 10 mM 2-(N-morpholino)ethanesulfonic acid (MES) buffer at pH = 6.0, 0.1 mM EDTA, and a linear concentration gradient of KCl. The purity of C2α was evaluated using SDS-PAGE. The molecular weight was verified by MALDI-TOF mass spectrometry.

All buffer solutions used in this study were treated with Chelex 100 (Sigma-Aldrich) to remove residual divalent metal ions. Decalcification of C2α was accomplished by incubating the protein with 0.1 mM EDTA, followed by extensive exchange of the protein solution into the EDTA-free buffer. For the NMR assignment experiments, the buffer composition for the final exchange step was 10 mM MES (pH 6.0), 8% D_2O, and 0.02% NaN_3. For the NMR-detected Ca^{2+} and Pb^{2+} binding experiments, 100 mM KCl was included in the buffer solution.

NMR spectroscopy

All NMR experiments presented in this chapter were carried out at 25 °C on Varian Inova spectrometers operating at ^{1}H Larmor frequencies of 500 MHz (11.7 Tesla) and 600 MHz (14.1 Tesla). The temperature was calibrated using methanol. Sequence-specific assignments of the ^{1}H, ^{13}Cα, ^{13}Cβ, and ^{15}N resonances for the apo C2α were obtained using gradient-enhanced triple-resonance NMR experiments HNCACB, CBCA(CO)NH,[89] and C(CO)NH.[90] ^{2}H-decoupled three-dimensional HNCACB and HN(CO)CACB experiments[91] were used to assign the [U-^{13}C,^{15}N; 55%-^{2}H] C2α samples in complex with Ca^{2+} and Pb^{2+}. NMR data were processed with nmrPipe[92] and assigned with Sparky.[93]Binding of Ca^{2+} and Pb^{2+} to C2α was monitored using ^{15}N-^{1}H Heteronuclear Single Coherence (HSQC) spectra of [U-^{15}N]-enriched 160 μM C2α domain. The desired concentration of divalent metal ions in the NMR sample was achieved using concentrated stock solutions of Ca(II) chloride and Pb(II) acetate. The Pb(II) acetate stock solution was prepared in the absence of chloride ions (10 mM MES, 8% D2O, 0.02% NaN_3) at pH 6.0 to avoid the formation of $Pb(Cl)_2$ species. The binding curves for Ca^{2+} and Pb^{2+} were constructed by plotting the absolute value of the change in ^{1}H and/or ^{15}N chemical shifts as a function of total metal concentration. The dissociation constant, K_d, for all single-site binding equilibria described in this work, was determined by globally fitting the binding curves using the following equation:

$$\Delta\delta = (\Delta\delta_{PL} / 2P_0)(P_0 + L_0 + K_d - \sqrt{(P_0 + L_0 + K_d)^2 - 4P_0L_0}) \quad \textbf{Equation 1}$$

where Δδ is the residue-specific absolute value of the observed change in the chemical shift for ^{15}N or $^{1}H_N$ at total ligand concentration L_0, $\Delta\delta_{PL}$ is the absolute value of the residue-specific chemical shift difference between the bound and apo forms of the protein, and P_0 is the total protein concentration.[94]

To estimate the Ca^{2+} binding affinity, we fit the binding curves individually using the Hill equation:

$$\Delta\delta = \Delta\delta_{PL}\,\frac{(L_0 - ((P_0 + L_0 + K_d - \sqrt{(P_0 + L_0 + K_d)^2 - 4P_0L_0})/2))^n}{K_d^n + (L_0 - ((P_0 + L_0 + K_d - \sqrt{(P_0 + L_0 + K_d)^2 - 4P_0L_0})/2))^n} \quad \textbf{Equation 2}$$

or the free ligand concentration correction equation, as implemented for the C2 domain of rabphilin-3A.[95]

To estimate the dissociation constant of the C2α·Pb·Ca complex the following mass balance equation for the system was derived:

$$\frac{[Ca^{2+}]_T}{P_0} = \frac{[Ca^{2+}]_F}{P_0} + P_{PbCa} + 2P_{Ca2} + 3P_{Ca3} = \frac{[Ca^{2+}]_F}{P_0} + P_{PbCa} + 2P_{Ca2} + P_{Ca3} \quad \textbf{Equation 3}$$

where $P_{Ca}=P_{Ca}^{2+}P_{Ca3}$. $[Ca^{2+}]_T$ is the total concentration of Ca^{2+}; $[Ca^{2+}]_F$ is the concentration of free Ca^{2+}; P_0=160 μM is the total concentration of C2α; P_{PbCa}, P_{Ca2}, and P_{Ca3} are the fractional populations of the C2α·Pb·Ca, C2α·Ca_2, and C2α·Ca_3 species, respectively. P_{Ca} was determined experimentally as described in the results section.

Here, P_{Ca3} was assumed to be 0, 0.5, and 1 for the three selected Ca^{2+} concentration points. Using Equation 3, $[Ca^{2+}]_F + [C2\alpha \cdot Pb \cdot Ca]$ was calculated to be 3.1, 7.8, and 19.7 mM. These numbers are within 4% of the corresponding $[Ca^{2+}]_T$ values. This means that total Ca^{2+} concentrations can be used instead of $[Ca^{2+}]_F$ to construct the binding curves (*vide infra*).

For chemical shift perturbation analyses in this chapter, the normalized change in the chemical shift was determined according to the following equation:

$$\Delta = [\Delta\delta_H^2 + (\gamma_N / \gamma_H \Delta\delta_N^2)^2]^{1/2} \quad \textbf{Equation 4}$$

where $\Delta\delta_H$ and $\Delta\delta_N$ are the residue-specific chemical shift changes, and γ_H and γ_N are the gyromagnetic ratios of ^1H and ^{15}N nuclei, respectively.

Isothermal titration calorimetry (ITC)

ITC was used to determine the affinity of Pb^{2+} to the first metal-binding site of C2α. The experiments were carried out at 25 °C using a VP-ITC calorimeter (Microcal Inc., Northampton, MA). Prior to the measurements, decalcified C2α was extensively dialyzed into 10 mM MES buffer (pH 6.0) containing 10 mM KCl. The concentration of protein in the sample cell was 35.4 µM. The Pb^{2+} titration solution was prepared in the same buffer from a 10 mM stock of Pb(II) acetate that was standardized using Inductively Coupled Plasma (ICP) measurements. The volume of the titration solution injected into the sample cell varied from 2 to 10 µl per injection. Dilution effects were taken into account by injecting the titrant into the reference cell containing pure buffer. The molar ratio of Pb^{2+} to C2α was 2.5 at the end of the titration. The data were fit to the independent binding sites model involving two sites using the Origin 5.0 software provided by the VP-ITC manufacturer. The presence of two Pb^{2+} binding sites was independently demonstrated using NMR experiments. The errors reported for the thermodynamic parameters are the errors obtained in the fitting procedures.

Crystallization of apo and Pb^{2+}-bound C2α

The crystals of C2α in the presence and absence of Pb^{2+} were grown using the hanging-drop vapor diffusion method. Apo C2α (24 mg/mL) was mixed 1:1 with the crystallization buffer comprising 100 mM HEPES (pH 7.5), 0.25 M lithium sulfate monohydrate, and 20% PEG 3350. For the Pb^{2+} complex, C2α (24 mg/mL) was incubated with 7.5 mM Pb(II) acetate solution and mixed 1:1 with the crystallization buffer comprising 100 mM bis-tris (pH 5.5), 0.25 M lithium sulfate monohydrate, and 20% PEG 3350. The crystals appeared after 4-5 days and were allowed to grow for 3 weeks at 25°C.

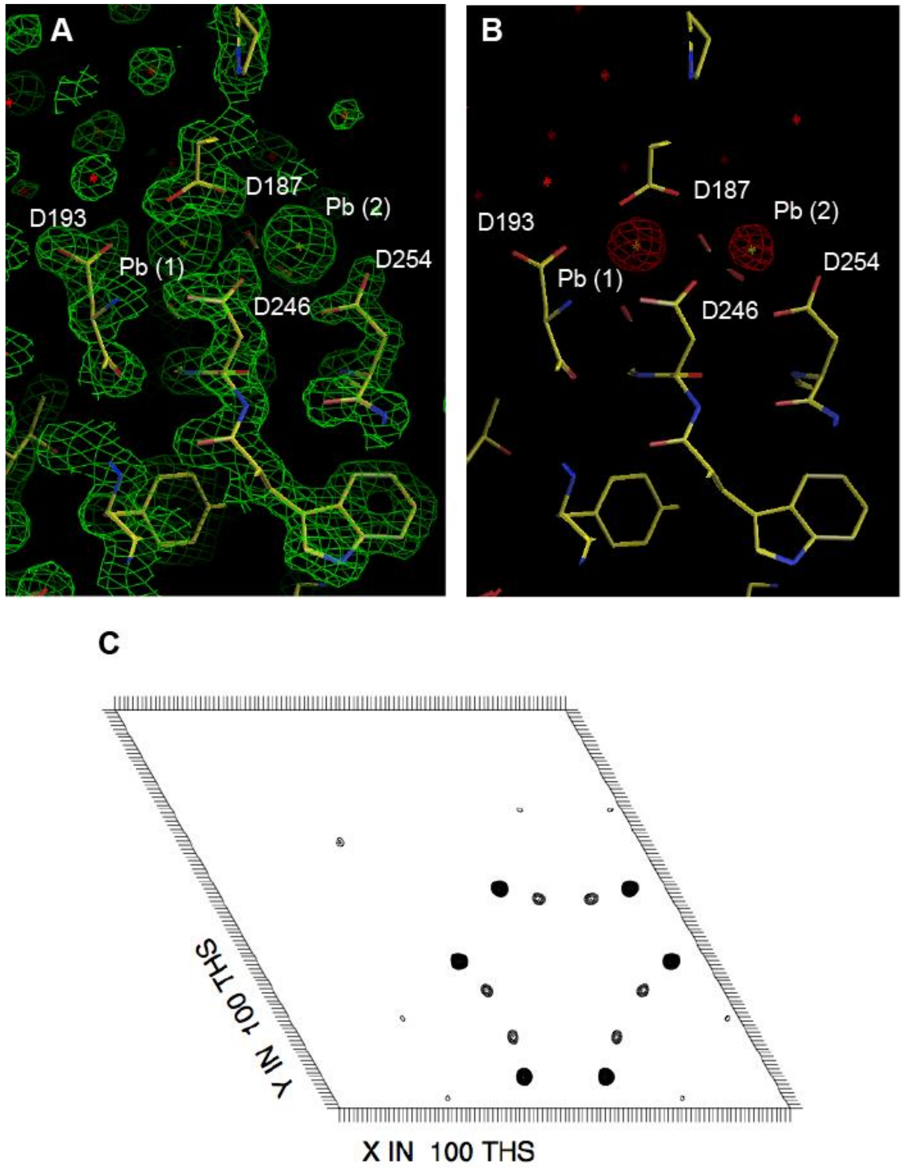

Figure 8. Electron density maps of the $C2\cdot Pb_2$ complex. (A) 2Fo-Fc map contoured at 1.2σ. (B) Anomalous difference map contoured at 15σ. The map was calculated with the model phases. (C) Harker section (z=1/3) of the anomalous difference Patterson map.

All diffraction data were collected using a Rigaku RAXIS IV^{++} image plate detector mounted on a Rigaku Micromax-007HF generator. The data were processed with the HKL2000 package.[96] The apo-C2α domain crystallized in space group $P3_221$ with the following cell parameters: a=41.49 Å, b=96.87 Å, c=103.40 Å, and γ=120°. The crystallographic asymmetric unit contains one C2α molecule. The Pb^{2+}-bound C2α also crystallized in space group $P3_221$ with slightly different unit cell dimensions: a=b=58.29 Å, c=87.98 Å. The structure of the Pb^{2+}-bound C2α was determined by molecular replacement using MOLREP in the CCP4 suite. The Ca^{2+}-bound C2α structure after the deletion of the Ca^{2+} ions (PDB ID: 1DSY)[52] was used as a search model. The electron density map for the Pb^{2+} ions was apparent in the 2Fo-Fc difference map (Figure 8A). Only two strong peaks corresponding to the lead ions were observed in the anomalous difference map (Figure 8B and Figure 8C), indicating that there was no nonspecific binding. The structural models were rebuilt using O and refined by several rounds of positional and B-factor refinement using CNS. Structure of the apo-C2α was refined using the high- resolution lead-bound C2 domain as a starting model. The structure was rebuilt with O and refined with CNS. The coordinates are available in the Protein Data Bank (http://www.pdb.org/) and the ID codes for the apo and Pb^{2+}-bound structures are 3RDJ and 3TWY, respectively.

Table 1. **Statistics of apoC2α and C2$\alpha\cdot$Pb$_2$ crystallographic analysis.**

Diffraction data	**Apo**	**C2·Pb^{2+}**
Wavelength (Å)	1.542	1.542
Space group	P3$_2$21	P3$_2$21
Unit cell	a=b=58.00 Å, c=90.46 Å	a=b=58.29 Å, c=87.98 Å
Resolution (Å)	50.0-1.90 (1.97-1.90)[a]	50.0-1.50 (1.55-1.50)[a]
Unique reflections	14383	27889
Redundancy	6.3 (6.2)	6.5 (4.0)
Completeness	99.8% (99.7%)	98.3 (93.2)
<I/σI>	47.5 (5.2)	60.4 (5.6)
R_{sym}(%)	5.3 (45.4)	7.4 (32.3)
Refinement		
Resolution (Å)	50-1.9	50.0-1.50
Reflections (F>0) (total/test set)	14022/1438	51491/5041
Protein atoms	1129	1129
Pb (II) ions	0	2
Sulfate ions	0	4
Solvent atoms	107	205
R_{cryst}/R_{free}	22.5%/24.5%	20.4%/21.9%
Rmsd bond length	0.010 Å	0.011 Å
Rmsd bond angle	1.67°	1.67°

[a] Values in the parentheses are for the highest-resolution shell; 10% of reflections are used in the test set for R_{free} calculation.

Metal-dependent membrane association of C2α by surface plasmon resonance

All Surface Plasmon Resonance measurements were performed at 24 °C using a lipid-coated Pioneer L1 chip (Biacore AB, Piscataway, NJ) in the BIACORE X system as described previously.[97] Briefly, after washing the sensor chip surface with the running buffer (20 mM HEPES, pH 7.4, containing 160 mM KCl), the active surface and the control surface of the sensor chip were coated with POPC/POPS (80:20) and POPC (100%) vesicles, respectively, to give the same resonance unit (RU) values. The level of lipid coating for both surfaces was kept at a minimum, which is necessary for preventing the non-specific adsorption to the sensor chips. This low surface coverage minimized the mass transport effect and kept the total protein concentration above the total concentration of protein binding sites on the vesicles. Equilibrium SPR measurements were carried out at the flow rate of 5 µl/min to allow sufficient time for the response values of the association phase to reach near-equilibrium values, R_{eq}. Each of the sensorgrams was corrected for a refractive index change by subtraction of the control surface response. We assumed a Langmuir-type binding between the protein (P) and protein-binding sites (L) on vesicles (i.e. P + L ⇔ PL). The K_d was determined by fitting the dependence of R_{eq} on the total protein concentration, P_0, with the following equation:

$$R_{eq} = \frac{R_{\max}}{(1 + \frac{K_d}{P_0})} \quad \textbf{Equation 5}$$

Metal-dependent membrane association of C2α by ultracentrifugation

Sucrose-loaded large unilamellar vesicles (LUVs) were prepared as described by Giorgione and Newton.[98] In brief, chloroform solutions of the lipid components were mixed at their desired molar ratios. The solvent was removed under N_2 followed by two hours under vacuum. The lipid film was hydrated with the sucrose buffer (10 mM MES at pH 6.0 and 170 mM sucrose), vortexed, and subjected to five freeze/thaw cycles. An Avanti Polar Lipids mini-extruder with a 100 nm polycarbonate filter was used to prepare LUVs. Phosphate quantification assays[99] were used to determine the lipid concentration after extrusion and the pelleting efficiency of the LUVs, which was >98%

for all experiments. 5 μM C2α was incubated with 1.5 mM or 10 mM total lipid LUVs (POPC/POPS, 67:33 mole percent) for one hour, followed by the addition of the divalent metal ion to the desired concentration. After a 20-minute incubation period, LUVs were centrifuged in a Beckman TL-100 tabletop ultracentrifuge for 30 minutes at 50,000 rpm and 25°C. The amount of C2α in the supernatant was quantified using the bicinchoninic acid (BCA) assay kit (Thermo Scientific). The fraction of membrane-bound C2α was calculated as:

$$f_{bound} = \frac{P_0 - P_{\mathrm{sup}}}{P_0} \quad \textbf{Equation 6}$$

where P_0 is the total amount of protein in the sample, and P_{sup} is the amount of protein present in the supernatant at a given metal concentration. Metal-free ultracentrifugation experiments were used to quantify the non-specific binding of C2α to membranes, which was <5% in all experiments.

Metal-dependent membrane association of C2α by FRET

Ca^{2+}- and Pb^{2+}-dependent membrane association of C2α was monitored by FRET between the tryptophan residues of C2α and the fluorescent lipid, dansyl-PE.[100] Pb^{2+} or Ca^{2+} from the concentrated stock solutions was added into a mixture of 0.5 μM C2α in 10 mM MES (pH 6.0) and 100 mM KCl, and LUVs with a total lipid concentration of 150 μM. $PbCl_2$ remains soluble at these concentrations of Pb^{2+} and Cl^{-} ions. The LUVs' composition in the binding experiments was POPC/POPS/dansyl-PE (60:33:7).

POPC/dansyl-PE (93:7) LUVs were used to test the PtdSer specificity of C2α in the presence of Pb^{2+}.

The change in dansyl-PE fluorescence at 25°C was monitored using an ISS Koala fluorometer (ISS, Champaign, IL). Excitation and emission wavelengths were 295 and 494 nm, respectively. The “blank” sample contained all reactants but C2α; its signal was subtracted from that of the C2α- containing sample. The change in fluorescence upon metal binding, ΔF, relative to the maximal change, ΔF_{max}, was plotted as a function of the total metal concentration. The binding curves were fit with the Hill equation:

$$\Delta F / F_{\max} = \frac{[M^{2+}]^{H}}{[M^{2+}]^{H} + [M^{2+}]_{1/2}^{H}} \quad \textbf{Equation 7}$$

where H is the Hill coefficient and $[M^{2+}]_{1/2}$ is the metal concentration required to achieve the half-maximal fluorescence change.

Cryoelectron microscopy of LUV suspensions in the presence of divalent metal ions

To verify the integrity of the LUVs in the presence of Pb^{2+}, we collected cryoelectron microscopy (cryoEM) images of the vesicle suspensions. For comparison, we also acquired images of LUVs in the presence of Ca^{2+}. The total concentrations of metal ions and lipid were 1 mM and 1.5 mM, respectively. For metal ions, 1 mM is the maximum concentration that was used in our ultracentrifugation binding assays. The concentration of the PtdSer lipid component adjusted for the leaflet distribution was 247.5 μM.

5 μl of the LUV suspension pre-incubated with the respective metal ion was applied onto a carbon-coated copper grid. The grids were rendered hydrophilic by glow discharging. The grids were then plunge-frozen in ethane using an FEI Vitrobot. Samples were observed on a Tecnai G2 F20 FE-TEM instrument equipped with a GATAN Tridiem imaging filter. The acceleration voltage was 200 kV.

Association of Pb^{2+} with PtdSer-containing membranes quantified by inductively coupled plasma (ICP) measurements

To determine if Pb^{2+} can associate with lipid membranes, we carried out an ultracentrifugation binding experiment as described in the Experimental Section, but without the protein. The concentrations of Pb^{2+} in the supernatant ($[Pb^{2+}]_{free}$) and pellet ($[Pb^{2+}]_{bound}$) fractions were determined using ICP measurements. In brief, samples were digested with Fisher Optima nitric acid, hydrogen peroxide, and hydrochloric acid and diluted to the desired volume with 18.2 MΩ MilliQ water. The measurements were carried on a Perkin Elmer DRC 2 inductively coupled plasma mass spectrometer. The samples were run in the "standard mode" using external calibration, with Bi-209 as the internal standard.

The total Pb^{2+} concentration varied from 0 to 1 mM, and the total lipid concentration was 1.5 mM. The total concentration of the PtdSer component, adjusted for the distribution between the inner and outer leaflets of the bilayer was 247.5 μM. The fractional population of Pb^{2+}-bound PtdSer, θ, was calculated as:

$$\theta = [Pb^{2+}]_{bound}/[PtdSer]_{total} \quad \textbf{Equation 8}$$

The data were fit using the following equation for single-site binding:

$$\theta = \frac{[Pb^{2+}]_{free}}{K_d + [Pb^{2+}]_{free}} \quad \textbf{Equation 9}$$

where K_d is the dissociation constant for the Pb^{2+}-PtdSer interaction.

Results

C2α binds Pb^{2+} with high affinity

To establish if C2α is indeed capable of binding Pb^{2+} and if the modes of protein-metal interaction are different for Pb^{2+} and Ca^{2+}, the interaction of [U-^{15}N]-enriched apo C2α with both metal ions was characterized using NMR. Expansions of the protein ^{15}N-^{1}H Heteronuclear Single Quantum Coherence (HSQC) spectra in the presence of varying concentrations of Ca^{2+} (Column A) and Pb^{2+} (Column B) are shown in Figure 9 for four representative residues: Gly190, Asp248, Ile215, and Asp254.

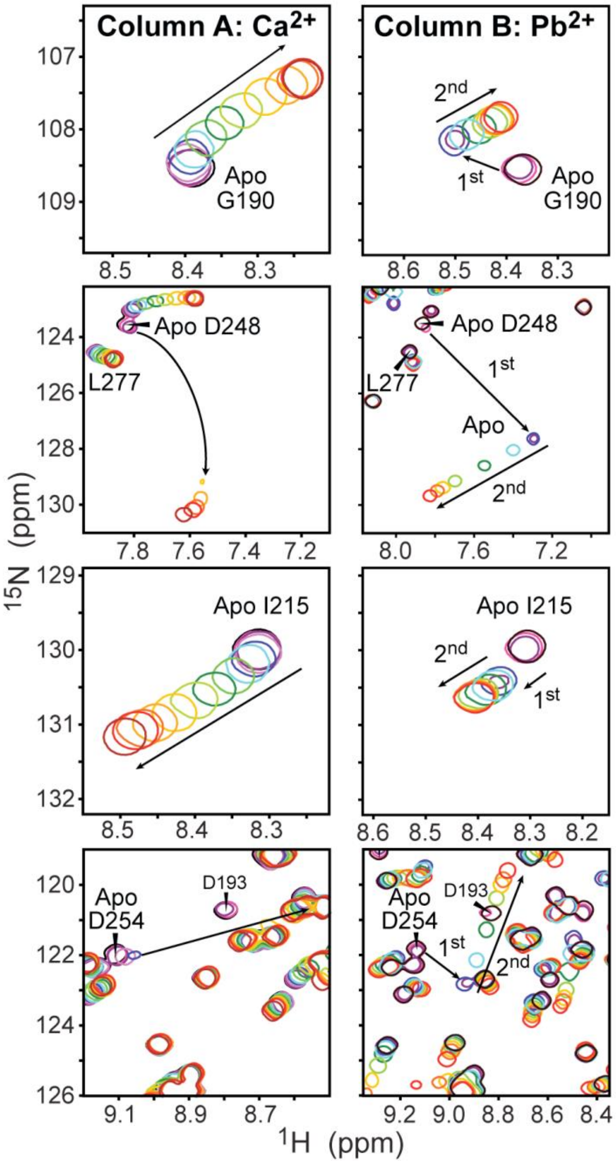

Figure 9. C2α binds Pb^{2+} with higher affinity than Ca^{2+}. Expansions of the ^{15}N-^{1}H HSQC spectra illustrate the differences in the response of Gly190, Asp248, Ile215, and Asp254 to Ca^{2+} (column A) and Pb^{2+} (column B). The protein concentration was 160 µM. The arrows point in the direction of increasing concentration of metal ions, which varies from 0 to 3.2 (1.28) mM for Ca^{2+} (Pb^{2+}).

Two of these residues, 248 and 254, are involved in direct coordination with Ca^{2+}.[52] The arrows in the spectra point towards the increasing concentration of metal ions, which ranges from 0 to 3.2 mM for Ca^{2+} and from 0 to 1.28 mM for Pb^{2+}. The binding regime of Ca^{2+} to C2α is intermediate-to-fast on the chemical-shift timescale. For residues that are in the fast exchange regime, such as Gly190 and Ile215, the cross-peaks follow a smooth curved trajectory. This behavior is analogous to what has been observed previously for C2 domains from synaptotagmin and PKCβ,[101] and is indicative of C2α binding two Ca^{2+} ions with comparable affinities (*vide infra*).

As shown in Column B, the spectra of C2α in the presence of Pb^{2+} exhibit a very different pattern. The NMR spectra clearly show the presence of two Pb^{2+} binding sites with different binding affinities. The first Pb^{2+}-binding event is slow on the chemical-shift timescale, which manifests itself in the appearance of cross-peaks corresponding to single-Pb^{2+} bound species in addition to the apo form. The binding of the second Pb^{2+} is in fast exchange, with the cross-peaks following a linear trajectory. The slow exchange behavior of the first Pb^{2+} binding event precluded the determination of the dissociation constant, K_{d1}^{Pb}, based on the NMR spectra. Instead, we used ITC to characterize the thermodynamics of the first binding step. A typical ITC titration profile is shown in Figure 10A. The ITC data were fit as described in the experimental procedures to obtain the following parameters for the first site: n_1=0.566±0.002, K_{d1}^{Pb}=66.7±0.3 nM, ΔH_1=-5.59±0.04 kcal/mol, and ΔS_1=14.1 cal/mol·K. In separate ITC experiments, the stoichiometry of binding n_1 ranged from 0.6 to 1.1 for the first site in our ITC experiments. The deviation of the binding stoichiometry from 1 in C2α has been reported previously.[58] In our case, this behavior is likely caused by variable amounts of binding-competent apo C2α, which is extremely sensitive to stirring and other types of mechanical agitation. The apparent stoichiometry of binding had no effect on the obtained values of the thermodynamic parameters. Because of the low affinity of Pb^{2+} to the second site of C2α, the isotherm for this binding event is extremely shallow with no clear transition. The isotherm shape parameter c is estimated at ~0.4, whereas it needs to be between 5 and 500 to enable reliable determination of the second site parameters. To circumvent this problem, we reduced the total number of fitting parameters by holding n_2 constant at 1 and obtained the following values for the second site: $K_{d2,ITC}^{Pb}$=91±1 μM, ΔH_2=-1.8±0.6 kcal/mol, and ΔS_2=12.4 cal/mol·K. These values should be treated as estimates only. We used solution NMR experiments to obtain an accurate value of K_{d2}^{Pb}. To determine K_{d2}^{Pb}, we constructed binding curves for the second site by plotting the absolute values of ^{15}N and/or ^{1}H chemical shift changes as a function of the total Pb^{2+} concentration. Several representative binding curves for residues that belong to CBL3 (top), and CBL1/CBL2 (bottom) are shown in Figure 10B. The relevant regions of the primary structure are indicated in Figure 10C, with the metal-coordinating residues shown in boldface/italics. The fitting of 34 residue-specific ^{1}H and ^{15}N binding curves with Equation 1 produced K_{d2}^{Pb}=129±4 μM.

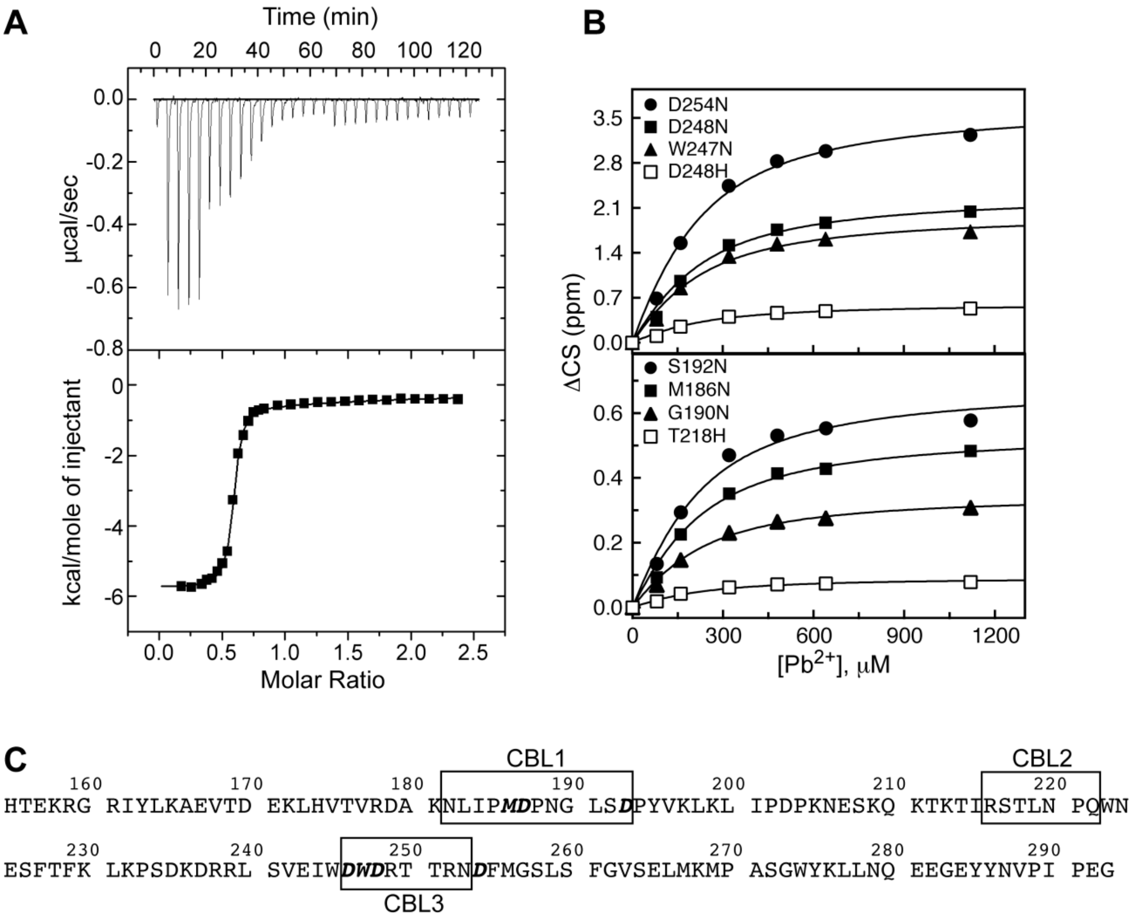

Figure 10. Differential affinities of the two C2α Pb^{2+} metal-binding sites. (A) The ITC profile for the titration of site (1) with Pb^{2+}. (B) NMR binding curves constructed using Pb^{2+} titration experiments for site (2). (C) Primary structure of C2α highlighting the loop regions (boxed) and coordinating residues (boldface/italicized).

The binding behavior in the presence of Ca^{2+} is very different. It is evident from the Ca^{2+} titration spectra that the metal-binding sites of C2α have comparable affinities to Ca^{2+} ions. The presence of three species, C2α-Ca(1), C2α-Ca(2) and C2α-(Ca)$_2$, each having its own chemical shift, precludes the use of an analytical function to describe the binding process. In addition, all Ca^{2+} binding curves show a lag period, indicating some degree of positive cooperativity. To estimate the binding affinity, we fit the binding curves individually with the Hill equation (Equation 2). The range of apparent K_d values is 250-530 μM, with the median of 350 μM. This range reflects the differential response of C2α residues to Ca^{2+} binding and the approximation, under which the concentration of free ligand is considered to be approximately equal to the total concentration of the ligand. Correction for the free ligand concentration, implemented as described for the C2 domain of rabphilin-3A,[95] gives a K_d range of 150-480 μM with the median of 270 μM. Several representative Ca^{2+} binding curves are shown in Figure 11 for the residues that belong to Ca^{2+}-binding loop regions CBL1, CBL2, and CBL3.

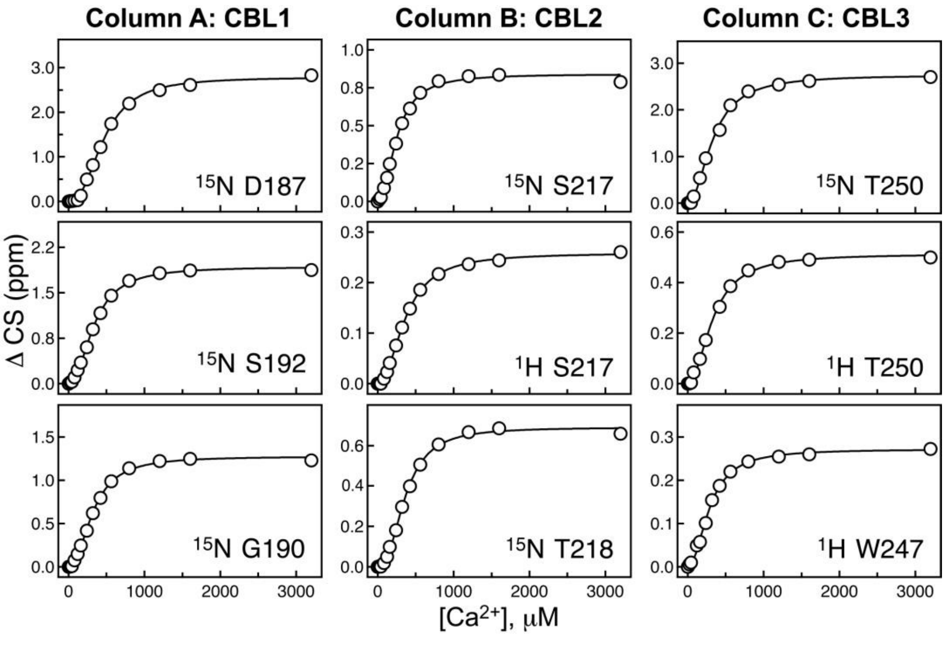

Figure 11. Representative Ca^{2+} titration curves for residues that belong to Ca^{2+}-binding loops 1, 2, and 3. The absolute change in chemical shift is plotted as a function of the total Ca^{2+} concentration. The fits were generated using Equation 2. C2α concentration is 160 μM.

From this set of experiments, we concluded that C2α binds Pb^{2+} with significantly higher affinity than Ca^{2+}. In addition, there is a 2000-fold difference in the K_d values for the two sites of Pb^{2+}. We will hereafter refer to these two sites as high- and low-affinity.

Identification of the high-affinity Pb^{2+} binding site

Chemical shifts are exquisitely sensitive to the changes in the electronic environment of nuclei caused by binding events. We used chemical shift perturbation analysis to identify the high-affinity Pb^{2+} site of C2α and determine which regions of the protein are selectively affected by the binding of the first and second Pb^{2+} ions. To probe individual Pb^{2+}-binding events, the chemical shift perturbations, Δ, were calculated using Equation 4 for the C2α·Pb complex relative to the apo form, and for the $C2\alpha\cdot Pb_2$ complex relative to the C2α·Pb. The results are plotted as a function of primary structure in Figure 12A, and mapped onto the three- dimensional structure of apo C2α (*vide infra*) in Figure 12B. It is evident that filling the high-affinity Pb^{2+} site affects both CBL1 and CBL3 regions, while filling the low-affinity site mainly affects CBL3.

Based on our NMR data, the crystal structure of the ternary C2α·Ca·PtdSer complex,[52] and the crystal structure of the Pb^{2+}-bound C2α reported in this work (*vide infra*), we could immediately assign the high-affinity site to site (1) and low-affinity site to site (2), in the nomenclature used for Ca^{2+}.[52]

To compare the effects of Pb^{2+} and Ca^{2+} on C2α, we also carried out the chemical shift perturbation analysis of $C2\alpha\cdot Ca_2$ relative to the apo form. The results are shown in

Figure 12C and Figure 12D. Overall, the perturbation pattern is similar to that observed for C2α·Pb_2, with the CBL1, CBL2, and CBL3 regions being affected the most. Some differences between Pb^{2+} and Ca^{2+} are observed in the region between the N-terminus and CBL1. This region is not responsive to Ca^{2+} but is perturbed upon binding of the second Pb^{2+} ion. The chemical shift changes induced by metal binding within this region were proven to originate from changes in the conformational dynamics, and are detailed in Chapter V (*vide infra*). There are several features that are worth noting at the level of individual amino acids. The most responsive residue to binding of both Ca^{2+} and Pb^{2+} is Asp248, whose sidechain carboxyl group serves as a ligand to both metal sites, according to the crystal structure of the ternary C2α·Ca_2·PtdSer complex.[52] Another notable residue is Asn189, which belongs to CBL1. Although Asn189 is not involved in metal-ion coordination, the binding of the first Pb^{2+} and Ca^{2+} ions significantly perturbs the chemical shifts of its backbone N-H group. This residue has been implicated in the interactions of C2α with the PtdSer component of plasma membrane.[64,102] Phe255 of the CBL3 region showed a strong chemical shift response to Ca^{2+} binding but none to Pb^{2+}. Phe255 is thought to be involved in putative intra-domain interactions within full-length PKCα that get disrupted when the enzyme associates with lipid membranes upon binding Ca^{2+}.[40] In summary, solution NMR experiments enabled us to identify the high-affinity Pb^{2+} site, and revealed that binding of Pb^{2+} and Ca^{2+} has a similar effect on the backbone conformation and electrostatic properties of C2α.

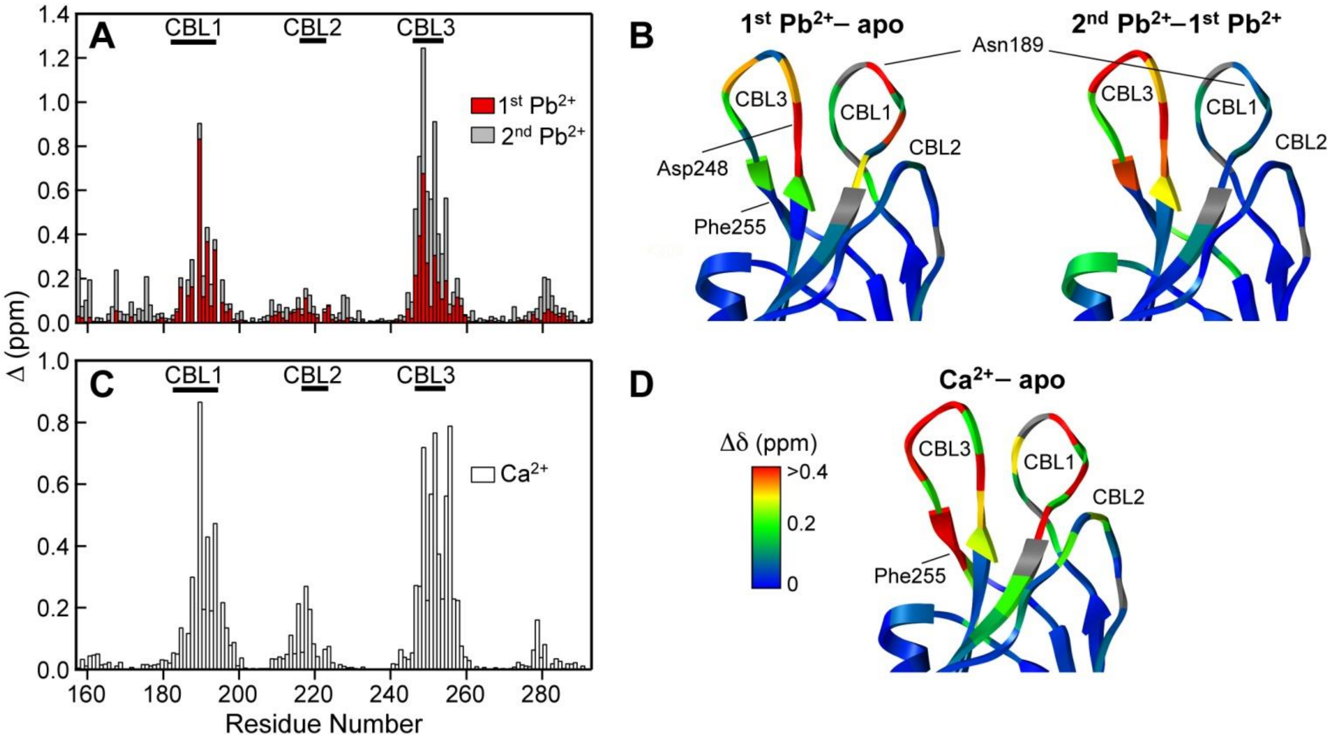

Figure 12. Pb^{2+} and Ca^{2+} induced chemical shifts to C2α Δ values for the first and second (gray) Pb^{2+} binding events plotted as a function of primary structure in (A), and mapped onto the CBL region of apo C2α in (B). Δ values for the Ca^{2+}-bound C2α plotted as a function of primary structure in (C), and mapped onto the CBL region of apo C2α in (D). Proline residues, for which data are not available, are shown in gray.

Pb(2) adopts a hemidirected coordination geometry in the C2α·Pb$_2$ structure

To gain insight into the conformational preferences of metal-ion ligands and the coordination geometry of protein-bound Pb^{2+}, we determined the crystal structures of C2α in apo and Pb^{2+}-bound forms. The 1.9 Å resolution structure of apo C2α is the first and only ligand-free structure of a C2 domain from a conventional PKC isoenzyme. The 1.5 Å resolution structure of Pb^{2+}-bound C2α has two well-defined Pb^{2+} ions specifically coordinated by the protein, and is referred to as the C2α·Pb$_2$ complex in this work. Non-specific association of Pb^{2+} ions with the charged sidechains on the protein surface was not observed. High resolution of both crystal structures enabled us to analyze the conformation of the CBL regions and determine the detailed geometry of both metal-binding sites. Figure 13A shows the backbone superposition of apo C2α, C2α·Pb$_2$, and C2α·Ca·PtdSer[52] complexes. With the apo form as a reference structure, the pair-wise root-mean-squared deviations (RMSDs) for the backbone atoms are 0.49 Å and 0.37 Å for the C2α·Ca2·PtdSer and C2α·Pb$_2$ complexes, respectively. At least in protein crystals, the binding of divalent metal ions has little effect on the backbone conformation of the protein core and the CBLs regions. However, detailed inspection of the metal coordination site in apo and C2α·Pb$_2$ structures revealed significant differences in the positions of metal-coordinating oxygen atoms.

The metal coordination sites in apo C2α and the C2α·Pb$_2$ complex are contrasted in Figure 13B. Amino acid sidechains that contribute an oxygen ligand to the metal-coordination sphere in either Ca^{2+} or Pb^{2+}-bound forms are labeled. Notable differences are observed in the sidechain conformations of Asp246, Asp248, and Asp254. As shown in Figure 13C, the carboxyl oxygens of Asp246 and Asp248 sidechains are involved in coordination bonds with both metal sites, while the Asp254 sidechain coordinates only to site (2). In addition to the coordinating residues, we observed a significant change in the conformations of the Arg252 and Arg216 sidechains. Both residues belong to the CBL regions, with Arg216 implicated in the interactions with PtdSer.[102]

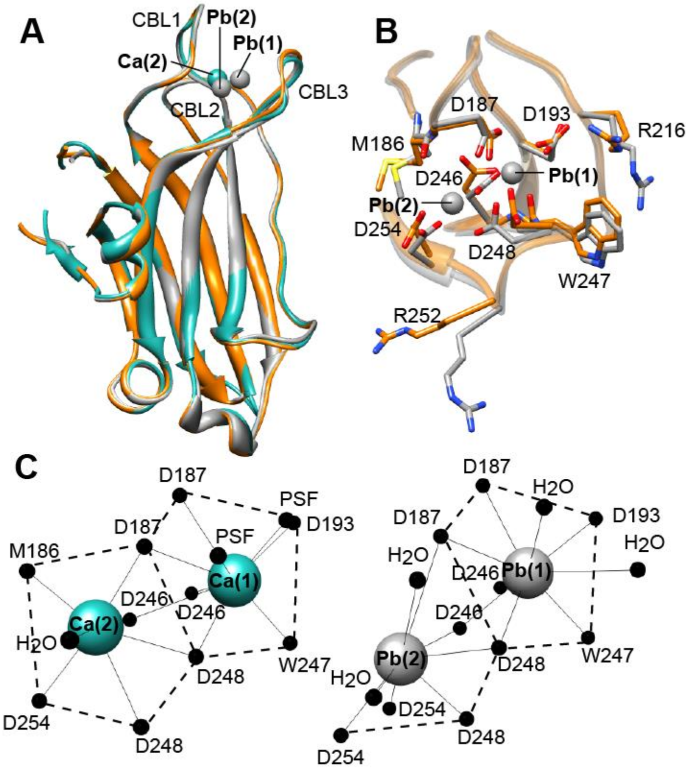

Figure 13. C2α structural characterization reveals hemidirected coordination for Pb(2). (A) Backbone superposition of apo C2α (orange), C2α·Pb_2 (gray), and C2α·Ca_2·PtdSer (cyan) complexes. The corresponding PDB ID codes are 3RDJ, 3 3TWY, and 1DSY. Ca(1) and Pb(1) are superimposable. (B) Detailed view of the metal coordination sites in apo and Pb^{2+}-bound C2α using the same color-coding scheme as in (A). (C) Top view of the metal coordination geometries in Ca^{2+}- and Pb^{2+}-bound C2α. PSF stands for 1,2-dicaproyl-sn-phosphatidyl-L-serine.

The metal coordination geometries for Ca^{2+} and Pb^{2+} are compared in Figure 13C. Pb(1), which we identified as a high-affinity site, has nine ligands that are arranged around the metal center in a manner similar to that of Ca(1). To identify the ligands, we used the 3.5 Å cutoff distance determined in the analysis of the Pb-O bond lengths in protein-Pb^{2+} complexes[104] deposited in the Protein Data Bank. The seven protein ligands are: Asp187 Oδ1 and Oδ2; Asp193 Oδ2; Asp246 Oδ1 and Oδ2; Trp 247 O; and Asp248 Oδ1. There are also two water molecules whose oxygens provide the two top axial ligands. In the Ca(1) coordination sphere, these positions are occupied by the phosphoryl oxygens of PtdSer, although some uncertainty about the ligand conformation in the structure was noted by the authors.[52]

A striking difference was observed in the metal coordination geometries of site (2). In Pb^{2+}-bound structure, we observed that eight ligands occupy one coordination hemisphere, while the other hemisphere is devoid of any ligands. This is the hallmark of the hemidirected coordination geometry of lead. The hemidirected geometry is characterized by the spatial expansion of the $6s^2$ lone pair of Pb, forcing all ligands to be accommodated on one side of the coordination sphere. The protein ligands for Pb(2) are: Asp187 Oδ1; Asp246 Oδ2; Asp254 Oδ1 and Oδ2; and Asp248 Oδ2. There are two additional oxygen ligands that are provided by water molecules.

Another signature of the hemidirected geometry is shorter than average metal-ligand distances for ligands opposite of the active lone pair, and longer than average distances for ligands adjacent to the lone pair.[105] The Pb-O coordination bond lengths for Pb(1) and Pb(2) are summarized in Table 2. Pb(1) has a holodirected geometry characterized by uniform distribution of ligands in the coordination sphere. As a result, the Pb-O distances are fairly uniform and do not deviate significantly from the average of 2.7±0.4 Å, which was reported in the Protein Data Bank analysis by Kirberger et al.[104] In the Pb(2) coordination sphere, we detected <2.4 Å distances for two ligands that are directly opposite to the active lone pair, Asp246 (Oδ2) and Asp248 (Oδ2). In contrast, the two ligands that are flanking the "void" in the coordination sphere, D187 Oδ1 and H_2O (3), have coordination bond lengths of 3.4-3.5 Å (Table 2).

Table 2. Pb-O Distances in the C2α·Pb_2 structure.

Pb(1), CN=9 Holodirected	Bond length (Å)	Pb(2), CN=8 Hemidirected	Bond length (Å)
D187 (Oδ1)	2.69	D187 (Oδ1)	**<u>3.40</u>**[b]
D187 (Oδ2)	2.69	D246 (Oδ2)	**2.38**[c]
D193 (Oδ2)	2.57	D248 (Oδ1)	2.80
D246 (Oδ1)	2.53	D248 (Oδ2)	**2.34**
D246 (Oδ2)	2.61	D254 (Oδ1)	2.59
W247 (O)	2.70	D254 (Oδ2)	2.55
D248 (Oδ1)	2.74	H_2O (47)	**<u>3.47</u>**
H_2O (26[a])	3.28	H_2O (76)	2.61
H_2O (85)	2.98		
Average distance	2.75 ± 0.23	Average distance	2.77 ± 0.44

[a] Water molecule labels are shown in Figure 13**C**.
[b] Distances that are longer than average are shown in boldface and underlined.
[c] Distances that are shorter than average are shown in boldface.

In summary, our structural work shows that the apo form of C2α is a rigid scaffold with flexible loops. The metal coordination site that is formed mostly by CBL1 and CBL3 is not pre-organized for metal binding. In contrast to Ca(2), Pb(2) adopts a hemidirected coordination geometry, in which the oxygen-donating ligands occupy a single coordination hemisphere.

Pb(1) reduces the affinity of C2α to calcium ions

Having determined the coordination geometries of Pb(1) and Pb(2), we tested the feasibility of the formation of mixed Pb(1)/Ca(2) C2α species. It has been suggested that binding of Ca^{2+} to site (2) when Pb^{2+} is present at high-affinity site (1) results in full activation of PKCα.[10] Taking advantage of the differential Pb^{2+}-binding affinities of C2α, we prepared the C2α·Pb complex. The progress of Ca^{2+} binding to C2α·Pb was monitored by ^{15}N-^{1}H HSQC NMR experiments. Figure 14 shows the expansion of the NMR spectra illustrating the response of Asp248 to increasing concentration of Ca^{2+}. The Ca^{2+} concentration ranged from zero (blue) to 20 mM (red). The maximum Ca^{2+} excess relative to C2α and Pb^{2+} was 125-fold. The titration behavior can be broken down into four steps that are summarized in Scheme 1 of Figure 14.

Step 1 corresponds to the formation of the high affinity C2α·Pb complex by adding a stoichiometric amount of Pb^{2+} to a 160 μM solution of C2α. Ca^{2+} binds to the vacant site (2) of the C2α·Pb in Step 2 to form the C2α·Pb·Ca complex. C2α·Pb and C2α·Pb·Ca are in fast exchange on the chemical shift timescale, as manifested by the smooth trajectory of the exchange-averaged cross-peak in response to increasing Ca^{2+}

concentration. At a total Ca^{2+} concentration of 3.2 mM, we observed an appearance of another cross-peak whose position is coincident with that of Asp248 in the $C2\alpha \cdot Ca_2$ complex, as shown in Figure 9. The two cross-peaks are shown in dark green and are connected with a double-headed arrow in Figure 14. This process, referred to as Step 3 in our reaction scheme, is the displacement of Pb^{2+} from the high-affinity site (1) by Ca^{2+}. The exchange of Pb^{2+} for Ca^{2+} in the $C2\alpha \cdot Pb \cdot Ca$ complex is a slow process on the chemical shift timescale. This means that the sum of the "on" and "off" kinetic rate constants in Step 3 is much smaller than the Asp248 chemical shift difference in the $C2\alpha \cdot Pb \cdot Ca$ and $C2\alpha \cdot Ca$ complexes.[106] At Ca^{2+} concentrations above 3.2 mM, we observed the titration of the newly formed $C2\alpha \cdot Ca_2$ species in what is defined as Step 4. We interpret this process as the binding of a third Ca^{2+} ion to the $C2\alpha \cdot Ca_2$ with the formation of $C2\alpha \cdot Ca_3$. The formation of the $C2\alpha \cdot Ca_3$ species is supported by the observation that the cross-peaks affected most by high concentrations of Ca^{2+} belong to Asp248, Asp254, Thr251, and Arg252. These residues coordinate the third Ca^{2+} ion in the two crystal structures of C2α that were obtained under conditions of large Ca^{2+} excess with respect to the protein.[59,107]

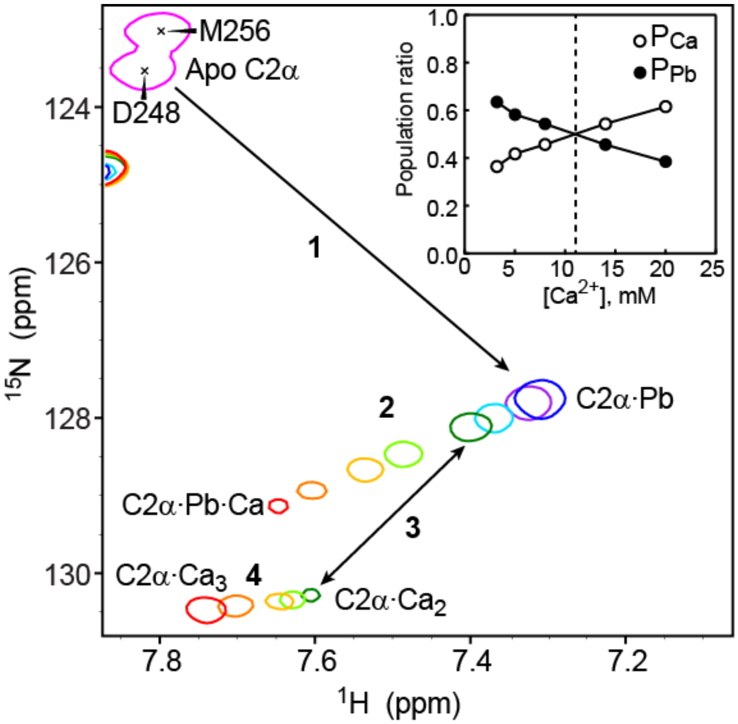

Scheme 1

$$\mathrm{C2\alpha + Pb^{2+} \overset{1}{\rightleftharpoons} C2\alpha{\cdot}Pb}$$

$$\mathrm{C2\alpha{\cdot}Pb + Ca^{2+} \overset{2}{\rightleftharpoons} C2\alpha{\cdot}Pb{\cdot}Ca}$$

$$\mathrm{C2\alpha{\cdot}Pb{\cdot}Ca + Ca^{2+} \overset{3}{\rightleftharpoons} C2\alpha{\cdot}Ca_2 + Pb^{2}}$$

$$\mathrm{C2\alpha{\cdot}Ca_2 + Ca^{2+} \overset{4}{\rightleftharpoons} C2\alpha{\cdot}Ca_3} \quad \text{125-fold Ca}^{2+}\text{ excess}$$

Figure 14. Pb(1) reduces the affinity of C2α to Ca^{2+}. Expansion of the ^{15}N-^{1}H HSQC spectra showing the response of residue Asp248 in the preformed C2α·Pb complex to the addition of Ca^{2+} ions. Concentration of Ca^{2+} ions ranged from 0 mM (blue) to 20 mM (red). Inset: fractional populations of Ca-only (P_{Ca}) and Pb-containing (P_{Pb}) protein species as a function of the total Ca^{2+} concentration.

Increasing Ca^{2+} concentration also results in the redistribution of the cross-peak intensities between the Pb^{2+}-bound and Ca^{2+}-only C2α complexes. This is illustrated in the inset of Figure 14, which shows fractional populations of Pb^{2+}-bound (C2α·Pb·Ca and C2α·Pb) and Ca^{2+}-only (C2α·Ca and C2α·Ca_3) protein species. The populations were calculated using the cross-peak volumes determined in Steps 2 and 4. Equal populations are reached around 11 mM total concentration of Ca^{2+}. Using the results of the titration experiments, we estimated the affinity of Ca^{2+} to the preformed C2α·Pb complex. We interpreted the results of the Ca^{2+} titration of the preformed C2α·Pb complex using the equilibria shown in scheme 1 of Figure 14. To estimate the dissociation constant of the C2α·Pb·Ca complex in Step 2 from the NMR titration data the dependence of the chemical shift on the total concentration of Ca^{2+} was fitted using Equation 1. However, Ca^{2+} is also consumed in Steps 3 and 4 to form the Ca^{2+}-bound protein species. Hence, the extent to which the total Ca^{2+} concentration has to be modified to reflect the depletion of the Ca^{2+} pool was estimated using Equation 3 as described in the methods section. We selected three Ca^{2+} concentration points for the analysis: 3.2, 8, and 20 mM. The corresponding populations of the Ca^{2+}-bound protein species (P_{Ca}) are 0.365, 0.457, and 0.615. The calculated concentrations were within 4% of the corresponding $[Ca^{2+}]_T$ values. In this case the total concentration was directly used to estimate the affinity. Several binding curves with fits generated using Equation 1 are shown in Figure 15. The apparent dissociation constant is 13±1 mM, which represents a ~50-fold reduction in Ca^{2+}-binding affinity compared to the apo C2α. Formation of the mixed C2α·Pb·Ca species as a result of Pb^{2+} exposure *in vivo* cannot be completely excluded. However, given the metal-binding affinities that we determined in this work, a more plausible scenario would involve the formation of either C2α·Pb complex or fully Ca^{2+}-bound species if Ca^{2+} were in large excess compared to Pb^{2+}.

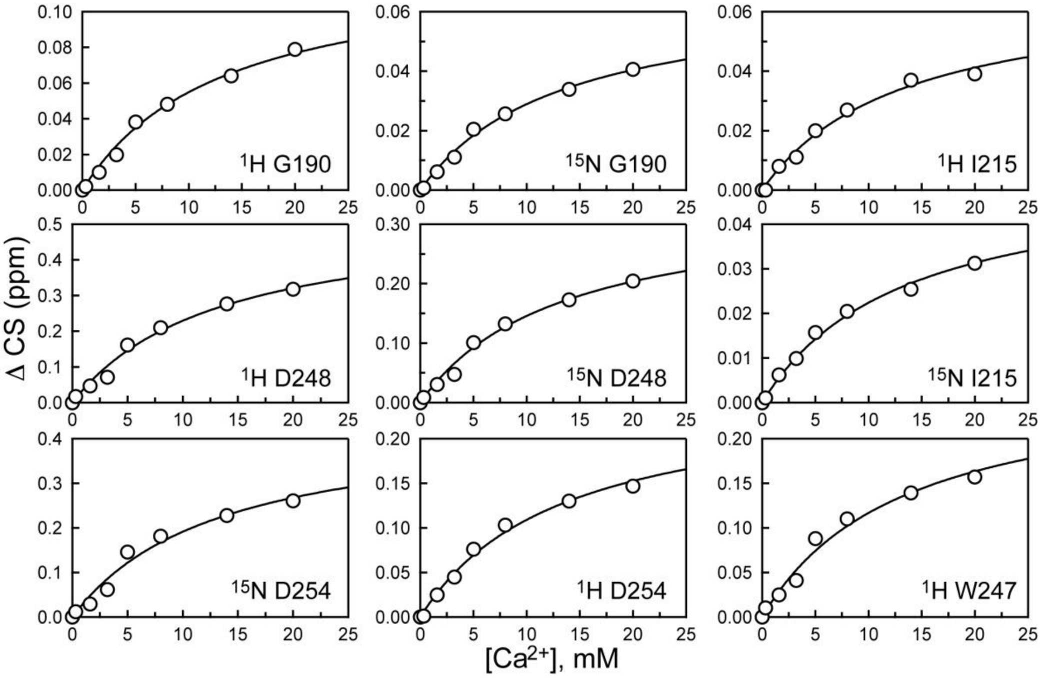

Figure 15. Ca^{2+} titration curves for residues of the preformed C2α·Pb·Ca complex. The absolute change in chemical shift is plotted as a function of the total Ca^{2+} concentration. The fits were generated using Equation 1.

Pb^{2+} binding drives membrane association of C2α and successfully competes with Ca^{2+} for C2α binding sites in the presence of lipid membranes

The next step was to understand the influence of Pb^{2+} on the interactions of C2α with PtdSer- containing membranes. Based on the functional and structural data obtained on multiple C2 domains, it has been hypothesized that one of the functions of metal ions is to serve as a “bridge” between the protein and lipid head-group by forming Ca-O coordination bond(s).[108] To understand if the unusual coordination geometry of Pb(2) has any effect on the C2α function, we tested the membrane-binding properties of C2α in the presence of Pb^{2+} using FRET spectroscopy, ultracentrifugation binding assays, and SPR. FRET experiments were carried out using LUVs comprising

POPC/dansyl-PE and POPC/POPS/dansyl-PE lipids with mole percentages of 93:7 and 60:33:7, respectively. The normalized change in protein-to-membrane FRET as a function of the total metal concentration is shown in Figure 16A for Ca^{2+} and Pb^{2+}. No membrane binding was observed in the absence of the PtdSer component, irrespective of the nature of the divalent metal ion. In the presence of 33% PtdSer, both Ca^{2+} and Pb^{2+} were capable of driving the C2α binding to the lipid membrane. The data were fitted with Equation 7 to obtain the following parameters: $H_{Pb}=2.17\pm0.04$, $[Pb^{2+}]_{1/2}=7.08\pm0.05$ μM, $H_{Ca}=1.88\pm0.05$, and $[Ca^{2+}]_{1/2}=5.00\pm0.07$ μM. The Ca^{2+} values are in good agreement with the previous studies of C2α.[61] From this set of experiments, we concluded that Pb^{2+} is almost as effective as Ca^{2+} in promoting the association of C2α with PtdSer-containing membranes.

To determine if Pb^{2+} can successfully compete with Ca^{2+} for C2α metal-binding sites in the presence of lipid membranes, we carried out the Pb^{2+}/Ca^{2+} competition experiment. C2α was saturated with Ca^{2+} at 100 μM in the presence of LUVs, and Pb^{2+} ions were subsequently added into the mixture.

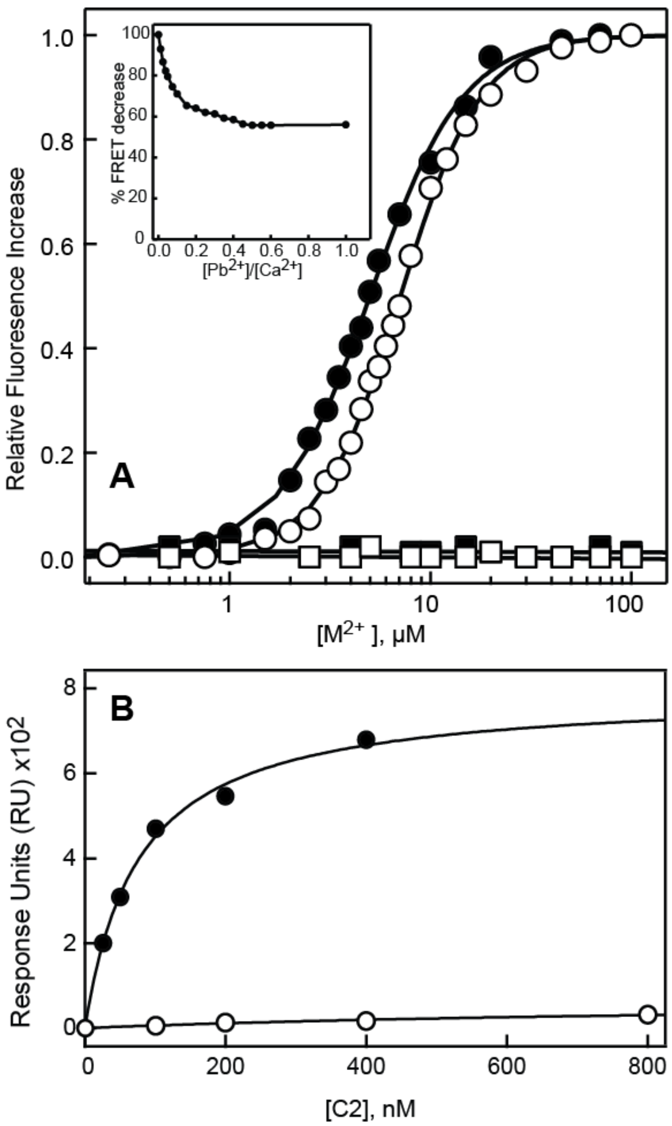

Figure 16. Pb^{2+} binding drives C2α membrane association. (A) Normalized protein-to-membrane FRET as a function of Pb^{2+} (empty circles) or Ca^{2+} (filled circles) concentration. No binding is observed in the absence of PtdSer membrane component (filled and open squares). Inset: Pb^{2+}/Ca^{2+} competition experiment showing the displacement of Ca^{2+} with Pb^{2+}. (B) C2α membrane-binding curves detected by SPR in the presence of 100 µM Ca^{2+} (filled circles) and Pb^{2+} (open circles). Response units (RUs) are plotted against total protein concentration.

The change in FRET intensity was monitored as a function of Pb^{2+} concentration. The maximum attainable protein-to-membrane FRET intensity in the presence of Pb^{2+} is ~56% of that in the presence of Ca^{2+}. The results of the competition experiment are shown in the inset of Figure 16A. The FRET intensity steadily decreases with the increase of Pb^{2+} concentration. A plateau region indicative of complete displacement of Ca^{2+} by Pb^{2+} is reached at the Pb^{2+}/Ca^{2+} ratio of 0.5. Given the comparable membrane affinities of Ca^{2+}- and Pb^{2+}-bound C2α, the displacement of Ca^{2+} by Pb^{2+} most likely occurs in the membrane-unbound form of the protein. Pb^{2+}-bound C2α can subsequently undergo membrane insertion and eventually replaces the Ca^{2+}-containing membrane-bound protein species at high Pb^{2+} concentrations.

Pb^{2+} competes with C2α for PtdSer binding sites

In addition to FRET, we used SPR experiments to test the effect of Pb^{2+} on the C2α membrane-binding properties. The experiments were carried out at 100 µM concentration of metal ions, while the C2α concentration varied from 0 to 800 nM. The active and control surfaces of the sensor chip were coated with POPC/POPS and POPC, respectively. The SPR binding curves are presented in Figure 16B. In the presence of Ca^{2+}, C2α showed the expected membrane-binding behavior with an apparent K_d of 76±9 nM, which is in good agreement with the previously reported K_d value of 71 nM.[63]

Surprisingly, hardly any signal was observed for the C2α in the presence of Pb^{2+}. Two possible explanations for this behavior are either a complete loss of PtdSer selectivity resulting in the equivalent signal from the active and control surfaces, or the absence of C2α binding to the vesicle-coated L1 chip. Either explanation would contradict the results of our FRET experiments, in which we observed both Pb^{2+}-driven binding and PtdSer selectivity.

We used ultracentrifugation-binding assays to gain insight into the apparent discrepancy between the SPR and FRET data. In these assays, apo C2α, LUVs, and metal ions in varying concentrations are mixed, incubated to allow for the membrane binding to occur, and subjected to ultracentrifugation to separate the membrane and aqueous fractions. The advantage of this method compared to FRET and SPR is that it enables direct detection of free protein in the supernatant after pelleting the membrane fraction by ultracentrifugation.

Figure 17A shows a plot of fractional population of the membrane-bound C2α as a function of the metal-to-protein ratio. As expected, addition of Ca^{2+} ions resulted in full membrane binding of C2α. Similarly, C2α associated with membranes in response to Pb^{2+}, reaching full binding at the metal-to- protein ratio of ~30. However, the Pb^{2+} binding curve showed a noticeable lag at low Pb^{2+} concentrations. In addition, at Pb^{2+} concentrations exceeding 0.5 mM (metal-to-protein ratio >100), we observed dissociation of C2α from the membrane.

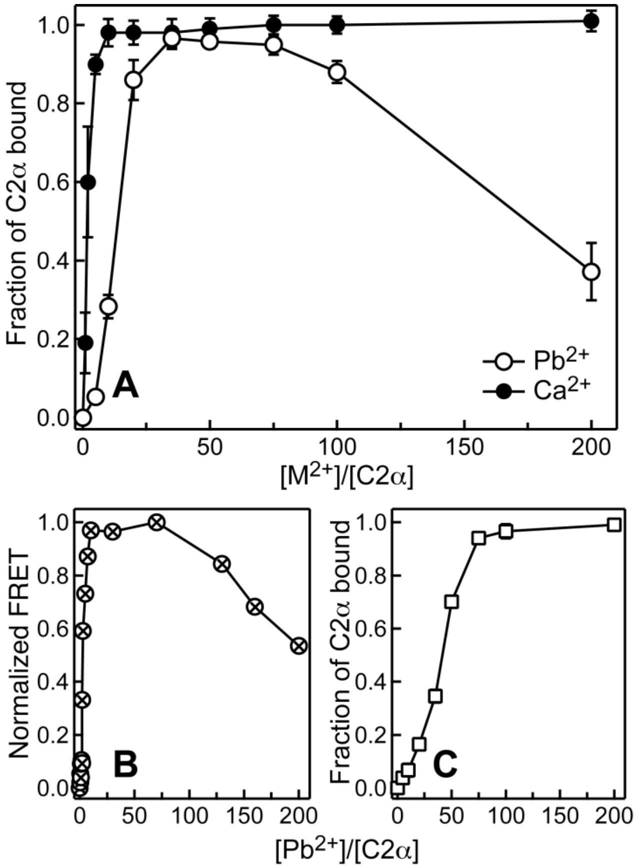

Figure 17. Metal-dependent membrane binding of C2α. (A) Fractional population of membrane-bound C2α obtained in ultracentrifugation binding assays as a function of Ca^{2+}-to-protein (filled circles) and Pb^{2+}-to-protein (open circles) ratios. (B) Pb^{2+}-dependent membrane binding monitored by protein-to- membrane FRET under conditions identical to those used in (A). (C) Ultracentrifugation binding experiments with a 7-fold higher lipid concentration but otherwise identical conditions to those of (A).

To rule out the technique-specific factors, we carried out a protein-to-membrane FRET experiment under conditions identical to those used in the ultracentrifugation assays. It is evident from Figure 17B that FRET data are in complete agreement with the ultracentrifugation results of Figure 17A. To determine if the membrane-dissociation behavior of C2α at high Pb^{2+} concentration can be “rescued” by adding more lipids into the system, we increased the concentration of LUVs 7-fold and carried out an ultracentrifugation binding assay. The “high-lipid” binding curve of Figure 17C demonstrates that full membrane binding of C2α can be achieved by increasing the lipid-to-Pb^{2+} ratio.

In summary, at low concentrations of Pb^{2+} and high lipid-to-metal ratios, Pb^{2+}-bound C2α readily associated with PtdSer-containing membranes. In contrast, at high concentrations of Pb^{2+} the fractional population of membrane-bound C2α decreased more than two-fold. No Pb^{2+}-driven C2α binding was observed in the SPR experiments, where the lipid-coated sensor chip was equilibrated with Pb^{2+}-containing buffer prior to the start of the measurements.

We test the integrity of PtdSer-containing LUVs in the presence of Pb^{2+} in order to rule out any changes that could produce dissociation of C2α from the vesicles at high concentration of Pb^{2+}. We collected the cryoelectron microscopy (cryoEM) images of LUVs under conditions identical to those of the ultracentrifugation binding assays. The concentration of Pb^{2+} of 1 mM was the highest we ever used in our experiments. Figure 18 shows that in contrast to Ca^{2+}, high concentrations of Pb^{2+} promote vesicle aggregation. However, the LUVs are intact and show a rather uniform size distribution (Figure 18). Based on these data, we concluded that Pb^{2+}-induced dissociation of C2α from membranes is not due to the loss of structural integrity of LUVs.

Although high concentrations of Pb^{2+} promote aggregation of vesicles, the integrity of the lipid bilayers is preserved. The most plausible explanation for the reduced membrane binding of C2α at high Pb^{2+}-to-lipid ratios is then a direct competition of Pb^{2+} with C2α for the PtdSer binding sites. To directly test association of Pb^{2+} with PtdSer-containing LUVs, we carried out ultracentrifugation binding assays in the absence of C2α. The amount of Pb^{2+} in the membrane and supernatant fractions was quantified using inductively coupled plasma (ICP) measurements. Indeed, increasing amounts of Pb^{2+} were detected in the membrane fraction upon increasing the total Pb^{2+} concentration. Based on the ICP data, we constructed the binding curve shown in Figure 19 for the association of Pb^{2+} with the PtdSer component of the LUVs. Fitting the data with a single-site binding model produced a K_d of 119 ± 12 μM. The results of the ICP experiments confirmed that Pb^{2+} could indeed compete for PtdSer binding with C2α, and hence modulate the protein-membrane interactions in a concentration-dependent manner.

The ability of Pb^{2+} ions to simultaneously associate with both C2α and PtdSer-containing membranes gives rise to complex binding equilibria, where the identity of the dominant species depends on the relative and total concentration of the protein, metal ion, and LUVs.

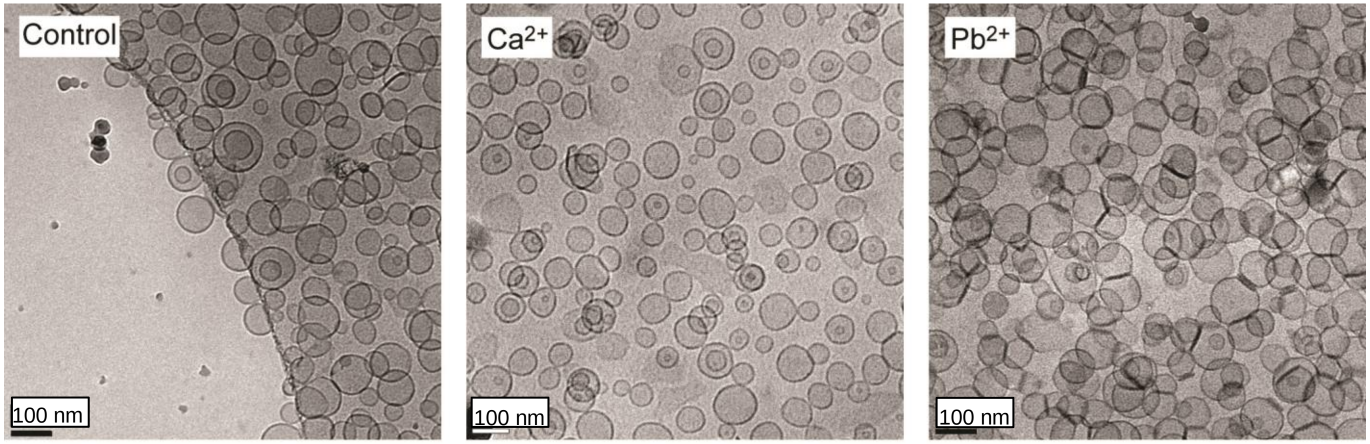

Figure 18. CryoEM images of LUVs in the presence of Ca^{2+} and Pb^{2+}. LUVs (1.5 mM total lipid, POPS/POPC molar fractions of 33/67), in the absence of divalent metal ions and in the presence of Ca^{2+} and Pb^{2+}.

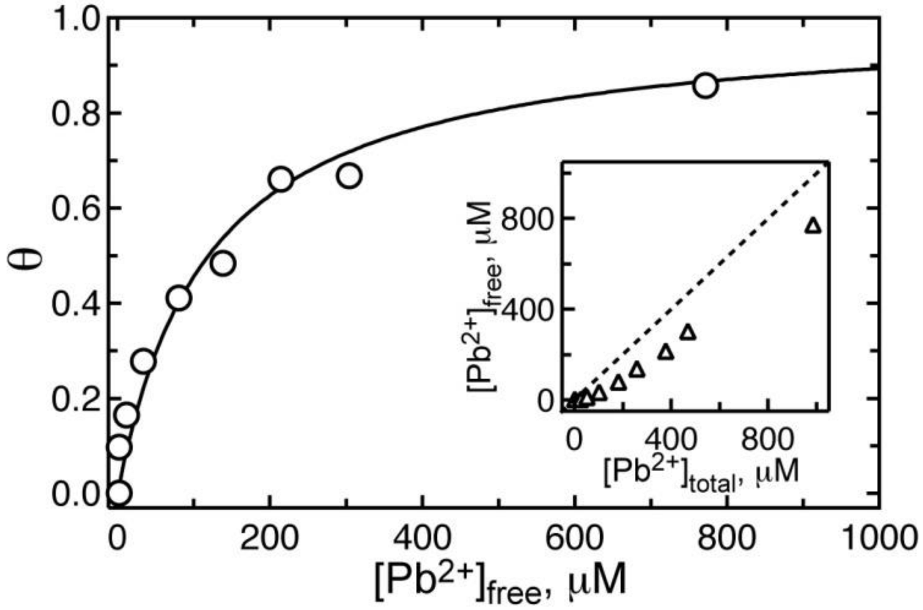

Figure 19. Pb^{2+} interactions with PtdSer containing vesicles measured by ICP. Pb^{2+} binding to 67% POPC:33% POPS LUVs quantified by ICP analysis. The inset shows the relationship between the total and free Pb^{2+}.

Discussion of results

The central objective of this work was to understand the effect of Pb^{2+} ions on the structure and membrane-binding properties of C2α, a calcium-dependent membrane-binding domain of PKCα. We used NMR, ITC, X-ray crystallography, SPR, and FRET techniques to gain insight into the molecular mechanism of the interactions between C2α, Pb^{2+}, and PtdSer-containing lipid membranes. The picture that emerged from our studies is that of Pb^{2+} acting as a concentration-dependent modulator of C2α- membrane interactions.

Using NMR spectroscopy, we established that there are two Pb^{2+}-binding sites on the C2α domain (Figure 9). There is a 2000-fold difference between the Pb^{2+} affinities of the two sites, with K_{d1}^{Pb} 67±1 nM and K_{d2}^{Pb} of 129±4 μM that were measured by ITC and NMR, respectively. In contrast, the two sites have comparable affinities to Ca^{2+} with an estimated K_d^{Ca} of 270 μM. Our finding that C2α binds Pb^{2+} tighter than Ca^{2+} is in agreement with the results of the divalent metal ion-Tb^{3+} competition studies of synaptotagmin I (a protein with two C2 domains)[110] and full-length PKC.[111] We determined that Pb^{2+} is almost as effective as Ca^{2+} in its ability to promote the association of C2α with PtdSer-containing membranes. Using protein-to-membrane FRET experiments of Figure 17A, we determined the concentrations at which the binding is half-maximal: $[Pb^{2+}]_{1/2}$=7.08±0.05 μM and $[Ca^{2+}]_{1/2}$=5.00±0.07 μM. Another C2-domain containing protein, synaptotagmin I, was shown to bind lipid membranes in the presence of Pb^{2+}.[110] In that study, Pb^{2+} was found to be ~1000-fold more potent than Ca^{2+} in driving the protein-membrane association. These differences can be attributed to the specifics of individual C2 domains, or the presence of two of them in synaptotagmin I, or both. Based on the relative binding affinities of Pb^{2+} and Ca^{2+}, it is likely that site (1) of C2α gets populated at low concentrations of Pb^{2+}. The formation of the mixed Pb^{2+}(1)/Ca^{2+}(2)-bound species was suggested as a plausible explanation of why high concentrations of Ca^{2+} reverse the inhibitory behavior of Pb^{2+} in the full-length PKCα.[10] To determine if the formation of the C2α·Pb·Ca species is feasible, we added Ca^{2+} ions to the preformed C2α·Pb complex. The analysis of the NMR data of Figure 14 revealed that the presence of Pb^{2+} at site (1) reduces the affinity of Ca^{2+} to site (2) ~50-fold. We conclude that given the 13 mM affinity of Ca^{2+} to site (2) in the presence of pre-bound

Pb^{2+}, the C2α·Pb·Ca complex is unlikely to be the most dominant species at physiological concentrations of Ca^{2+}.

Pb^{2+} can successfully compete with Ca^{2+} for the C2α metal-binding sites in the presence of PtdSer-containing membranes. We demonstrated this by titrating Pb^{2+} into the pre-formed ternary complex of C2α, Ca^{2+}, and PtdSer-containing LUVs (inset of Figure 16A). The displacement of Ca^{2+} by Pb^{2+} is evident from the change in FRET intensity, which reaches a plateau at ~$[Pb^{2+}]/[Ca^{2+}]$ ratio of 0.5. This behavior is consistent with Pb^{2+} displacing Ca^{2+} from site (1) in the membrane-free form, and then re-routing the membrane-binding process through the Pb^{2+}-driven path.

The activation sequence of PKCα requires an intra-domain rearrangement, which is initiated by the divalent metal ion binding. This rearrangement occurs concomitantly with the two membrane-binding events that involve both C2 and C1 domains of PKCα. Our data show that the affinity of C2α to PtdSer-containing membranes is comparable in the presence of Ca^{2+} and Pb^{2+}. It appears that the partial activation of full-length PKCα at picomolar-to-nanomolar concentrations of Pb^{2+} can be due to the domain rearrangement triggered by Pb^{2+} binding to a single high-affinity site on the C2 domain.

To evaluate the effect of Pb^{2+} binding on the structure of C2α, we used NMR chemical shift perturbation analysis combined with site-specific resonance assignments of the backbone ^{1}H-^{15}N groups. In addition, we determined the crystal structures of apo and Pb^{2+}-bound C2α. Chemical shift perturbation analysis enabled us to identify the high-(67 nM) and low-affinity (129 μM) Pb^{2+}-binding sites. Binding of Pb^{2+} to the high-affinity site (1) results in the perturbation of the CBL1 and CBL3 regions (Figure 12A and Figure 12B). In the crystal structure of the C2α·Pb_2 complex, the coordination geometry of Pb(1) is holodirected, with uniform distribution of the nine oxygen-donating ligands in the coordination sphere. Binding of Pb^{2+} to the low-affinity site (2) affects only the CBL3 region. In contrast to Pb(1), Pb(2) adopts a hemidirected coordination geometry, in which eight ligands occupy only one coordination hemisphere. In this geometry, the stereochemically active $6s^2$ pair of Pb^{2+} that has a partial p-character occupies the "empty" hemisphere. The differences between the Ca^{2+}- and Pb^{2+}-bound C2α structures are localized to the metal-coordination sites. In addition to the different coordination geometries, the positions of Ca(2) and Pb(2) in the C2α-metal complexes do not coincide. As a result, Pb(2) does not form a coordination bond with the carbonyl oxygen of Met186 like Ca(2) does, but instead acquires two additional bonds, one with the second carboxylate oxygen of Asp254 and the other with the water molecule. The sidechain of Asp254 may promote the hemidirected coordination of Pb(2) by serving as a bidentate ligand. Inspection of the metal-binding site in the apo C2α structure reveals that the sidechains of aspartate residues are not pre- organized for the metal binding (see Figure 13C). Thus, the metal coordination event involves a rotameric transition of the coordinating sidechains. Binding of the divalent metal ions to the CBL regions minimizes the electrostatic repulsion between the negatively charged aspartate sidechains, and results in a significant stabilization of the protein structure - the melting temperatures of the apo and Ca^{2+}-bound C2α are 50 and 80 °C, respectively.[58]

The crystal structures of the apo, Ca^{2+}-bound, and Pb^{2+}-bound C2α are essentially superimposable, indicating that metal binding does not significantly influence the average conformation of the protein backbone. The same conclusion was drawn for the only other pair of apo and Ca^{2+}-bound C2 structures, the C2A domain of synaptotagmin I.[57] Given the negligible changes in the backbone conformation, the large differences in chemical shifts between the apo and metal-bound forms reflect the changes in the electrostatic environment and dynamics of the loops. In fact, the CBL1 and CBL3 regions in the crystal structure of the apo form have elevated temperature factors. We also detected the presence of microsecond-to-millisecond timescale motions in the CBL1 and CBL3 regions of apo C2α, as manifested in the elevated ^{15}N transverse relaxation rate constants. These motions are attenuated upon addition of Ca^{2+} (See Chapter V).

In view of our findings that the coordination sphere of Pb(2) in C2α is hemidirected, we wanted to assess the prevalence of this coordination geometry among protein-bound oxygen-coordinated Pb^{2+} ions. Recently, Kirberger and Yang conducted a thorough analysis of the Protein Data Bank (http://www.rcsb.org/) to compare the structural properties of Ca^{2+} and Pb^{2+} binding sites in proteins.[104] The analysis provided invaluable information on the Pb-ligand bond lengths and coordination preferences. The holodirected and hemidirected Pb^{2+} coordination geometries were not explicitly addressed in that analysis.

Our search of PDB for Pb^{2+}-biomacromolecule complexes produced a total of 36 structures. Of those 36, we retained 23 by eliminating the nucleic acid and duplicate structures, as well as those where oxygen was not present in the coordination sphere of Pb^{2+} sites. The selected 23 structures, in which Pb^{2+} has at least one oxygen ligand have the following PDB identifiers: 1AFV, 1E9N, 1FJR, 1HD7, 1HQJ, 1KA4, 1N0Y, 1NA0,

1QNV, 1QR7, 1SN8, 1SYY, 1XXA, 1ZHW, 1ZHY, 2ANI, 2CH7, 2EX3, 2FP1, 2G0A, 2O3C, 2V01, and 2XAL. The structure of the zebra fish apurinic/apyrimidinic endonuclease (PDB ID 2O3C) was excluded from the analysis because of the partial occupancy of Pb^{2+} sites. We further refined our criteria by requiring that (i) all ligands are oxygens and (ii) Pb^{2+} replaces a metal cofactor rather than being non-specifically adsorbed on the protein surface. The 14 Pb^{2+} sites that met these criteria and their corresponding PDB identifiers are listed in Table 3. The distribution of Pb-O bond lengths for these 14 sites is shown in Figure 20.

Table 3. Pb^{2+} sites selected for the Pb-O distance analysis.

PDB ID	Total number of Pb sites	Retained unique all-oxygen sites	Pb serial numbers
1E9N	4	2	4339, 4342
1HD7	1	1	2072
1N0Y	14	4	1315, 1317, 1328, 1330
2G0A	2	1	4655
2XAL	4	2	6758, 6759
2V01	8	4	1117, 1118, 1119, 1120
Total: 14 sites			

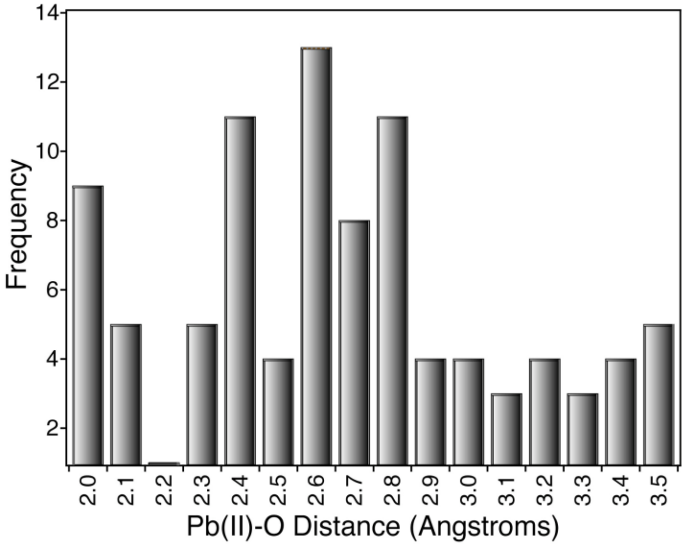

Figure 20. Histogram of the Pb-O distances measured for 14 all-oxygen Pb^{2+} sites.

The Pb-O distances ranged from 2.0 Å to 3.5 Å, as evident from the histogram presented in Figure 20, with the mean of 2.63±0.43 Å. For the analysis of the coordination geometry (*vide infra*) we used the 3.5 Å cutoff, as prescribed by Kirberger and Yang.[104] We found that only 5 structures from the original group of 23: 2G0A (mouse pyrimidine 5'-nucleotidase type 1, P5N-1),[112] 2XAL (inositol 1,3,4,5,6-pentakisphosphate 2-kinase),[113] 1E9N (human apurinic/apyrimidinic endonuclease),[75] 1QR7 (phenylalanine-regulated 3-deoxy-D-arabino- heptulosonate-7-phosphate synthase, DAHPS),[114] and 2V01 (vertebrate Calmodulin),[86] contained hemidirected Pb^{2+} that replaced the metal cofactor and had at least one oxygen in the coordination sphere. The coordination numbers, ligand identities, and natural metal cofactor for the unique hemidirected Pb^{2+} sites are summarized in Table 3. For two out of five proteins listed in Table 4, DAHPS (1QR7) and P5N-1 (2G0A), the inhibitory effect of Pb^{2+} on enzyme activity was linked to the coordination geometry of Pb^{2+}. In both enzymes, Pb^{2+} binding to the active site compromises its geometry and proper positioning of the substrate(s).

Table 4. Unique Pb^{2+} sites with hemidirected coordination geometry.

PDB ID	Pb SN[a]	CN[b]	Coordination sphere atoms	Displaced Cofactor
1E9N	4339	7	7O	Mg(II)
1E9N	4340	5	3O and 2N	Mg(II)
1QR7	10296	5	3O, 1N and 1S	Mg(II)
2G0A	4655	7	7O	Mg(II)
2XAL	6758	6	4O	Mn(II)
2XAL	6759	5	6O	Mn(II)
2V01	1117	7	7O	Ca(II)
2V01	1118	7	7O	Ca(II)
2V01	1120	6	6O	Ca(II)
TOTAL number of all-oxygen Pb^{2+} hemidirected sites: 7				

[a] SN is the serial number of Pb in the PDB file.
[b] CN is the coordination number of Pb^{2+} ion.

7 out of 9 Pb^{2+} sites listed in Table 4 have an all-oxygen coordination sphere. Comparing the results of our PDB analysis presented in Table 3 and Table 4, we conclude that half, 7 out of 14 total all-oxygen coordination sites that Pb^{2+} occupies in lieu of the metal cofactor, have hemidirected coordination geometry. These findings are in general agreement with the conclusions of the Cambridge Structural Database (CSD) analysis conducted by Shimoni-Livny et al.[115] It was found that for the divalent Pb^{2+} complexed with small molecules, hemidirected and holodirected geometries are preferred when the coordination number is <5 and 9-10, respectively. For the

coordination numbers between 6 and 8, Pb^{2+} can adopt either coordination geometry. The nature of Pb^{2+} ligand is also a factor, with hard ligands such as oxygen and nitrogen favoring the hemidirected geometry. The structure of the C2α-Pb^{2+} complex that was determined in our study provides a remarkable example of how both holodirected and hemidirected Pb^{2+} ions, both oxygen-coordinated with similar coordination numbers, can coexist within one macromolecular structure. A recent ab initio study of Pb^{2+} substitution in the C2B domain of synaptotagmin I[59] predicts that (i) the displacement of Ca^{2+} with Pb^{2+} would result in the rearrangement of the coordination sphere with Pb^{2+} adopting a hemidirected coordination; and (ii) a single site replacement of Ca^{2+} with Pb^{2+} would be energetically favorable, implying higher binding affinities of Pb^{2+} to C2B. It appears that for the calcium-binding C2 domains in general, one would expect a combination of holodirected and hemidirected Pb^{2+} geometries, depending on the identity and properties of the oxygen-donating amino acid sidechains.

It has been hypothesized that divalent metal ions play three roles in the C2 domains of conventional PKC isoenzymes: (i) modulation of the electrostatic potential to facilitate C2 insertion into lipid bilayers, (ii) serving as a "bridge" between the protein and PtdSer head-group, and (iii) modulation of the intra- and inter-domain interactions in PKC.14 The hypothesis that Ca^{2+} is involved in forming a protein-membrane "bridge" by coordinating PtdSer oxygens was formulated based on the crystal structures of C2α in complex with Ca^{2+} and short-chain PtdSer molecules.[52,59,107] As shown in Figure 13, in the crystal structures the phosphoryl oxygens of the lipid provide an axial ligand to the Ca(1) site, while Ca(2) site coordinates water[52] or phosphate group of the crystallization buffer.[107] Mutations of Ca(1)- and Ca(2)-coordinating aspartate residues to asparagines in the C2α domain resulted in diminished binding of the full-length PKCα to lipid vesicles, with site (1) having a more pronounced effect.[34] Thus, if we assume that both metal sites are filled prior to membrane-binding and both of them form coordination bonds with oxygens of PtdSer headgroups, then Pb(2) is likely to undergo hemidirected to holodirected conversion. The activation energy for such a conversion was estimated to be 8-12 kcal/mol for the tetracoordinated Pb^{2+},[115] but would be expected to be much lower for coordination numbers of 6-8 that could be accommodated by either geometry.

Two types of membrane-binding behavior of C2α in the presence of Pb^{2+} are illustrated in Figure 16A and Figure 17A. Protein-to-membrane FRET experiments of Figure 16A were conducted under "dilute" conditions-0.5 μM C2α and 150 μM total lipid-and showed full C2α membrane binding at 100 μM Pb^{2+}. Ultracentrifugation experiments of Figure 17A were conducted with a 10-fold proportional increase in the concentration of all components - 5 μM C2α and 1.5 mM total lipid. Under those conditions, we observed a lag period at low Pb^{2+} concentrations, and partial dissociation of C2α from the PtdSer-containing membranes at high Pb^{2+} concentrations. This result is not technique-dependent. Both features were reproduced in the FRET experiment of Figure 17B, in which the concentration of all components matched exactly the conditions of the ultracentrifugation experiments. The pronounced dependence of the membrane association of C2α on the total concentration of all reactants in the system implies the presence of competing binding processes that involve Pb^{2+} ions, PtdSer-containing membranes, and C2α.

The partial dissociation of C2α from membranes at Pb^{2+} concentrations exceeding 0.5 mM could in principle be caused by the effect of Pb^{2+} on the LUV properties. The majority of research efforts to understand the interactions of divalent metal ions with PtdSer-containing membranes have so far focused on Ca^{2+}. It is well-documented that Ca^{2+} promotes the fusion of both pure PtdSer vesicles[116] and multilamellar structures,[117] and that Ca^{2+}-PtdSer interactions can be weakened substantially by incorporating neutral lipids into the system.[118] In addition to fusion, Ca^{2+} induces lateral segregation of lipid components in the membrane, as monitored by the auto-quenching of fluorescent lipids.[119] Similar to Ca^{2+}, Pb^{2+} promotes lateral segregation in PtdSer vesicles.[120] Although these findings indicate that Pb^{2+} could potentially change the physical properties of the PtdSer-containing LUVs in our experiments, the extent of segregation decreases significantly with decreasing the molar fraction of PtdSer to <~0.3 and metal-to-lipid ratio to <~1-2.[119,120] Because our experiments were conducted with a 33 % molar fraction of PtdSer and Pb^{2+}-to-lipid ratios less than 0.7, Pb^{2+}-induced segregation of lipid components is not likely to be a major factor that influences the affinity of C2α to the membranes.

A comparison of the cryoEM images of 100 nm LUVs in the presence of Ca^{2+} and Pb^{2+} (Figure 18) revealed that 1 mM Pb^{2+} but not Ca^{2+} promotes the aggregation of vesicles. We hypothesized that the vesicle aggregation occurs because Pb^{2+} interacts with the PtdSer component of the LUVs. The ICP analysis of the membrane-bound and free Pb^{2+} concentrations confirmed that Pb^{2+} associates with LUVs, with an apparent K_d of 119±12 µM. We conclude that in the low mM range, Pb^{2+} can successfully compete with C2α for the PtdSer binding sites on the membrane. The 10-fold reduction in the concentration of all components in the FRET experiments of Figure 16A results in the smaller fractional population of membrane-bound Pb^{2+}. As a result, there is sufficient free Pb^{2+} to enable full membrane binding of C2α.

Given the complexity of the binding equilibria that involve Pb^{2+}, PtdSer-containing lipid membranes, and C2α, how do we extrapolate our findings to explain the modulation of PKCα activity by Pb^{2+}? Pb^{2+} has both activating and inhibitory effects on full-length PKCα.[10] In vitro studies of Pb^{2+}-dependent activity of recombinant PKCα showed that the enzyme is activated in the range of Pb^{2+} concentrations from 0.1 to 10 nM, reaching 40% of the maximum Ca^{2+}-dependent activity. The stimulatory effect of Pb^{2+} was attributed to its interactions with the high-affinity metal-binding site residing on the C2 domain. The inhibitory effect of Pb^{2+} at concentrations exceeding 10 nM was attributed to two factors: binding of Pb^{2+} to the second site on the C2 domain, and the interaction of Pb^{2+} with the catalytic domain at micromolar concentrations of metal ion. The work was carried out with 0.13-0.25 nM PKCα in the presence of 100% PtdSer.[10] The blood level of 10 μg/dL translates into 0.48 μM concentration of Pb^{2+}. The concentration of bioavailable Pb^{2+} is much lower and is on the order of picomolar to nanomolar.[105] Based on the Pb^{2+} affinities to C2α determined in this work, we expect the high-affinity metal-binding site (1) of C2α to be at least partially occupied in vivo. We did not detect any substantial inhibitory effect of Pb(2) on the interactions of C2α with membranes - Pb^{2+} is almost as effective as Ca^{2+} in driving the membrane association process (Figure 16A). We conclude that the C2α-mediated activation of

PKCα by Pb^{2+} is likely to occur through a change in the intra-domain orientation in the enzyme, rather than through a direct modulation of metal-dependent membrane binding. The association of Pb^{2+} with PtdSer-containing membranes can in part be responsible for the inhibitory effect of Pb^{2+}. At low concentrations of Pb^{2+}, we observed a lag period in the C2α membrane-binding curve of Figure 17A. The lag is likely caused by the sequestration of Pb^{2+} by the PtdSer-containing membranes (inset of Figure 19). High concentration of PtdSer facilitates the formation of the Pb^{2+}-PtdSer complex resulting in a more pronounced lag period as shown in Figure 17C. Based on these considerations, it is feasible that Pb^{2+} can interfere with the membrane binding of C2α (and hence PKC) even at low concentrations. This process would be facilitated by high local concentration of acidic lipids and phosphoinositides.

CHAPTER III

METAL AND PHOSPHOINOSITIDE BINDING SITES SYNERGY: IMPLICATIONS IN C2-PB(II) MEMBRANE INTERACTIONS[*]

Background

As described in Chapter II and C2 domains can interact with Pb^{2+} ions and act as a Ca^{2+} surrogate in the context of specific molecular targets.[121] Interaction of Pb^{2+} with several Ca^{2+}-dependent C2 domain-containing proteins has been implicated in the disruption of neurotransmitter release,[11] which is a hallmark of Pb^{2+} poisoning.

C2 domain is responsible for the Ca^{2+}-induced activation of cPKCs. Following the original report of Pb^{2+} modulating the cPKC activity, a number of studies demonstrated that conventional cPKCs are activated by picomolar-to-nanomolar and partially inhibited by micromolar concentrations of Pb^{2+}. Experiments on the recombinant PKCα isoform provided evidence for the existence of three Pb^{2+} interaction sites.[10] We established that the high-affinity Pb^{2+} interaction site resides on the C2 domain of PKCα (See Chapter II).[48]

Despite the well-documented effect of Pb^{2+} on the membrane-dependent activity of C2 domain-containing proteins, the molecular mechanism of Pb^{2+} action at the membrane is not fully understood. The objective of this work was to determine the

---

[*] Reproduced with permission from: Krystal A. Morales and Tatyana I. Igumenova. *Biochemistry* 2012, *51*, 3349. Copyright 2012 © by the American Chemical Society.

influence of a lipid second messenger, phosphatidylinositol-4,5-biphosphate (PIP_2), on the interactions of C2 domains with Pb^{2+}.

PIP_2 is involved in the regulation of a variety of cellular processes[122,123] including synaptic vesicle trafficking.[124] PIP_2 is selectively enriched in the cytoplasmic leaflet of the plasma membrane, where it occurs at a molar concentration of 1-3%. The significance of PIP_2 as a modulator of C2-membrane interactions became apparent upon detection of its specific binding to the C2 domains from conventional PKC isoforms,[64,65] synaptotagmin I,[125,126] and rabphilin-3A.[95,127] The presence of PIP_2 in PtdSer-containing lipid membranes increases the Ca^{2+} affinity of C2 domains[63,64,68,128] and makes them responsive to Ca^{2+} concentrations that are typically associated with the Ca^{2+} spike during signaling. The role of PIP_2 as a sole determinant of PKCα localization to plasma membrane is still being debated.[39,63] However, there is general agreement that the presence of PIP_2 in the membrane results in the decrease of the C2α off-rate and, as a result, the increased residency time of the protein on the plasma membrane.[63,68]

To determine the influence of PIP_2 on the C2-Pb^{2+} interactions, we used the C2 domain from PKCα (C2α) as a paradigm for Ca^{2+}-responsive C2 domains. In one of the first studies of the C2α-PIP_2 system, Corbalán-García et al.[65] demonstrated that C2α could bind to membrane-embedded PIP_2 even in the absence of the PtdSer component, albeit with a lower affinity. Another unexpected finding was that the association of C2α and PIP_2 occurred even in the absence of Ca^{2+}. The specific region of C2α involved in PIP_2 interactions, which is distinct from the PtdSer binding site, was identified using mutagenesis.[65,129] A subsequent determination of the crystal structure of the ternary

C2α-Ca^{2+}-PIP$_2$ complex revealed the molecular details of the PIP$_2$ site.[59] Figure 21 shows the structure of the complex with all functional regions highlighted. The tip of the C2α domain comprises three calcium-binding loops (CBLs). Two of them, CBL1 and CBL3, coordinate calcium ions. EPR studies identified CBL1 and CBL3 as the protein segments that penetrate the lipid headgroup region of the PtdSer-containing membranes.[56]

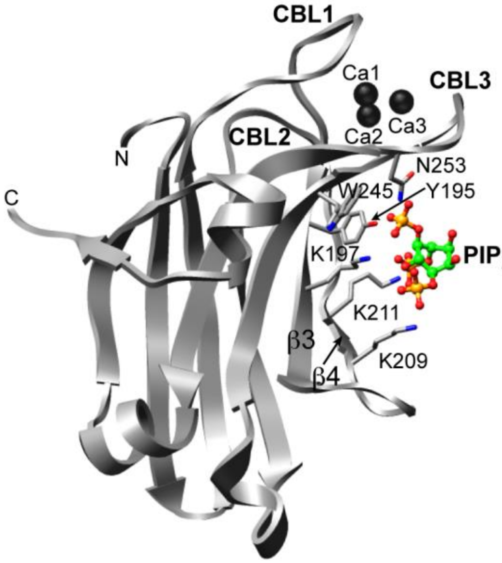

Figure 21. Structure of the C2α-Ca^{2+}-PIP$_2$ complex. The structure of the C2α-Ca^{2+}-PIP$_2$ complex (PDB ID: 3GPE)[59] showing the details of the PIP$_2$ interaction site. CBL1, CBL2, and CBL3 are the Ca^{2+}-binding loops.

The PIP$_2$ binding site is mostly formed by two beta-strands, β3 and β4. A total of six residues are involved in the interactions with the oxygen atoms of the three phosphate groups in PIP$_2$: Y195, K197, K209, K211, W245, and N253. The three lysines that belong to strands β3 and β4 - K197, K209, and K211 - are part of the region that has been referred to in the literature as the "β-groove", "polybasic cluster", or "lysine-rich cluster".

In Chapter II, we characterized the interactions of C2α with Pb^{2+} in the presence and absence of PtdSer-containing model membranes.[48] We determined the crystal structure of Pb^{2+}-complexed C2α, established that C2α has two Pb^{2+}-binding sites with a 2,000-fold difference in binding affinities, and demonstrated that Pb^{2+} can outcompete Ca^{2+} from C2α in the presence of PtdSer-containing model membranes. In this work, we employed Nuclear Magnetic Resonance (NMR) spectroscopy, protein-to-membrane Förster Resonance Energy Transfer (FRET), and vesicle sedimentation experiments to determine the effect of PIP_2 on the C2α-Pb^{2+} and C2α-Pb^{2+}-membrane interactions. Our findings not only shed light on the molecular mechanism of C2α-Pb^{2+}-PIP_2 interactions, but also illustrate the contribution of PIP_2 to Pb^{2+} interfering with the Ca^{2+}-dependent function of C2α.

Experimental procedures

Materials

L-α-phosphatidylinositol-4,5-bisphosphate (Brain, Porcine) (bp-PIP_2) was obtained from Avanti Polar Lipids Inc. (Alabaster, AL). Short chain (C4) D-myo-phosphatidylinositol-(4,5)-bisphosphate (C4-PIP_2) used for NMR-detected titrations was purchased from Echelon Bioscience (Salt Lake City, UT). The ion-chelating resin, Chelex 100 (Sigma-Aldrich), was used to treat all buffers to remove residual divalent metal ions.

C2α over-expression and purification

Over-expression and purification of C2α was carried out as described in Chapter II.[48]

Binding of C4-PIP$_2$ to C2α monitored by NMR

The binding of C4-PIP$_2$ to [U-^{15}N] C2α was monitored using NMR-detected titration experiments. All experiments were carried out at 25 °C on a Varian Inova spectrometer operating at a ^{1}H Larmor frequency of 600 MHz (14.1 T). A series of ^{15}N-^{1}H Heteronuclear Single Quantum Coherence (HSQC) spectra were collected for C2α in three different states of metal ligation: apo, Ca^{2+}-bound, and single Pb^{2+}-bound, at increasing concentrations of C4-PIP$_2$.The Ca^{2+}-bound state, C2α·Ca$_2$, was prepared by adding Ca^{2+} to a final concentration of 2.5 mM to the 100 μM apo C2α. The single Pb^{2+}-bound C2α, C2α·Pb, was prepared by adding Pb^{2+} to a final concentration of 100 μM to the 100 μM apo-C2α. We observed significant precipitation of C4-PIP$_2$ at Pb^{2+} concentrations that are required to generate the C2α·Pb$_2$ state. This prevented us from carrying out the C4-PIP$_2$ titration experiments on the C2α·Pb$_2$ complex. To determine the affinity of Pb^{2+} to the second C2α site in the presence of saturating C4-PIP$_2$, we titrated Pb^{2+} into the preformed C2α·Pb·PIP$_2$ complex. The concentration of C4-PIP$_2$ in the mixture was 1.5 mM. The NMR buffer for all experiments was 10 mM MES (pH 6.0), 100 mM KCl, 8% D_2O and 0.02% NaN_3. The C4-PIP_2 stock solution was standardized using phosphate quantification assay.[99]Site-specific chemical shift perturbations of C2α due to ligand binding were calculated according to the following equation:

$$\Delta = [\Delta\delta_H^2 + (0.152\Delta\delta_N)^2]^{1/2} \quad \textbf{Equation 10}$$

where $\Delta\delta_H$ and $\Delta\delta_N$ are the residue-specific chemical shift changes between the two states that are being compared, and 0.152 is the scaling factor.[130]

Binding curves were constructed by plotting the change in C2α chemical shifts as a function of the total ligand concentration. The dissociation constants, K_d, were determined by globally fitting the binding curves with the single-site[94] binding equation Equation 1).

Association of C2α with PIP_2-containing membranes measured by FRET

Protein-to-membrane FRET experiments were carried out using the ISS Phoenix spectrofluorometer. The Trp residues of C2α and the dansyl-PE lipid component of the large unilamellar vesicles (LUVs) were used as the donor and acceptor, respectively. The lipid composition of LUVs was POPC/POPS/bp-PIP_2/dansyl-PE with a molar ratio of 61:30:2:7. Fluorescence emission spectra of the sample containing 0.5 μM C2α and LUVs (150 μM total lipid concentration) were collected at increasing concentrations of the metal ion, Ca^{2+} or Pb^{2+}. The spectra were corrected by subtracting the fluorescence of the reference sample that contained all components but C2α. The change in FRET intensity at 505 nm generated upon C2α membrane binding, ΔF, relative to the maximum attainable change, ΔF_{max}, was plotted as a function of the total metal concentration. Data were fitted using Equation 7.

Calculations of the protein electrostatic potential

The calculations were carried out using the Adaptive Poisson-Boltzmann Solver (APBS)[131] implemented through the Visual Molecular Dynamics (VMD)[132] plugin. The PDB files were prepared for electrostatics calculations using the PDB2PQR software package.[133] The parameterization of the PIP_2 ligand produced a net charge of -4, which is consistent with the available experimental evidence.[134] Pb^{2+} ions were parameterized with a Born radius of 2.17 Å.[135] Figures showing the surface-mapped electrostatic potential were generated with VMD.

Divalent metal ions do not appreciably quench the fluorescence of membrane-embedded dansyl group

To determine if Pb^{2+} and Ca^{2+} directly quench the fluorescence of the dansyl group, we carried out control experiments with no C2α added to the mixture. The fluorescence spectra of membrane-embedded dansyl-PE collected with the excitation wavelength of 336 nm.

Ca^{2+}/Pb^{2+} competition experiments

To determine if Ca^{2+} can outcompete Pb^{2+} in the presence of lipid membranes, we prepared the ternary C2α–Pb^{2+}–LUV complex and titrated it with Ca^{2+}. The vesicle suspension was thoroughly decalcified for this set of experiments. The total concentration of Pb^{2+} was 20 μM. The LUV composition was POPC/POPS/bp-PIP_2/dansyl-PE with molar ratios of 61:30:2:7. The total concentration of C2α and lipids were 0.5 and 150 μM, respectively. The concentration of Ca^{2+} was varied from 0 to 350 μM.

Interactions of Pb^{2+} with PIP_2-containing LUVs

Sucrose-loaded LUVs were incubated with Pb^{2+} at the desired total metal concentration. After a 20-minute incubation period, LUVs were centrifuged in a Beckman TL-100 tabletop ultracentrifuge for 30 minutes at 50,000 rpm and 25°C. The pelleting efficiency of LUVs, determined by the phosphate quantification assay, was always > 95 %. Two lipid concentrations, 150 μM (same as in our FRET experiments) and 1.5 mM, were chosen for these experiments. The composition of LUVs was POPC/POPS/bp-PIP_2 with molar ratios of 68:30:2. For each Pb^{2+} concentration point, the amount of Pb^{2+} in the supernatant ($[Pb^{2+}]_{free}$) and pellet ($[Pb^{2+}]_{bound}$) fractions was quantified using ICP as described in Chapter II.

Cryo-EM studies of PIP$_2$-containing LUVs

We used Cryo-EM to examine the influence of Pb^{2+} on the integrity and aggregation state of LUVs. The total lipid and Pb^{2+} concentrations were 150 μM and 100 μM, respectively. 100 μM was the maximum Pb^{2+} concentration used in our FRET experiments. No vesicle aggregation was observed under this set of conditions.

Binding of metal ions to C2α does not perturb the conformational dynamics of the protein backbone in the β3-β4 region

We carried out Hahn-Echo (HE) experiments[136] to determine if the binding of metal ions to C2α affects the microsecond-to-millisecond backbone dynamics of the β3-β4 region. The data were collected for the three forms of C2α: apo, Pb^{2+}-bound, and Ca^{2+}-bound using a 600 MHz Varian INOVA instrument. For each C2α form, 12 spectra were collected in an interleaved manner with time delays of 0 and 36 ms. The R_2^{HE} values, which carry the full contribution of the conformational exchange term, R_{ex}, were calculated from the corresponding intensity ratios as described by Massi et al.[137]

Estimation of the C2α affinities to metal ions in the presence of lipid membranes

To estimate the dissociation constants for the C2α-metal ion complexes in the presence of PIP$_2$-containing LUVs, we simulated the binding curves using the equation given in Riley-Lovingshimer et al.[138] that assumes two independent metal-binding sites and accounts for the free and total ligand concentrations explicitly. The binding data simulated using the Hill equation (Equation 7) with the best-fit parameters for our experimental data (H_{Ca}=1.5, $[Ca^{2+}]_{1/2}$=0.7 μM, H_{Pb}=2.1, $[Pb^{2+}]_{1/2}$=1.3 μM) is shown in black for Ca^{2+} (Figure 22A) and Pb^{2+} (Figure 22B). Curves simulated using the K_d values that are either equal to $[M^{2+}]_{1/2}$ or reduced by two- (green) or five-fold (red) are shown on the same graphs. These data illustrate that the factor by which we are under-estimating the affinities of C2α to metal ions is less than 5.

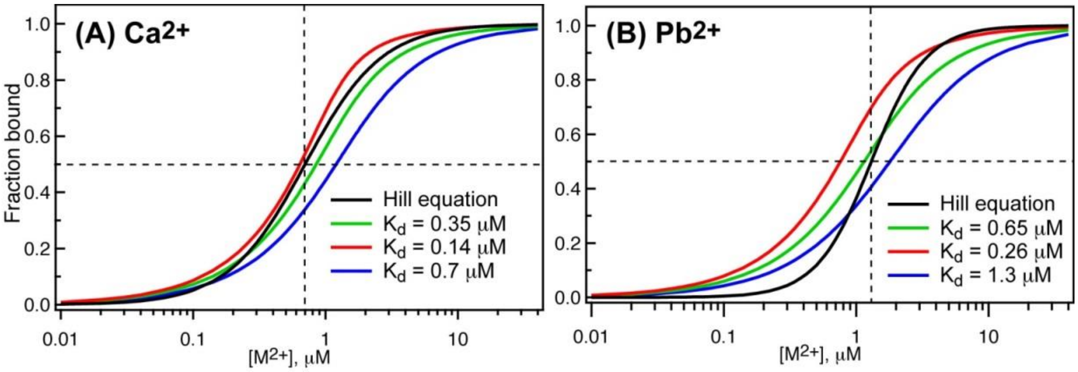

Figure 22. Simulated curves for C2α metal binding in the presence of PIP_2-containing membranes. Simulated curves for C2α binding to PIP_2-containing membranes in the presence of Ca^{2+} (A) and Pb^{2+} (B).

Results

C2α binds PIP_2 in all three states of metal ligation

We made use of the single high-affinity Pb^{2+}-binding site on C2α and prepared the C2α·Pb state by mixing the equimolar quantities of protein and metal ion. To provide the reference for our Pb^{2+} data and determine the general role of divalent metal ions in modulating the affinity of C2α to PIP_2, we also tested the binding of the water soluble C4-PIP_2 to the apo- and Ca^{2+}-complexed forms of C2α. ^{1}H-^{15}N HSQC spectra were collected on the [U-^{15}N] C2α that was prepared in three states of metal ligation: apo, Ca^{2+}-saturated (C2α·Ca$_2$), and single Pb^{2+}-bound (C2α·Pb), with C4-PIP$_2$ concentrations ranging from 0 to 1.5 mM.

The results are presented in Figure 23 Panels A, B, and C are the expansions of the ^{1}H-^{15}N HSQC spectra that illustrate the response of the C2α N-H resonances (or cross-peaks) to increasing concentrations of C4-PIP$_2$. The amino-acid identities of the C2α cross-peaks were determined previously using a set of triple-resonance NMR assignment experiments.[48] In all three states of metal ligation, the binding of C4-PIP$_2$ to C2α falls into the exchange regime that is fast on the NMR chemical-shift timescale. In this regime, the cross-peak positions change smoothly as a result of increasing ligand concentration. Based on the absolute value of chemical shift changes, Ca^{2+}- and Pb^{2+}-complexed forms of C2α show a more pronounced response to the C4-PIP$_2$ binding than the apo-form.

Chemical shift perturbations that are experienced by C2α residues between 0 and 1-1.5 mM C4-PIP$_2$ were calculated using Equation 10. In all cases, we used the chemical shifts of the appropriate metal-ligated form as a reference state. Panels D, E, and F in Figure 23 show the color-coded Δ values mapped onto the corresponding C2α crystal structures: apo (PDB ID: 3RDJ),[48] Ca^{2+}-complexed (PDB ID: 1DSY),[52] and Pb^{2+}-complexed (PDB ID: 3TWY).[48] In the latter, only the Pb^{2+} ion that occupies the high-affinity C2α site is shown. The protein region affected by the C4-PIP$_2$ binding is not limited to the lysine-rich cluster, but also includes the calcium-binding loops.

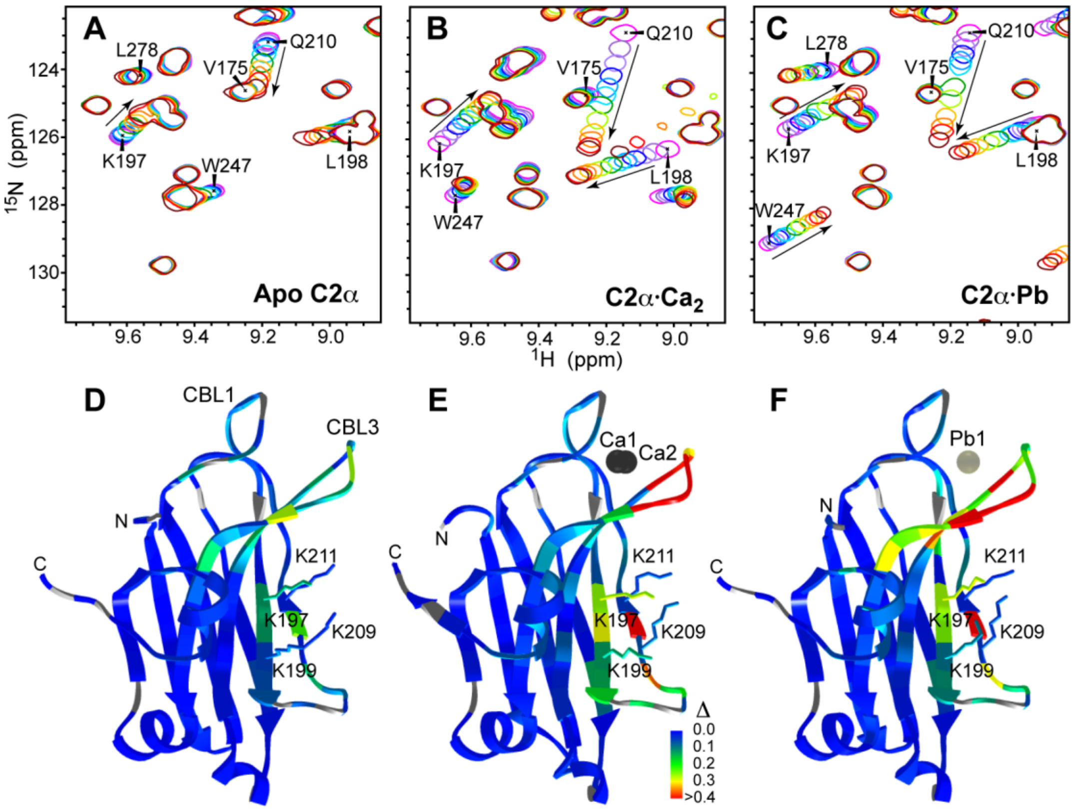

Figure 23. PIP$_2$ binding on three different metal-ligated states monitored by NMR. Expansions of ^{15}N-^{1}H HSQC spectra of 100 μM apo C2α (A), C2α·Ca$_2$ (B), and C2α·Pb (C) at different concentrations of C4-PIP$_2$. The arrows point in the direction of increasing C4-PIP$_2$ concentration, which varies from 0 to 1.5 mM for apo-C2α and C2α·Pb; and from 0 to 1 mM for C2α·Ca$_2$. Site-specific Δ values were calculated according to Equation 10, color-coded, and mapped onto the structures of apo (D), Ca^{2+}-complexed (E), and Pb^{2+}-complexed (F) C2α. The side-chains of K197, K199, K209, and K211 indicate the position of the lysine-rich cluster. Proline residues, for which NMR data are not available, are shown in grey.

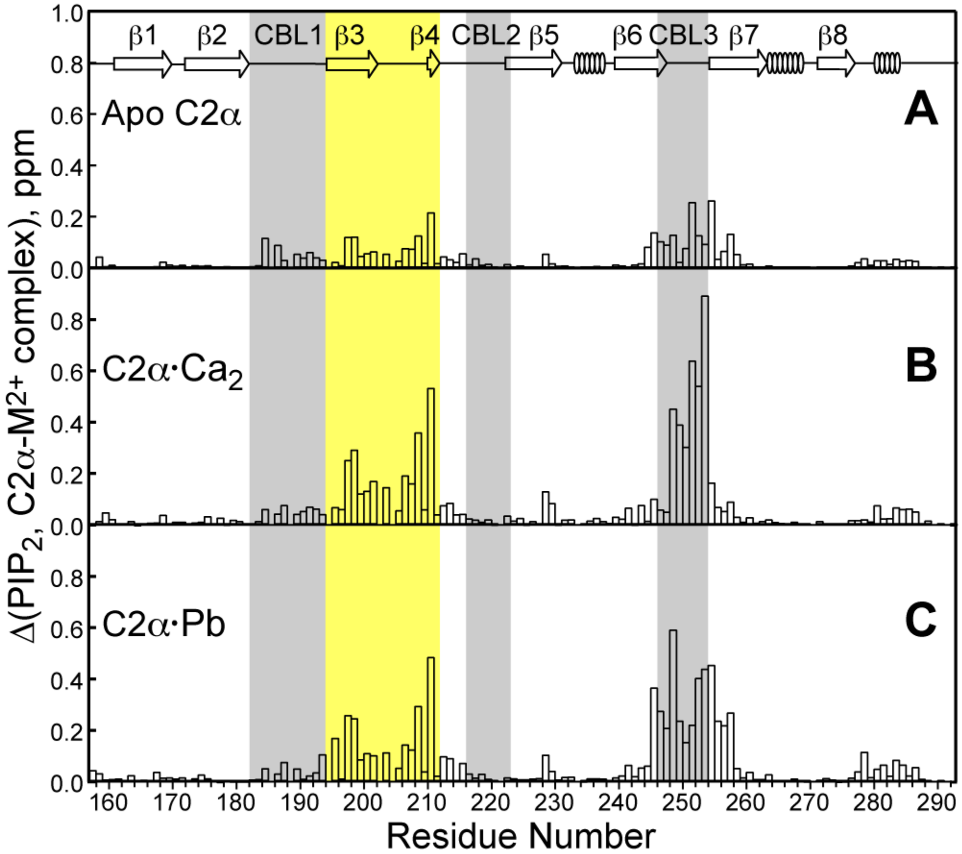

Figure 24. Site-specific chemical shift changes induced by PIP$_2$ binding. Chemical shift perturbation Δ due to PIP$_2$ binding plotted as a function of primary structure for apo C2α (A), C2α·Ca$_2$ (B), and C2α·Pb (C). Calcium-binding loops – CBL1 (residues 182-193), CBL2 (residues 216-222), and CBL3 (residues 246-253) are highlighted in gray. The β3-β4 region (residues 194-211) that directly interacts with PIP$_2$ is highlighted in yellow.

This effect is further illustrated in Figure 24 by plotting the Δ values as a function of primary structure. Three C2α regions - irrespective of the metal-ligation state - experience chemical shift perturbation upon C4-PIP$_2$ binding: the lysine-rich cluster located on the β3-β4 segment; CBL1, which immediately precedes the β3-β4 region; and CBL3, which is distant from the β3-β4 region in the primary structure but is close to it in the tertiary structure. The smaller effect of PIP$_2$ binding on the apo state of C2α is evident from the magnitude of chemical shift perturbations. Given that the backbone conformation of the C2α-Ca^{2+}-PIP_2 complex is close to that of the apo-form (the RMSD for the backbone atoms is 0.40 Å), the chemical-shift perturbations are likely due to the changes in the electrostatic properties and/or conformational dynamics of the protein. The chemical shift perturbation pattern is very similar for C2α·Ca_2 and C2α·Pb (Figure 24B and Figure 24C), indicating that a full complement of metal ions is not a stringent requirement for the C2α-PIP_2 interactions.

Pb^{2+} enhances the affinity of C2α to PIP_2

To obtain the affinities of C2α to C4-PIP_2, we constructed binding curves for all N-H groups whose combined ^{15}N and ^{1}H chemical shift changed by more than 0.05 in the course of the titration. The data are presented in Figure 25 for 2 representative residues: K197 and Q210. Each panel in Figure 25 shows the residue-specific binding curves for three different states of metal ligation: apo C2α, C2α·Pb, and C2α·Ca_2. In the apo C2α, the binding curves for all but two PIP_2-responsive residues could be globally fitted with Equation 1, which yielded a K_d of 1130±38 μM. These data indicate that, in the absence of metal ions and lipid membranes, C2α is a low-affinity PIP_2 binding module. Having a single Pb^{2+} bound to the high-affinity C2α site increases the affinity of the protein to PIP_2. The global fit of the C2α·Pb binding curves produced a K_d of 198±2 μM. The C2α·Ca_2 state showed a more complex response to PIP_2. To facilitate the analysis of binding data, we separated the 38 responsive residues into three groups based on their titration behavior. Group 1 comprises 27 members that either belong to the β3-β4 region or are in its immediate vicinity. Group 1 data can be well fitted with the single-site binding equation to obtain a K_d of 48 ± 1 μM (Figure 25). Groups 2 and 3 are further described in the "Interplay between Ca^{2+} and PIP_2" section.

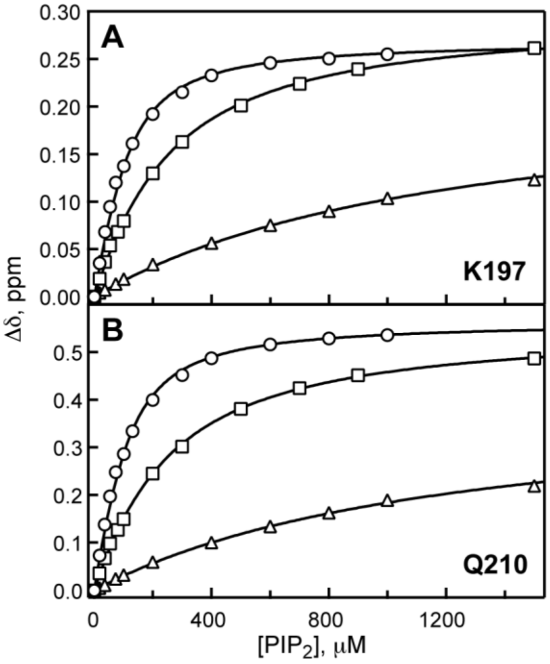

C2 state	K_d (μM)	# Residues used for fit
△ Apo C2α	1130 ± 38	16
□ C2α·Pb	198 ± 2	35
○ C2α·Ca_2	48 ± 1	27

Figure 25. Progressive loading of C2α metal sites enhances the affinity for PIP_2. C4-PIP_2 binding curves for K197 (A) and Q210 (B) in apo-C2α (triangles), C2α·Ca_2 (circles), and C2α·Pb (squares). Solid lines represent the fits to Equation 1. Δδ is the absolute value of the chemical shift change in ppm. The table summarizes the PIP_2 dissociation constants determined for three states of metal ligation.

In summary, the affinity of metal ion-complexed C2α to PIP_2 is significantly enhanced compared to that of the apo-form. The K_d for the C2$\alpha\cdot$Pb$\cdot PIP_2$ complex falls in between the K_d values of the C2$\alpha\cdot PIP_2$ and C2$\alpha\cdot Ca_2\cdot PIP_2$ complexes. This effect - the 4-6 fold decrease in K_d upon progressive saturation of C2α metal-binding sites - appears to depend mostly on the number of bound metal ions (and hence the overall charge of the protein).

Figure 26 highlights the contributions of individual metal-binding sites of C2α to PIP_2 binding. For this analysis, we chose the sub-stoichiometric concentration of C4-PIP_2 - 80 μM - to avoid the saturation regime, where the effect of the increased PIP_2 affinity would not be discernible. The residues chosen for the chemical shift perturbation analysis belong to the β3-β4 region. The residues from this region respond weakly if at all to metal ions but show significant perturbations in response to PIP_2 binding, as illustrated in Figure 26A (blue, purple, and orange spectra). The binding of the second Pb^{2+} ion to C2α results in the shift of cross-peaks that is solely due to the enhancement of the C2α affinity to PIP_2 (green spectrum). The spectra of Pb^{2+}- (green) and Ca^{2+}-complexed (grey) C2α in the presence of 80 μM PIP_2 are virtually identical for the β3-β4 region, which is not the case for the CBLs. The results of the chemical shift perturbation analysis are shown in Figure 26B. For the Pb^{2+} data, there are two processes that contribute to the observed C2α chemical shift change: the binding of PIP_2 to the C2$\alpha\cdot$Pb state (orange bars) and the binding of additional PIP_2 upon filling the second Pb^{2+}-binding site (green bars). For many residues in the β3-β4 region, the sum of these two contributions is virtually identical to the Δ values obtained for the PIP_2 binding to the C2α·Ca_2 state (grey bars). This "additive" behavior illustrates that the enhancement of the C2α affinity to PIP_2 brought about by metal ions does not depend on the identity of metal ions, at least for the Ca^{2+} and Pb^{2+} pair.

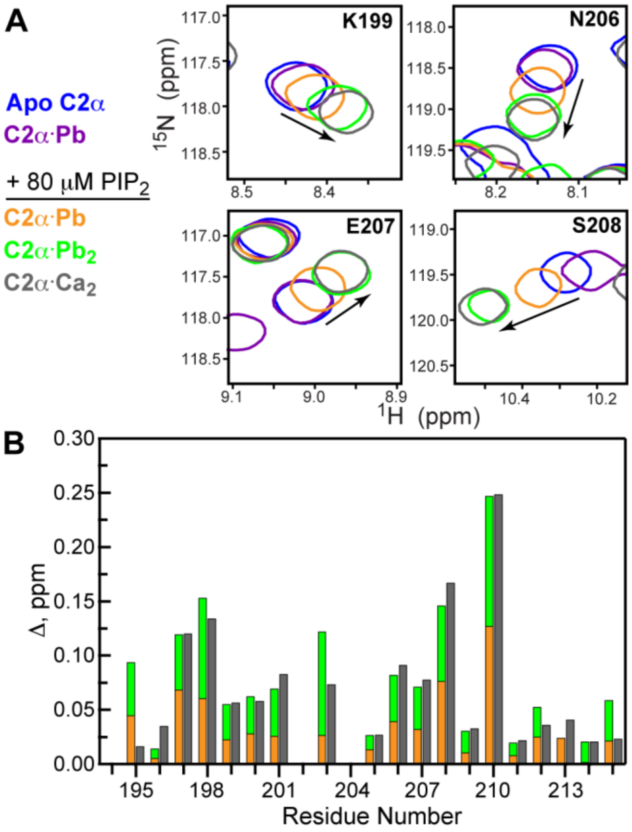

	Final	Initial
🟧	C2α·Pb / 80 μM PIP_2	C2α·Pb
🟩	C2α·Pb_2 / 80 μM PIP_2	C2α·Pb / 80 μM PIP_2
⬛	C2α·Ca_2 / 80 μM PIP_2	C2α·Ca_2

Figure 26. Individual contributions of C2α metal sites to PIP_2 binding. (A) The expansions of the ^1H-^{15}N HSQC spectra for four C2α residues from the β3-β4 region. (B) The chemical shift perturbations Δ for the β3-β4 region. Δ values were calculated according to Equation 10 using the final and initial states listed in the table.

PIP_2 enhances the affinity of C2α to Pb^{2+}

The next step was to determine the binding affinities of C2α to Pb^{2+} in the presence of saturating PIP_2. The Pb^{2+} affinities of two C2α metal-binding sites, (1) and (2), differ 2,000-fold. The K_d for the high-affinity site (1) was determined in our previous study by isothermal titration calorimetry [115].[48] However, the quantities of C4-PIP_2 required to produce the PIP_2-saturated state of apo C2α make the ITC experiments cost-prohibitive in this case. Instead, we determined the K_d for the low-affinity Pb^{2+} site (2) in the presence of saturating PIP_2. This value, $K_{d2}^{Pb,PIP}$, was then used to calculate the dissociation constant for the first site, $K_{d1}^{Pb,PIP}$ (*vide infra*).

We prepared the C2α·Pb·PIP_2 complex by combining the equimolar amounts of C2α and Pb^{2+}, followed by the addition of C4-PIP_2 to the final concentration of 1.5 mM. According to the binding data of Figure 25, under these conditions, the C2α·Pb·PIP_2 complex is the dominant protein species in solution. The titration of the C2α·Pb·PIP_2 complex with Pb^{2+} was monitored using ^{15}N-^{1}H HSQC experiments. We identified the residues that responded to Pb^{2+}(2) binding and constructed a total of 8 binding curves. All of them were fitted globally with Equation 1, which produced a $K_{d2}^{Pb,PIP}$ of 17±1 μM. An example of the binding curve for D248 is shown in Figure 27A. For comparison, on the same graph, we plotted the D248 data for Pb^{2+}(2) binding to the C2α·Pb complex in the absence of PIP_2. The K_d for this process, 129±4 μM, was determined in our previous work.[48] These data indicate that the pre-bound PIP_2 results in the 8-fold increase of the C2α affinity to Pb^{2+}(2).

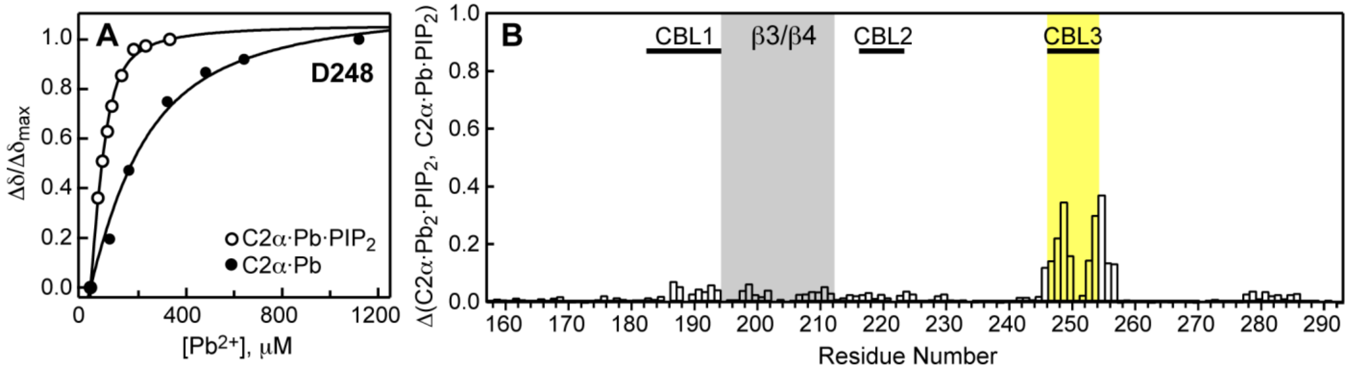

Figure 27. PIP_2 increases the affinity of C2α to Pb^{2+}(2). (A) D248 binding curves for the titration of C2α·Pb·PIP_2 (open circles) and C2α·Pb (filled circles) complexes with Pb^{2+}(2). Δδ values are normalized to the maximum observed change, $\Delta\delta_{max}$. (B) Chemical shift perturbation analysis of the C2α·Pb_2·PIP_2 using C2α·Pb·PIP_2 as a reference state. The β3/β4 and CBL3 regions are highlighted in grey and yellow, respectively.

To understand the effect of $Pb^{2+}(2)$ binding on the PIP_2-complexed C2α, we carried out chemical shift perturbation analysis for the pair of PIP_2 complexes, $C2\alpha{\cdot}Pb_2{\cdot}PIP_2$ and $C2\alpha{\cdot}Pb{\cdot}PIP_2$, with the latter used as a reference state. The results are shown in Figure 27B. It is evident that the binding of $Pb^{2+}(2)$ to C2α mostly affects CBL3, and has little effect on CBL1 or the lysine-rich cluster.

Combining the data obtained in this and Chapter I,[48] we constructed a full scheme of thermodynamic equilibria present in the C2α, Pb^{2+}, and PIP_2 system. We have experimentally determined the dissociation constants for the five out of seven binding equilibria, as indicated in Figure 28. Using simple thermodynamic considerations, we were able to calculate the two remaining dissociation constants. $K_{d1}^{Pb,PIP}$ for the reaction of $Pb^{2+}(1)$ dissociation from the $C2\alpha{\cdot}Pb{\cdot}PIP_2$ complex is 12 nM; this represents a ~6-fold increase in the $Pb^{2+}(1)$ affinity compared to the PIP_2-lacking system. $K_d^{PIP,Pb(2)}$ for the reaction of PIP_2 dissociation from the $C2\alpha{\cdot}Pb_2{\cdot}PIP_2$ complex is 26 μM, which corresponds to a ~43-fold increase in PIP_2 affinity compared to the apo C2α. In summary, our binding data clearly illustrate that Pb^{2+} and PIP_2 significantly enhance each other's interactions with C2α.

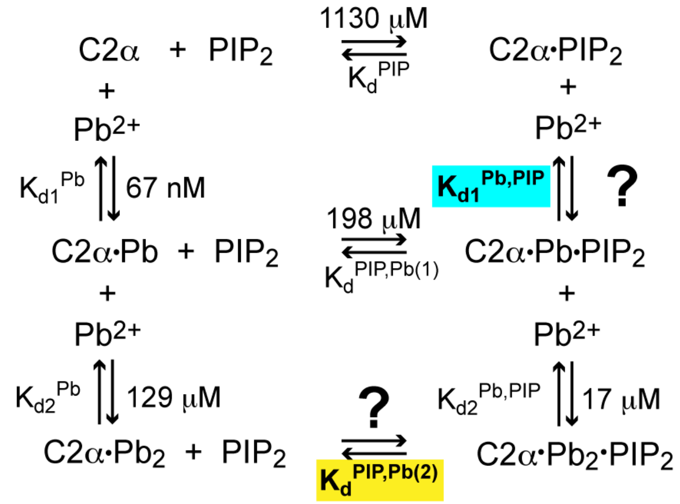

$$\mathbf{K_{d1}^{Pb,PIP}} = \frac{K_{d1}^{Pb} K_d^{PIP,Pb(1)}}{K_d^{PIP}} = 12 \pm 1 \text{ nM}$$

$$\mathbf{K_d^{PIP,Pb(2)}} = \frac{K_d^{PIP,Pb(1)} K_{d2}^{Pb,PIP}}{K_{d2}^{Pb}} = 26 \pm 3 \ \mu\text{M}$$

Figure 28. Thermodynamic binding equilibria and dissociation constants in the C2α, Pb^{2+}, and PIP_2 system. The constants calculated from the experimentally measured K_d values are highlighted for the Pb^{2+} (cyan) and PIP_2 (yellow) dissociation reactions.

Interplay between Ca^{2+} and PIP_2

The NMR response of C2α·Ca_2 to PIP_2 binding was rather complex, which prompted us to separate the responsive residues into three groups. The 27 residues of Group 1 - the largest - belong to the lysine-rich cluster and adjacent protein regions (*vide supra*). The residues of Groups 2 and 3 could be fit with K_d values that are either above or below the K_d values that were obtained for the residues of Group 1. Figure 29 and Figure 30 show the NMR-detected binding curves the members of Groups 2 and 3, respectively. Table 5 summarizes the K_d values that were obtained from either global (Group 2) or individual (Group 3) fits.

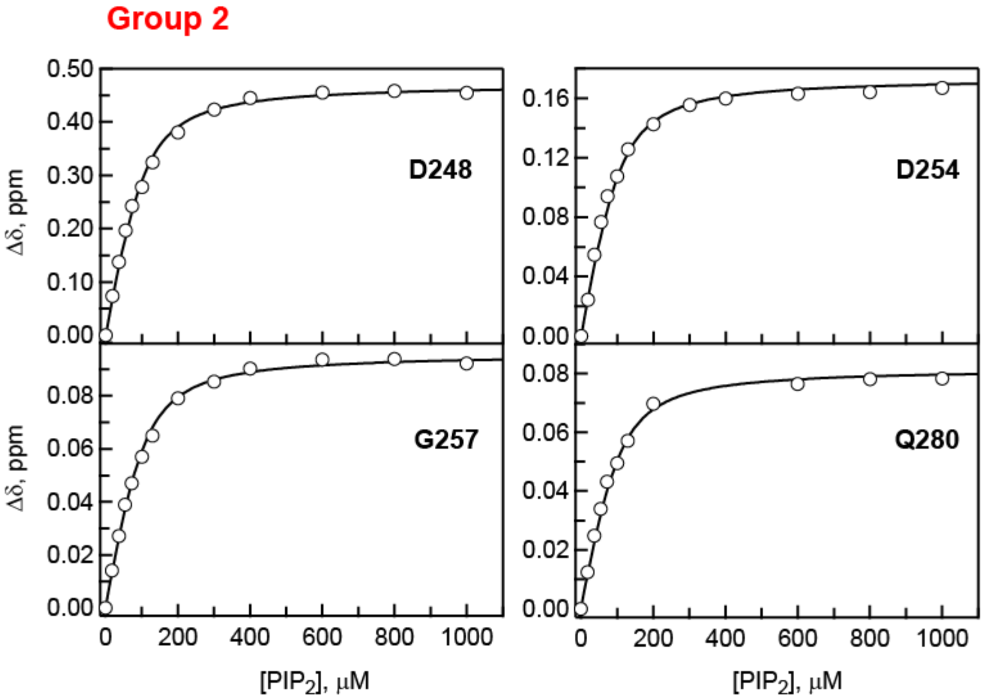

Figure 29. NMR-detected PIP$_2$-binding curves for Group 2 residues. Solid line corresponds to global fit using Equation 1. F255 and T250 show behavior consistent with the "high-affinity" Group 2, but their respective dissociation constants cannot be quantified due to the curvature in the chemical shift trajectory (F255) and intermediate-exchange behavior (T250).

Table 5. K$_d$ values obtained for PIP$_2$ binding in C2-Ca$_2$ state.

Group 2	***Global Fit***	
Residue	**K$_d$, μM**	**Location**
D248	24 ± 1	CBL3
D254	24 ± 1	CBL3
G257	24 ± 1	CBL3
Q280	24 ± 1	Helix 3
Group 3	***Individual Fits***	
D187	308 ± 21	CBL1
L191	735 ± 56	CBL1
G190	1165 ± 158	CBL1
Y195	328 ± 16	β3
N253	175 ± 12	CBL3

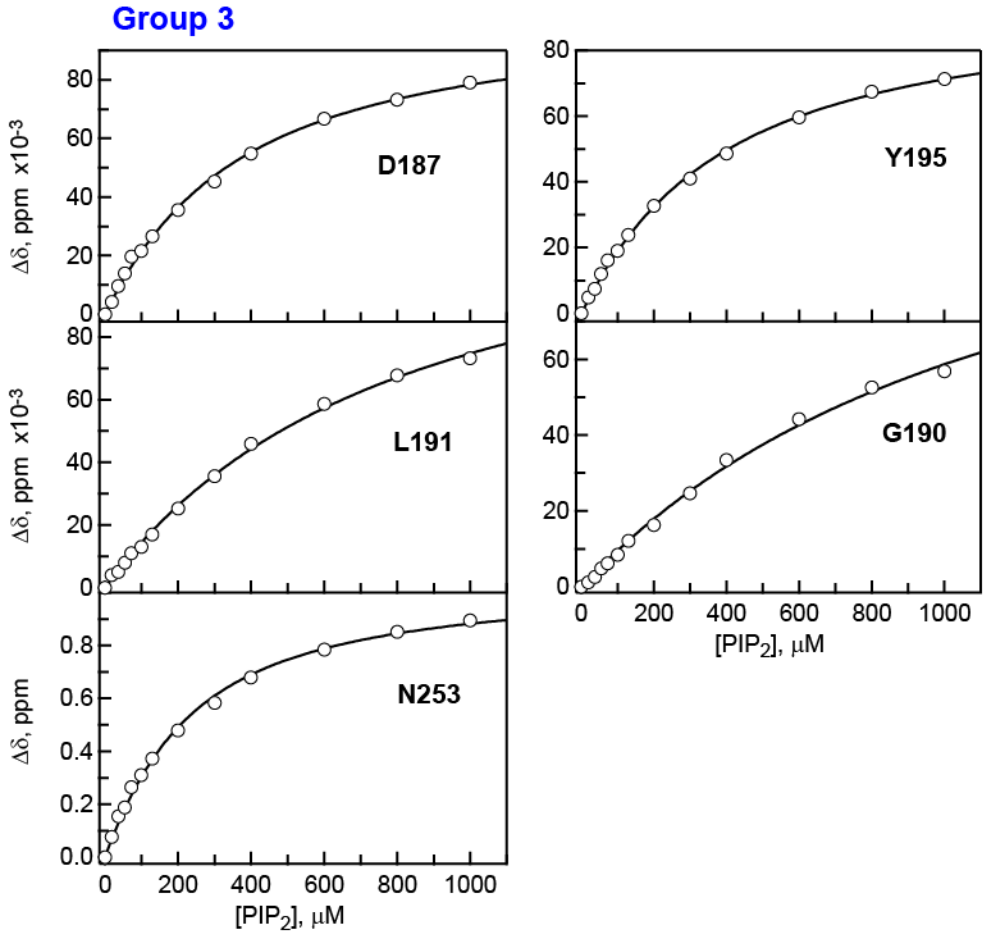

Figure 30. NMR-detected PIP$_2$-binding curves for Group 3 residues. Solid line corresponds to residue individual fits using Equation 1.

There are six residues in Group 2: D248, T250, D254, F255, G257, and Q280. Four of them: D248, T250, D254, and F255 belong to the CBL3 or its hinges, as shown in Figure 8C. Group 3 with five members: D187, G190, L191, Y195, and N253 maps onto the CBL1 region of C2α (Figure 31, blue) with the exception of Y195 and N253, which reside on the β3 strand and CBL3, respectively.

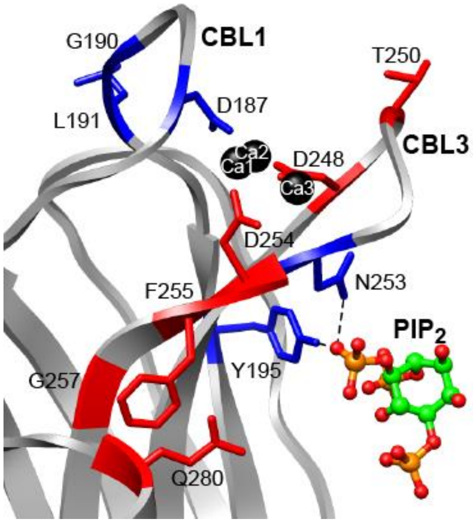

Figure 31. Residues exhibiting complex response in PIP_2 NMR-detected binding. Group 2 (red) and Group 3 (blue) residues mapped onto the crystal structure of Ca^{2+}- and PIP_2-complexed C2α (PDB ID: 3GPE).

There could be two possible explanations for the differences in the apparent PIP_2 dissociation constants. First, if the conformational dynamics of the PIP_2- and Ca^{2+}-complexed C2α is different from that of the Ca^{2+}-complexed C2α, this difference could contribute to the observed chemical shift changes during the PIP_2 titration. Second, an additional binding process that affects the backbone chemical shifts of specific protein segments and manifests itself as an apparent change in the C2α affinity to PIP_2 could be present in the system. This additional process is likely to be the binding of the third Ca^{2+} ion to the PIP_2-complexed C2α. In the crystal structure of the PIP_2-complexed C2α, Ca^{2+}(3) is coordinated by the carboxyl oxygens of D254 and D248, the sidechain oxygen of T251, and the backbone carbonyl oxygen of R252. We know from our previous work that, in the absence of PIP_2, the Ca^{2+}(3) site is not populated under the conditions of our

NMR experiments. However, the binding of PIP_2 to the $C2\alpha \cdot Ca_2$ complex may enhance the affinity of $C2\alpha$ to Ca^{2+}(3) in much the same way it enhances the affinity of $C2\alpha \cdot Pb \cdot PIP_2$ to Pb^{2+}(2) (*vide supra*). As a result, some protein residues may show the titration behavior that essentially reflects the two binding processes that involve PIP_2 and Ca^{2+}(3). As a final note, the heterogeneity in the apparent K_d values for Group 2 and 3 residues is specific to the $C2\alpha$-Ca^{2+} system where Ca^{2+} is in 25-fold excess with respect to protein, and is not observed in the $C2\alpha \cdot Pb$ complex, where there is no excess of metal ions.

A similar behavior with respect to PIP_2 binding was reported for another domain C2 domain, the C2A domain of rabphilin-3A.[95] Those data were interpreted as the existence of an additional - albeit weaker - PIP_2 binding site.

Pb^{2+} promotes the association of $C2\alpha$ with PIP_2-containing membranes

Our next step was to determine the effect of Pb^{2+} on the interactions between $C2\alpha$ and PIP_2 embedded into lipid bilayers. This was accomplished using protein-to-membrane FRET experiments. The tryptophan residues of $C2\alpha$ served as a donor. Dansyl-PE, a fluorescent lipid that was incorporated into the LUVs, served as an acceptor. The LUVs were composed of POPC/POPS/bp-PIP_2/dansyl-PE with molar ratios of 61:30:2:7.

To provide the baseline for Pb^{2+} experiments, we first measured the protein-to-membrane FRET in the absence of metal ions. We determined that, in addition to our standard decalcification procedures applied to $C2\alpha$ and buffers, the LUV preparations had to be decalcified as well to eliminate sub-micromolar concentrations of contaminating Ca^{2+} that were sufficient to promote the C2α-membrane association. The metal titration experiments shown in Figure 32A were carried out with decalcified lipids. In these experiments, we titrated the divalent metal ion into the mixture of C2α and LUVs containing 2% PIP_2, and monitored the increase in the intensity of the dansyl emission band at 505 nm. The Ca^{2+}-driven protein-membrane binding curve was fitted with Equation 7, which produced $[Ca^{2+}]_{1/2}=0.7\pm0.1$ μM and $H_{Ca}=1.5\pm0.1$. This represents a ~7-fold decrease in the $[Ca^{2+}]_{1/2}$ concentration compared to that obtained for the PIP_2-lacking membranes.

Similar to Ca^{2+}, the addition of Pb^{2+} ions to the mixture of apo C2α and PIP_2-containing LUVs resulted in a systematic increase in the protein-to-membrane FRET, albeit with a lower overall FRET efficiency. Fitting the Pb^{2+}-driven membrane-binding curve produced $[Pb^{2+}]_{1/2}=1.3\pm0.1$ μM and $H_{Pb}=2.1\pm0.1$. This represents a ~5-fold increase in the apparent C2α affinity to Pb^{2+} compared to the PtdSer-containing PIP_2-lacking LUVs.[48] Overall, our results show that the ability of Pb^{2+} and Ca^{2+} to drive protein-membrane associations is comparable, and that the presence of PIP_2 in the membrane increases the affinity of C2α to metal ions several-fold.

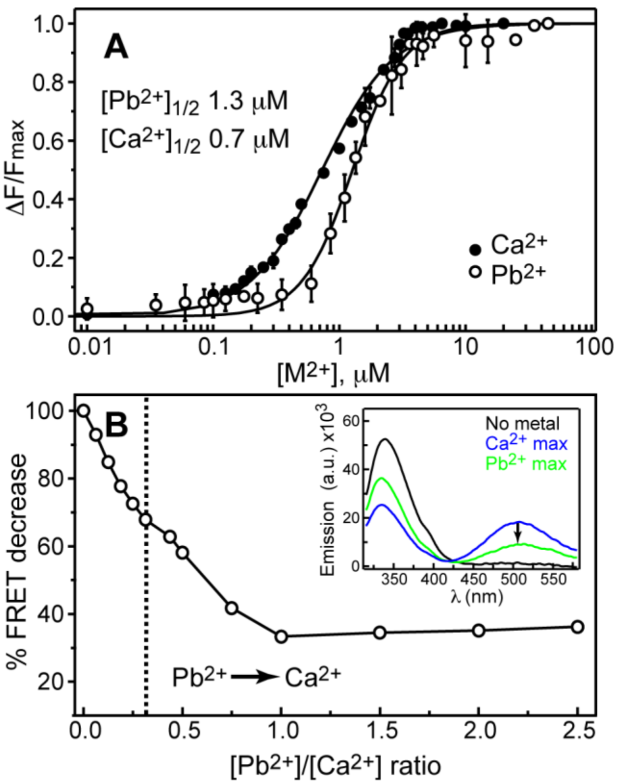

Figure 32. C2α-metal dependent binding to PIP$_2$-containing membranes (A) Normalized protein-to-membrane FRET as a function of total Ca^{2+} and Pb^{2+} concentration in the presence of POPC/POPS/bp-PIP$_2$/dansyl-PE (61:30:2:7) LUVs. The error bars were calculated as standard deviations in triplicate experiments. (B) Decrease in FRET efficiency as a result of Ca^{2+} displacement with Pb^{2+}. The Ca^{2+} concentration was kept constant at 10 μM while the Pb^{2+} concentration was varied. The dashed vertical line marks the [Pb^{2+}]/[Ca^{2+}] ratio of 0.3, at which about half of the protein is in Pb^{2+}-bound form. For comparison, the inset shows the FRET spectra of the C2α-LUV system at zero metal ion concentration (black), 10 μM Ca^{2+} (blue), and 20 μM Pb^{2+} (green).

To characterize the competitive behavior of Pb^{2+} with respect to Ca^{2+}, we prepared the ternary C2α-Ca^{2+}-LUV complex by adjusting the final concentration of Ca^{2+} to 10 μM. We titrated the complex with Pb^{2+}, while monitoring the intensity of the dansyl emission band.

A steady decrease in FRET efficiency was observed (Figure 32B) with increasing Pb^{2+} concentration. However, neither Pb^{2+} nor Ca^{2+} appreciably quench the dansyl fluorescence, as shown in Figure 33.

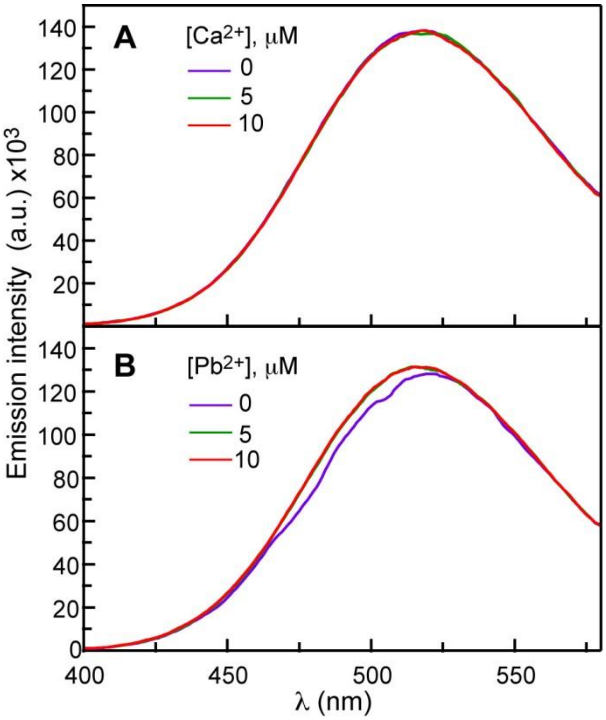

Figure 33. Pb^{2+} nor Ca^{2+} quench dansyl fluorescence Fluorescence emission spectra of the LUV-metal ion mixtures collected with the excitation wavelength of 336 nm.

Moreover, the maximum attainable FRET efficiency in the Pb^{2+}-driven membrane association experiments is typically ~40-60% of that attainable in Ca^{2+}-driven experiments. This is illustrated in the inset of Figure 9B with the FRET spectra of metal-free (black), Pb^{2+}-containing (green), and Ca^{2+}-containing (blue) C2α-LUV. Given these properties of the C2α-LUV-metal ion system, we interpreted the decrease in

FRET efficiency in the competition experiments as Pb^{2+} gradually displacing Ca^{2+} from the protein. A plateau region – indicative of full Ca^{2+} displacement by Pb^{2+} – is reached at the Pb-to-Ca ratio of 1.0.

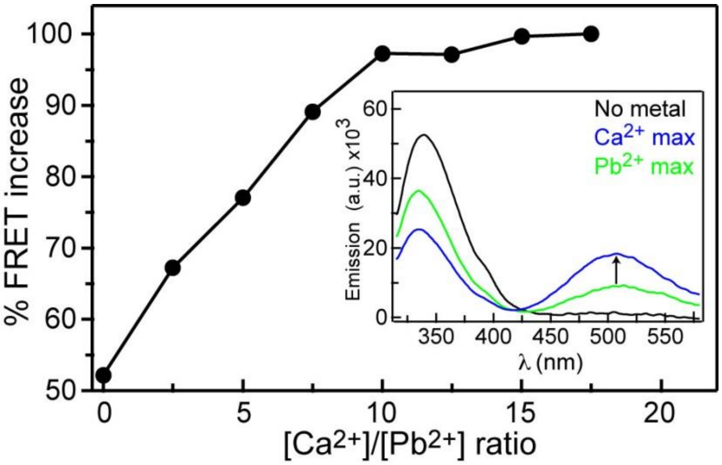

Figure 34. Ca^{2+}/Pb^{2+} competition experiments in the presence of LUVs having 2% PIP_2 content. The inset shows the fluorescence spectra of C2α-LUV system at 0 concentration of metal ions (black), 20 μM Pb^{2+} (green), and 10 μM Ca^{2+} (blue).

The results of the reverse experiment, in which we attempted to outcompete Pb^{2+} with Ca^{2+}, are shown in Figure 34. In agreement with our previous observations, we detected a steady increase in FRET efficiency with increasing Ca^{2+} concentration, until it reached a plateau value at the Ca-to-Pb ratio of ~10. A comparison of the competition data demonstrates that Pb^{2+} is more effective than Ca^{2+} in displacing the competing metal ion from C2α in the presence of PIP_2-containing membranes. *In vivo*, the specifics of the Pb^{2+}/Ca^{2+} competition behavior would depend on the relative and absolute bio-available concentrations of these metal ions.

As we established in the work described in Chapter II shown that, in addition to mediating the protein-membrane interactions, Pb^{2+} itself could associate with PtdSer-containing LUVs. To test the influence of PIP_2 on this process, we combined vesicle sedimentation assays with Inductively Coupled Plasma (ICP) detection of Pb^{2+} in the pellet and supernatant fractions. No protein was added to the samples. We explored two total lipid concentration regimes: 1.5 mM and 150 μM (as used in FRET experiments of Figure 32). The composition of LUVs was POPC/POPS/bp-PIP_2 with molar ratios of 68:30:2. For each Pb^{2+} concentration point, the amount of Pb^{2+} in the supernatant ($[Pb^{2+}]_{free}$) and pellet ($[Pb^{2+}]_{bound}$) fractions was quantified using ICP as described in Chapter II.

The data for the 1.5 mM total lipid concentration are shown in Figure 35. For comparison, we also plotted the data for the PIP_2-free membranes obtained in our previous work.[48] These results demonstrate that the affinity of Pb^{2+} to lipid membranes increases in the presence of PIP_2. At 1.5 mM total lipid, the amount of Pb^{2+} taken up by membranes is a substantial fraction of the total metal added.

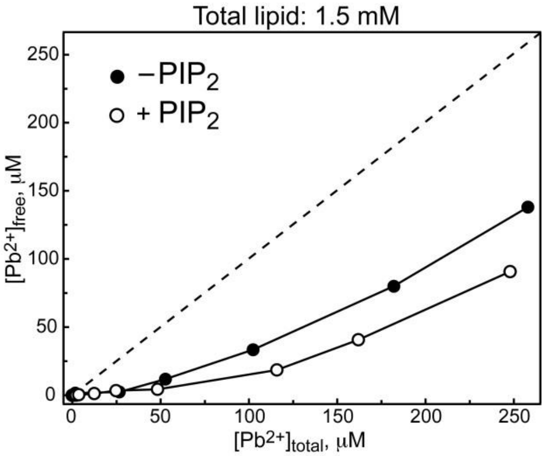

Figure 35. Relationship between $[Pb^{2+}]_{free}$ and $[Pb^{2+}]_{total}$ obtained using ICP analysis at high lipid concentrations. The total lipid concentration was 1.5 mM. The LUV composition was POPC/POPS/bp-PIP_2 with molar ratios of 68:30:2 and POPC/POPS with molar ratios of 70:30.

Compared to the "high-lipid" regime, the interaction between Pb^{2+} and membranes becomes less prominent when the total concentration of lipids is decreased 10-fold to 150 μM. However, when the total concentration of Pb^{2+} is much smaller than that of lipids, the fraction of membrane-bound Pb^{2+} is non-negligible. The results are shown in Figure 36 for the PIP_2-lacking (**A**) and PIP_2-containing (B) membranes. For comparison, when the total Pb^{2+} concentration is 2.2 μM, 76% of Pb^{2+} is in the supernatant fraction for the PIP_2-lacking, PtdSer-containing vesicles; this value decreases to 33% in the presence of 2% PIP_2. The relationship between the free and total Pb^{2+} concentrations in the 10-micromolar range is shown in the insets of Figure 36. For comparison, we also included the data obtained in our previous work on the Pb^{2+} association with PIP_2-lacking vesicles.

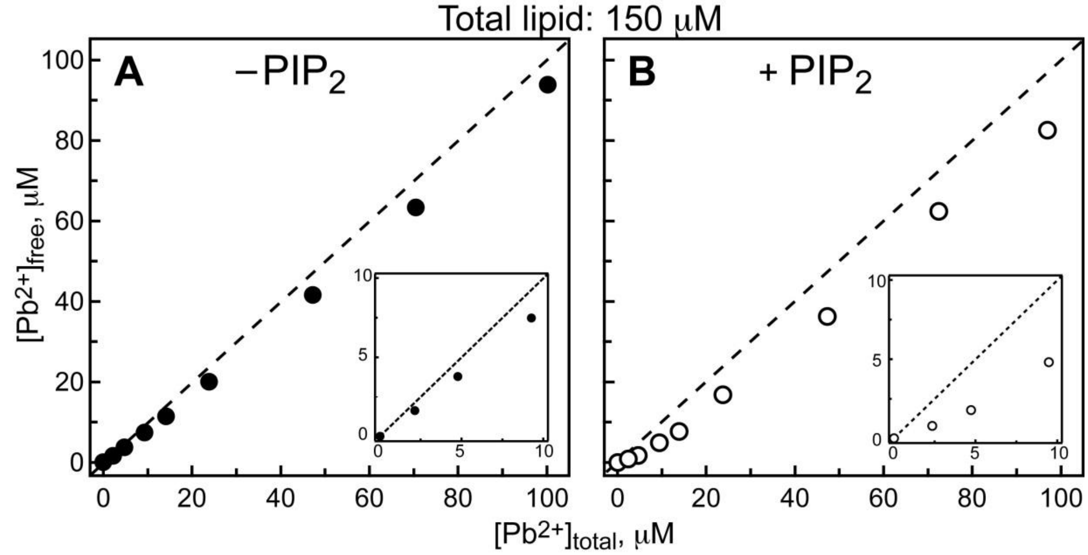

Figure 36. Relationship between $[Pb^{2+}]_{free}$ and $[Pb^{2+}]_{total}$ obtained using ICP analysis at low lipid concentration. The total lipid concentration was 150 μM. The LUV composition was POPC/POPS/bp-PIP_2 with molar ratios of 68:30:2 (A) and POPC/POPS with molar ratios of 70:30 (B). The insets show the 0-10 μM region.

Furthermore, we used Cryo-EM to examine the influence of Pb^{2+} on the integrity and aggregation state of LUVs. The total lipid and Pb^{2+} concentrations were 150 μM and 100 μM, respectively. 100 μM was the maximum Pb^{2+} concentration used in our FRET experiments. Cryo-EM images shown in Figure 37 were obtained as described in Chapter II.[48] No vesicle aggregation was observed under this set of conditions.

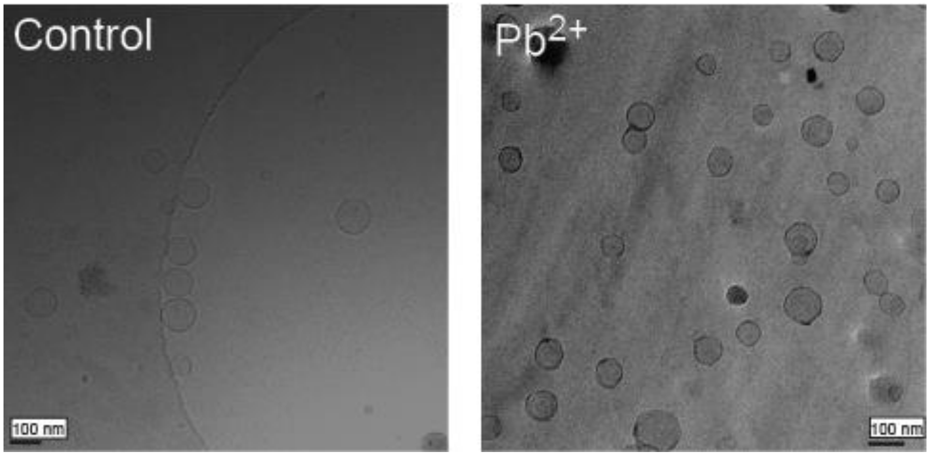

Figure 37. Liposomes integrity assessed by Cryo-EM imaging. Cryo-EM images of POPC/POPS/bp-PIP$_2$ LUVs (68:30:2) in the absence (control) and presence of 100 μM Pb^{2+}. The total concentration of lipids was 150 μM.

Together the data clearly demonstrate that the presence of PIP$_2$ in the LUVs increases the fractional population of the membrane-associated Pb^{2+}. This trend is especially prominent for the "high-lipid" regime of 1.5 mM, in which, depending on the total Pb^{2+} concentration, 60 to 90% of total Pb^{2+} is membrane-associated. Under conditions of our FRET experiments (150 μM total lipids and 2.2 μM total Pb^{2+}), 76% of Pb^{2+} is in the supernatant fraction for the PIP$_2$-lacking, PtdSer-containing vesicles; this value decreases to 33% in the presence of 2% PIP$_2$. This binding equilibrium effectively reduces the amount of Pb^{2+} available for C2α and would have an effect of over-estimating the [Pb^{2+}]$_{1/2}$ value from the data shown in Figure 32A.

Discussion of results

The experiments described in this chapter were designed to determine the influence of PIP_2 on the C2α-Pb^{2+} interactions, with the ultimate objective of gaining insight into the molecular mechanism of Pb^{2+} interference with the Ca^{2+}-dependent function of C2 domains. There are three "checkpoints" where Pb^{2+} interference can occur: (1) interaction with the membrane-free C2 via the high-affinity Pb^{2+}-binding site(s) of the protein; (2) modulation of the metal-dependent C2-membrane association; and (3) direct interaction with the anionic membrane-binding sites. In our previous studies of the ternary system composed of C2α, Pb^{2+} ions, and PtdSer-containing LUVs, we determined that (1) and possibly (3) are the most likely routes. Given the significant role of PIP_2 in C2α localization and membrane binding, we sought to determine the mutual effect of PIP_2 and Pb^{2+} on their respective interactions with C2α. Along with the Pb^{2+}-specific data, we obtained PIP_2-binding information for the apo and Ca^{2+}-complexed states of C2α. Taken together, this information enabled us to dissect the contribution of individual metal-binding sites to the PIP_2 binding and evaluate the competitive behavior of Pb^{2+} with respect to Ca^{2+}.

Using NMR-detected titration of apo C2α with a soluble C4-PIP_2, we identified protein regions whose electronic environment changed as a result of PIP_2 binding. The chemical shift perturbation data of Figure 24 show that this region is not limited to the lysine-rich cluster, but also involves three calcium-binding loops: CBL1, CBL2, and CBL3. The β-strands flanking CBL3, β6 and β7, are also affected by PIP_2. Superposition of the apo- and ligand-bound C2α crystal structures revealed aside from the minor differences in the side-chain conformations, there are no significant ligand-induced structural changes observed for the functional regions, such as the CBLs and the β3-β4 segment. The pairwise RMSD values for the backbone atoms do not exceed 0.5 Å. The relevant information is summarized in Table 6.

Table 6. Backbone root-mean-square deviation (RMSD) of C2α available crystal structures in different ligand bound states.

PDB ID	C2α state	Resolution (Å)	RMSD (bb atoms, Å)	Ref.
3RDJ	apo	1.9	0	[48]
1DSY	Ca^{2+}- & PSF[a]-bound	2.6	0.496	[52]
3GPE	Ca^{2+}-, PSF-, & PIP_2-bound	2.0	0.404	[59]
3TWY	Pb^{2+}-bound	1.5	0.346	[48]

[a] PSF stands for 1, 2-dicaproyl-sn-phosphatidyl-L-serine

This means that large chemical shift perturbations upon PIP_2 binding are most likely due to the changes in the electrostatic environment and/or conformational dynamics of the CBLs rather than in their average conformation.

The affinity of C2α to PIP_2 is rather weak -1.13 mM-in the absence of metal ions. The NMR-detected binding curves could be fit well with Equation 1, indicating the presence of a single PIP_2 binding site on the apo C2α. These data are in agreement with the results of previous studies on the GST-fused C2 domains[65] and the SPR study of the C2-membrane interactions.[63] The metal-independent association of C2α with PIP_2-

containing membranes was not detectable under the conditions of our FRET experiments (Figure 32).

How prevalent are the metal-ion-independent interactions with PIP_2 among the C2 domains? Both C2 domains of rabphilin-3A can interact with inositol-1,4,5-triphosphate, a head group of PIP_2, in Ca^{2+}-independent manner.[95] Calcium-independent association with PIP_2-containing membranes was reported for the C2B domains of synaptotagmin 1[126,139] and synaptotagmin 9.[140] The physiological significance of the apo C2-PIP_2 interaction, as formulated for the C2B domain of synaptotagmin 1, is to increase the speed of response of the host protein to Ca^{2+} by generating the protein state that is already pre-bound to the membrane.[126]

The 2000-fold difference in C2α affinities to $Pb^{2+}(1)$ and $Pb^{2+}(2)$ enabled us to prepare the state of C2α with the metal ion bound to site (1) only. This state, C2α·Pb, along with the apo C2α and C2α·Ca_2, was used to determine the contribution of individual metal sites to PIP_2 binding. The equilibria of Figure 31 indicate that the affinity of C2α to PIP_2 increases several-fold upon progressive saturation of metal binding sites. The K_d is reduced 6-fold for C2α·Pb·PIP_2 compared to C2α·PIP_2, from 1.13 mM to 198 μM. The K_d is further reduced 8-fold for C2α·Pb_2·PIP_2 compared to C2α·Pb·PIP_2, from 198 μM to 26 μM. Expressed in terms of free energies, the $\Delta(\Delta G^0)$ contribution of the first and second Pb^{2+} ions to the C2α-PIP_2 binding reactions are -1.7RT and -2.0RT, respectively. We conclude that metal ions make individual and comparable contribution to the energetics of the PIP_2 binding to C2α. The increase in the

C2α affinity to PIP_2 does not appear to depend on the nature of the metal ion. We reached this conclusion by comparing the dissociation constants of PIP_2 from the C2α·Pb_2·PIP_2 and C2α·Ca_2·PIP_2 complexes. The K_d values are similar - 48 μM and 26 μM - for the Ca^{2+} and Pb^{2+} complexes, respectively.

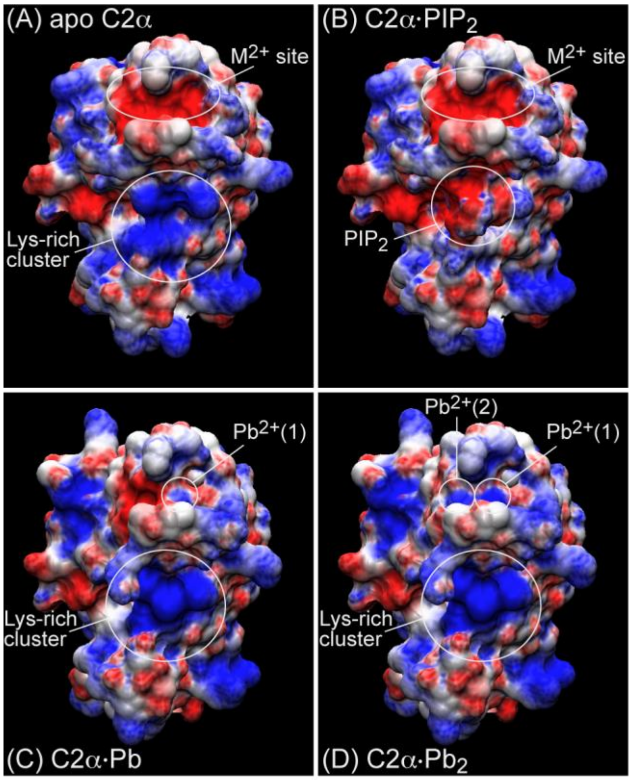

Figure 38. C2α-metal and ligand dependent electrostatic potential. Electrostatic potential mapped onto the surface of (A) apo C2α, (B) C2α·PIP_2, (C) C2α·Pb, and (D) C2α·Pb_2. The color-coding corresponds to the electrostatic potential ranging from -6k_bT/e (red) to +6k_bT/e (blue). Structures in (A) and (B) were generated using the PIP_2-bound C2α (PDB ID: 3GPE), and structures in (C) and (D) were generated using the Pb^{2+}-complexed C2α (PDB ID: 3TWY).

The ability of Ca^{2+}-dependent C2 domains to associate with anionic lipids and protein partners in response to binding Ca^{2+} has been attributed to the "electrostatic switch" mechanism.[50,141,142,143] The basic premise of this mechanism is that the binding of Ca^{2+} ions increases the electrostatic potential of C2 domains and hence its attraction to the negatively charged interacting partner. Figure 38 shows the calculated electrostatic potential of C2α mapped onto the crystal structures. The apo C2α has a negatively charged metal binding site formed by the aspartate residues, and a positively charged lysine-rich cluster (panel A). The interaction of PIP_2 with the lysine-rich cluster results in the decrease of the electrostatic potential of the complex (panel B). In contrast, Pb^{2+} (or Ca^{2+}) binding to C2α increases the electrostatic potential of the complex and its attraction to the negatively charged PIP_2. The individual contributions of Pb^{2+} ions are illustrated in panels (C) and (D). In addition, we carried out Hahn-Echo (HE) experiments[136] to determine if the binding of metal ions to C2α affects the microsecond-to-millisecond backbone dynamics of the β3-β4 region. The data were collected for the three forms of C2α: apo, Pb^{2+}-bound, and Ca^{2+}-bound. The R_2^{HE} values, which carry the full contribution of the conformational exchange term, R_{ex}, were calculated from the corresponding intensity ratios as described by Massi et al.[137] The differences in R_2^{HE} values between the apo and metal-bound forms of C2α are plotted against the primary structure in Figure 39. Given that metal binding to C2α does not appreciably change the conformational dynamics of the β3-β4 segment (Figure 39), we conclude that the modulation of the C2α affinity to PIP_2 by metal ions is mostly electrostatic in nature.

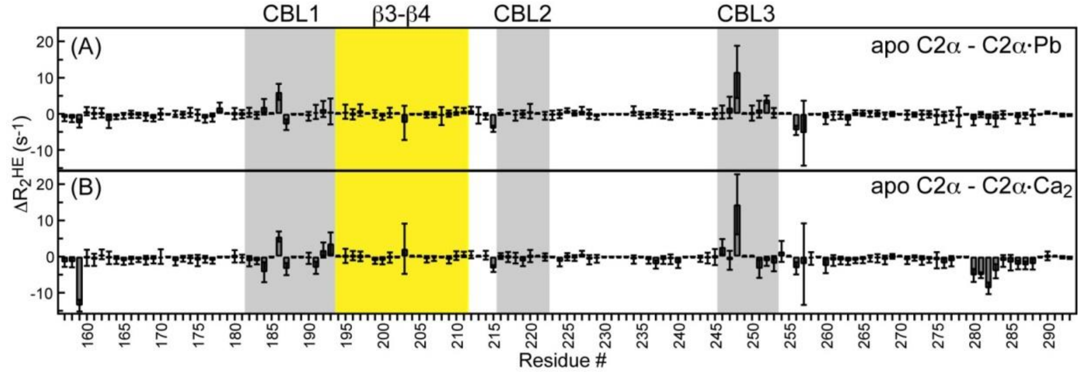

Figure 39. C2α does change the conformational dynamics of the β3-β4 segment. The R_2^{HE} difference plots for the apo and Pb^{2+}-bound (A) and Ca^{2+}-bound (B) C2α. The CBL and β3-β4 regions are highlighted in grey and yellow, respectively.

Pre-bound PIP_2 enhances the affinity of C2α to metal ions. In the presence of saturating PIP_2, the affinity of C2α to Pb^{2+}(1) increased 6-fold, from 67 to 12 nM. Similarly, the binding affinity of C2α to $Pb^{2+(2)}$ increased 8-fold, from 129 to 17 μM. Our data lend support to the TAMA ("target activated messenger affinity") mechanism that was proposed by Falke's laboratory to explain how C2 domains, while being poor Ca^{2+} sensors in membrane-free environment, are able to respond to micromolar concentrations of Ca^{2+} in the cell.[68] In the context of TAMA, membrane-embedded PIP_2 is the target and the metal ion is the messenger. The proximity (or pre-binding) of C2α to PIP_2-containing membranes makes C2α more responsive to low concentrations of metal ions by increasing its binding affinity. This behavior has an immediate relevance to Pb^{2+} being a Ca^{2+} surrogate, because the presence of PIP_2 in the membranes will effectively sensitize C2α to the bioavailable concentrations of Pb^{2+}.

We used protein-to-membrane FRET experiments to probe the Pb^{2+}-dependent association of C2α with the PIP_2-containing membranes. Similar to Ca^{2+}, we observed a steady increase in FRET efficiency as a function of metal ion concentration. In the Ca^{2+}-driven experiments, the incorporation of 2% PIP_2 into the membranes decreased the $[Ca^{2+}]_{1/2}$ value from 5 μM to 0.7 μM, or ~7-fold. Our data are in general agreement with the results of the previous SPR work[63] (4-fold decrease in Ca^{2+} K_d) and FRET studies with multi-component mimics of the plasma membrane[68] (20-fold decrease in $[Ca^{2+}]_{1/2}$). In the Pb^{2+}-driven experiments, the incorporation of 2% PIP_2 into the membranes decreased the $[Pb^{2+}]_{1/2}$ value from 7 μM to 1.3 μM, or ~5-fold. This value is probably underestimated by a factor of ~2-3, because the sequestration of Pb^{2+} by the PIP_2- and PtdSer-containing membranes reduces the amount of Pb^{2+} available to C2α. Figure 35 and Figure 36 illustrate how the presence of membrane-embedded PIP_2 enhances the interactions of Pb^{2+} with anionic membranes. In summary, the presence of PIP_2 in the membranes results in the enhancement of the C2α affinity to divalent metal ions by roughly one order of magnitude.

The ability of Pb^{2+} to compete with Ca^{2+} for protein binding sites is what makes Pb^{2+} a potent environmental toxin. To assess the competitive behavior of Pb^{2+} in the context of C2α function, we carried out a Pb^{2+}/Ca^{2+} competition experiment in the presence of PIP_2-containing membranes. As shown in Figure 32B, the displacement of Ca^{2+} from the ternary C2α-Ca^{2+}-LUV complex by Pb^{2+} can be readily monitored because of the differences in the maximum attainable FRET efficiency. Our data indicate that the equal population of Pb^{2+}- and Ca^{2+}-bound C2α species is reached at

$[Pb^{2+}]/[Ca^{2+}]$ of 0.3. This corresponds to Pb^{2+} concentration of 3.0 μM, which is ~2-fold smaller than the value obtained in our previous experiments with the PIP_2-lacking PtdSer-containing lipid membranes.[48]

Given the comparable ability of Pb^{2+} and Ca^{2+} to promote the association of C2α with lipid membranes, how does Pb^{2+} displace Ca^{2+}? We speculate that the displacement occurs through the interaction of Pb^{2+} with the high-affinity site on C2α (Figure 40). The Ca^{2+}-bound form of C2α exists in equilibrium between membrane-bound and membrane-free states (reaction 1). By itself, C2α is a low-affinity Ca^{2+}-binding module, which makes the exact Ca^{2+} ligation state of membrane-free C2α difficult to ascertain. The interaction of Pb^{2+} with a single high-affinity site displaces Ca^{2+} from the protein (reaction 2), including the second metal-binding site.

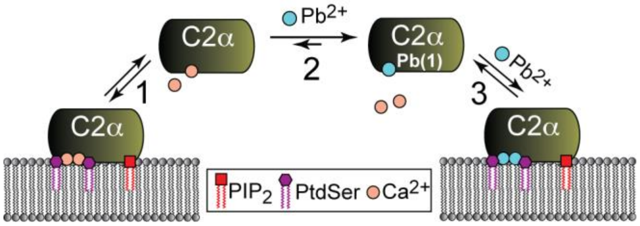

Figure 40. Pb^{2+}/Ca^{2+} competition through the interaction with the C2α high-affinity metal-binding site.

This occurs because saturating the high-affinity Pb^{2+}(1) site on the C2α decreases the affinity of the Ca^{2+} ion to the second site to ~13 mM,[48] thereby precluding the formation of the mixed Pb^{2+}/Ca^{2+} species.

The concentration of free Ca^{2+} in the cytosol is ~100 nM and 1 μM in the resting and stimulated states, respectively.[144] The concentration of bioavailable Pb^{2+} is picomolar-to-nanomolar.[105] Given that the C2α affinity to Pb^{2+}(1) exceeds its affinity to Ca^{2+} by more than 1,000-fold, the formation of the C2α·Pb species in the cell is plausible. Further fate of the C2α·Pb species depends on the bioavailable Pb^{2+} concentration. According to our FRET data, the high affinity of Pb^{2+}(1) to C2α does not translate into high affinity of the C2α·Pb complex to the lipid membranes. The Hill coefficient of 2 that we obtained from the fit of the Pb^{2+}-driven FRET membrane-binding curve implies that the binding of the second Pb^{2+} ion to C2α is required for protein-membrane association (reaction 3). The affinities of C2α to Pb^{2+}(2) and Ca^{2+} are comparable in the membrane-free form of the protein, which in turn results in the comparable ability of these two ions to drive the C2α-membrane association (Figure 32A). If the concentration of Pb^{2+} in the cell is not sufficient to promote the association of C2α with membranes, Pb^{2+} binding may still activate PKCα by inducing the intra-domain rearrangement within the regulatory domain of the enzyme. In either scenario, the presence of Pb^{2+}(1) at the high-affinity C2α site will interfere with the normal catalytic activity of PKCα by making the enzyme unresponsive to Ca^{2+} activation during the signaling event.

Lastly, the saturation of one Pb^{2+} site is not sufficient for the C2α to undergo membrane association under the conditions of our experiment. However, given the proposed mechanistic roles of individual Ca^{2+} sites[68] and our NMR results on PIP_2

binding to the C2α·Pb complex, we cannot completely exclude the possibility that, at high local concentrations of anionic lipids, such as PtdSer and PIP_2, the association of C2α·Pb with membranes may in fact occur. This situation can arise upon the interaction of PKCα with its substrates, such as MARCKS (myristoylated alanine-rich C kinase substrate), that laterally sequesters PIP_2 molecules[145] and releases them upon phosphorylation by PKC or interactions with calmodulin.

CHAPTER IV

CD (II) AS A STRUCTURAL BUT NOT FUNCTIONAL SURROGATE OF C2 DOMAINS*

Background

While it is well established that heavy metal ions interfere with the function of Ca^{2+}-binding proteins (CBPs),[8,146,147] the selectivity and mechanisms are not well understood. The experiments carried out in this chapter use C2α as a paradigm to investigate the ionic and molecular mimicry capabilities of Cd^{2+} with respect to the (i) structure, (ii) metal coordination geometry, (iii) affinity, and (iv) metal-dependent interactions with PtdSer containing membranes.

The objective of this work is to understand the functionally relevant aspects of the bio-inorganic chemistry of heavy metal ions, such as Cd^{2+} and Pb^{2+} (See Chapter II), and their effect on the structure and function of CBPs. This is of particular significance for peripheral membrane binding domains such as C2 and annexins, which undergo membrane association in a Ca^{2+}-dependent manner. They exhibit specificity towards negatively charged phospholipids, such as PtdSer. Moreover, direct metal ion and phospholipid headgroup coordination have been proposed to function as a bridge between the protein and the membrane.[52,148] The direct role of metal-phospholipid

---

* Reproduced in part with permission from: Krystal A. Morales, Yuan Yang, Zheng Long, Pingwei Li, Alexander B. Taylor, P. John Hart, and Tatyana I. Igumenova. *Journal of the American Chemical Society* 2013, 135 (35), 12980-12983.

interactions is also supported by a mutagenesis study carried out in the C2 domain PKCβ (C2β). The studies carried out in this Chapter, established that changes in the electrostatic potential by metal binding to the CBLs are not sufficient to promote the membrane-association of C2. These observations propose a direct role of metal binding in promoting membrane association, than simply acting as a non-specific switch.[51] With the increasing number of C2 domain containing proteins, this work will not only impact the understanding of the structural and functional chemistry of heavy metal ions, but also understanding the role of Ca^{2+}-dependent C2 domains in heavy metal ion toxicity.

Based on known toxicity and potential for human exposure, the Agency for Toxic Substance and Disease Registry (ATSDR) ranked Cd^{2+} as the 7th most hazardous substance out of 275 substances.[27] The primary route of exposure for non-smokers is through the ingestion of food supplies from contaminated water sources, typically fish.[27] There are no safe limits of exposure, and Cd^{2+} has adverse effects on almost every organ, predominantly the liver and kidneys where it is continuously reabsorbed.[149] The most prominent effects include: (i) Ca^{2+} homeostasis disruption [150,151], (ii) increase in Reactive Oxygen Species (ROS)[152,153], DNA damage[40], gene expression changes[146,154,155], and interference with signaling pathways[156].

Upon ingestion, Cd^{2+} is rapidly absorbed into the blood stream, where it is predominantly found complexed with metallothioneins. Metallothioneins are small, cysteine-rich, metal-binding proteins associated with Cd^{2+} detoxification. Although the complex is filtered in the kidneys, metallothioneins are degraded by lysosomes, releasing Cd^{2+}.[27] Free Cd^{2+} can then be transported inside cells by either direct transport or co-transport. Direct transport uses ionic mimicry mechanisms through Ca^{2+} channels, while in co-transport Cd^{2+} gains entry by opportunistic interaction with sulfhydryl-containing compounds, such as Glutathione [138], Cysteine, and homocysteine.[147,153,157] This is in contrast to Pb^{2+} cell entry, for which no clear transport targets have been identified.[153]

Due to the high similarity in ionic radius (Ca^{2+}=0.99 Å and Cd^{2+}=0.97 Å), advantageous spectroscopic properties in NMR (nuclear spin=½) and X-ray crystallography (anomalous signal), Cd^{2+} has been used as a structural surrogate for CBPs. Ca^{2+} is a hard acid, with preferences for hard bases such as carboxylates. As a soft acid, Cd^{2+} also appears to follow the hard-soft acid base (HSAB) theory by displaying preferential interactions with sulfhydryl containing ligands in proteins (soft bases).[158] However, accumulating evidence indicates that it predominantly influences Ca^{2+}-dependent processes by either indirect increase of Ca^{2+} intracellular concentrations or direct interactions with CBPs involved in signaling and channels in order gain entry to the cell.[146,147] Nonetheless, the HSAB theory is only one factor that impacts metal ion selectivity; site selectivity is also influenced by the pre-formed coordination geometry and identity of the side chain ligands in the metal-coordinating sites. According to the structural protein data bank analysis of metal-bound proteins performed by Rulíŝek and Vondráŝek, Cd^{2+} is the only metal ion that does not have a preference for a single coordination number.[158] Cd^{2+} was found primarily in either octahedral or square planar geometries, with a slight preference for octahedral. Detailed analysis of the protein ligand sidechains indicated that the Cysteine is predominantly found around the Cd^{2+} coordination sphere; however taking into account all ligands analyzed, about 50/50 were soft (S and N) and hard ligands (O). Reduction potential and speciation of metal ions in the environment and in our body, are also contributing factors that need to be considered when establishing availability and selectivity.[153] All aspects discussed above have a stronger impact in cases where the coordination chemistry of the metal ion carries a specific function other than structure stabilization such as: catalysis, membrane interactions, or induced changes in the average conformation or flexibility of the protein. Hence, the mechanistic possibilities by which heavy metal ions toxicity is achieved are far more diverse and complex.

In addition to the studies presented in Chapter II, the work carried out in this chapter provides insights into the effect of Cd^{2+} on the structure and membrane-binding properties of the C2α. Remarkably, despite the high affinity and almost identical coordination geometry between with respect to Ca^{2+}, Cd^{2+} is unable to support the membrane-binding function of the protein. This is in contrast to Pb^{2+}, which adopts a hemidirected coordination geometry for the second metal site, yet its ability to drive the C2α-membrane association is comparable.[48] The Cd^{2+}-binding sites within C2α were identified using NMR spectroscopy, and characterization of the metal-ion-dependent interactions between C2α and phospholipid membranes was carried out using fluorescence spectroscopy and ultracentrifugation experiments. The results from this work provide the first direct evidence concerning the specific role of divalent metal ions in mediating protein-membrane interactions, which illustrates the potential diversity of functional responses caused by toxic metal ions. Lastly, this work has important implications for metal substitution studies in proteins.

Experimental procedures

Materials

1-palmitoyl-2-oleoyl-*sn*-glycero-3-phosphocholine (POPC) and 1-palmitoyl-2-oleoyl-*sn*-glycero-3-phospho-L-serine (POPS) were obtained from Avanti Polar Lipids (Alabaster, AL).

C2α purification

U-^{15}N and natural abundance C2α (139 residues) was expressed and purified from BL21 (DE3) cells in pET-SUMO vector as described in Chapter II.[48]

NMR spectroscopy

NMR experiments were carried out at 25 °C on a Varian Inova spectrometer operating at ^{1}H Larmor frequency of 500 (11.7 Tesla). The temperature was calibrated using methanol. Sequence-specific assignments of the $^{1}H_{N}$, $^{13}C\alpha$, $^{13}C\beta$, and ^{15}N resonances for the apo-C2α were carried out previously and described in Chapter II.[48]

Binding of Cu^{2+} to C2α was monitored using ^{15}N-^{1}H Heteronuclear Single Quantum Coherence (HSQC) spectra of [U-^{15}N] enriched 110 μM metal-free [25] C2α domain. Apo C2α was obtained by carrying out the last purification step in the presence of 0.1 mM EDTA, followed by extensive exchange of protein solution into the EDTA-free buffer. The desired concentration of divalent metal ions in the NMR sample was achieved using concentrated stock solution of Cu(II) chloride. Cu^{2+} binding experiments were carried out in10 mM MES (pH 6.0), 100 mM KCl, 8% D_20, 0.02% NaN_3. All buffer used were treated with Chelex 100 (Sigma-Aldrich) to remove residual divalent metal ions.

Metal-dependent membrane association of C2α by vesicle ultracentrifugation

Sucrose-loaded large unilamellar vesicles (LUVs) were prepared as described in Chapter II.[48] An additional EDTA wash was carried out to remove divalent metal ions from the liposome suspension. EDTA was subsequently removed trough four buffer exchange G-25 spin-columns into decalcified binding assay buffer (10 mM MES (pH 6.0), 100 mM KCl). 5 μM C2α was incubated with 1.5 mM total lipid LUVs with either POPC:POPS, 70:30 or 80:20 mole percent, followed by the addition of the divalent metal ion from a concentrated stock.

The interaction of Cd^{2+} with the PtdSer-containing LUVs was characterized using ultracentrifugation lipid-binding assays. The assays were carried out as described in Chapter II,[48] at a total lipid concentration of 1.5 mM but without C2α. The total lipid concentration and the mole fraction of PtdSer (20%). The sucrose-loaded LUVs comprising POPC/POPS (80:20) were incubated with Cd^{2+} at different concentrations and then subjected to ultracentrifugation. The concentration of Cd^{2+} in the supernatant fraction was determined using the fluorescence-based Leadmium™ kit (Invitrogen).

Results

C2α Cd^{2+}-interaction sites

Characterization of C2α Cd^{2+}-binding sites was carried out using a solution NMR ^{1}H-^{15}N HSQC-based titration as described in Morales and Yang et al.[159] The residue specific information obtained from the ^{1}H-^{15}N HSQC amides spectra allowed for the identification of two distinct binding regions with differential binding kinetic responses in the NMR spectra. These manifested as slow-to-intermediate and fast exchange behavior, respectively (Figure 1 in Morales and Yang et al.[159]). The first subset of residues, which will be referred hereinafter as Group I, responded readily to the presence of Cd^{2+} and exhibited a slow-to-intermediate exchange behavior on the chemical shift timescale.[159] As described for the binding of Pb^{2+} to the Pb1 site (See Chapter II)[48], this behavior corresponds to slow binding kinetics, usually but not always indicative of tight binding. In this case, the Cd^{2+}-bound C2α species builds up and the free protein is depleted as the concentration of metal increases. The second subset, Group II, was in the fast exchange regime, thus a single cross-peak report on the average chemical shift of the bound and unbound C2α specie. In this case, the chemical shift change smoothly to the bound position upon increasing metal concentration and in this case is indicative of weak binding.

In this study, the differential response and residue-specific information was utilized to separate the influenced regions by the two groups. Group I and Group II were mapped on to the CBLs and N-terminal/Helix 3 regions, respectively.[159] The binding sites are in agreement with 3 out of the 6 Cd^{2+} ions observed in the C2α Cd^{2+}-bound crystal structure (PDB ID: 4L1L[159]). Accordingly, these are the highest occupancy sites and the only three sites that have four or more ligands originating from C2α sidechains (Figure 41).

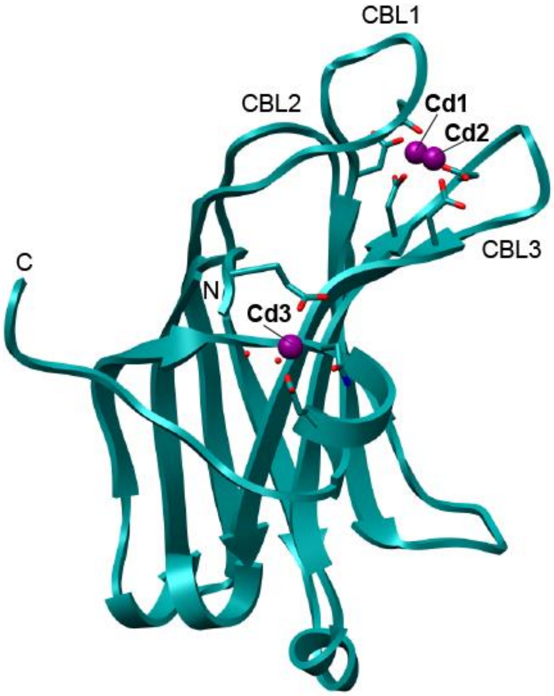

Figure 41. Crystal structure of C2α Cd^{2+}-complex. Illustration shows the high occupancy sites which are formed by: the Cd^{2+} binuclear cluster, Cd1 and Cd2, in the CBLs region, with occupancies of 1.0 and 0.72 respectively, and Cd3 located between the N-terminal region and Helix3, with the occupancy of 0.4. The other 3 sites are not appreciably populated in the NMR-detected binding experiments and are low-affinity. Each of them has < 4 protein ligands. One Cd^{2+} ion is coordinated by the two side-chain oxygen atoms of the Glu265 side chain and 3 water molecules. The other two Cd^{2+} ions are located in the CMBL region (for detailed structural information on the low populated sites referred to Morales and Yang et al.)[159].

For the binding of Cd3, the smooth change in chemical shift as a function of Cd^{2+} concentration was plotted and fitted using Equation 2 and an apparent K_d of 450 μM was reported.[159] For the high-affinity site, equilibrium fluorescence experiments enabled us to establish the upper limit of 1.1 μM for the binding of at least two Cd^{2+} ions in the CBL region.[159] This set of experiments revealed striking differences with regards to both affinity and metal-binding sites preferences in comparison to Ca^{2+} and Pb^{2+} (See Chapter II), as the pair did not bind to the N-terminal/Helix3 region.[48,52,59]

Analysis of Cd^{2+} coordination geometry for Cd1 and Cd2 in the CBLs region revealed a pentagonal bipyramidal geometry equivalent to that observed for Ca1 and Ca2 (Figure 42A and Figure 42B). The protein ligands are: the carbonyl oxygens of W247 and M186; and the carboxyl oxygens of aspartate side-chains in either bi-dentate (D187 and D248) or mono-dentate (D193, D246, and D254) coordination modes (Figure 42 and Table 7). According to C2α Ca^{2+}-PtdSer short-chain analog complex (PDB ID: 1DSY[52]), the PtdSer phosphoryl oxygens serve as axial ligands for Ca1 (Figure 42B). In the case of the C2α Cd^{2+}-complex, the bottom axial ligands are identical (carboxyl oxygens of the D246 sidechain), while both top axial ligands of Cd1 and Cd2 sites are water molecules (Figure 42A).

C2α structural comparisons revealed two important aspects: (i) coordination geometries adopted for Cd^{2+} and native ligand Ca^{2+} are identical, and (ii) no substantial changes in the average backbone structure are observed when compared to any of the available C2α structures (Table 8).

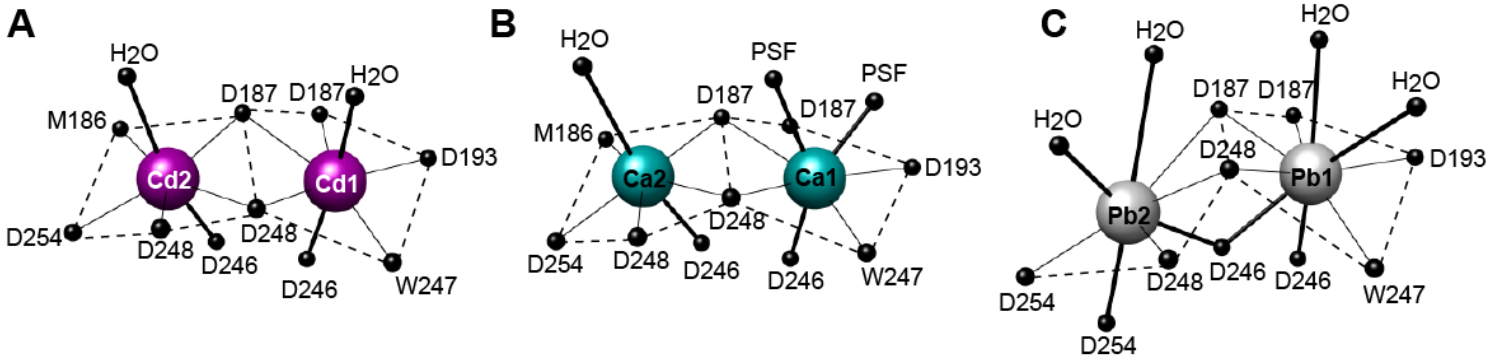

Figure 42. Coordination geometry of native ligand Ca^{2+} and heavy metals Cd^{2+} and Pb^{2+}. Coordination geometry of C2α CBLs bound to (B) Cd^{2+} (PDB ID: 4L1L)[159], (C) Ca^{2+} (PDB ID: 1DSY)[52] and (D) Pb^{2+} (PDB ID: 3TWY)[48]. PSF stands for 1, 2-dicaproyl-sn-phosphatidyl-L-serine.

Table 7. Cd-O distances in Cd^{2+}-complexed C2α.

Cd1 CN[a]=7	Bond length (Å)	**Cd2** CN=7	Bond length (Å)	**Cd3** CN=6	Bond length (Å)
D187 (Oδ1)	2.57	D187 (Oδ1)	2.45	E157 (Oδ2)	2.62
D187 (Oδ2)	2.52	D248 (Oδ2)	2.67	E282 (Oδ2)	2.67
D193 (Oδ2)	2.35	D248 (Oδ1)	2.55	E282 (Oδ1)	2.59
D248 (Oδ1)	2.40	D254 (Oδ2)	2.45	N279 (Oδ1)	3.04
D246 (Oδ1)	2.35	D246 (Oδ2)	2.34	H_2O (141)	2.84
W247 (O)	2.36	M186 (O)	2.53	H_2O (142)	2.20
H_2O (10)	2.46	H_2O (43)	2.54		
Average	2.43±0.09		2.50±0.10		2.66±0.28

[a] CN stands for coordination number.

Table 8. Backbone root-mean-square deviation (RMSD) between C2α available structures and the C2α-Cd^{2+} complex.

PDB ID	C2α state	Resolution (Å)	RMSD (bb atoms, Å)	Ref.
4L1L	Cd^{2+}-complexed	1.6	0	[159]
3RDJ	Apo	1.9	0.310	[48]
1DSY	Ca^{2+}- & PSF[a]-complexed	2.6	0.325	[52]
3TWY	Pb^{2+}-complexed	1.5	0.220	[48]

[a] PSF stands for 1, 2-dicaproyl-sn-phosphatidyl-L-serine

Cd^{2+} binding prevents C2α membrane association with PtdSer-containing membranes

Due to the structural and metal-coordination similarities between Ca^{2+} and Cd^{2+}, the ability of Cd^{2+} to promote C2α metal-dependent membrane association was probed. Two independent approaches were used: sucrose-loaded LUVs ultracentrifugation and protein-to-membrane FRET experiments, as described in Chapter II. For the vesicle ultracentrifugation experiments, the amount of protein left in the supernatant was quantified and used to calculate the fraction bound to the membrane (See Chapter II, Equation 6). Figure 43 shows the fraction of bound C2α in the presence of Cd^{2+}. Remarkably, the addition of Cd^{2+} does not result in productive C2α membrane binding. These results were confirmed with the use of FRET experiments as described in Morales and Yang et al.[159] This was strikingly different from Pb^{2+}, which despite of adopting a hemidirected coordination geometry for the second metal binding site (Pb2, Figure 42C), is almost as effective as Ca^{2+} in driving C2α membrane binding (Figure 43).

Since Cd^{2+} alone neither quenches dansyl fluorescence[159] nor associates appreciably with the PtdSer component of the LUVs under the conditions of our experiments (Figure 44), we proposed that the differences observed must have been imposed by the divalent metal ion ligand coordination capacity and preferences.

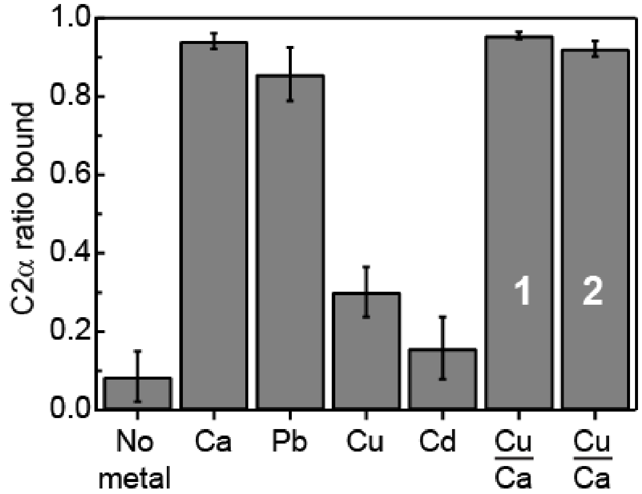

Figure 43. C2α-membrane association as a function of divalent metal ion identity. (A) Fractional population of membrane-bound C2α obtained in ultracentrifugation binding assays with LUVs having 30% PtdSer component. Total concentration of metal ions was 175 μM, except for the Cu^{2+}/Ca^{2+} displacement experiments that were carried out at 12.5/175 μM (Bar 1) and 175/2450 μM (Bar 2). The non-specific binding in the absence of metal was < 3%. The total metal concentration of 175 μM ($[M^{2+}]/[C2\alpha]$ ratio of 35), was chosen based on the Pb^{2+} experiments carried out in Chapter II (Figure 17). Two independent binding experiments were carried out for each metal ion or metal ion mixture. For each binding experiment, one or two independent BCA assays were done, giving a total of 3-4 measurements per metal ion or metal ion mixture. The error bars of were calculated as the standard deviation of the mean fraction bound.

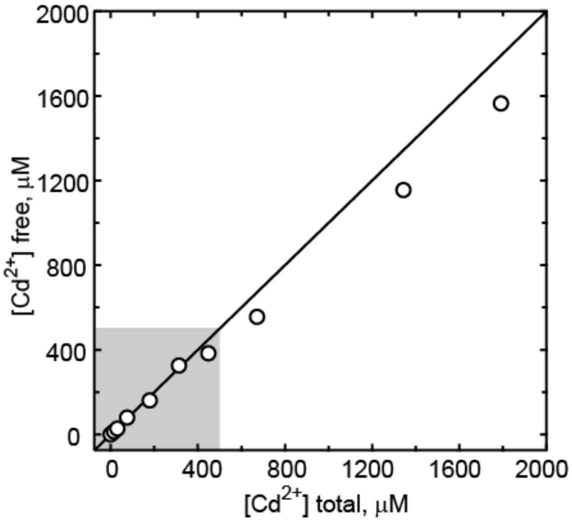

Figure 44. Cd^{2+} does not interact with PtdSer-containing LUVs. Plot of free versus total Cd^{2+} concentration showing negligible interactions between Cd^{2+} and PtdSer-containing LUVs up to 500 μM of Cd^{2+}.

Coordination geometry of metal ions does not correlate with their ability to mediate C2α-membrane association.

To test whether the metal ion ability to expand the coordination sphere is important for membrane binding, we characterized the interactions of C2α with Cu^{2+}. Cu^{2+} is a borderline Lewis acid with well-known preferences for low coordination numbers and soft bases in protein sites, such as Histidine and Cysteine ligands.[158] Moreover, Cd^{2+} and Cu^{2+} have been successfully used as a diamagnetic-paramagnetic pair in NMR structural studies.[160] The addition of 50 μM Cu^{2+} induced cross-peak broadening in the NMR spectra beyond the level of detection for C2α residues in the N-terminal/Helix3 region. This is the result of paramagnetic relaxation enhancement induced by the bound Cu^{2+} ion in this region (Figure 45). Increasing the concentration of Cu^{2+} to 150 μM, results in efficient relaxation of all CBLs region. These data suggest that Cu^{2+} populates the same set of C2α sites as Cd^{2+}, albeit with an opposite affinity pattern (Figure 46). Interestingly, the lipid-binding assays show that similar to Cd^{2+}, Cu^{2+} is not an effective mediator of protein-membrane interactions: only ~30% of Cu^{2+}-complexed C2α is membrane-bound (Figure 43). However, reducing the concentration of PtdSer from 30% to 20% eliminates the membrane binding of C2α in the presence of Cu^{2+} (Figure 47). These observations suggest that the high affinity Cu^{2+} has for the N-terminal/Helix3 site, and the notorious strong interactions between Cu^{2+} and PtdSer[161] caused a small fraction of C2α to partition into the membrane fraction. As a result, decreasing PtdSer content eliminates the apparent binding of C2α in the presence of Cu^{2+}.

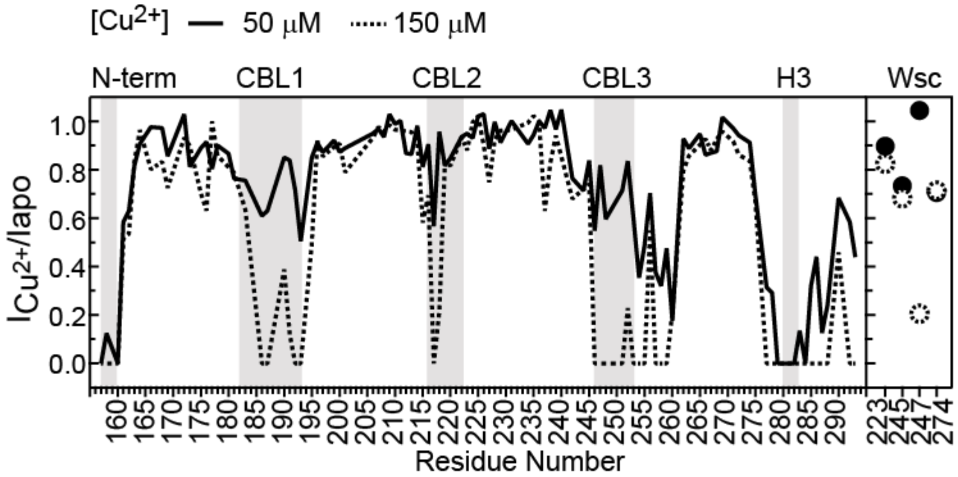

Figure 45. C2α Cu^{2+} and Cd^{2+} are equivalent but with opposite affinities. PRE, calculated as the ratio of NMR cross-peak intensities in Cu^{2+}-bound C2α to those in apo C2α, for two Cu^{2+} concentrations: 50 and 150 μM. The data were normalized to residue K236.

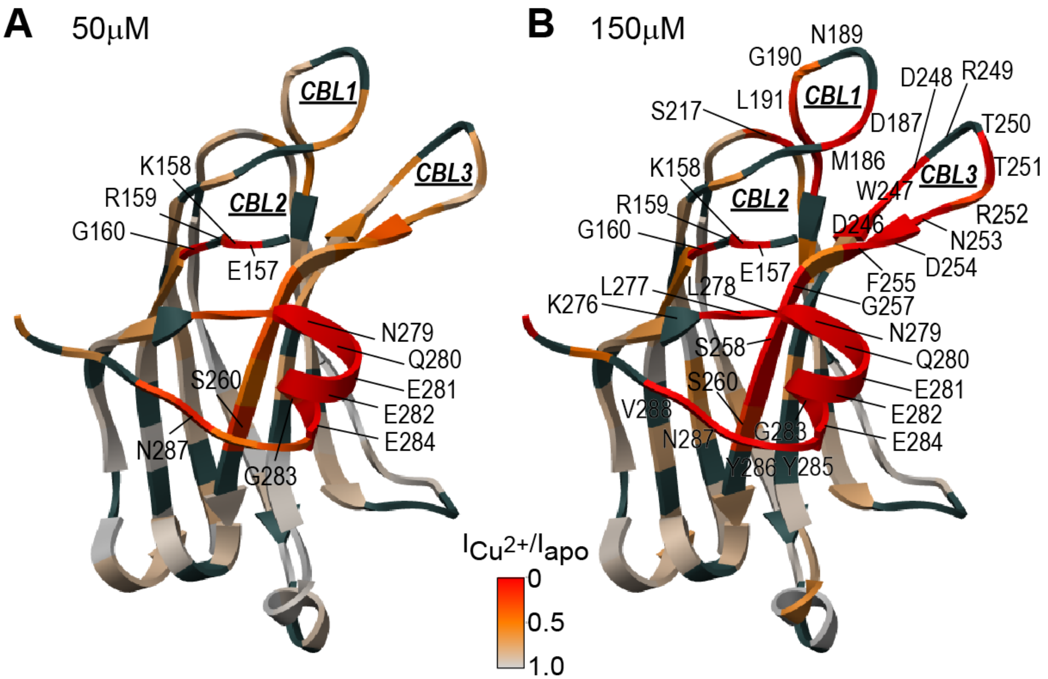

Figure 46. PRE identified C2α Cu^{2+} binding sites PRE mapping of Cu^{2+} binding sites onto the structure of apo C2α (PDB ID: 3RDJ). PRE was calculated as the ratio of cross-peak intensities in Cu^{2+}-complexed C2α to those in apo C2α for two Cu^{2+} concentrations: 50 and 150 µM. The data were normalized to residue K236.

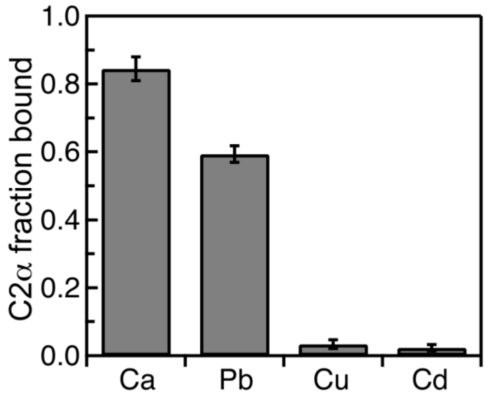

Figure 47. Fractional population of membrane-complexed C2α at 20 % PtdSer. Total concentration of C2α and M^{2+} was 5 and 175 µM, respectively. 3 independent ultracentrifugation experiments were carried out for Cd^{2+} and Cu^{2+}; and 2 independent experiments were carried out for Ca^{2+} and Pb^{2+}. For each experiment, BCA assay was conducted to determine the amount of protein in solution. This value was used to calculate the fraction of the protein bound to the LUVs. The error bars were calculated as either the standard deviation of the mean fraction bound (Cd^{2+} and Cu^{2+}), or estimated as the difference between the two fraction bound values (Ca^{2+} and Pb^{2+}).

The role of the N-terminal/Helix3 Cd^{2+} and Cu^{2+} binding site in C2α protein-membrane interactions was investigated further. We exploited the site resolution from the ^{1}H-^{15}N HSQC spectra to follow the effects of Cu^{2+} displacement by Ca^{2+}. In this membrane-free environment experiment, the cross-peaks of CBL residues were recovered upon addition of 3.0 mM Ca^{2+} (Figure 48A and Figure 48B). This excess corresponds to a 27-fold and 12-fold excess with respect to the total C2α and Cu^{2+}, respectively. In contrast, the resonances corresponding to residues on the vicinity of the N-terminal/Helix3 region remained broadened. This indicates that Cu^{2+} remains bound to this region and supports the formation of a mixed metal-ion species, with Ca^{2+} and Cu^{2+} bound to the CBLs and N-terminal/Helix3 regions of C2α, respectively.

The ability of this mix species to associate with PtdSer-containing membranes was tested in ultracentrifugation lipid-binding experiments for two concentration regimes and membrane binding was observed in both cases (Figure 43C, Bars 1 and 2). Thus, having a divalent metal ion bound to the N-terminal/Helix3 site neither enhances nor negatively affects C2α membrane-binding. These results exclude the possibility of an inhibitory effect of the N-terminal Cd3 and Cu1 sites in C2α membrane association.

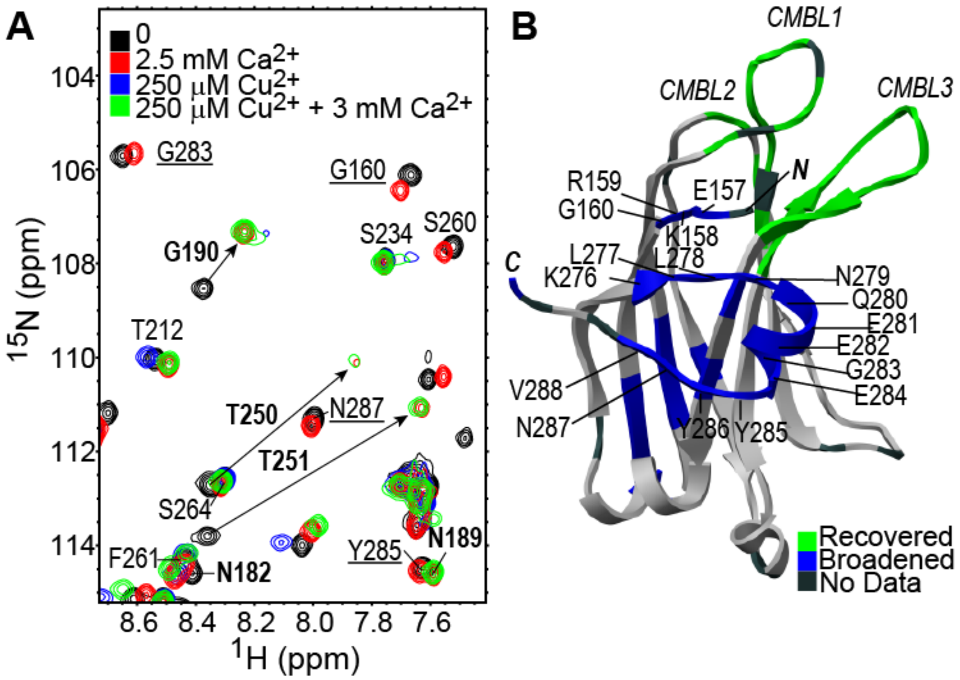

Figure 48. Ca^{2+} displaces Cu^{2+} from the CBLs region of C2α, with the formation of mixed Ca^{2+}/Cu^{2+}-bound species. (A) Overlay of ^{1}H-^{15}N HSQC spectra of 100 μM C2α at several concentrations of Ca^{2+} and Cu^{2+}. Residues that remain broadened upon addition of 12-fold Ca^{2+} excess over Cu^{2+} are underlined. Residues whose intensity fully recovers upon addition of Ca^{2+} are shown in boldface. The arrows indicate the direction of cross-peaks' shift due to Ca^{2+} binding. (B) Mapping of broadened residues (blue) and residues recovered upon Ca^{2+} addition (green) onto the structure of apo C2α (PDB ID: 3RDJ)[48].

Discussion of results

The data presented in this chapter shows a combined structural and functional assessment of divalent metal ions identity and their ability to promote membrane association. Using C2α as a paradigm, these findings support the view that divalent metal ions play a specific role in mediating protein-membrane interactions, rather than acting as a nonspecific "electrostatic switch." All three non-native metal ions: Cd^{2+}, Cu^{2+}, and Pb^{2+} can increase the electrostatic potential of C2α through direct binding to the aspartate-rich CBL region. However, the formation of a metal ion-protein complex is not sufficient to promote protein-membrane association, as demonstrated for Cd^{2+} and Cu^{2+}. We conclude that specific interactions of a divalent metal ion with PtdSer group(s) are required for productive protein-membrane interactions.

The available crystal structures of Ca^{2+}-bound C2α[52] and annexin V[148] in complex with PtdSer analogs, suggest that a water molecule is replaced by either phosphoryl and/or carboxyl oxygen(s) of PtdSer upon ligand binding. In addition, membrane binding may also be accompanied by an expansion of the coordination sphere, unfavorable for Cd^{2+}. In fact, Rulíŝek and Vondráŝek's analysis of PDB revealed that Cd^{2+} is most frequently found in protein sites with low coordination numbers (4 and 6).[158] Whereas Ca^{2+} (a hard Lewis acid) prefers coordination numbers between 6 and 8. Cu^{2+} and Pb^{2+} are classified as borderline Lewis acids. However, Cu^{2+} displays a notorious preference for a coordination number of 4, whereas Pb^{2+} has been observed to expand its coordination number up to 9 ligands. As discussed in Chapter II, the Pb2 site adopts a hemidirected geometry, where half the coordination sphere is free from any ligands, yet it accommodates 8 ligands in the remaining half (Figure 42C, Figure 13C, and Table 2). Hence, the behavior observed in the presence of Cd^{2+} and Cu^{2+} is consistent with the differences in metal ion coordination preferences and their inability to expand the coordination sphere. Together, the structural data suggests that ligand binding may be accompanied by an expansion of the metal ion coordination sphere, as shown for Ca^{2+}-bound C2α in Figure 42B.

Structural and functional studies carried out in the prototypical EF-hand Ca^{2+}-sensor, Calmodulin, have shown the effects of magnesium (Mg^{2+}) in Ca^{2+}-binding affinity, selectivity, and cooperativity. Similar to C2α, the canonical EF-hand members adopt a pentagonal bipyramidal geometry in an oxygen rich coordination sphere. In this case, the smaller ionic radius and preferred octahedral coordination were proposed to affect the affinity for Ca^{2+}, selectivity, and differential roles of Mg^{2+} and Ca^{2+} *in vivo*.[162]

The Cd^{2+} and Ca^{2+} ionic radii are virtually identical (Ca^{2+}=0.99 Å and Cd^{2+}=0.97 Å). The affinity of Cd^{2+} to the CBL region exceeds the previously reported Ca^{2+} value[61] by > 30-fold. Moreover, Cd^{2+} can adopt a hepta-coordinated state when bound to C2α, yet the rearrangement and possible expansion of its all-oxygen coordination sphere may be unfavorable for PtdSer interactions. This work shows that the preferred coordination geometry of metal ions, their ability to expand the coordination sphere, and the chemical identity of protein ligands need to be taken into account when designing metal substitution studies.

With no safe limit of exposure[149], it is plausible that bioavailable Cd^{2+} can influence the function of C2-domain containing proteins through direct competition with Ca^{2+} for the CBL regions. These results together with the work described in Chapters II and III, illustrate that toxic metal ions such as Cd^{2+} and Pb^{2+} can elicit very different functional responses with respect to *in vitro* membrane binding; Pb^{2+} promotes membrane association of C2α, whereas Cd^{2+} does not. Either scenario, if occurring in the cell, would lead to the aberration in the Ca^{2+} signaling response.

CHAPTER V

METAL-BINDING TRIGGERS C2 CONFORMATIONAL DYNAMIC RESPONSE THAT PROPAGATES TO N- AND C-TERMINI

Background

Ca^{2+} functions as a universal second messenger and is responsible for controlling a myriad of processes including transcription, division, apoptosis, secretion, contraction, and motility.[163,164] As a result, signal specificity is achieved by the variability among calcium binding proteins (CBPs) and their unique mechanisms to sense and transduce Ca^{2+} signals.[165-167] The general mechanism for signal transduction has been the generation of large conformational changes upon Ca^{2+}-biding, evident from the evaluation of structures in the apo and Ca^{2+}-bound states. However, this mechanism does not fully explain the variable responses among CBPs. Simultaneously, the role of conformational dynamics has been recognized to play a critical role in the specific "tuning" response. In this chapter, we investigate the potential role and contributions of C2α Ca^{2+}-dependent conformational dynamics in signal transduction and intra-domain communication during PKC activation.

The consensus view of the C2 domain role takes place during the first step of cPKC activation, in which Ca^{2+}-binding targets C2 to the plasma membrane where it recognizes the anionic phospholipids phosphatidylserine (PtdSer) and phosphatidylinositol (PIP_2).[37,73] This event is implicated in the disruption of intra-domain interactions between the C1 and C2 domains that subsequently allow the C1 domains to laterally search for DAG in the plasma membrane and sustain full cPKC residency at the membrane.[36,43,168] Upon membrane binding, the pseudo-substrate region is pulled out from the active site of the catalytic domain, thereby activating the enzyme.[2,73] Accordingly, the role of Ca^{2+}-binding during cPKC activation has been proposed to be at least three fold: (i) function as a bridge between C2 and the anionic PtdSer headgroup in the plasma membrane,[52] (ii) modulate C2 electrostatic potential,[50] and (iii) bring about a conformational change that dissociate intra-domain interactions and prepares the enzyme for the membrane association.[40]

C2 domains also convey isoform-specific subcellular localization through their diverse lipid specificities (i.e. phosphatidylserine, phosphatidylinositol, phosphatidic acid, and retinoic acid), protein-protein interactions (i.e. RACKS and phosphotyrosine recognition), and inter-domain interactions.[2,43,44,102] Due to the lack of acidic residues critical for Ca^{2+} coordination in novel PKC (δ, θ, ε , η) and the absence of a C2 domain in atypical PKC (ζ, ι/λ), these isoforms are unresponsive to Ca^{2+} ions, making the cPKC isoforms the only class uniquely controlled by Ca^{2+}.

Despite the low sequence similarity among C2 domains from cPKCs and nPKCs, and other C2-containing proteins, including the cytosolic phospholipase A_2 ($cPLA_2$-C2), Phospholipase C delta-1 (PLCδ-1 C2), Rabphilin-3A (Rab3A-C2A and C2B), and synaptotagmin I (Syn-1 C2A and C2B), they all share a common three-dimensional fold (See reference Nalefski et al.[44] for detailed C2 sequence alignment). As shown in Figure 5, the C2 domain from PKCα (C2α) has a fold characterized by eight β-strands that form a canonical β-sandwich. These are interconnected by three loops at the tip of the protein, which contain the residues responsible for Ca^{2+} and membrane binding. These are designated the Ca^{2+} binding loops (CBL) 1, 2 and 3 in Ca^{2+}-dependent C2 domains (Figure 49). For the conventional C2α domain, CBLs are involved in the binding of at least two Ca^{2+} ions, in addition to PtdSer head group recognition in the plasma membrane. The second lipid-recognition motif consists of a Lysine rich conserved region within the β3-β4 groove, designated the "Lysine rich cluster," and involved in PIP_2 interactions. As described, detailed information of C2 lipid-recognition sites has been acquired. However, little is known about the regions involved in intra-domain interaction and how these are disrupted in the first step of activation when Ca^{2+} binds to C2. Shedding light into this matter, two recent efforts identified two sites of C2 that are involved in interactions with the C-terminal V5[53] region and the upstream C1A[40] domain. Disruption of these interactions resulted in PKCα with increased affinity for membranes and activity under non-activating conditions, as well as loss of PtdSer selectivity.[40,53,54] The C-terminal helix 3 (C-term/H3), was implicated as the potential C1A interaction site along with two other sites in the CBL3 vicinity (Figure 49).[40] The region involved in V5 interaction was mapped to the lysine rich cluster region (Figure 49).[53]

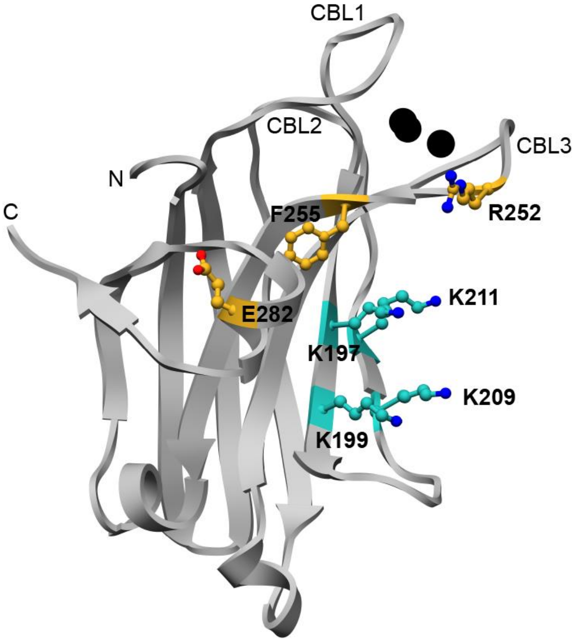

Figure 49. Putative C2α intra-domain interaction sites. CBL1, CBL2, and CBL3 are the Ca^{2+}-binding loops. Residues identified by C2 mutagenesis studies to be critical in auto-inhibitory interactions with the C1A domain and the V5 region are colored gold and cyan, respectively.

From the mechanistic standpoint, biochemical data have proposed a Ca^{2+}-induced conformational change within C2α as the trigger of intra-domain rearrangement in the first step of PKC activation.[34,56,168] However, the lack of substantial structural changes observed within C2α[48] and other C2 domains suggests a different mechanism by which these Ca^{2+}-dependent membrane-binding modules are functioning.[57] In Chapter II we reported the first apo structure for a cPKC C2 domain (C2α).[48] C2α lacked substantial backbone structural changes when compared to the Ca^{2+}- and Pb^{2+}-bound complex state (RMSD 0.49 and 0.37 Å, respectively).[48] Similar studies carried out on $cPLA_2$-C2,[169,170] PLCδ-1 C2,[49,171] Rab3A-C2A,[172] and Syn-1 C2A,[57,173] also suggests that the average structure of the domain remains unperturbed. On the other hand, a high degree of flexibility has been observed for the CBLs, which accounts for the major differences between apo and metal-bound states and the reduced number of apo C2 crystal structures available. These observations are supported by the absence of electron density as well as elevated B-factors for CBLs in the absence of Ca^{2+}.[171] Because of these aspects the use of solution NMR structure determination has increased in order to expand the limited number of apo structures for CBPs, including C2 domains. This was recently done in the apo and Ca^{2+}-bound states for the C2A domain from Synaptotagmin I.[57] CBLs were disordered in the apo state, however the addition of Ca^{2+} resulted in rigidification of the CBLs, suggesting that Ca^{2+} functions to stabilize the structure, rather that generating a well-defined conformational change as seen previously for other CBPs.[57]

Extensive structural analyses of CBPs specifically for members of the EF-hand family with the availability of apo and Ca^{2+}-bound structures, have established that Ca^{2+} binding induces large conformational changes that are necessary for signal transduction and protein-protein interactions. Examples of these include the canonical EF-hand (helix-loop-helix motif containing proteins) Calmodulin (CaM), S100, and Troponin C. For these CBPs, the large conformational change that follows Ca^{2+} binding, transforms the Ca^{2+} signal into a mechanical response by increasing the solvent exposure for hydrophobic residues required for association with their interacting partners.[166,174-180] Mechanistic generalization has been attempted from sequence comparison analyses and structural studies. It proposes that Ca^{2+}-sensors (involved mainly in signal decoding) such as CaM, undergo large conformational changes, whereas a pre-arranged Ca^{2+}-

binding site in Ca^{2+}-buffers (major role in Ca^{2+} homeostasis) "attenuates" the binding response accounting for the lack of structural reorganization.[181] However, even among EF-hand members with high sequence homology and structural similarities, the Ca^{2+} magnitude response is rather diverse.[181] This complex behavior has elicited an increase in the use of NMR not only for structure determination, but also for the characterization of the conformational dynamics changes induced by Ca^{2+} binding that can contribute to the diverse response, affinities, cooperativity, and metal ion selectivity among CBPs.[182] A handful of dynamics studies have been carried out primarily on fast timescale motions (ps-ns) and mainly for members of the EF-hand family such as Calmodulin,[183,184] Calbindin D_{9k},[185-192] Troponin C,[193,194] and the Neuronal Calcium Sensors (NCS), Calsensin[195] and Recoverin.[196] Together these studies have shown the role of conformational dynamics in specific "tuning" of Ca^{2+} signals among different CBPs.

In contrast, there is a very limited description of C2 domains conformational flexibility and its potential role in their Ca^{2+} response, protein-protein interactions, and multi-modular proteins function.[109,197] In Chapter II we characterized C2α interactions with divalent metal ions Ca^{2+} and Pb^{2+}. Using ^{15}N-HSQC-based metal titrations, we detected large chemical shifts for the CBLs region. Nonetheless, the apo C2α crystal structure showed no significant backbone changes when compared to the Ca^{2+}-bound structure. However, inspection of the B-factors, suggested the presence of high mobility for the CBLs in the apo structure. In this work, we report a full dynamic characterization for the C2 domain from PKCα, C2α, to determine the effects of Ca^{2+} binding in the fast (ps-ns) and slow (μs-ms) time scale motions. The fast motions were characterized using using the model-free Lipari-Szabo and spectral density mapping (SDM) analyses of the ^{15}N relaxation data. Motions on the millisecond (ms) timescales were quantified using relaxation compensated Carr-Purcell-Meiboom-Gill (rcCPMG) experiments. Together the information obtained from quantitative analysis of relaxation data revealed the following: (i) the sub-nanosecond dynamics remain unperturbed by the presence of metal as judged by the order parameters derived from model-free analysis; however, spectral density mapping reveals high mobility of CBL1 that is attenuated by metal-binding, highlighting the importance of using both techniques for the analysis of sub-nanosecond motions; (ii) conformational exchange, distinctive of the metal-bound state, is observed for the N-terminus and the C-terminal helix 3 (H3) (helix implicated in intra-domain interactions with the C1A domain). Lastly, (iii) the R159G-C2α variant suggests a direct involvement of the N-terminus of the domain in the regulation of this exchange. These dynamic changes rather than a well-defined conformational change could be responsible for affecting intra-domain interactions upon metal-binding during PKC activation.

Experimental procedures

Materials

Dodecylphosphocholine (DPC) and 2-Dihexanoyl-sn-Glycero-3-[Phospho-L-Serine] (DPS) were obtained from Avanti Polar Lipids (Alabaster, AL). Dipalmitoyl phosphatidylinositol 4,5-bisphosphate diC16 (C16-PIP$_2$) was purchased from Echelon Bioscience (Salt Lake City, UT).

C2α sample preparation

Uniformly $^2H^{15}N$-enriched ([U-^{15}N] and ~70% ^2H incorporation) isolated C2 domain from PKCα (C2α) was expressed using the method developed by Marley et al.[88] and purified as described in Chapter II.[48] The R159G C2α mutant was generated from wild type (WT) C2α gene using the Stratagene QuickChange™ site-directed mutagenesis kit and appropriate PCR primers. Mutagenic plasmid was transformed, expressed and purified using the same procedure as for WT C2α.

C2α concentration and buffer composition for all relaxation experiments was 0.41 mM and 10 mM MES buffer at pH 6.0, 150 mM KCl, 8% D_2O, and 0.02% Sodium Azide, respectively. The concentration for relaxation experiments was determined based on the R_2-CPMG measurements as a function of C2α concentration for the apo state. The ion-chelating resin, Chelex 100 (Sigma-Aldrich), was used to treat all buffers for removal of residual divalent metal ions. Apo-C2α was obtained by decalcification, carrying out the last purification step in the presence of 0.1 mM ethylenediaminetetraacetic acid (EDTA). EDTA was subsequently removed by several rounds of solvent exchange into decalcified buffer. The Ca^{2+}-bound state, $C2\alpha\cdot Ca_2$, was prepared by adding a 25- or 50-fold excess of Ca^{2+} to the apo C2α. The single Pb^{2+}-bound C2α, $C2\alpha\cdot Pb$, was prepared by adding Pb^{2+} to a final concentration of 0.41mM to 0.41mM apo-C2α.

NMR spectroscopy

All experiments were carried out at 25 °C on Varian Inova spectrometers operating at a ^{1}H Larmor frequency of 600 MHz (14.1 T) and 500 MHz (11.7 T). Temperature was calibrated using methanol. C2α assignments for the apoC2α, C2·Ca$_2$, and C2·Pb states were carried out previously using standard triple-resonance experiments.[48] Sequence-specific assignments of the ^{1}HN, ^{13}Cα, ^{13}Cβ, and ^{15}N resonances for the R159G C2α in the apo and Ca^{2+}-complexed states were obtained using gradient-enhanced triple-resonance NMR experiments HNCACB and CBCA(CO)NH[89] on a [U-^{13}C,^{15}N] R159G C2α mutant sample. Tryptophan indole side chain (^{15}N-^{1}Hε) assignments were obtained using two-dimensional (HB)CB(CGCD)HD[198] experiment in a [U-^{13}C,^{15}N] C2α·Ca$_2$ sample and transferred to all other metal-bound states.

C2α sub-nanosecond dynamics

Relaxation parameter sets comprising the longitudinal relaxation rate constant (R$_1$), transverse relaxation rate constant (R$_2$-CPMG), and ^{1}H-^{15}N nuclear Overhauser enhancement (NOE) were measured for all spectrally resolved ^{15}N-^{1}H backbone and the four tryptophan side chain resonances for apoC2α, C2·Ca$_2$, and C2·Pb, using standard methods at two static magnetic fields, 11.7 T and 14.1 T.[199] The data were acquired in an interleaved manner. A number of 10 total points including 3 duplicates were collected for R$_1$ from 0.05 s to 1 s and R$_2$ from 0.008 s to 0.140 s. For the NOE, a 3s saturation period and a 5 s recycle delay was used. Cross-peak intensities were used to quantify the relaxation and their uncertainties were estimated from the root-mean-square noise level of the base plane (NOE) or from duplicates measurements in the case of R_1 and R_2.

The analysis of ^{15}N spin-relaxation times and ^{1}H-^{15}N heteronuclear NOE values were performed in the context of the extended Lipari-Szabo model-free formalism.[200-202] Prior to model-free analysis, an estimate of the rotational diffusion properties of C2α was obtained using HYDRONMR[203] calculations. Rotational diffusion properties were determined at two atomic element radii , a = 2.8 Å and 3.3 Å, for C2α available crystal structures in the apo (PDB ID: 3RDJ)[48], Pb^{2+}-bound (PDB ID: 3TWY)[48] and Ca^{2+}-bound (PDB ID: 1DSY)[204] states (Table 9).

The corresponding resolutions are 1.9 Å, 1.5 Å, and 2.6 Å. The rotational diffusion tensor elements were then determined using the *R2R1_diffusion* software (A. G. Palmer III, Columbia University) for residues selected based on the Tjandra et al. criteria[205] and used as input for model-free calculations. The programs FAST-Modelfree and Modelfree 4.2 were interfaced during the rotational diffusion tensor and motional parameters fit of the spin-relaxation data. In the first stage, FAST-Modelfree was used for motion model selection and the generation of Modelfree input files, while the rotational diffusion tensor parameters were held fixed. There are five models to which a given spin can be assigned, characterized according to the number of parameters included to describe the motion: model 1 (S^2); model 2 (S^2, τ_e); model 3 (S^2, R_{ex}); model 4 (S^2, τ_e, R_{ex}); and model 5 (S_f^2, S_s^2, τ_e). S^2 is the square of the generalized order parameter, S_f^2 and S_s^2 are the squared generalized order parameter for the fast and slow motions, τ_e is effective internal correlation time associated with S_s^2, and R_{ex} is the conformational exchange contribution to R_2.

After each spin was assigned to a motion model, the second phase consisted of diffusion tensor parameters optimization using residues that were assigned to models 1 and 2. The optimized rotational diffusion tensor parameters were subsequently used for model re-assignment and the process was repeated until diffusion tensor parameters converged and spin model assignment remained unchanged. All residues with assigned models were subsequently included and the diffusion tensor and internal motion parameters were optimized simultaneously. Finally, the globally optimized rotational diffusion tensor parameters were fixed and used for tryptophan side chain model assignment. The final model-free calculation was carried with the incorporation of the tryptophan side chains while fixing the optimized tensor parameters. Calculations were performed using an amide H-N bond length of 1.04 Å and ^{15}N chemical shift anisotropy of -162 ppm and -89 ppm[206] for backbone and tryptophan indole side chain, respectively.

Table 9. Rotational diffusion properties of C2α in different states of metal ligation.

C2α	**Method**							
	R_2/R_1		HYDRONMR				Model Free	
	τ_C (ns)	$D_\parallel$/ $D_\perp$	AER (Å)	$\Delta D_{xy}/D_x$, %	$D_{xy,av}/D_z$	τ_C (ns)	D_{II}/ $D_\perp$	τ_C (ns)
Apo, 3RDJ	8.81 ± 0.01	1.22 ± 0.01	2.8	6.8	1.35	8.78	1.23 ± 0.03	8.95 ± 0.03
			3.3	6.7	1.33	9.34		
Pb^{2+}, 3TWY	8.65 ± 0.01	1.12 ± 0.01	2.8	9.4	1.27	9.22	1.26 ± 0.03	8.91 ± 0.03
			3.3	9.7	1.25	9.87		
Ca^{2+}, 1DSY	9.18 ± 0.01*	1.21 ± 0.02*	2.8	6.7	1.36	8.52	1.29 ± 0.03*	9.33 ± 0.03*
			3.3	6.3	1.34	9.07		

*R2/R1 and model-free calculations for Ca^{2+} data were carried with the higher resolution structure of C2α complexed with Pb^{2+} (PDB ID: 3TWY).

The high-frequency motions were also evaluated by directly calculating the high-frequency motions component of the spectral density function, $J(0.87\omega_H)$, using the reduced[207,208] spectral density mapping (SDM) approach[209,210] from the R1 and NOE values:

$$J(0.87\omega_H) = \frac{4\gamma_N}{5d^2\gamma_H}(NOE-1)R_1 \quad \textbf{Equation 11}$$

where $d = \frac{\mu_0 h \gamma_H \gamma_N}{8\pi^2 r_{NH}^3}$; μ_0 is the permeability of free space; *h* is Planck's constant; γ_H (γ_N) is the gyromagnetic ratio of ^{1}H (^{15}N), and r_{NH} is the length of the N-H bond.

C2α microsecond-millisecond (μs-ms) dynamics

Relaxation compensated Carr-Purcell-Meiboom-Gill (rcCPMG) were carried out using the pulse sequence established by Loria et al.[211] with a constant time CPMG period and implemented as Connor et al.,[212] for all resolved amide groups at 11.7 T and 14.1 T. For each pseudo-3D experiment 11 frequencies (50, 75, 100, 125, 150, 200, 250, 300, 350, 400 and 520 Hz) and a reference experiment were measured. The experiment was repeated 6 (metal-bound states) or 3 (apoC2α state) times. A peak intensity file was generated for each frequency containing all repeats, exported from Sparky and used for $R_2(1/\tau_{cp})$ calculation with an in-house protocol modified from Joel Butterwick (The Rockefeller University). The exchange regime was determined using alpha (α) value calculation,[213] using initial k_{ex} and $\Delta\omega$ estimates obtained from the Carver-Richards general equation.[214,215] This analysis indicated that the processes was in the fast exchange regime with the exception of R159 (residue with the largest chemical shift difference) that falls somewhere in the intermediate-to-fast regime for the C2α·Pb complex and slow-to-intermediate for C2α·Ca_2. Individual fits from Carver-Richards equation were also used to perform an F-test between the two-state model expression and a straight line fit to identify the residues exhibiting statistically significant dispersion. Data was imported and fitted with the two-state fast exchange model (Equation 12) using Igor Pro 6.22A.

A two-site $A \underset{k_{-1}}{\overset{k_1}{\leftrightarrow}} B$ fast exchanging reaction can be described with the following simplified equation:

$$R_2(\tau_{cp}) = R_2^o + \Phi_{ex} / k_{ex}[1 - \tanh(k_{ex}\tau_{cp}/2)/(k_{ex}\tau_{cp})] \quad \textbf{Equation 12}$$

Where $\Phi_{ex} = p_A p_B \Delta\omega^2$, p_A p_B and $\Delta\omega$ are the populations and chemical shift difference between the two-exchanging states, respectively; and k_{ex} is the sum of the forward (k_1) and reverse (k_{-1}) rates between A and B. The delay between pulses in the spin-echo pulse train is given by τ_{cp}. The chemical exchange contribution to R_2 is given by Equation 13. Residues with R_{ex} values less than 1.5 s^{-1} were excluded from the fit.

$$R_{ex} = \Phi_{ex} / k_{ex} \quad \textbf{Equation 13}$$

Chemical Shift perturbation analysis

The normalized change in chemical shift induced by the R159G mutation was determined according to Equation 10.

C2α binding in the presence of PtdSer containing mixed micelles and the effect of PIP_2

Mixed micelles, were prepared by combining chloroform solutions of DPC:DPS or DPC:DPS:C16-PIP_2 at the desired ratios. Solvent was removed under N_2 stream, followed by 2 hours under vacuum. The film was re-suspended in 10 mM MES pH 6.0, 100 mM KCl, 8% D_2O, and 0.02 % NaN_3 followed by thorough vortex until suspension became clear.

To map the regions affected by C2α membrane association, we carried out a series of HSQC-based experiments in the presence of DPC:DPS (80:20) and DPC:DPS:C16-PIP_2 (78:20:2) mixed micelles as the membrane mimicking environment suitable for NMR solution techniques. The objective was to identify the C2α regions that interact with PtdSer and PIP_2 in the micellar environment. The reference state (apo·C2α + mixed micelles) for the C2αCa_2 in the presence of mixed-micelles was not possible to attain due to complete C2α unfolding as observed in the NMR spectra when DPC:DPS mixed-micelles where added (Figure 50). However, prior knowledge in C2α membrane binding properties, in addition to the experiments carried out in Chapter II in the absence of metal, demonstrate C2α is a clear Ca^{2+}-conditional membrane binding domain. For this reason we do not expect any changes in chemical shift due to the presence of mixed-micelles when no metal is present.

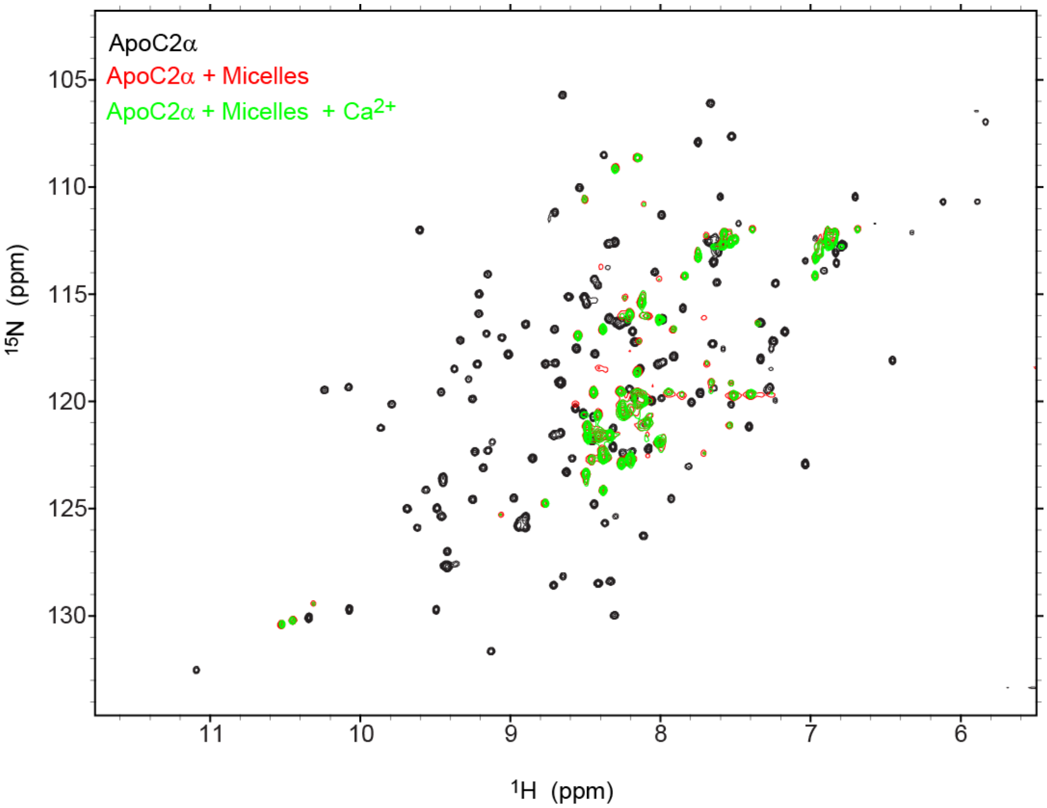

Figure 50. Apo·C2α unfolds in the presence of DPC:DPS mixed-micelles. ^{1}H-^{15}N HSQC spectra overlays of apo·C2α (black), apo·C2α in the presence of 20mM DPC:DPS mixed micelles (red), and apo·C2α in the presence of 20mM DPC:DPS mixed micelles followed by the addition of Ca^{2+} (green). The spectra overlays illustrate how the addition of mixed-micelles caused C2α unfolding when compared to the reference apoC2α spectra and judged by the clustered resonances in the center of the amide region, between ^{1}H 7.5-8.5 ppm. The subsequent addition of metal in this state does not induce any changes on the NMR spectra.

We established that the only condition that mixed-micelles experiments can be carried out is by pre-incubating C2α with Ca^{2+}, followed by the addition of mixed-micelles (Figure 51). The addition of DPC:DPS mixed-micelles induced significant changes on C2α H-N cross-peaks for residues located on the CBL1, 2 and 3 in addition to β-strand 3, which belong to the “lysine rich cluster” region. The addition of 40 mM does not results in any further changes in chemical shifts, indicating that saturation is reached at concentrations of 20 mM . However, poor sample stability is observed if the total detergent concentration is increased to 40 mM. For this reason all micelles experiments in this work were carried out at 20 mM. The effects of incorporating PIP_2 in mixed micelles were also assessed, and these corresponded to specific changes located in the lysine rich cluster region (Figure 52).

Lastly, PtdSer specificity was assessed by the addition of 100% DPC micelles, and no significant changes on C2$\alpha \cdot Ca_2$ ^{1}H-^{15}N HSQC spectra were observed (Figure 53). However we do detect some degree of C2α unfolding crosspeaks that correspond to the state when the protein was not pre-incubated with Ca^{2+} (green overlaid spectra in Figure 53).

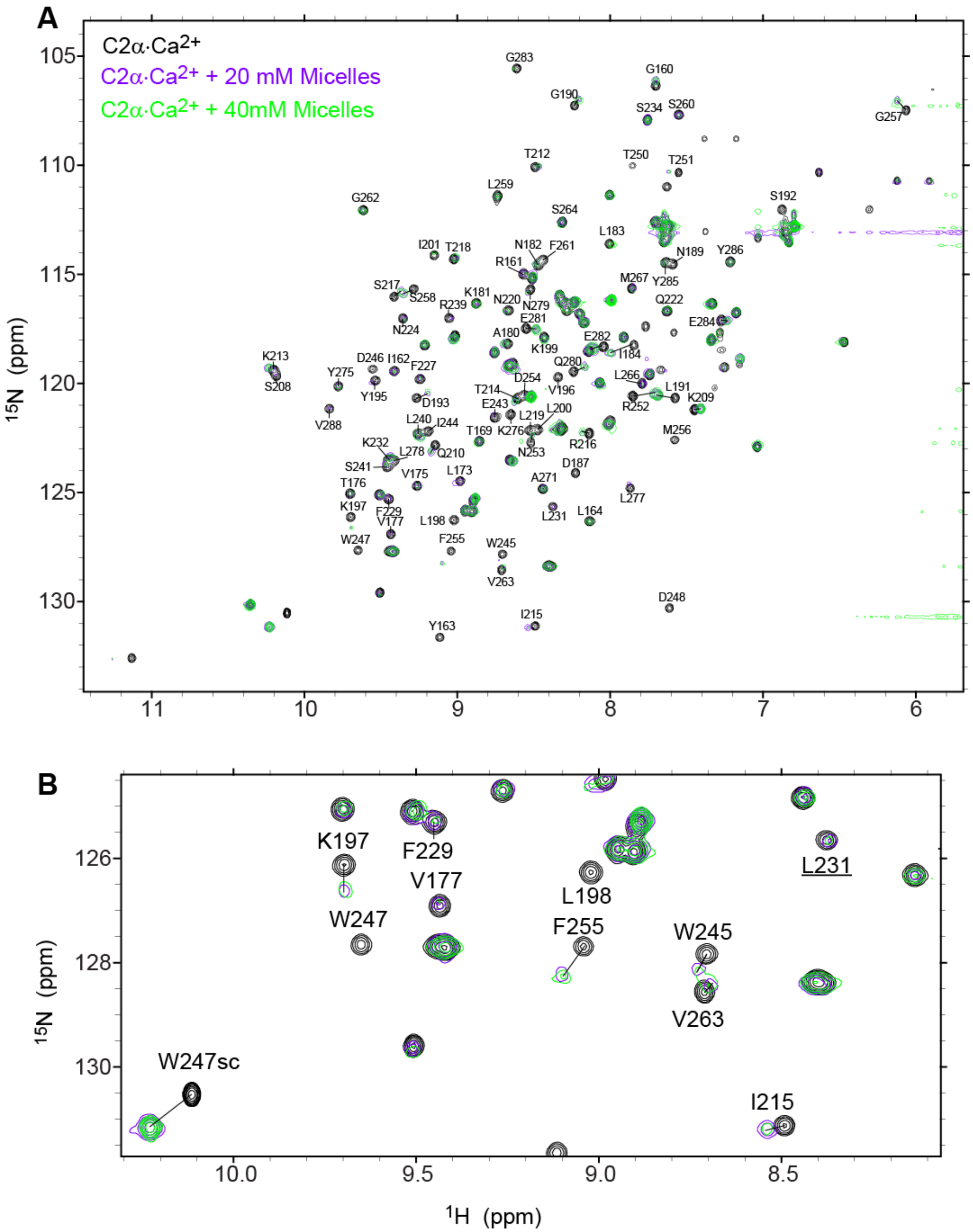

Figure 51. C2α·Ca$_2$ interactions with DPC:DPS mixed micelles. (A) ^{1}H-^{15}N HSQC spectra overlays of C2α·Ca$_2$ (black) after the addition of 20 mM (purple) and 40 mM (green) DPC:DPS (80:20) mixed-micelles. (B) ^{1}H-^{15}N HSQC spectra expansion from the spectra overlay shown in A.

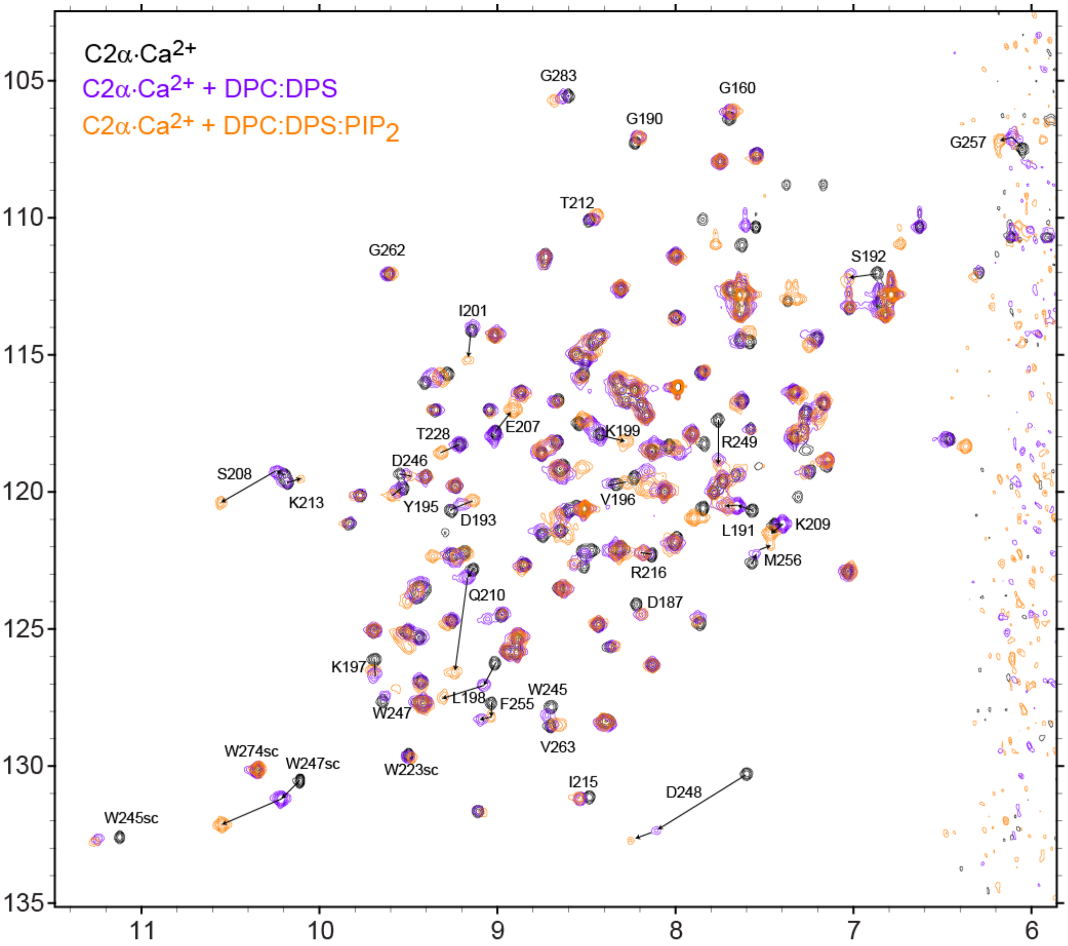

Figure 52. C2α·Ca$_2$ interactions with DPC:DPS:PIP$_2$ mixed-micelles. (A) ^{1}H-^{15}N HSQC spectra overlays of C2α·Ca$_2$ (black) after the addition of 20 mM DPC:DPS:C16-PIP$_2$ (78:20:2) micelles (orange). C2α spectra in the presence of DPC:DPS is shown for comparison (purple). Further changes are observed mostly for residues located on the "lysine rich cluster region" and CBL3.

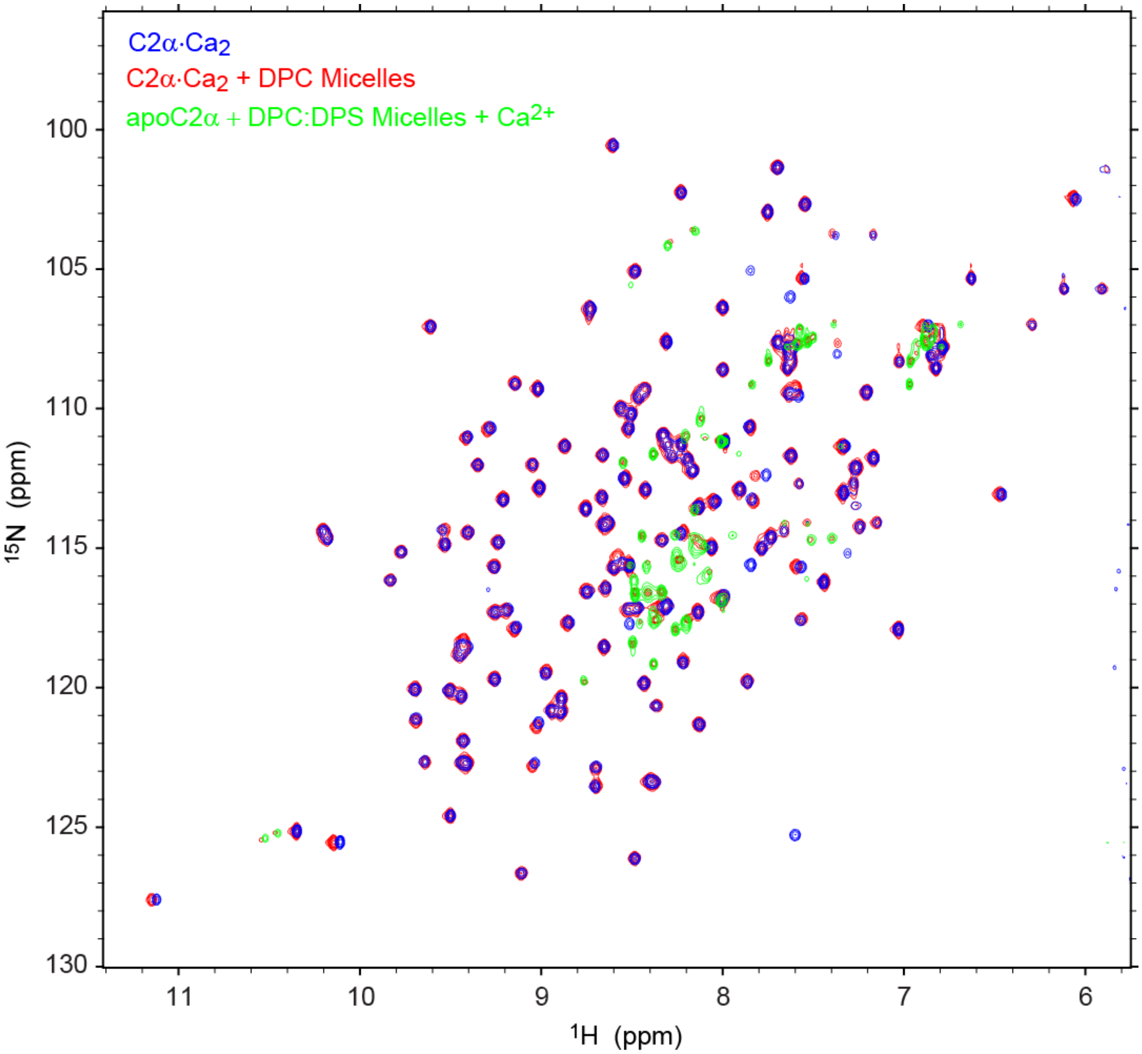

Figure 53. C2α·Ca$_2$ mixed-micelles interactions are PtdSer specific. ^{1}H-^{15}N HSQC spectra overlays of C2α·Ca$_2$ (blue) after the addition of 20 mM DPC micelles (red). The C2α unfolded spectra in the presence of DPC:DPS mixed micelles when C2α was not pre-incubated with metal is overlaid (green). These illustrate how some of the crosspeaks that appear in the presence of DPC micelles (red) correspond to partial unfolding of C2α.

Results

Metal-binding alters the μ*s dynamics of C2*α *CBLs*

C2α relaxation parameter sets comprising R_1, R_2-CPMG, and steady-state ^{1}H-^{15}N nuclear Overhauser enhancement (NOE) were measured for all spectrally resolved ^1H_N-^{15}N resonances at two static magnetic fields, 11.7 T and 14.1 T. Three different metal-ligated states were investigated: apoC2α, C2α·Ca_2 (25-fold excess), and C2α·Pb (only high affinity site occupied, 1:1 protein-to-Pb^{2+} ratio). C2α differential affinity for Lead (Pb^{2+}) (See Chapter II) was used strategically to generate a single-site metal bound state (C2α·Pb) that would provide a scenario where the contributions arising from individual metal ions could be studied. This is not possible with Ca^{2+} due to the cooperative nature of the binding. Figure 54 summarizes the residues that were excluded due to low signal-to-noise and poor spectral resolution in all three states. Residue-specific internal motions contribute to the relaxation rates, thereby reporting on sub-nanosecond (ps-ns) motions through their dependence on the spectral density function, *J*. For each H_N-N vector in the protein backbone, the spectral density function is sampled at three frequencies: 0, ω_N, and $\omega_H{}^N$, where ω_N and $\omega_H{}^N$ are the angular Larmor frequencies of the amide ^{15}N and $^1H^N$, respectively. In the particular case of the R_2 rate constants, conformational exchange processes that occur on the microsecond-to-millisecond (μs-ms) timescale can also contribute to R_2 via the R_{ex} term for residues undergoing motions on this timescale. This will be manifested as elevated R_2 rates (above average), indicating that a particular H_N-N group is subject to chemical exchange.

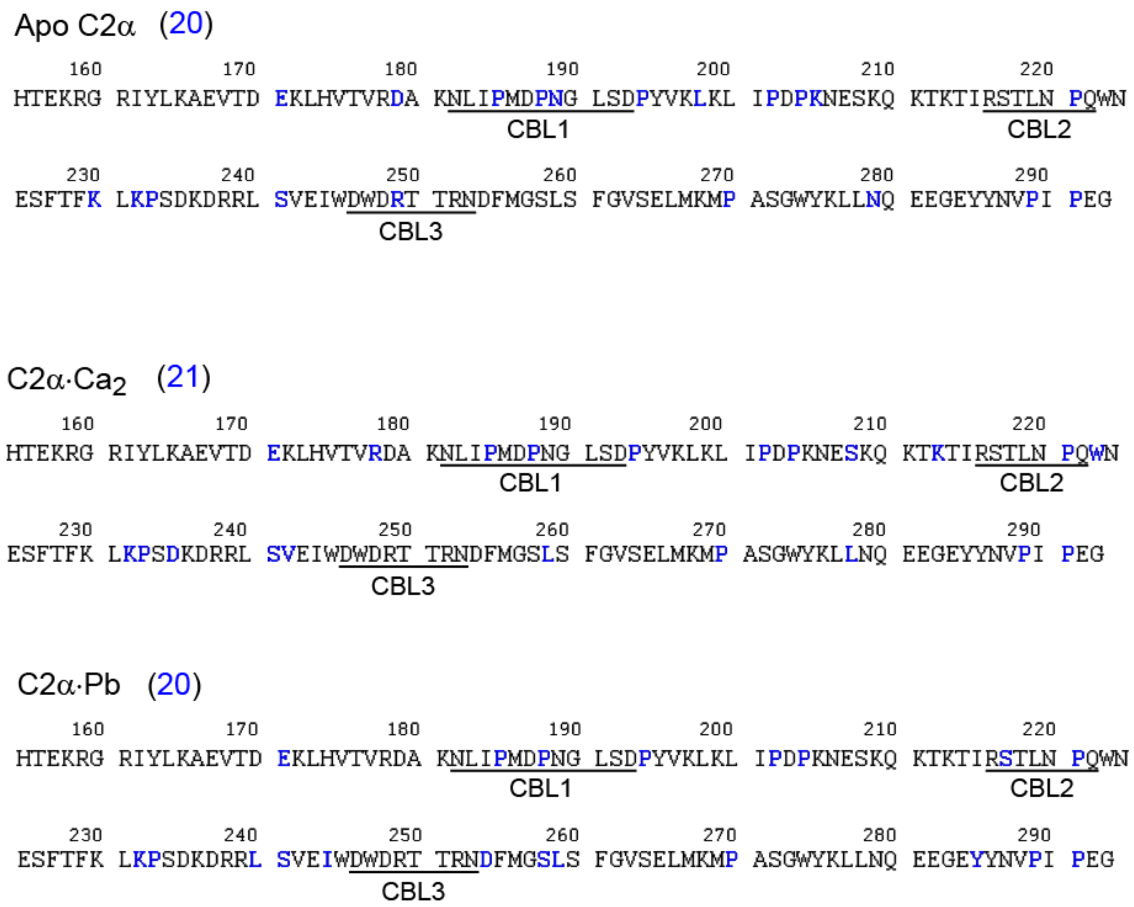

Figure 54. Residue exclusion for relaxation data analysis for the three states of metal ligation. Colored in blue are the excluded residues due to poor spectral resolution and low signal-to-noise in addition to prolines.

Two approaches were used to study the effects of C2α metal-binding on the sub-nanosecond timescale motions from ^{15}N spin-relaxation data: (i) the generalized order parameters (S^2_{NH}) obtained from the extended Lipari-Szabo model-free formalism of the spectral densities,[200-202] which were contrasted to direct spectral density analysis using the (ii) reduced spectral density mapping (SDM) approach.

Prior to model-free analysis, an initial estimate of the rotational diffusion properties of C2α was obtained using HYDRONMR, R2R1_diffusion calculations and C2α available crystal structures. A summary of the overall rotational correlation time (τ_m) and the eigenvalues of the diffusion tensor parameters obtained with the use of these two approaches is shown in Table 9 for all three metal-ligated states. After a motional model was assigned to each spin, the S^2_{NH} and tensor parameters were optimized iteratively as described in the Materials and Methods section. The average for the optimized τ_m and diffusion tensor anisotropy ($D_{II}/D_{\perp}$) using model-free analysis for all three-metal ligated states was 9.06 ± 0.23 ns and 1.26 ± 0.03, respectively (See Table 9 for apoC2α, C2$\alpha\cdot$Ca$_2$, and C2$\alpha\cdot$Pb individual parameters).

The S^2_{NH} obtained from model-free analysis report on the ^1H_N-^{15}N vector's spatial restriction in the protein backbone. Values range from 1 to 0, where 1 and 0 correspond to the extremes for a completely restricted and unrestricted vector, respectively. S^2_{NH} are shown in Figure 55A as a function of the C2α primary structure for residues that were assigned to a motional model in all three states (Table 10). Residues that were not assigned to any motional model are also listed in Table 10. In addition to the N- and C-terminal residues, unassigned residues are mapped primarily onto the CBL3 region for the apoC2α and C2$\alpha\cdot$Ca$_2$ states.

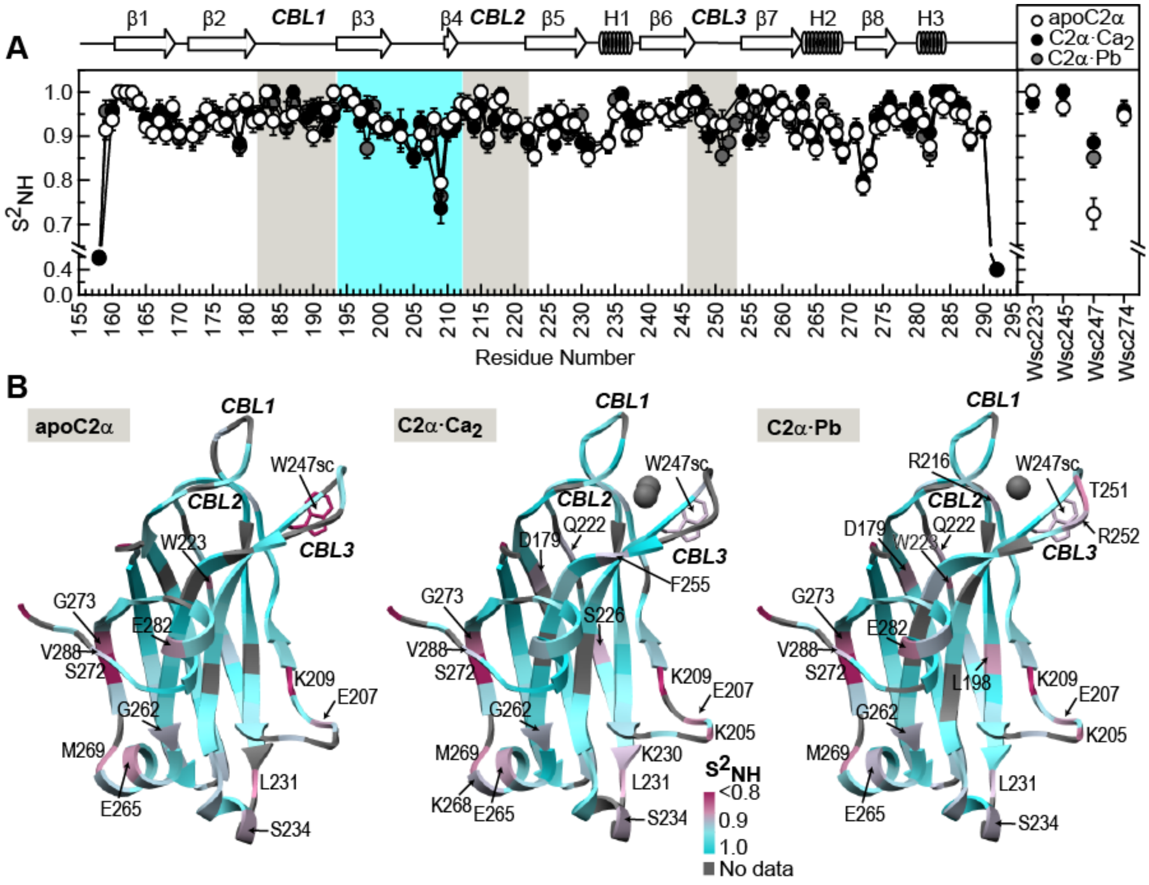

Figure 55. Generalized order parameters (S^2_{NH}) extracted for three states of metal-ligation. (A) Generalized order parameters (S^2_{NH}) as a function of C2α primary structure for apoC2α, C2α·Ca$_2$, and C2α·Pb. The S^2_{NH} for the four existing tryptophan side-chains (Wsc) in C2α are shown in the adjacent plot. (B) S^2_{NH} mapped onto C2α apo structure (PDB ID 3RDJ) for the apoC2α state and the Pb-bound structure (PDB ID: 3TWY) for the C2α·Ca$_2$ and C2α·Pb states. Grey spheres correspond to Pb^{2+} ions in the structure. Only one out of the two Pb^{2+} ions present in the C2α Pb-bound structure is shown in C2α·Pb for better representation of the real state. Color grey shows residues for which data was not available due to: poor signal-to-noise, spectrally unresolved, no model assignment, and prolines. The corresponding secondary structure is shown at the top and the CBLs and lysine rich cluster are highlighted in grey and cyan, respectively.

Table 10. Model unassigned spins in model-free analysis for all three metal-ligated states.

Metal-ligated state	Model 1	Model 2	Model 3	Model 5	Unassigned
apoC2α	160 161 162 163 164 165 166 167 168 169 173 174 175 176 177 178 180 181 182 183 190 193 195 196 197 199 200 201 203 208 210 211 212 213 214 215 216 217 218 219 220 222 224 225 226 227 228 229 234 236 238 239 240 242 243 244 245 256 258 259 260 261 262 263 264 266 267 268 271 274 275 276 277 278 280 281 283 284 285 286 287 288 290	159 170 187 192 206 207 209 223 231 235 237 250 251 265 269 272 273 282	172 184 186 246 247 248 254	158 292	157 191 252 253 255 257
C2α·Ca$_2$	160 161 162 163 164 165 166 167 168 169 170 173 174 175 176 177 179 180 181 182 183 184 186 187 190 191 192 193 195 196 197 198 199 200 201 203 206 210 211 212 214 215 216 217 218 219 220 222 224 225 226 227 228 229 230 234 236 237 238 239 240 243 244 245 246 247 248 254 255 256 257 258 260 261 262 263 264 265 266 267 268 271 273 274 275 276 277 279 280 283 284 285 286 287 288 290	189 205 207 231 269 272 281 282	172 249	158 209 292	157 159 250 251 252 253
C2α·Pb	159 160 161 162 163 164 165 166 167 168 169 173 174 175 176 177 178 179 180 181 182 183 184 186 187 189 190 191 192 193 195 196 197 198 199 200 201 210 211 212 213 214 215 216 218 219 220 222 223 224 225 226 227 228 229 230 234 235 236 238 239 242 243 245 246 247 249 255 256 257 260 261 262 263 264 265 266 268 271 273 274 275 276 277 278 279 280 283 284 286 287 288 290	170 203 205 206 207 208 209 231 237 250 251 252 253 267 269 272 281 282	172 248	158 292	157

The average S^2_{NH} value observed for secondary structured and (unstructured) elements, excluding the N- and C-terminal residues, were virtually undistinguishable and suggest that the domain is considerably rigid, with values of 0.936±0.039 (0.936±0.043), 0.937±0.040 (0.939±0.052) and 0.933±0.040 (0.931±0.045) for the apoC2α, C2$\alpha\cdot$Ca$_2$, and C2$\alpha\cdot$Pb, respectively. As shown in Figure 55A, neither the absence nor presence of metal considerably affects the sub-nanosecond motions, irrespective of the metal ion identity (Ca^{2+} or Pb^{2+}) and saturated state (25-fold versus 0.5-fold). However, there are noteworthy regions that exhibited lower than average S^2_{NH} in all three states. The S^2_{NH} were mapped onto the crystal structure of each metal-ligated state, and residues with S^2_{NH} values lower than average by at least one standard deviation from the average, were identified (Figure 55B). Interestingly, these residues were mapped onto the following regions: CBL3, β3-β4 groove or lysine rich-cluster (PIP$_2$ binding site), β-strand 8 (β8), and the C-terminus helix 3 (C-term/H3). In addition, the tryptophan 247 side-chain indole moiety (Wsc247), located on CBL3 and implicated in hydrophobic interactions with the membrane, exhibit substantial motions in the apo state (Figure 55A). Considerable attenuation is observed in the presence of metal, but the average motions are still noticeably greater when compared to Wsc245, and Wsc223 and Wsc274, all of which are considerably rigid.

Direct SDM was used as a complementary approach to detect regions undergoing motions on the sub-nanosecond timescale. This is of particular importance for residues located on CBL3 and CBL1 that were underrepresented during model free analysis either due to lack of model assignment (no S^2_{NH} value available) or model selection influences on S^2_{NH} values caused by R_{ex} contributions (Table 10 and Figure 56 for model-free estimated R_{ex} values). $J(0.87\omega_H)$ was calculated directly based on the relation to R_1 and ^1H-^{15}N NOE using Equation 11(Figure 57B). $J(0.87\omega_H)$ and NOE, both of which report strictly on sub-nanosecond time scale motions, showed substantial motions for CBL1 in the apoC2α that are attenuated in the C2·Ca_2 and C2·Pb bound states (Figure 57). This comparison revealed substantial differences, especially for CBL1 between the apo and metal-bound states that were not evident from S^2_{NH} values. $J(0.87\omega_H)$ not only confirms Wsc247 flexibility, but also reveals substantial motions by Wsc245 for which significant elevated order parameters were observed (Figure 55A).

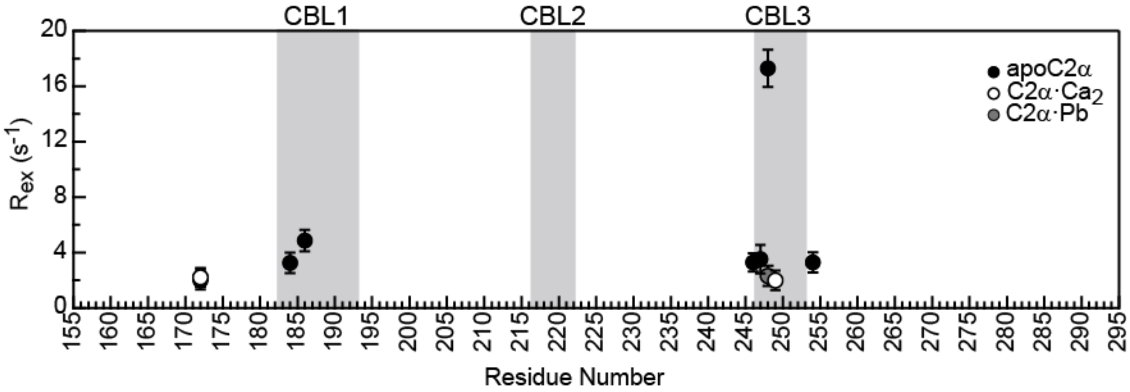

Figure 56. Chemical exchange contributions estimated from model-free analysis. R_{ex} as a function of residue number for residues whose model (model 3) included R_{ex} component in order to described the motions.

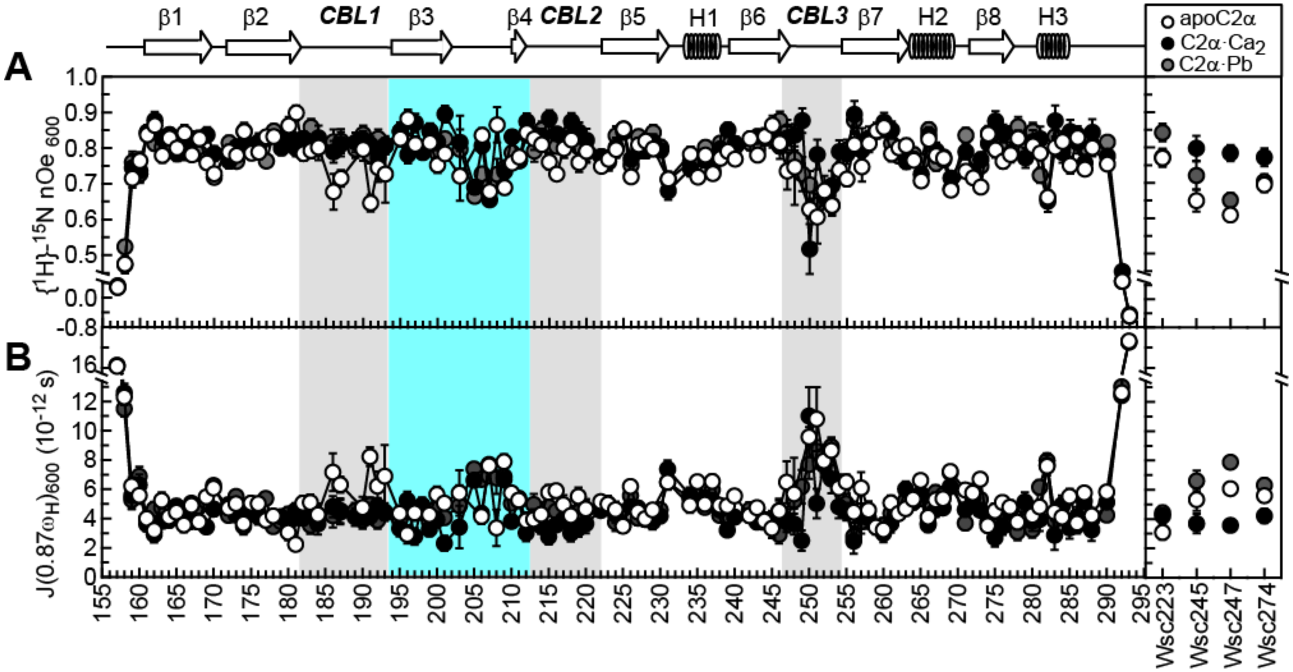

Figure 57. C2α sub-nanosecond motions under three different metal-ligated states.(A) Steady-state ^{1}H-^{15}N nuclear Overhauser enhancement (NOE) at 14.1 T as a function of C2α primary structure for apoC2α, C2α·Ca$_2$, and C2α·Pb. ^{1}H-^{15}N NOE for the tryptophan side-chains (Wsc) is shown in the adjacent plot. (B) Spectral density values $J(0.87\omega_H)$ at 14.1 T for all three metal-ligated states as a function of C2α primary structure. $J(0.87\omega_H)$ for the tryptophan side-chains (Wsc) is shown in the adjacent plot. The corresponding secondary structure is shown at the top and the CBLs and lysine rich cluster are highlighted in grey and cyan, respectively.

While the overall sub-nanosecond timescale motions remained nearly unaffected among the different metal-bound states, a significant subset of residues showed significantly elevated R_2-CPMG rates in the apoC2α CBL1 and CBL3 that are attenuated in the presence of metal (Figure 58A). This increase in R_2-CPMG suggests contributions arising from a conformational exchange processes that occurs on the microsecond-to-millisecond (μs-ms) timescale via the R_{ex} component.

A comparison of the R_2-CPMG rates between apoC2α and the C2$\alpha\cdot$Ca$_2$ and C2$\alpha\cdot$Pb bound states highlights regions attenuated by metal-binding from regions with increased dynamics in the presence of metal (Figure 58B and C). In the C2$\alpha\cdot$Pb complex (Figure 55B), significant attenuation is observed for CBL1, 2, and 3, whereas in the presence of Ca^{2+} (Figure 55C) attenuation is observed primarily for CBL1 and CBL3. Interestingly, the presence of Ca^{2+} also induces an increase in the R_2-CPMG rates for CBL3 residues T250 and T251, and a subset of residues located at the N-terminus (e.g. R159) and C-term/H3 (e.g. E282).

C2α crystal structure in Figure 49 illustrates how these regions are far apart in primary structure but close in three-dimensional space. Given that all dynamically perturbed regions of C2 have a functional role,[40,54] we characterized the dynamics of N-H groups using NMR relaxation dispersion techniques.

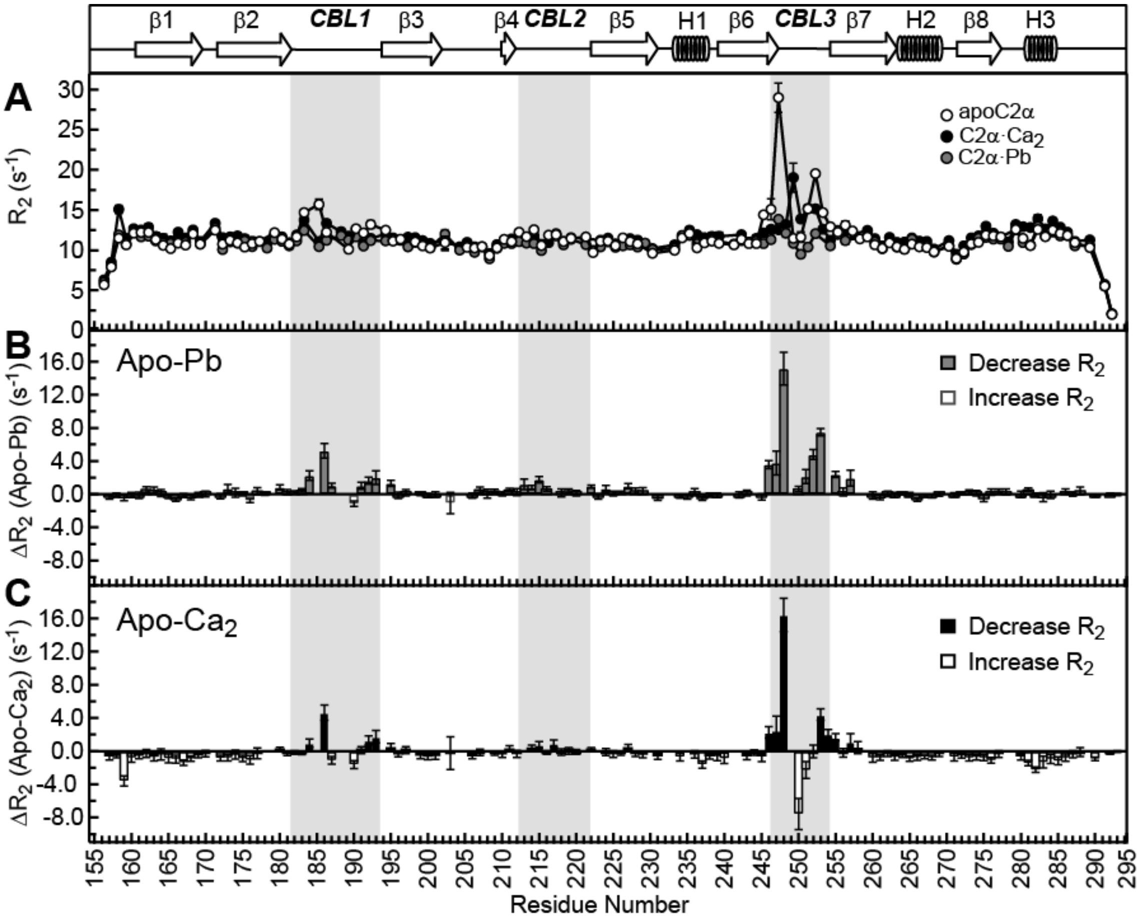

Figure 58. Metal-binding alters the μs dynamics of C2α CBLs. (A) Transverse relaxation (R_2-CPMG) rates as a function of C2α primary structure for apoC2α, C2α·Ca$_2$, and C2α·Pb metal-ligated states. Calculated ΔR_2-CPMG values corresponded to the difference between the apoC2α residue-specific R_2-CPMG rates and the (B) C2α·Pb and (C) C2α·Ca$_2$ states. Grey (black) solid and open bars correspond to decrease and increase in dynamics upon Pb^{2+} (Ca^{2+}) binding. The corresponding secondary structure is shown at the top and the CBLs and lysine rich cluster are highlighted in grey and cyan, respectively.

Dynamic response of C2α to metal-binding propagates to N- and C-termini

To characterize the exchange kinetics, thermodynamics, and structural contributions induced by metal-binding effects, relaxation-compensated Carr-Purcell-Meiboom-Gill (rcCPMG) dispersion measurements were implemented as described in Material and Methods section. This technique is suitable to quantify R_{ex} contributions to R_2 on the ms timescale (exchange rates between 100-3000 s^{-1}). These experiments were carried out for the three metal-ligated states described above. A two-state fast exchange model was assumed for the interpretation and fitting of dispersion curves. The exchange regime was determined to be fast based on the alpha (α) value calculation[213] and initial k_{ex} and $\Delta\omega$ estimates obtained from the Carver-Richards general equation.[214,215] In the fast-exchange regime the relaxation dispersion profile is fitted using Equation 12, where the exchange rate between the two-states (k_{ex}) and the transverse relaxation rate in the absence of exchange (R_2^o) are obtained directly. The population of the states (p_A and p_B) and chemical shift difference between ($\Delta\omega$) the two, is convoluted in the Φ_{ex} component ($\Phi_{ex}=p_Ap_B\Delta\omega^2$). Figure 59A shows ^{15}N rcCPMG relaxation dispersion curves for representative residues from the three regions where quantifiable dispersion was observed in the presence of metal. Interestingly, the three regions include the N-terminus, the C-terminal H3, CBL1, and CBL3. R159, E282, and I184 are the residues with the largest amplitude change in each region, respectively. The site-specific chemical exchange R_{ex} contributions were extracted accordingly from the dispersion profile (Φ_{ex} and k_{ex} fitted values) and mapped onto C2α crystal structure (Figure 59B and C).

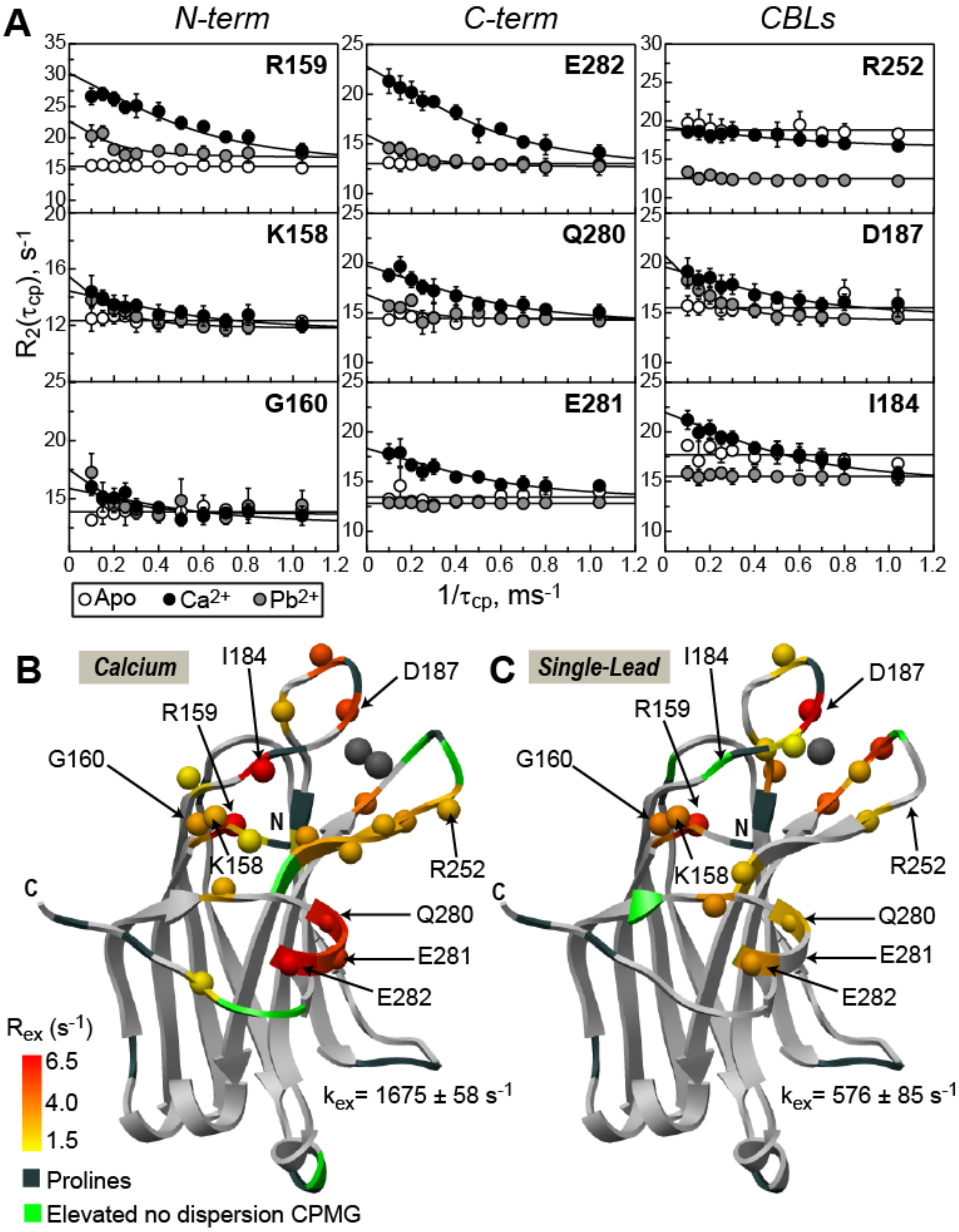

Figure 59. Comparison of conformational changes observed for all three metal-ligated states. (A) Relaxation dispersion curves for representative residues of the three exchanging regions (N-term, C-term and CBLs) for (○) apoC2α, (●) C2α·Ca$_2$ and (●) C2α·Pb. R$_{ex}$ values mapped onto the Pb-bound crystal structure (PDB ID: 3TWY) for the (B) C2α·Ca$_2$ and (C) C2α·Pb sates. Prolines are highlighted in grey and residues that exhibit elevated R$_2$(1/τ$_{cp}$) but showed no significant dispersion are colored green.

Although consistently elevated $R_2(1/\tau_{cp})$ were observed for a subset of residues in the CBLs, no appreciable dispersion is detected under rcCPMG experiments. ^{15}N rotating-frame relaxation rate measurements ($R_{1\rho}$), suitable for quantifying faster processes (exchange rates between 5,000-50,000 s^{-1}) were used in order to determine if quantifiable dispersion could be obtained for apoC2α and the nature of the process could be better described. No appreciable dispersion was observed for apoC2α suggesting that the process is too fast and not accessible through the techniques used in this study.

Together, apoC2α, C2α·Ca_2 and C2α·Pb data reveals important aspects regarding the increase in dynamics at the N- and C-terminus. First, the conformational exchange process observed in this region is exclusive of C2α metal-bound states, irrespective of the metal identity (Ca^{2+} or Pb^{2+}) and saturation state (C2α·Ca_2 and C2 single-Pb). However, the exchange rates do show dependence on the metal saturated state of the protein, as the Pb^{2+} single-site and Ca^{2+} states illustrate (Figure 59A-C). The k_{ex} becomes faster when the second metal-site is occupied, but the identity of the residues exchanging at the N and C-termini in both states are the same, suggesting that the identity of the process is unchanged. These observations suggest an indirect metal-binding network from the CBLs all the way to the C-terminus, via the N-terminus (Figure 59B).

The dynamic response of CBLs is more complex (Figure 59A). Direct metal-binding exchange contributions, especially in the C2α·Pb state, and the potential binding of a third Ca^{2+} ion can contribute to the variable response, although no chemical shift correlation to metal-binding was observed. Direct metal binding or partial induced oligomerization was discarded as an explanation for the increase in dynamics at the N- and C-terminus by performing metal concentration dependent rcCPMG experiments, in addition to analytical ultracentrifugation (data not shown). The low concentration state is represented by C2α·Pb state for which no free metal is available in solution due to the high affinity for Pb1 (K_d^{Pb1}=64 nM). As discussed above, this state shows the presence of the N- and C-terminus conformational exchange and provides clear evidence of how direct metal-binding to this region is implausible. To assess a potential metal-induced aggregation and third calcium binding contributions to the observed exchange, the concentration of Ca^{2+} was increased to a 50-fold excess. An increase in R_{ex} was observed, which corresponded to a 2.4-fold change in the population product ($\Phi_{ex}=p_A p_B \Delta\omega^2$), given that k_{ex} and the chemical shift difference between the exchanging conformers at 25- and 50-fold Ca^{2+} remain unchanged (Figure 60). This increase illustrates the conformational exchange dependence of the metal-bound state, highlighting that the observed exchange is a property of the metal-bound state that is consequently enhanced by a higher metal occupancy.

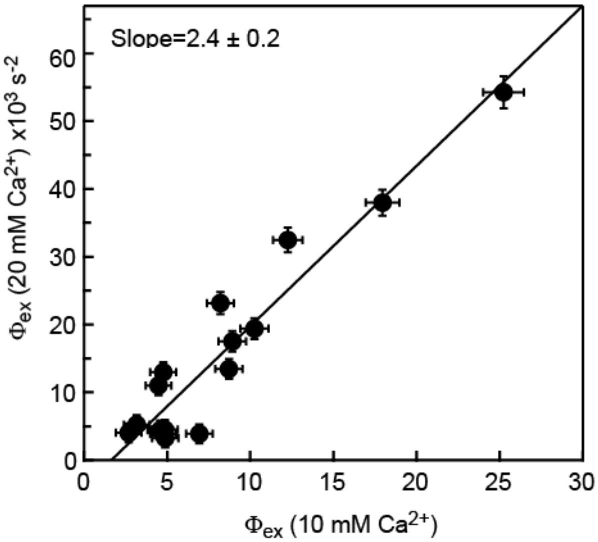

Figure 60. Correlation of Φex and Δω for 20mM and 10mM Ca^{2+}. The slope of 2.4 may represent a 2.4-fold increase in the population product ($\Phi_{ex}=p_A p_B \Delta\omega^2$) that is induced by higher occupancy of Ca^{2+} third site. This assumption holds true if we assumed that the chemical shift difference between the two saturated states remains unchanged.

Dynamic "uncoupling" of N- and C-termini by the R159G mutation

The potential involvement of the N-terminus as a mediator between the CBLs metal-binding and the C-term/H3 increased dynamics was further investigated. The mutant R159G-C2α was generated to understand the role of the N-terminus region. According to the crystal structure, the only interaction that is disrupted by this mutation is a hydrogen bond (2.9 Å) between R159 side chain (NH1) and the backbone carbonyl (CO) of M256 located on β7 (Inset of Figure 61A). Strikingly, this mutation resulted in large chemical shift changes that mapped onto the same regions affected by conformational exchange (Figure 61A-C, Figure 62, and Figure 63). The chemical shift changes are shown as a function of the C2α primary structure for the apo and Ca^{2+}-

bound states (Figure 61A), and they are mapped onto the structures (Figure 61B and C). Interestingly, the areas affected by the mutation were: the N-terminus region where the mutation site is located, CBL1, 2 and 3, β7 and the C-terminus (β8 and H3). Another observation was a reduced change in the total chemical shift perturbation in the presence of Ca^{2+} for several residues on the CBLs. This behavior suggests that, at least for CBLs, the observed changes in the apo state could be due to changes in dynamics between WT and the R159G mutant that are attenuated upon Ca^{2+} binding. This is further confirmed by severe cross-peak exchange broadening in the ^1H-^{15}N HSQC spectra for residues on the CBLs for the apo R159G-C2α mutant (Figure 62 exchange broadened beyond detection: M186 and D248, and R249; severely broadened: G257) and Ca^{2+}-bound complex (Figure 63; exchange broadened beyond detection, T251), suggesting that these are in the intermediate exchange regime in contrast to WT (Figure 61B and C). On the other hand, the addition of Ca^{2+} induced severe exchange broadening in the ^1H-^{15}N HSQC spectra for the C-terminus region where conformation exchange is observed in the presence of metal (i.e. V288, Figure 63). Specifically residues E282, G283, E284, Y285, Y286, N287, and V288 exhibit severe exchange broadening.

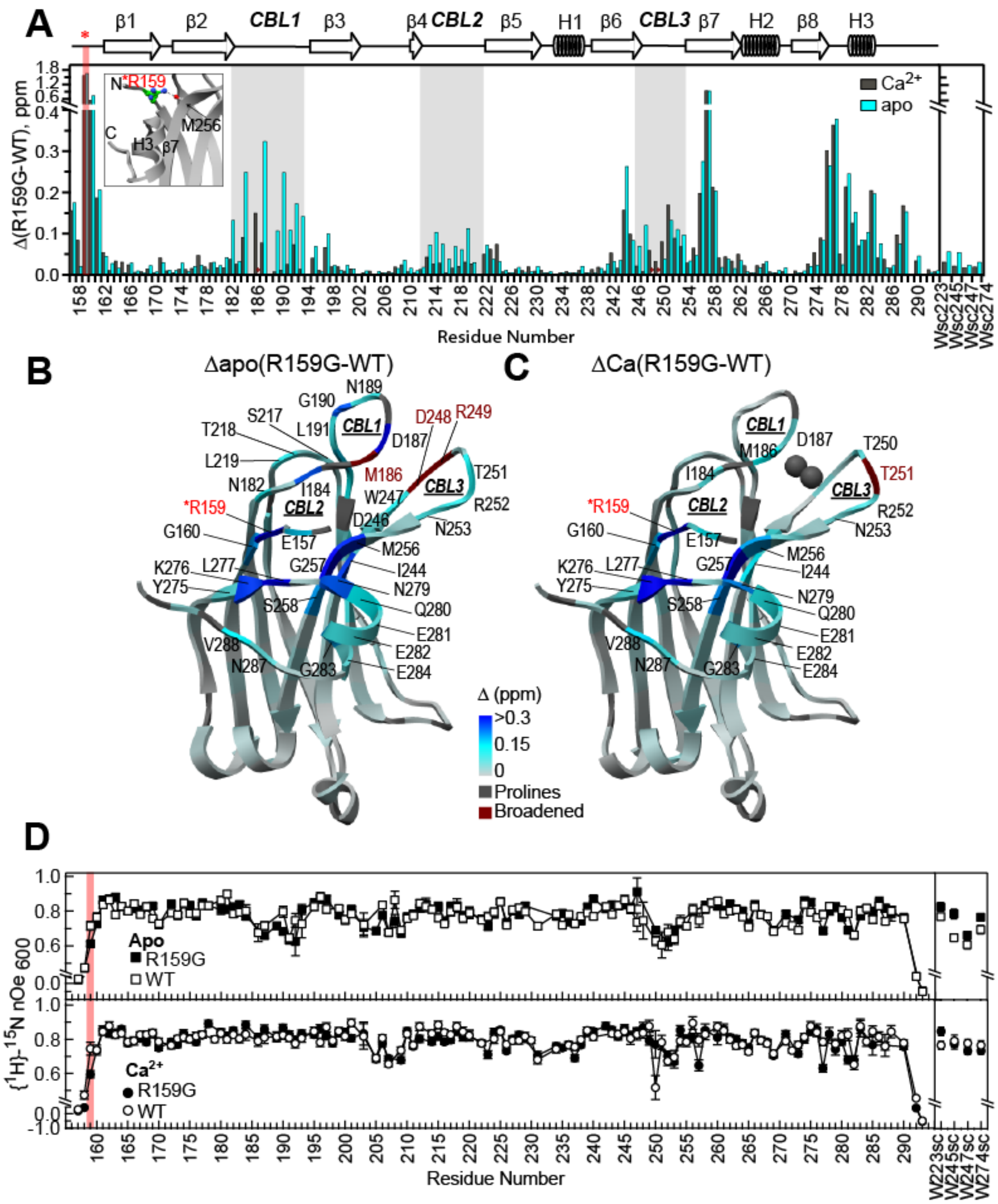

Figure 61. Chemical shift changes induced by the R159G C2α mutation. Chemical shift changes induced by the R159G C2α mutation in the (A) apo and Ca^{2+}-bound states as a function of C2α primary structure. Inset shows a structure expansion showing R159G hydrogen bond with the M256 backbone carbonyl in CBL3. Δ was calculated using Equation 10. Δ values for apo and Ca^{2+}-bound states mapped onto the apoC2α structure (PDB ID: 3RDJ) and Pb^{2+}-bound (PDB ID: 3TWY) crystal structures, respectively. (D) WT and R159G C2α mutant steady-state ^{1}H-^{15}N NOE at 14.1 T as a function of C2α primary structure for the apo and Ca^{2+}-bound states.

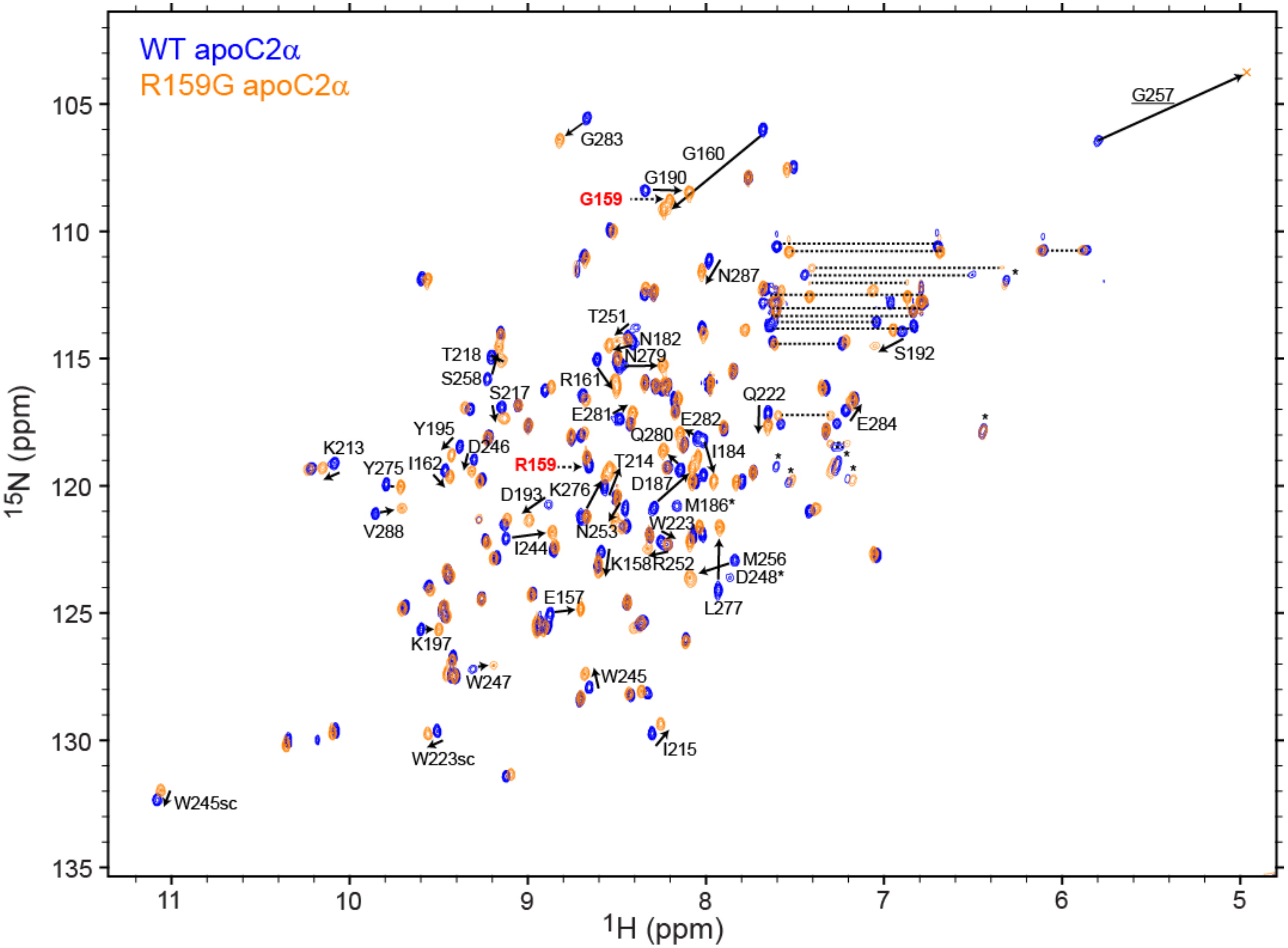

Figure 62. ^{1}H-^{15}N HSQC spectra comparison for the Ca^{2+}-bound state of WT and R159G C2α at 600 MHz.

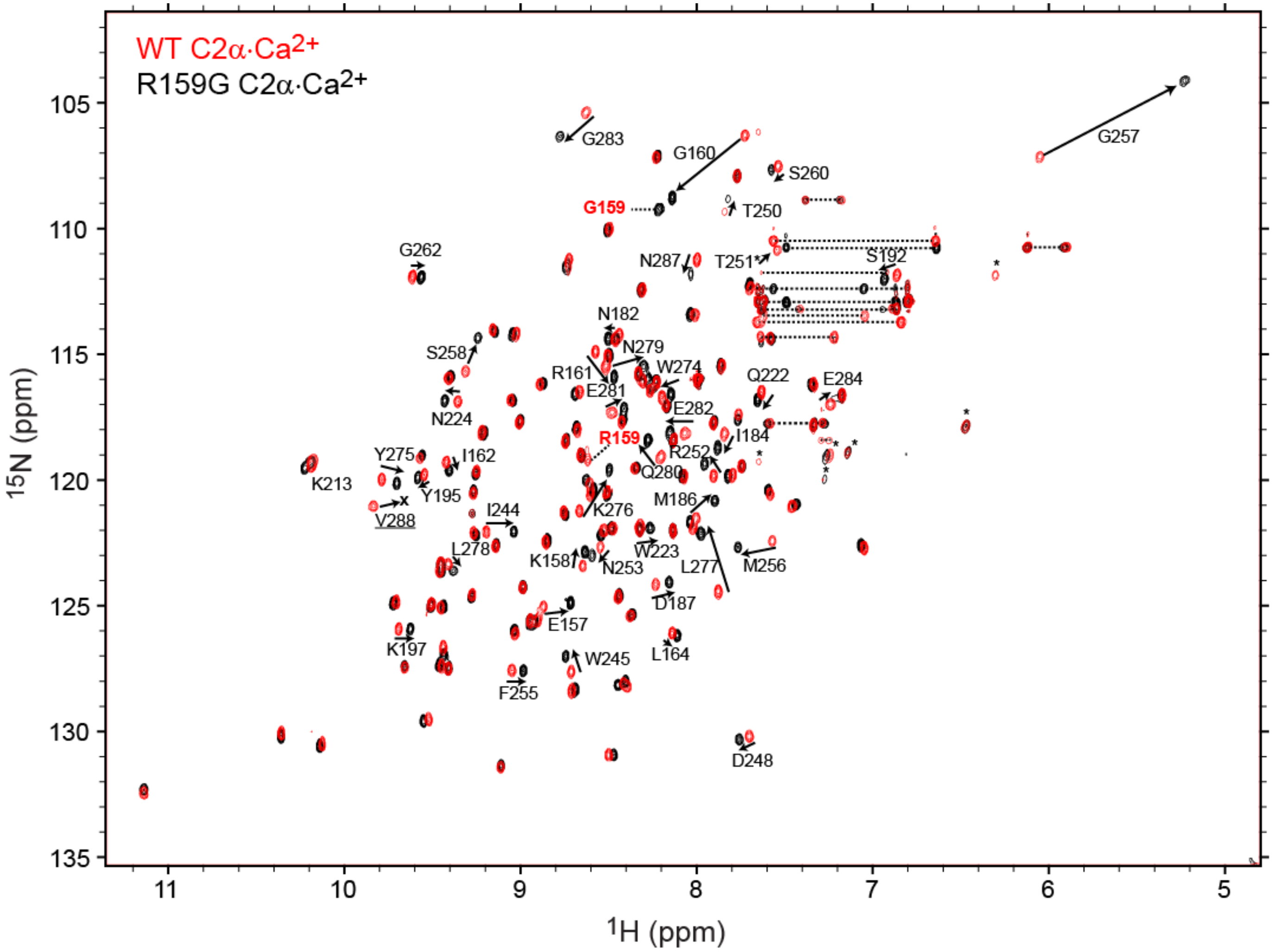

Figure 63. ^{1}H-^{15}N HSQC spectra comparison for the apo state of WT and R159G C2α at 600 MHz.

Despite the large changes in chemical shifts and exchange broadening induced by the mutation, the sub-nanosecond timescale motions between WT and R159G-C2α in the presence and absence of Ca^{2+} remained nearly unperturbed (Figure 61D). Additionally, the calcium binding properties of the domain are also unchanged as judged by the similarity of chemical shift changes induced by Ca^{2+} binding between WT and R159G mutant (Figure 64).

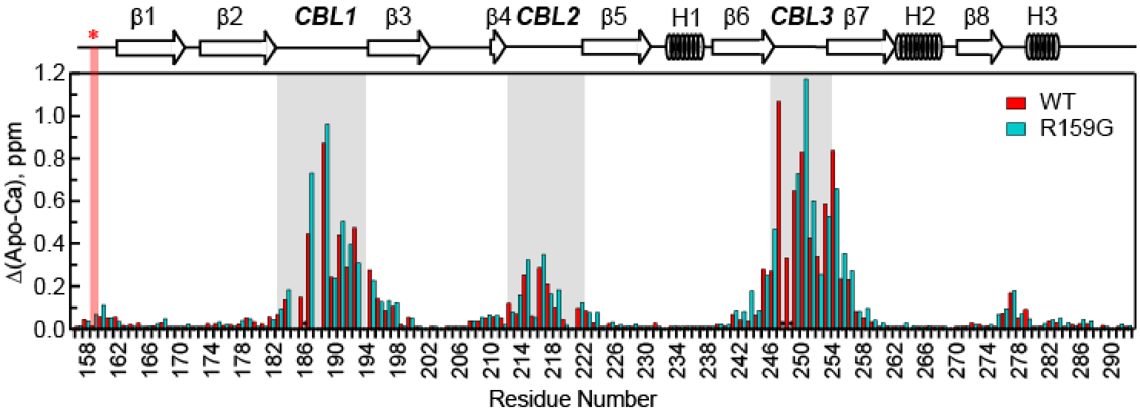

Figure 64. C2α chemical Shift perturbations induced by Ca^{2+}-binding to WT and R159G mutant. Δ values were calculated for WT (red) and R159G mutant (cyan) using Equation 10. CBLs and mutation site are highlighted in grey and red, respectively.

However, inspection of the transverse relaxation rates for the apo R159G-C2α revealed substantially elevated R_2-CPMG rates for the region between the β3-β4 groove and CBL2, in addition to the C-terminus (Figure 65A). Furthermore, the addition of Ca^{2+} dramatically enhanced the exchange at the C-terminus and increased R_2-CPMG rates for the β7, where M256 is located (residue that forms a hydrogen bond with R159 side chain). The changes in the conformational exchange behavior were characterized using rcCPMG relaxation dispersion experiments as described above and contrasted to those observed in WT.

The behavior observed in the apo state resembles that of the WT, where no appreciable dispersion was detected in rcCPMG experiments. However, remarkable differences were observed between WT and R159G-C2α dispersion profiles in the presence of Ca^{2+}. Figure 65B shows representative residues from the three exchanging regions (CBLs, N-terminus, and C-terminus) and contrasts the observed behavior between WT and the R159G mutant in the presence of Ca^{2+}. First, the N-terminal region is not exhibiting dispersion and the $R_2(1/\tau_{cp})$ rates are not elevated.

On the contrary, the C-term/H3 region now shows elevated transverse $R_2(1/\tau_{cp})$ rates with very weak dispersion or no dispersion at all (Figure 65B and C). Only 8 residues in contrast to 22 in WT are showing quantifiable dispersion in the presence of Ca^{2+}. However, it is noteworthy that compared to the WT, the exchange rate in R159G variant is elevated. The absence of the R159 and M256 hydrogen bond affects the exchange rate between the states, suggesting a direct involvement of the N-terminus in regulating the conformational dynamics at the C-terminus (H3) in response to metal-binding. The μs-ms dynamic changes rather than well-defined conformational change could be responsible for affecting intra-domain interactions upon metal-binding during PKC activation.

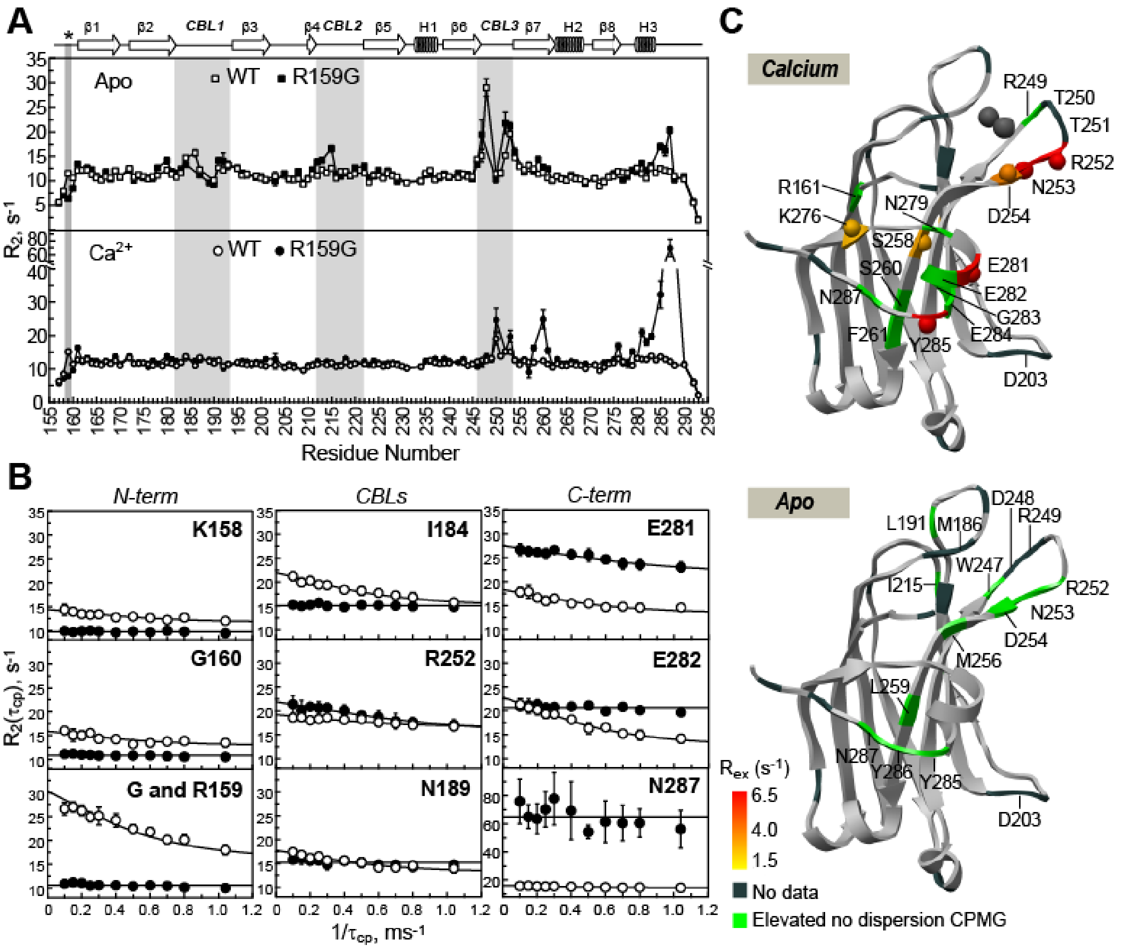

Figure 65. Comparison of the conformational dynamics changes induced by the R159G mutation. (A) Transverse relaxation (R_2-CPMG) rates for WT and R159G mutant as a function of C2α primary structure in the apo (open key) and Ca^{2+}-bound states (solid key). (B) ^{15}N transverse relaxation rate as a function of CPMG pulse train frequency for representative residues of the three exchanging regions (N-term, CBLs and C-term) in the presence of Ca^{2+} for (○) WT and (●) R159G C2α mutant. (C) R_{ex} values mapped onto the Pb-bound and apo crystal structures (PDB ID: 3TWY and 2RDJ) for the C2α·Ca_2 and apo C2α states. In addition to Prolines, residues for which NMR data was not available due to severe chemical exchange broadening are highlighted in grey. Residues that exhibit elevated $R_2(1/\tau_{cp})$ but showed no significant dispersion are colored green.

Discussion of results

The objective of this work was to gain insight into the mechanistic implications of C2α Ca^{2+}-dependent conformational dynamics. C2 domains currently constitute the second most conserved lipid-binding motif, after PH domains. Although unique regulation has been attributed to their wide range of lipid selectivity and affinities for Ca^{2+}, less is known about their structural organization and dynamical contributions with regards to the function they play within their multi-modular host enzymes.

As shown for numerous systems, the site-specific characterization of conformationally available states by solution NMR techniques under timescales relevant to ligand-binding, conformational rearrangement, catalysis, and folding provides information about the mechanism of action and ligand binding adaptability. Here we present the first full dynamic study for a Ca^{2+}-dependent C2 domain (C2α) and introduce a conformationally dynamic driven mechanism for the dissociation of intra-domain interactions in response to Ca^{2+}-binding.

We first extracted S^2_{HN} from ^{15}N spin-relaxation data to identify backbone sub-nanosecond (ns-ps) timescale fluctuations that could be associated with potential entropic changes due to metal-binding. Although some regions displayed lower than average S^2_{HN} values, this was true for all three metal-ligated states tested (apoC2α, $C2\alpha\cdot Ca_2$, and $C2\alpha\cdot Pb$). Therefore, we conclude that the ns-ps dynamics is not altered by metal-binding, suggesting that there are no significant entropic contributions arising from metal binding on this timescale. Reduced spectral density mapping, $J(0.87\omega_H)$, unmasked potential motions under this timescale for CBL1 in the apoC2α state that are attenuated in the presence of metal, highlighting the importance of combining both methodologies. The characterization of μs-ms timescale motions for apoC2α (*vide infra*), suggest that these motions fall on a fast regime.

In contrast, inspection of R_2-CPMG rates revealed substantial elevated values for residues on the CBLs for the apoC2α state. Considering that there are no significant motions on the sub-nanosecond timescale, the R_{ex} component (μs-ms) is the only remaining factor capable of inducing the increase in R_2 rates. Moreover, the difference between the R_2-CPMG rates for apoC2α and metal-ligated states shows that there is significant attenuation of the microsecond dynamics for the CBLs upon metal-binding. This advocated the use of adequate NMR techniques for the quantitation of motions on the μs-ms timescale, where information about the exchange rate, populations and chemical shift difference between the exchanging states were obtained. We employed rcCPMG relaxation dispersion methodology for the characterization of the conformational exchange in the same three metal-ligated states described above. Interestingly, metal-binding results in a concerted change for the millisecond dynamics of N- and C-termini regions, which have been implicated in interactions with other PKCα domains (C1Aα). Moreover, the sequential loading of metal-binding sites (represented by C2α·Pb and $C2\alpha\cdot Ca_2$) increases k_{ex} approximately 3-fold (576 ± 85 s^{-1} in C2α·Pb to 1,675 ± 58 s^{-1} $C2\alpha\cdot Ca_2$) between the conformationally exchanging states, which we believe are not correlated to metal-binding, based on chemical shift correlation of ^{15}N Ca^{2+}-induced chemical shifts (ΔN) and Δω extracted from ^{15}N CPMG data using Carver Richards general equation (data not shown). In addition, we inspected the metal-binding dependence further by increasing the Ca^{2+} concentration twice (from 25-fold to 50-fold). This generated an increase in R_{ex} that is accompanied by a change in the population term rather than a significant change in k_{ex} (Figure 60). In light of negligible change in k_{ex}, correlation of Φ_{ex} suggests that the increase in R_{ex} would correspond to a change in the population product, p_Ap_B of ~2.4-fold. We hypothesize that this is due to Ca^{2+} binding into the third metal-binding site previously observed within C2α. This would induce a further shift in the equilibrium towards the Ca^{2+}-bound state, the condition for which we observed the conformational exchange.

$$C2\alpha Ca_2 + Ca^{2+} \leftrightarrow C2\alpha Ca_3(A) \leftrightarrow C2\alpha Ca_3(B)$$

On the other hand, the behavior observed for the apoC2α state was remarkably different. Elevated R_2-CPMG rates were observed only for CBL1 and CBL3 residues with no appreciable dispersion, suggesting that the process might be faster and hence not accessible with the rcCPMG dispersion experiments employed in this study. ^{15}N-R1ρ techniques were attempted, but no quantifiable dispersion was obtained (data not shown), which foresees the utilization of ^{1}H-R1ρ to characterize the faster microsecond processes that are happening in the apoC2α CBLs. Regardless, our data clearly shows that the conformational exchange we are detecting at the N- and C- termini is characteristic of the metal-bound state only. We therefore propose that this could be a potential mechanism for propagating the information about the Ca^{2+}-binding event to other PKCα domains during activation. In particular, the concerted change in the millisecond dynamics at the N-terminus, which connects C2α to the C1B domain, provides a plausible mechanism to communicate the metal-binding event. The exchange at the C-terminus/H3 can provide evidence of direct communication to the C1A domain further upstream in the cPKC primary structure, given the implications in direct contacts by recent mutagenesis studies between these two domains. Furthermore, the strongly coupled increase in the exchange rate (Figure 66) as the metal-binding sites are sequentially populated may represent a sensing mechanism that “tunes” cPKC responsiveness to available Ca^{2+} concentrations and controls the tethering to C1A as it was previously proposed.[54] The current activation mechanism proposes that C2α Ca^{2+}-dependent recognition of PtdSer in the plasma membrane provides the energy required to disrupt such interactions, allowing the C1 domains to search laterally for the second required messenger, DAG. The engagement of all membrane binding modules increases the residence time at the plasma membrane resulting in full enzyme activation. In fact, we observed chemical shift changes at H3, associated with C2α binding to mixed micelles containing PtdSer or PtdSer/PIP_2 (Figure 67).

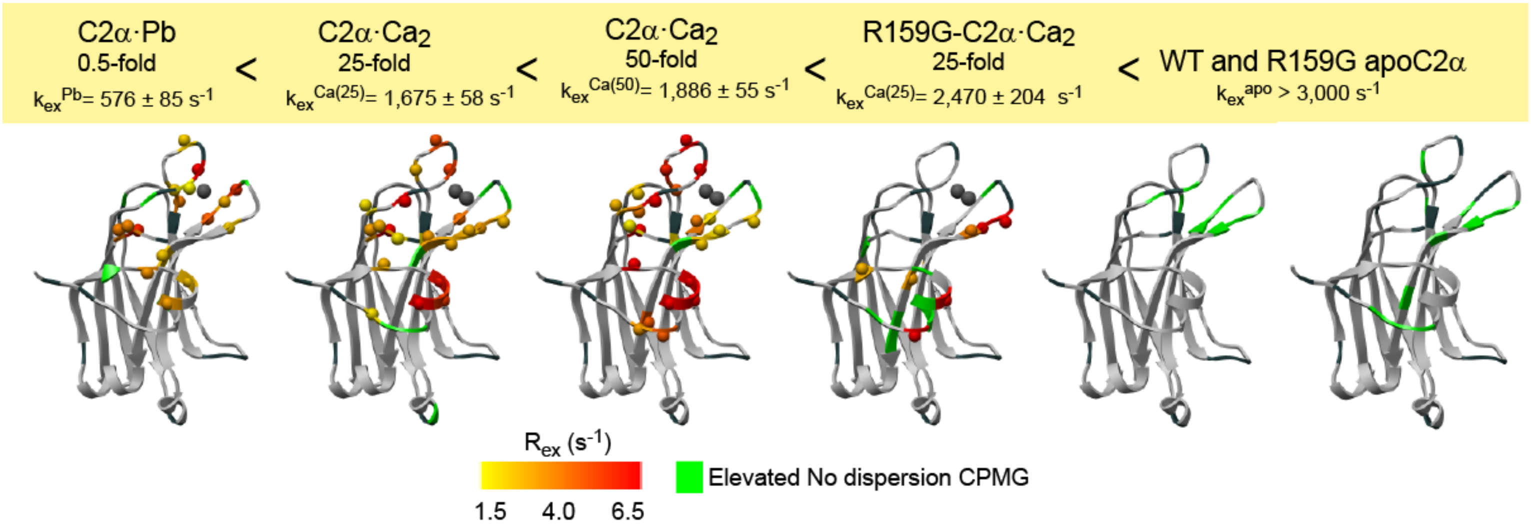

Figure 66. Rates of conformational exchange obtained for C2α and its R159G mutant in different states of metal ligation.

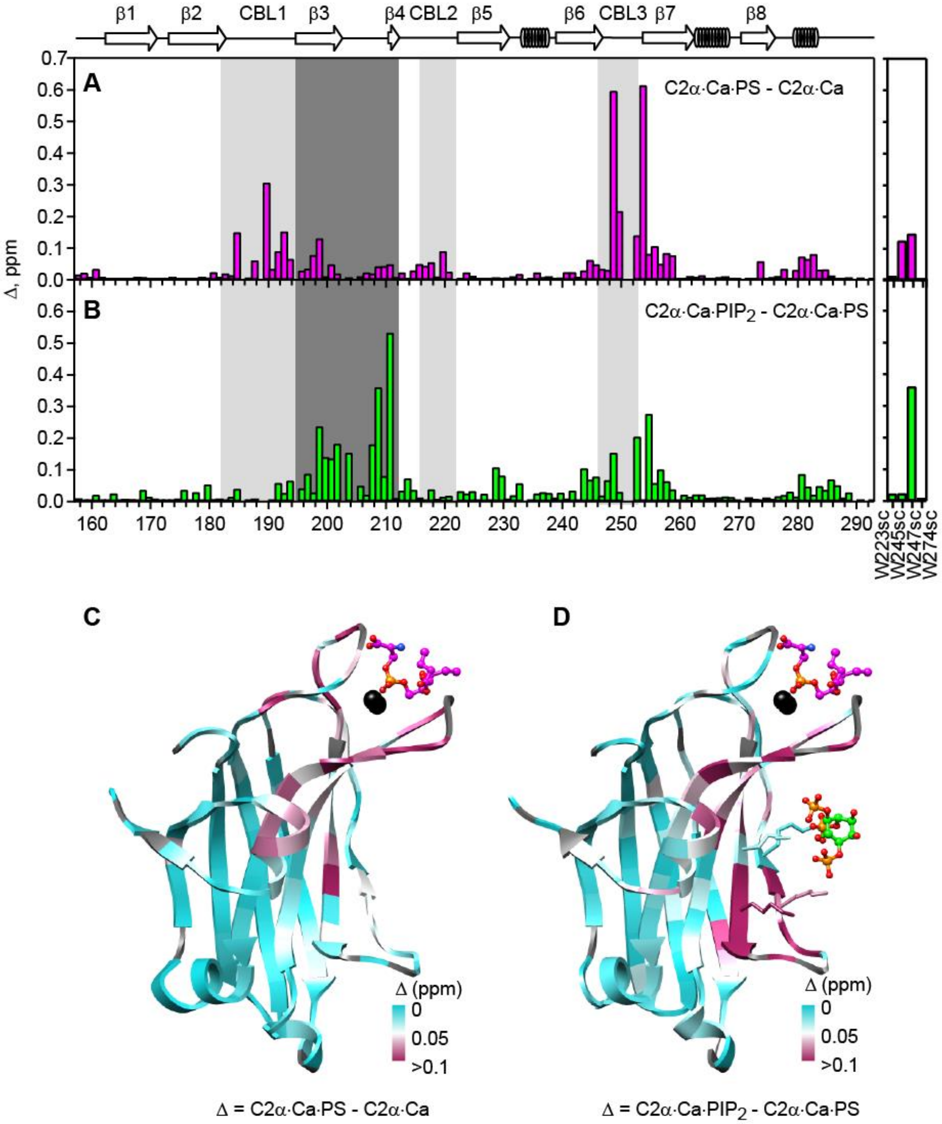

Figure 67. Effect of PtdSer and PIP_2 in mixed-micelles binding. (A) Chemical shift perturbation Δ due to PtdSer and PIP_2 binding plotted as a function of primary structure. Calcium-binding loops - CBL1, CBL2, and CBL3 are highlighted in gray. The β3-β4 region that directly interacts with PIP_2 is highlighted in dark gray. (B) Site-specific Δ values, color-coded, and mapped onto the structures of (C) C2α·Ca^{2+}·PS complex (PDB ID: 1DSY) and (D) C2α·Ca^{2+}·PIP_2 (PDB ID: 3GPE), respectively. The PS molecule was added into the PIP_2 complex structure two illustrate the location of PS and PIP_2 binding sites. Proline residues, for which NMR data are not available, are shown in grey.

We further investigated the Ca^{2+}-dependent mechanism for the conformational dynamic propagation, with the preparation and characterization of the C2α-R159G mutant. Remarkably, the elimination of a single hydrogen-bond via the R159G mutation "uncouples" the conformational dynamics of terminal regions in response to Ca^{2+}-binding at the CBLs. This was confirmed by a comparison of CPMG-R2 rates, which showed prominently elevated R_2-CPMG rates for the C-term region of R159G-C2α in contrast to WT C2α, in addition to greater exchange broadening for CBLs residues in the mutant. We attributed this manifestation to changes in the millisecond timescale dynamics, since sub-nanosecond motions are unperturbed by the mutation (Figure 61D). Moreover, we observed significant chemical shift changes induced by the R159G mutation that are localized to the CBLs, N-term, and C-term regions of the domain, which mapped onto the same regions that were undergoing conformational dynamic changes in the presence of metal. Although, no direct structural comparison between the R159G mutant was carried out, based on the chemical shift similarity between WT and R159G mutant Ca^{2+}-bound states and the profound changes in the millisecond timescale for the R159G mutant, we proposed that these changes are due to changes in the conformational dynamics rather that the average structure. Furthermore, chemical shift perturbation analysis confirms that R159G binds Ca^{2+} in an identical manner to WT (Figure 64).

The initial idea of C2 domains as flexible domains came from crystallographic and NMR data where a lack of structural definition was observed, as evaluated by the lack of electron density and NMR restraints in the absence of Ca^{2+}, particularly for the

CBLs. The results shown in this study bring about the idea of C2 domains as conformationally dynamic modules rather than rigid domains as they have been perceived. Despite the high structural homology among C2 domains, there are some differences in the interconnection of the strands which has led to the classification of C2 domains in two different topologies: topology I (i.e. Syt I C2A domain) and II (i.e. C2 from PLA_2). This places the N- and C-termini of the domain in opposite directions. Interestingly, topology I exists for cPKC C2 domains and topology II exists for novel PKC. While no clear functionality has been established, we speculate that the conformational dynamics of the N-terminus points to the potential role of the C1B-C2 linker region in modulating the inter-domain interactions and orientation.

As a final note, binding of Pb^{2+} to the high-affinity site may be sufficient to disrupt the inter-domain interactions within conventional PKCs. This can have important implications for the mechanism of Pb^{2+} toxicity.

CHAPTER VI

PROBING CA^{2+}-INDUCED STRUCTURAL CHANGES IN THE REGULATORY DOMAIN OF PKC

Background

Conventional PKC (cPKC) isoforms are multi-domain enzymes containing tandem C1A and C1B, C2, and catalytic domains existing as independently folded modules connected by flexible linkers. In resting cells, cPKC isoforms are localized in the cytosol under the acute regulation of intra-molecular interactions.[73,216,217] Changes in the intra-domain interactions within the regulatory domains that affect their accessibility to bind second messengers have been proven to be critical both in the activation and specificity among PKC isoforms.[38,54] The disruption of these interactions by second messenger binding represents one of the mechanisms by which PKC isoforms are selectively regulated and activated. As discussed in Chapter I, the phosphorylation state of the catalytic domain and inter-domain interactions with specific adaptor proteins at particular cellular locations corresponds to the other two general mechanisms of PKC isoform regulation. During activation, second messenger binding is responsible for the modulation and disruption of intra-molecular interactions that lead to the membrane translocation and activation of the full enzyme. The use of PKC isoforms chimeras has revealed that the nature of the regulatory modules can affect both the substrate specificity and function of the full-length protein.[217] Hence, the distinct intra-molecular interactions within PKC represent a mechanism of isoform-specific regulation and modulation.[217]

Ca^{2+}-binding to the C2 domain leads the way as the first step in the activation of cPKC isoforms.[37] Accordingly, the role of Ca^{2+} binding to C2 has been proposed to serve at least three purposes: (i) function as a bridge between C2 and the anionic PtdSer headgroup in the plasma membrane,[204] (ii) modulate C2 electrostatic potential,[50] and lastly (iii) bring about a conformational change that alters intra-domain interactions and prepares the enzyme for the membrane association.[40] In Chapters II-V, the effects of Ca^{2+} binding in the structure, dynamics and function of the isolated C2 domain from PKCα were investigated. However, this only comprises the electrostatic potential changes and membrane-bridging function of Ca^{2+}-binding in cPKC isoforms. The work presented here applies the knowledge acquired from the characterization of the isolated C2 and C1B[218,219] domains and takes the first step into assembling the regulatory region with the objective of characterizing the interactions and domain rearrangements that occur upon Ca^{2+}-binding.

The first and best characterized inhibitory interaction is the binding of the pseudo-substrate segment to the substrate binding pocket in the catalytic domain (Figure 68).[220] This long-range association constitutes the main, however not the solely inhibitory intra-molecular interaction identified to stabilize the inactive cytosolic enzyme.[31] The elusive element in the activation is how this main inhibitory interaction is released by second messengers binding to the regulatory domains. For conventional isoforms the Ca^{2+} requirement along with the generation of the membrane-anchored

DAG, represent the two required messengers for activation. Activation is proposed to be a sequential event, where an increase in intracellular Ca^{2+} concentrations recruits C2 domain to the membrane, which then reduces the dimensionality search of DAG by the C1 domains (C1A and C1B).[37] It is the consecutive engagement of all the lipid binding modules to the membrane that is thought to provide the energy required to pull out the pseudosubstrate from the catalytic domain and sustain the activated state of the enzyme in the membrane.[38] Hence the disruption and rearrangement within N-terminal regulatory domains play a crucial role in the disruption of the pseudo-substrate interaction, and the C2 domain has been placed as a central regulator of intra-domain interactions in the first step of activation.

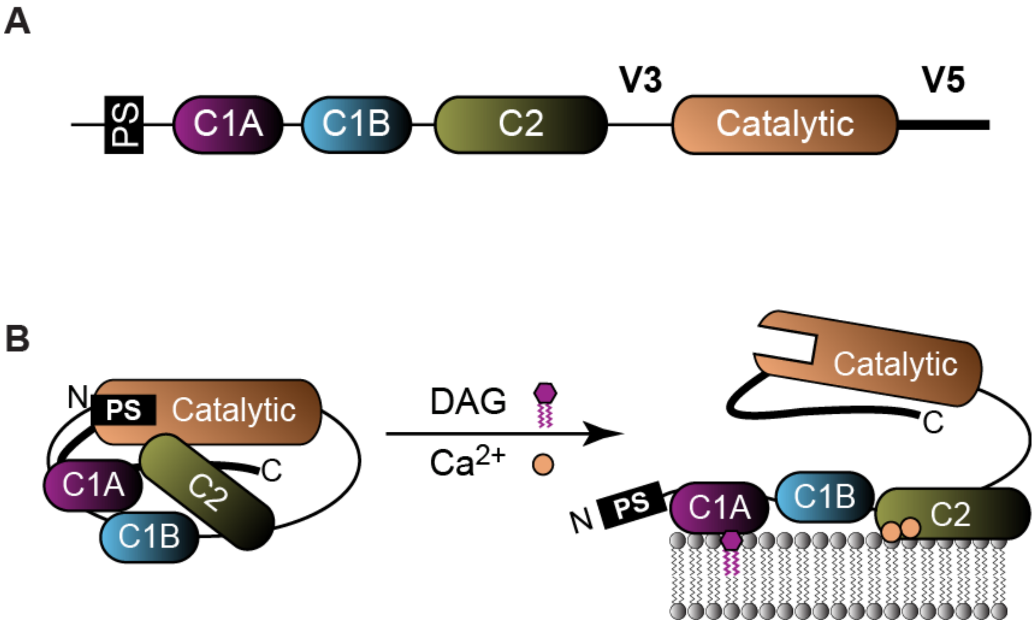

Figure 68. Module composition and activation model of cPKC (A) Illustration of multi-modular structure organization of cPKC. (B) Current activation model for cPKC isoforms. PS and DAG stands for pseudo-substrate and diacylglycerol, respectively.

Two inhibitory interactions involving C2 with the V5[53] and C1A[40] segments have been proposed to be disrupted during activation. These interactions were supported by functional mutagenesis studies carried out on the full length enzyme as well as isolated domains. The first interaction was mapped between the phosphorylated hydrophobic motif on V5 and C2. Early work showed that phosphorylation in the V5 terminal region increased the Ca^{2+} affinity of the enzyme.[221] This interaction was later confirmed with reverse mutagenesis studies, which identified that C2 was the interaction site of V5.[53] The second interaction was provided by the C1Aα D55A mutation.[54] This single substitution, resulted in reduced PtdSer selectivity and increased activity under non-activating conditions.[54] The corresponding mutation was carried out for the equivalent position in C1Bα, and the activity was equivalent to WT suggesting that C1Aα is the responsible for tethering the enzyme in the inactive state via intra-domain interactions. Subsequent mutagenesis studies carried out by Stahelin et al. identified the potential interface and residues involved in this interaction.[40] These involved C2α C-term/H3 and CBL3 regions.[40] Interestingly, the equivalent mutagenesis study was carried out for the C1A domain from cPKCγ (C1Aγ). Intriguingly, these studies revealed differences in the C1 domain accessibility to DAG and less contributions of C2 inhibitory interactions providing underlying differences between the conventional PKCα and PKCγ isoforms. Based on this study, it was proposed that the C1Aγ and C1Bγ were more conformationally flexible in PKCγ and were consequently ready to penetrate the membrane without a PtdSer requirement in the presence of DAG.[222]

Ca^{2+} signal transduction is known to induce long-range conformational changes in several Ca^{2+} binding protein families. However, the lack of evident backbone structural changes in C2 domains in combination with the changes in conformational dynamics discussed in Chapter V, provides mechanistic evidence that Ca^{2+}-binding could be transmitted via changes in the conformational dynamics. This provides additional evidence that both the intra-domain interactions and conformational flexibility of the regulatory domains play an important role in the binding accessibility to second messengers, and thereby affects the specificity of the full enzyme. In this chapter we aimed to characterize both: (i) the changes in dynamics using relaxation experiments in combination with the (ii) relative orientation of the domains in solution using paramagnetic relaxation enhancement (PRE) as structural restraints. The size and inherent flexibility imparted by the multi-modular structure of these enzymes represent a challenge for NMR and crystallography, respectively. However, solution NMR techniques provide means of studying both structure and dynamic properties with site-specific resolution in solution. We took a divide-and-conquer approach with the preparation of a two-domain construct comprising C2 and its preceding domain, C1B, connected by their native linker (9 amino acids). This construct exploits the structural, dynamics, and functional knowledge of isolated domains and represents the first step into the characterization of the structural and conformational dynamics changes affecting the rearrangement and relative orientation of the regulatory region of cPKC upon Ca^{2+} binding. Preliminary results indicate that the two domains do not behave as fully independent modules in solution and that a distinct rearrangement in the presence of Ca^{2+} is plausible.

Experimental procedures

C1B-C2 expression and purification

The DNA sequence encoding the 194 residue (S100-G293) comprising the C1B and C2 domains from PKCα of *Mus musculus* was amplified by PCR using PKCα cDNA clone (Open Biosystems) as a template and cloned into the pET-SUMO vector (Invitrogen). Over-expression was carried out in *E. coli* BL21(DE3) cells. Cell cultures were grown to an OD_{600} of 0.6 and induced with 0.5 mM IPTG for 15 hours at 15 °C. 10 μM Zn^{2+} was added right before induction to ensure the proper folding of C1B. Isotopically enriched protein was over-expressed as described in Chapter II according to the method of Marley et al.[88]

C1B-C2 purification was carried out as described for C2α (Chapter II)[48] with the exception that final cation exchange chromatography was carried out in the presence of 100 μM Ca^{2+} and 0.1 mM tris(2-carboxyethyl)phosphine (TCEP). Fractions containing C1B-C2 were transferred to a 10 kDa concentrator where C1B-C2 decalcification was carried out. A total of 4 washes with a 10 μM ethylene glycol tetraacetic acid (EGTA) containing buffer (10 mM MES pH 6.0, 100 mM KCl, 1 mM TCEP, and 10 μM EGTA), followed by 4 washes into the desired NMR buffer were performed to ensure C1B-C2 decalcification and EGTA removal.

NMR spectroscopy

All NMR experiments presented in this chapter were carried out at 25 °C on a Bruker Avance III system equipped with a cryo-probe and a Varian Inova spectrometer operating at ^{1}H Larmor frequencies of 800 (18.8 Tesla) and 600 MHz (14.1 Tesla), respectively. The temperature was calibrated using deuterated methanol (methanol-d_4)[223] and protonated methanol, respectively. Sequence-specific assignments of the ^{1}H, ^{13}Cα, ^{13}Cβ, and ^{15}N resonances for the apo and Ca^{2+}-bound C1B-C2 were obtained using ^{2}H-decoupled three-dimensional HN(CA)CB, HNCA(CB), HN(COCA)CB, and HN(CO)CA experiments[91] in a [U-^{13}C,^{15}N; 55%-^{2}H] C1B-C2 sample. Assignments experiments were carried out in the presence of 10 mM MES pH 6.0, 50 mM KCl, 1 mM TCEP, 0.02 % NaN_3, 8 % D_2O and transferred to 0, 100, and 150 mM KCl conditions.

Chemical shift perturbations of the C1B and C2 domains in the C1B-C2 construct

Chemical shift perturbations for the isolated C2 (Chapter II) and C1B domains relative to the C1B-C2 domain construct were calculated using Equation 10. The C1B 72-mer construct comprising residues 92 to 163 (assigned by Mikaela D. Stewart at Texas A&M University)[224] was used for the analysis. Assignments were carried out in the absence of salt (20 mM MES pH 6.0, 8% D_2O, 0.02% NaN_3), for which C1B-C2 and isolated C2 spectra were collected under no salt conditions in the presence and absence of Ca^{2+} to provide the same conditions in this analysis.

^{1}H-^{15}N spin-relaxation measurements

All NMR relaxation experiments were carried out at 25 °C on a Bruker Avance III system equipped with a cryo-probe operating at ^{1}H Larmor frequencies of 800 (18.8 Tesla). The C1B-C2 concentration and buffer composition for all relaxation experiments was 0.30 mM and 10 mM MES buffer at pH 6.0, 150 mM KCl, 1 mM TCEP, 8% D_2O, and 0.02% NaN_3, respectively. Relaxation parameter sets comprising the longitudinal relaxation rate constant (R_1), transverse relaxation rate constant (R_2-CPMG), and ^{1}H-^{15}N nuclear Overhauser enhancement (NOE) were measured for all spectrally resolved ^{15}N-^{1}H backbone for C1B-C2 construct in the apo and Ca^{2+}-bound states.[199] The data were acquired in an interleaved manner as described in Chapter V. Delays use for R_1 and R_2 ranged from 0.080 s to 1.5 s and 0.006 s to 0.100 s, respectively.

In addition, Hahn-Echo (HE) experiments[136] were carried out to determine the effects on the microsecond-to-millisecond backbone dynamics induced by Ca^{2+}-binding relative to the isolated domains. Experiments were carried out as described in Chapter III.[69] Spectra were collected in an interleaved manner with time delays of 0 and 38.7 ms.

Rotational diffusion tensor calculations and domain alignment

The rotational diffusion tensor of the protein was determined from the ^{1}H-^{15}N relaxation parameters. The ARMOR package (Konstantin Berlin, University of Maryland), which interfaces with the software's ROTDIF[225] and ELMDOCK[226], optimizes the orientation of the domains according to the calculated full rotational diffusion tensor and the calculated tensor from the molecular coordinates provided (PDB) of each domain. The rotational diffusion tensor is defined by six parameters (D_{zz}, D_{xx}, D_{yy}, α, β, and γ), where D_{zz}, D_{xx}, D_{yy} are the three principal axes values and α, β, and γ are the angles that relate the diffusion tensor principal axes to the molecular frame (PDB). ELMDOCK takes the experimentally determined tensor from ROTDIF and minimized it with the calculated tensor from the 3D structure. It finds the optimal orientation and position of the second domain with respect to the first one; however, in the absence of a tight complex the resulting structure should be treated as an estimate only.[226] For this reason, we only evaluated the optimized orientation and ignored the translation step of the domains.

C1B-C2 cysteine mutagenesis for paramagnetic tag attachment

C1B-C2 cysteine mutants: K268C, S234C, K230C, N206C, N224C, S241C, S272C, K181C, Q280C, Y286C, and N189C were generated from wild type (WT) C1B-C2 gene using the Stratagene QuickChange™ site-directed mutagenesis kit and appropriate PCR primers. Mutagenic plasmids were transformed, expressed and purified using the same procedure as for WT C1B-C2.

C1B-C2 crystallization and structure determination

Crystals of C1B-C2 were grown using the sitting-drop vapor-diffusion method. Freshly purified C1B-C2 was concentrated to 1.5 mM (10mM MES pH 6.0, 0.02% NaN_3. $Pb(Ac)_2$ was added from a concentrated stock to a final 8-fold excess and incubated for 2 hours prior to setting drops. The protein was mixed with mother liquor (14% PEG3350, 0.3M Lithium sulfate, 50mM Ammonium citrate tribasic, 0.1 M HEPES pH 7.0) at a 1:1 ratio (protein:mother liquor) and incubated at 16°C. Crystals appeared within 3 days. Crystals were cryo-protected with 20% glycerol in the mother liquor and subsequently flash-frozen in liquid nitrogen.

X-ray diffraction data were collected on beamline and 23ID-D at the Advanced Photon Source, Argonne National Laboratory, Argonne, Illinois. Data was collected at a the Pb L-III absorbtion edge (λ=0.94967 Å) at a temperature of 120K. The X-ray diffraction data was reduced using HKL3000. Phases were obtained experimentally by Single-wavelength Anomalous Dispersion (SAD) using the Pb^{2+} anomalous signal and AutoSol, PHENIX version 1.7.3. Iterative steps of model building and refinement were performed with Coot version 0.6.1 and PHENIX Refine, respectively. Data collection and refinement statistics are reported in Table 11.

Table 11. Data collection and refinement statistics for C1B-C2-Pb^{2+} complex.

Diffraction data	**C1B-C2·Pb^{2+}**
Wavelength (Å)	0.94967
Space group	$P2_12_12_1$
Unit cell	a=34.04 Å b=58.97 Å, c=104.95 Å $\alpha=\beta=\gamma=90°$
Resolution (Å)	39.2-1.24 (1.26-1.24)[a]
Unique reflections	59843
Redundancy	5.3 (5.1)
Completeness	98.2 (93.2)
$<I/\sigma I>$	12.0 (2.6)
R_{sym}(%)	14.3 (58.3)
Refinement	
Resolution (Å)	39.2-1.24
Protein atoms	1603
Citrate atoms	36
Pb (II) ions	4
Zn (II) ions	2
Sulfate ions	3
Solvent atoms	238
R_{cryst}/R_{free}	15.1%/16.5%
RMSD bond length	0.013 Å
RMSD bond angle	1.26°

[a] Values in the parentheses are for the highest-resolution shell

Results

C1B and C2 domains are not independent in the C1B-C2 construct

The structural effects induced by the physical attachment of the C1B and C2 domains via their native 9 amino acid linker in the C1B-C2 construct, were first evaluated by comparison of their backbone chemical shifts. The ^{1}H-^{15}N HSQC spectra overlay of the isolated C1B and C2 domains along with the C1B-C2 construct in the C2 apo (Figure 69) and Ca^{2+}-bound (Figure 70) states, all qualitatively illustrate the presence of substantial chemical shift perturbations relative to the isolated domains. Standard triple resonance experiments were employed for the site-specific assignment of C1B-C2 crosspeaks in the apo and Ca^{2+}-bound states. These allowed the identification of the specific regions affected in the two-domain construct. Figure 71 shows the plots for the C1B-C2 chemical shift perturbation analysis in the apo and Ca^{2+}-bound states relative to the isolated domains. The regions affected in C1B correspond to the β4 strand and the segment preceding the linker. The linker region itself is profoundly affected and is followed by the C2 domain, where the CBLs and C-terminal regions are prominently perturbed. These data suggests that the physical attachment of the two domains results in the formation of an interface facilitated by the linker segment, since the isolated domains do not produce any changes in chemical shifts when mixed together (Figure 72). In addition, the large changes produced in the linker also suggest that in the two-domain construct this segment is not fully unrestricted and behaves as an independent segment, which furthers supports the significance of its role in the inter-domain rearrangement.

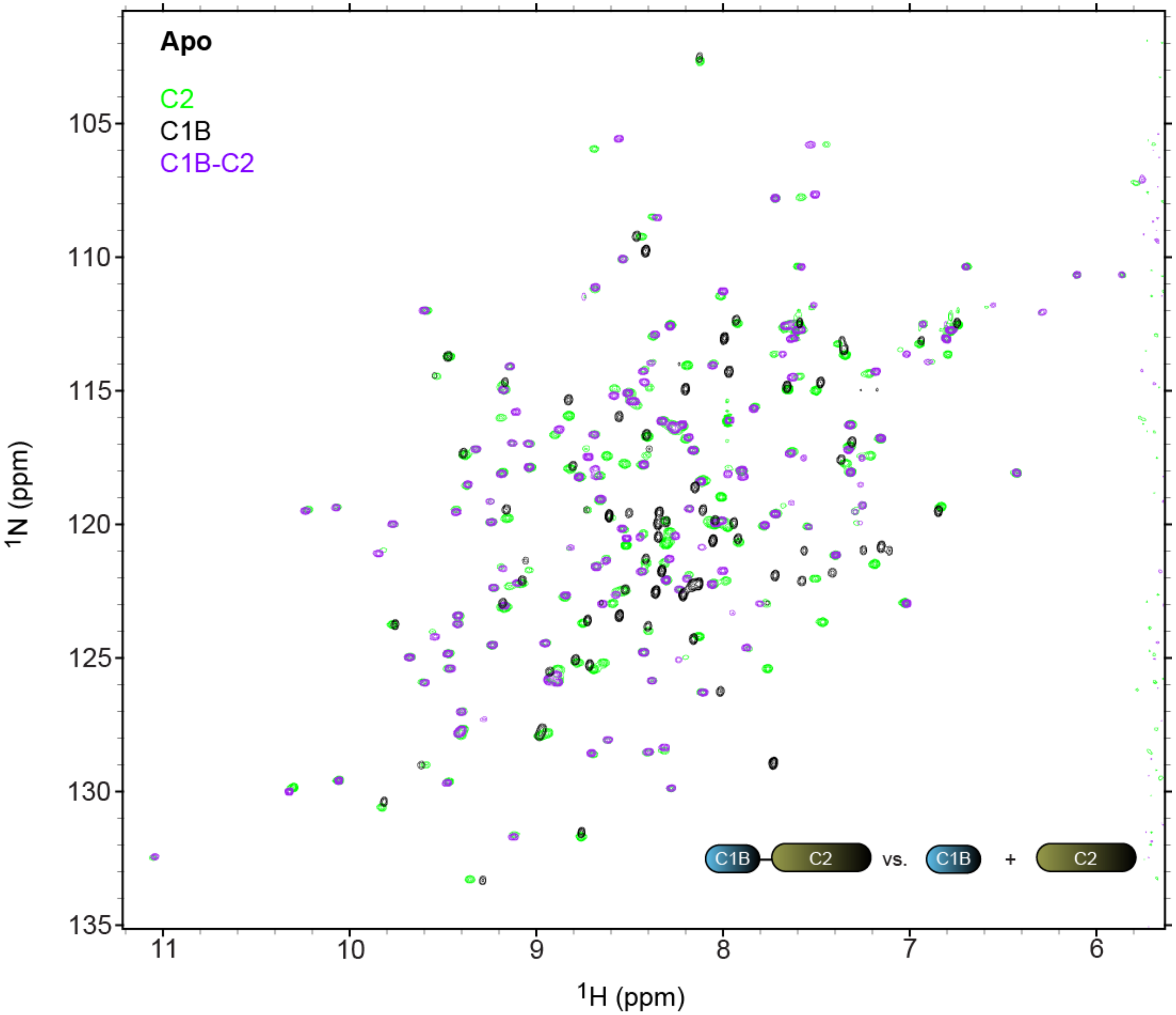

Figure 69. ^{1}H-^{15}N HSQC of apo C1B-C2 spectra overlaid with the isolated C1B 72-mer and apo C2 domains spectra collected at 600 MHz.

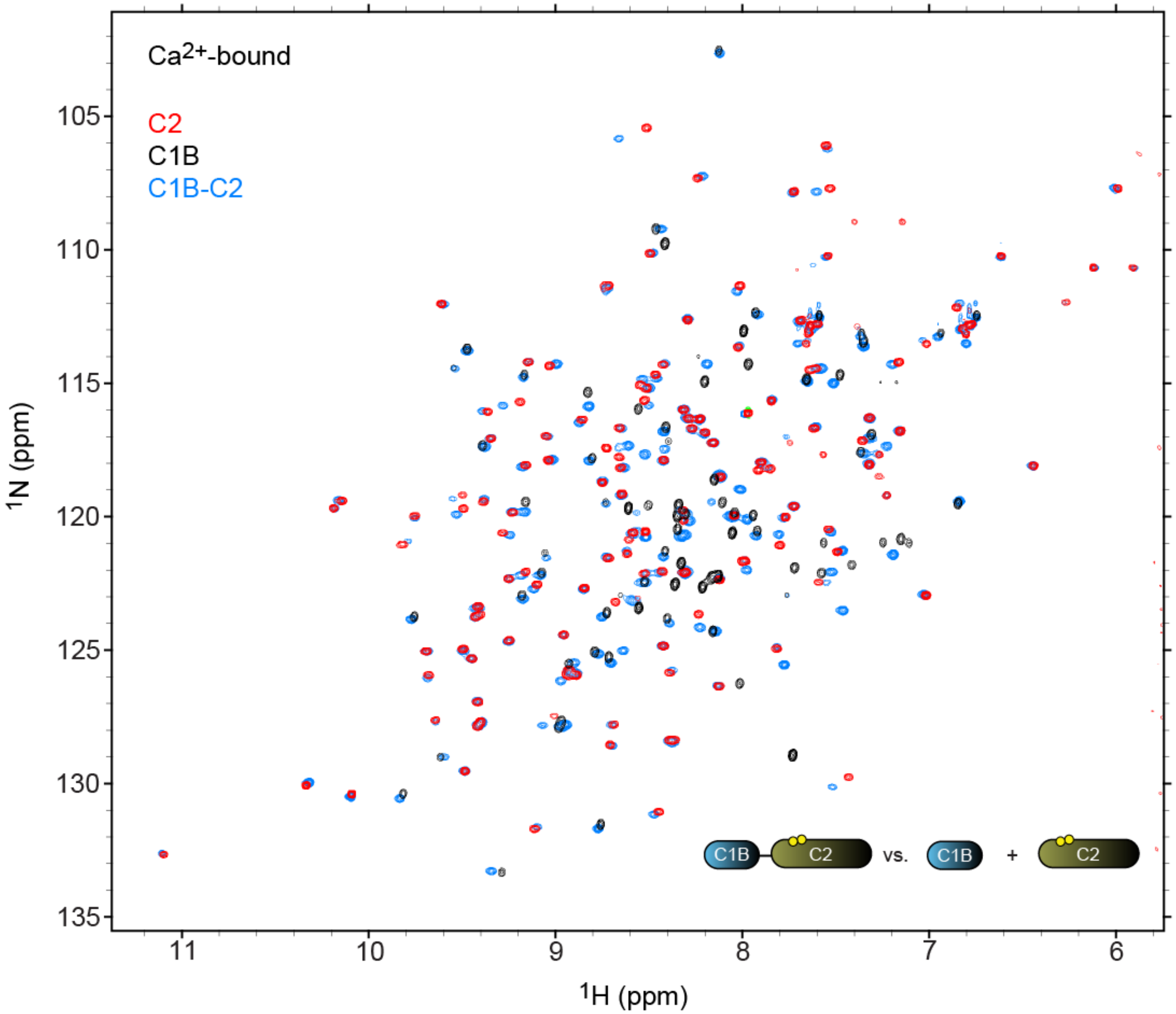

Figure 70. **^{1}H-^{15}N HSQC of Ca^{2+}-bound C1B-C2 spectra overlaid with the isolated C1B 72-mer and apo C2 domains spectra collected at 600 MHz.**

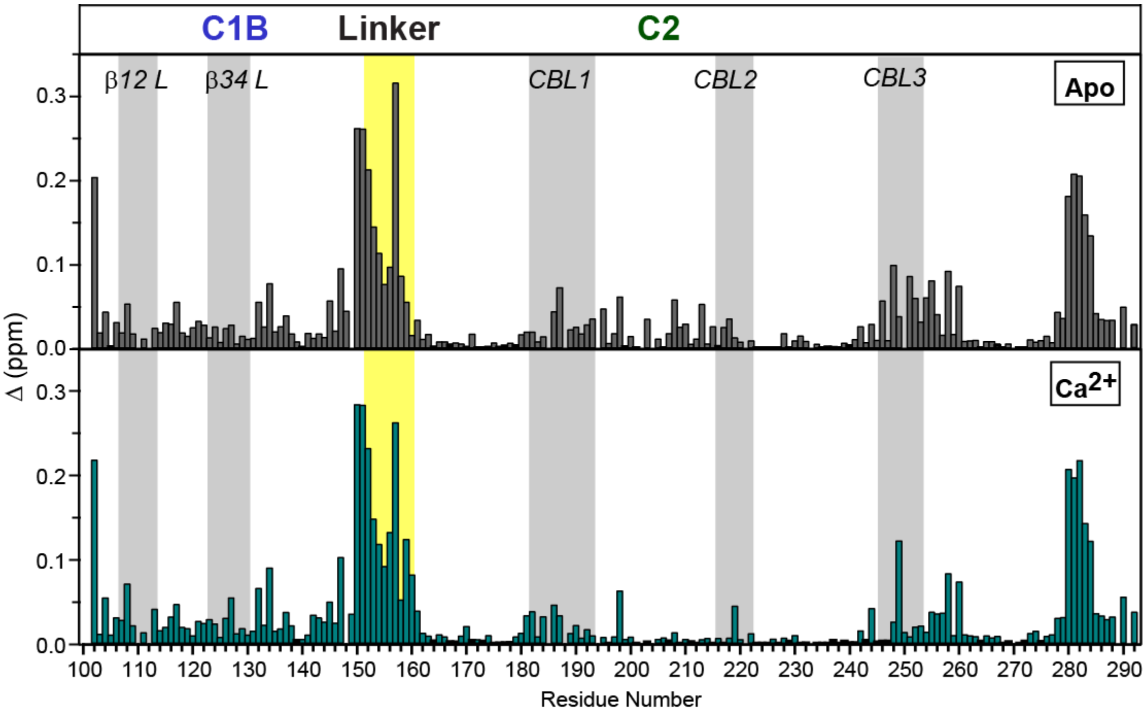

Figure 71. Chemical shift perturbations induced in the C1B-C2 construct relative to the C1B and C2 isolated domains. Δ values were calculated using Equation 10 and plotted as a function of primary structure. C1B β12 (residues 107-113) and β34 (residues 123-130) ligand binding loops located on the C1B domain are highlighted in gray. C2 Calcium-binding loops - CBL1 (residues 182-193), CBL2 (residues 216-222), and CBL3 (residues 246-253) are also highlighted in gray. The linker region between C1B and C2 is highlighted in yellow.

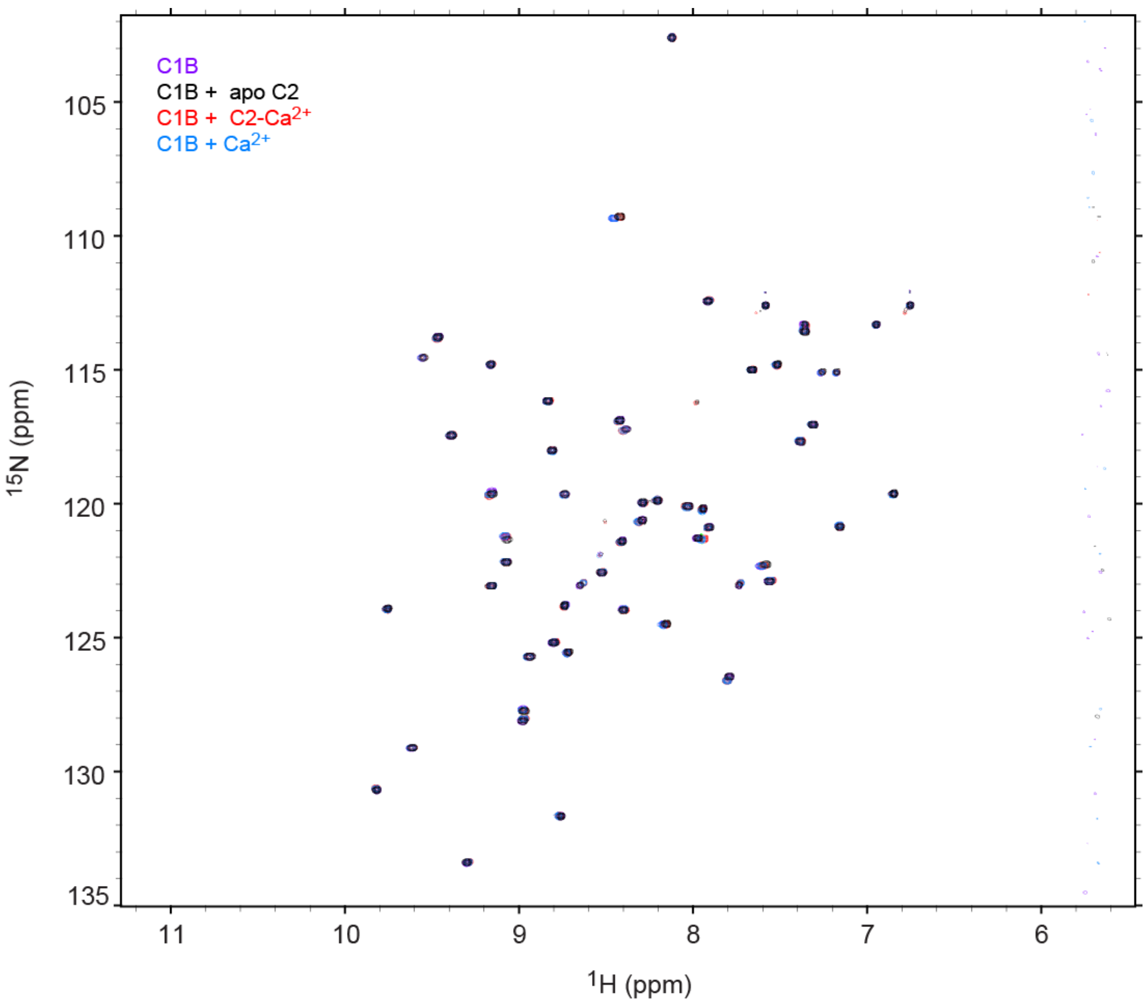

Figure 72. Probing the interactions of the isolated C1B and C2 domains. ^{1}H-^{15}N HSQC spectra of 100 µM ^{15}N labeled C1B (50-mer)[218] in the presence of 500 µM natural abundance C2 domain. The interaction was tested both in the absence (black) and presence of Ca^{2+}-bound (red) C2. The corresponding C1B reference spectra in the absence (purple) and presence of Ca^{2+} (blue) were also collected and overlaid.

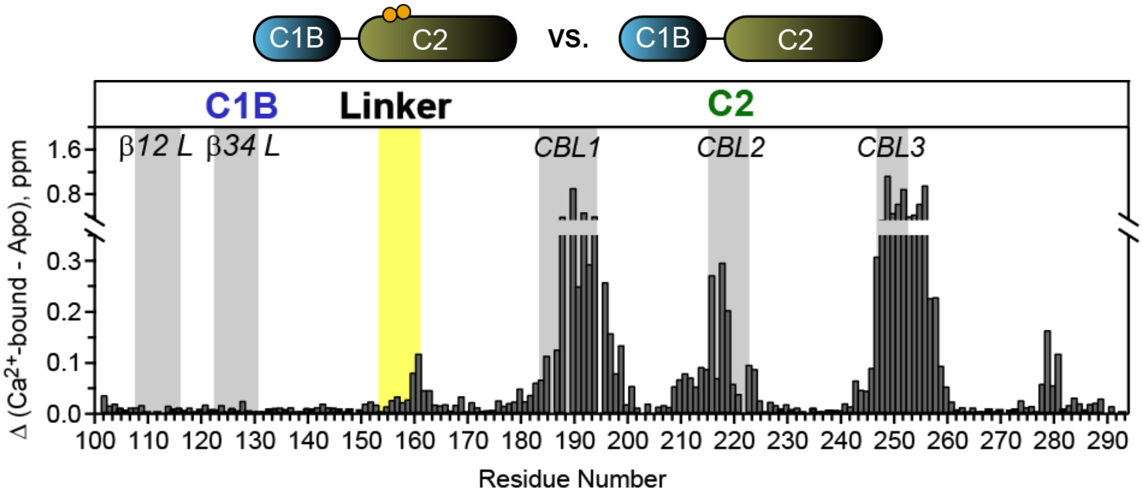

Figure 73. Chemical shift perturbations induced by Ca^{2+} binding in the C1B-C2 construct. Δ values were calculated using Equation 10 and plotted as a function of primary structure. C1B β12 (residues 107-113) and β34 (residues 123-130) ligand binding loops located on the C1B domain are highlighted in gray. C2 Calcium-binding loops - CBL1 (residues 182-193), CBL2 (residues 216-222), and CBL3 (residues 246-253) are also highlighted in gray. The linker region between C1B and C2 is highlighted in yellow. The linker region between C1B and C2 is highlighted in yellow.

Likewise, chemical shift comparison between the C1B-C2 apo and Ca^{2+}-bound states was carried out, to determine if any other regions outside the CBLs were affected by Ca^{2+}-binding in this construct. These data revealed that besides the CBLs, significant changes were observed for the C-terminal and linker regions (Figure 73). Interestingly, these were the regions that exhibited the Ca^{2+}-dependent conformational exchange in the isolated C2 domain (Chapter V). Since we know that direct Ca^{2+}-binding is not observed in this region, the changes that we are detecting might be in part induced by changes in dynamics (*vide infra*). This effect illustrated that the behavior observed in the isolated domain could also be detected in the C1B-C2 construct and highlighted once more the role of the linker region.

Crystal structure of the C1B-C2 multi-domain construct

The structural characterization was pursued in concert with the use of X-ray crystallography. The apo and Ca^{2+}-bound states were attempted; however, only the Pb^{2+}-complexed state in the presence of citrate as an additive in the crystallization condition, resulted in the formation of diffracting quality crystals. The 1.25 Å structure revealed a well-defined interface between the C1B and C2 domains that was mediated by the presence of a fourth Pb^{2+} ion, Pb(4) located at the interface of the two domains (Figure 74A and B). The interface was facilitated by two cysteine residues, C118 and C143, which were part of the conserved cysteine and histidine motifs involved in the coordination of the two structural Zn^{2+} sites in the C1 domains (Figure 74C). These two ligands were components of the first C1B Zn^{2+} site, Zn(1), and along with two citrate molecules bound to the CBLs region, contributed to the completion of the coordination sphere of Pb(4). The presence of this Pb^{2+} ion, along with the binding of citrate molecules in the CBLs region near the interface, might be the contributing factors that promoted crystal formation in the presence of Pb^{2+} over the other states attempted. Acting as a stabilizing factor of the domains, the Pb^{2+} ion and bound citrate molecules strictly influenced both the interface and relative orientation, since RMSD with respect to isolated C1B (NMR structure, PDB ID: 2ELI[227] RMSD=0.848 Å) and C2 (X-ray structure, PDB ID: 3TWY[48]=0.466 Å) domains showed no significant backbone changes.

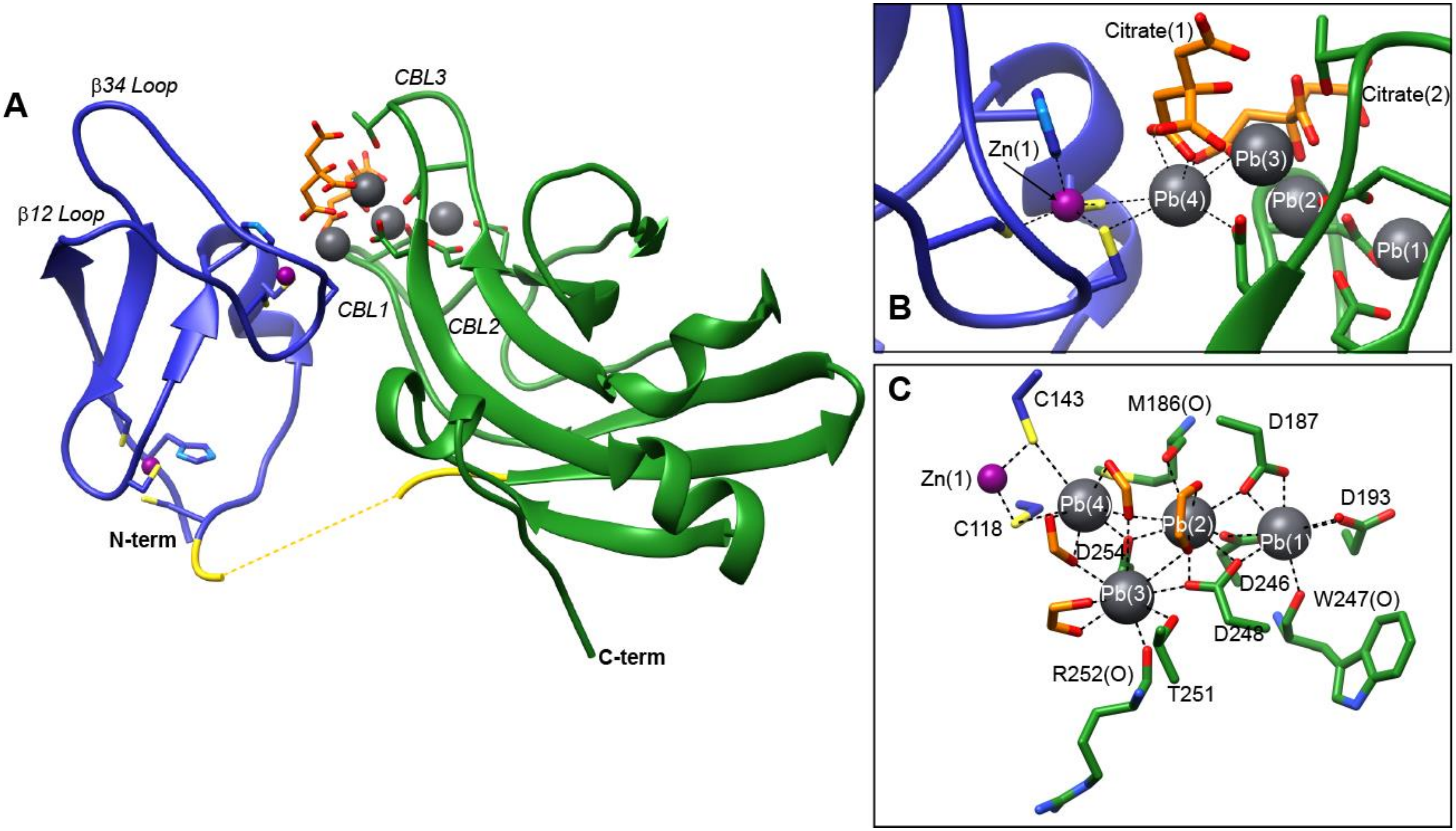

Figure 74. X-ray structure of the C1B-C2 tandem construct in complex with Pb^{2+}. (A) Ribbon representation of the C1B-C2-Pb^{2+} complex. The C1B, linker, and C2 regions are colored blue, yellow, and green, respectively. Zn^{2+} and Pb^{2+} ions are colored purple and gray respectively. Citrate molecules are shown in orange. The C1B β12 and β34 loops and C2 CBLs are identified. (B) Expansion of the C1B and C2 interface region illustrating the Zn(1) contribution to Pb(4) coordination site. (C) Top view of Pb^{2+} coordination network. For clarity purposes, only the citrate atoms involved in direct coordination of Pb^{2+} are shown.

However, despite these potential drawbacks and imposed orientation of the domains, this high resolution structure represents the highest resolution structure of a PKC C1 domain, and it will serve as a tool for the refinement of the solution conformation of the C1B-C2 construct both in the presence and absence of Ca^{2+}.

Characterization of C1B-C2 inter-domain relative orientation derived from NMR spin-relaxation data

NMR relaxation parameters were used in conjunction with the Pb^{2+}-complexed C1B-C2 structure to determine the relative orientation of the domains in solution. Relaxation rates comprising R_1, R_2, and NOE were collected for all spectrally resolved resonances in the apo and Ca^{2+}-bound states (Figure 75 and Figure 76). The spin-relaxation rates orientation dependence from the overall rotational diffusion was exploited to determine the relative orientation of the C1B and C2 domains in solution as described in the experimental procedure section. Figure 77 shows the top scored orientation consistent with the spin-relaxation data in the apo and Ca^{2+}-bound states, where an evident change in the orientation is observed. However, due to the tensor degeneracy, these oriented structures provide the first evidence of inter-domain rearrangement and will be used as the initial state for domain orientation refinement with the use of NMR PRE-based restraints. While this is not required for the proper domain orientation, it will aid the refinement stage and will serve for comparison with the rotational diffusion derived structures and inter-domain orientation influenced by crystal packing.

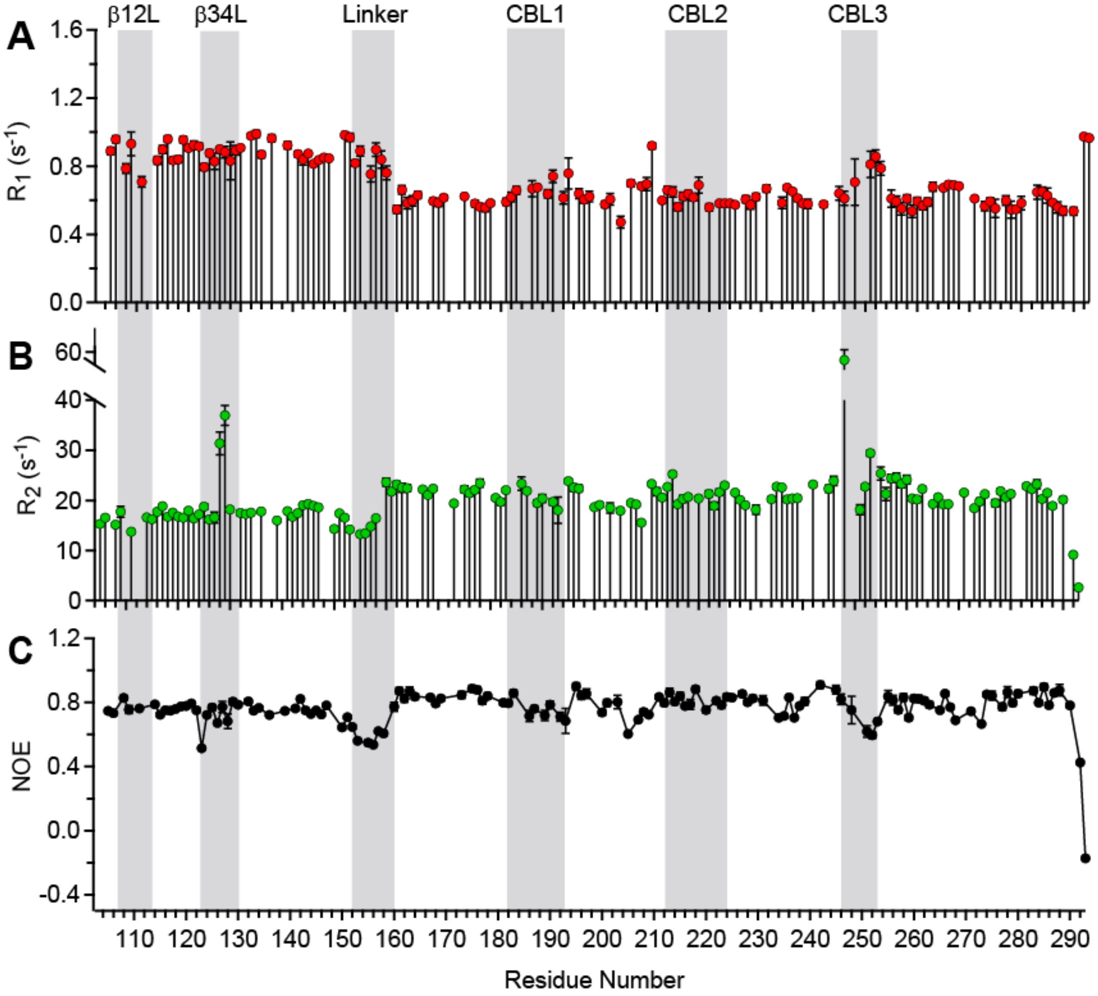

Figure 75. Apo ^{15}N C1B-C2 relaxation data comprising R_1, R_2, and NOE at 800 MHz. The CIB β12L, β13L, linker, and C2 CBLs regions are highlighted in gray.

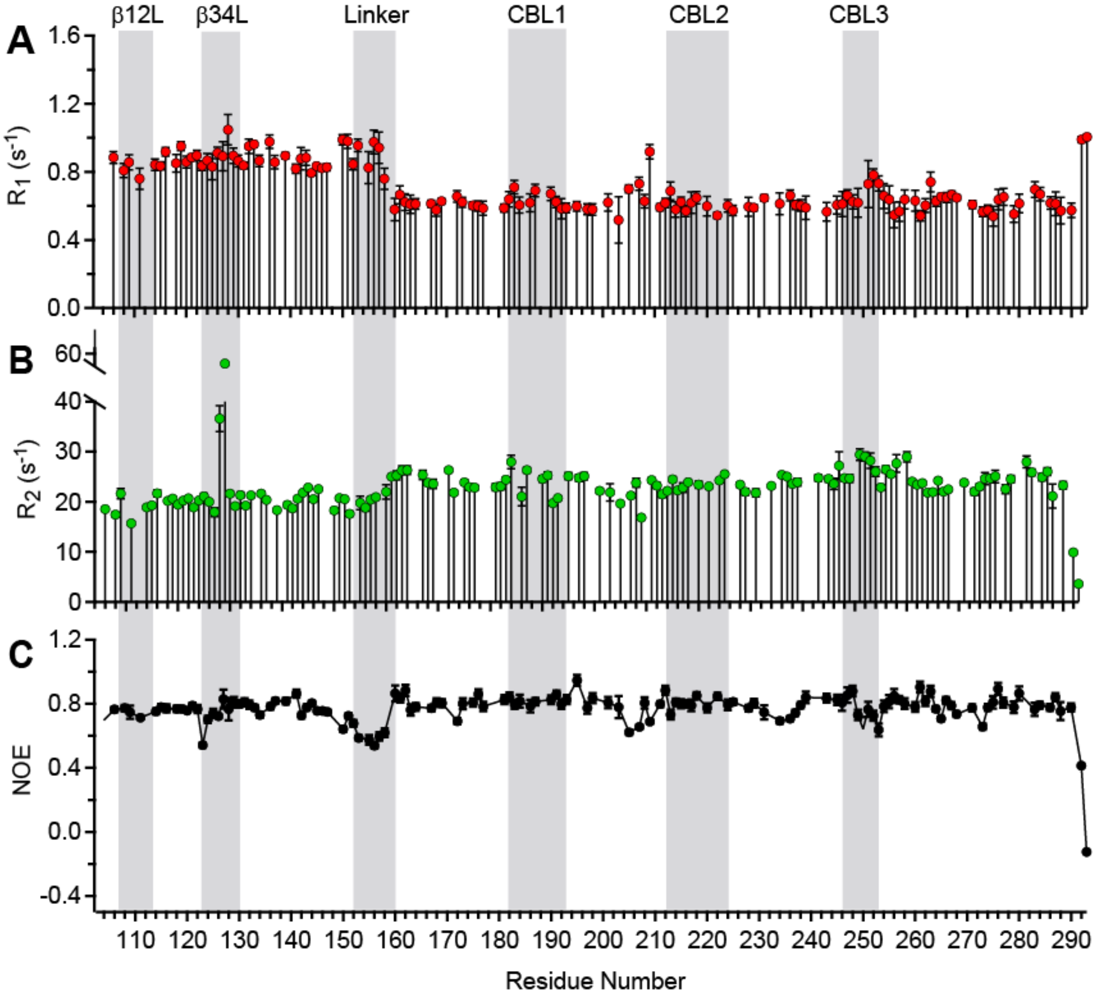

Figure 76. Ca^{2+}-bound ^{15}N C1B-C2 relaxation data comprising R_1, R_2, and NOE at 800 MHz. The CIB β12L, β13L, linker, and C2 CBLs regions are highlighted in gray.

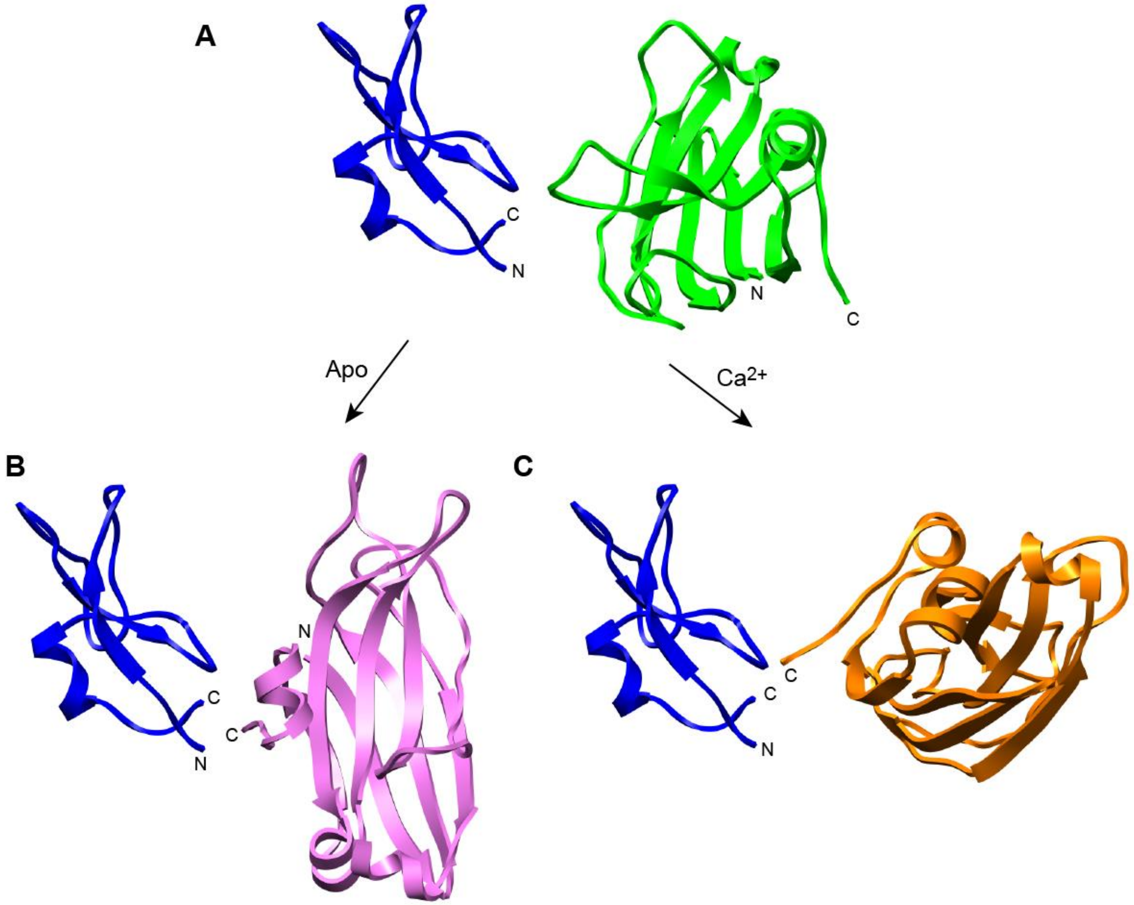

Figure 77. Solution conformations derived from the experimental rotational diffusion tensor. (A) Crystal structure of C1B-C2 complexed with Pb^{2+} represents the initial orientation as observed in the crystal structure. The linker region was removed during the orientation optimization. (B) and (C) shows the top-scored optimized orientation of C2 relative to the C1B based on the diffusion tensors obtained from the apo and Ca^{2+}-bound relaxation data, respectively. ARMOR software package was used to obtain the structures (Konstantin Berlin, University of Maryland).[225,226]

Conformational dynamics is preserved in the C1B-C2 construct

The second piece of evidence verifying that C1B and C2 domains are not independent comes from detailed inspection of the R_1 and R_2 rates measured in the C1B-C2 construct (Figure 75 and Figure 76) along with a comparison to those rates observed in the isolated domains. While there is a clear step transition between the C1B and C2 domain rates, which is indicative of some degree of freedom and independence between the two domains, the average R_2 rates obtained in the C1B-C2 construct are approximately inversely proportional to their molecular weight. The isolated C1B exhibits an average R_2 of ~5.5 s^{-1},[218] whereas as part of the C1B-C2 construct shows an average R_2 of ~20 s^{-1}. Similarly, the isolated C2 exhibits an average R_2 of ~11 s^{-1} and as part of the C1B-C2 construct, it shows average R_2 values of ~22 s^{-1}. Further estimation of the correlation times from the ratio of the transverse and longitudinal rates (R_2/R_1) using ROTDIF in the ARMOR package interface confirms these observations (Table 12). This indicates that they are in fact behaving as a larger unit, rather than each domain tumbling independently in solution, like “beads on a string”.

Table 12. Comparison of C1B and C2 correlation time estimation from NMR spin-relaxation data in the isolated and C1B-C2 construct.

Mw (kDa)		Apo	Ca^{2+}-bound
	Isolated[a]	τ_C (ns)	τ_C (ns)
5.81	**C1B**[218]	3.28 ± 0.02	/
16.22	**C2**	8.81 ±0.03	9.18 ± 0.03
	Two-domain[b]	τ_C (ns)	τ_C (ns)
22.34	**C1B**	10.44 ± 0.03	11.38 ± 0.05
22.34	**C2**	13.48 ± 0.12	14.94 ± 0.24

[a] Correlation times were estimated from the R_2/R_1 ratios using *R2R1_diffusion*.
[b] Correlation times were estimated from the R_2/R_1 ratios using the ARMOR package.

Lastly, a third piece of information can be extracted from the detailed inspection of the spin-relaxation data in the C1B-C2 construct in relation to the isolated domains. As previously described, the conformational dynamics of the isolated C2 and C1B domains was characterized in Chapter V and earlier work carried out by Stewart et al.[218] In both cases, encouraging mechanistic implications can be derived with respect to ligand binding and intra-molecular interactions. Inspection of the C1B-C2 rates (Figure 75 and Figure 76) shows the retained mobility on the C1B “QG motif” at the hinge region of the ligand binding loops, the linker, and C-terminal region of the C2 domain. As shown in Chapter V, the conformational exchange in the μs-ms time scale within the latter C2 regions is a Ca^{2+}-dependent process. Without going into full characterization of dynamics in this time-scale, information about its contribution to R_2 can be obtained by measuring the R_2 rates in the presence of full R_{ex} contribution using the Hahn-Echo (HE) experiments. Figure 78 shows a difference plot between the apo and Ca^{2+}-bound

C1B-C2 R_2^{HE} rates. Interestingly, the C1B β34 loop and the region preceding the linker showed an increase in dynamics. The linker region and the C2 domain C-terminal region showed an increase in dynamics as well. The fact that we observed this behavior in C1B-C2 provides evidence that the conformational dynamics is also present in the C1B-C2 construct. Future quantitation of these will serve for direct comparison of dynamics changes that are induced in the C1B-C2 domain construct relative to the isolated domains, and will provide the first evidence of conformational dynamics changes within the regulatory domain of PKC.

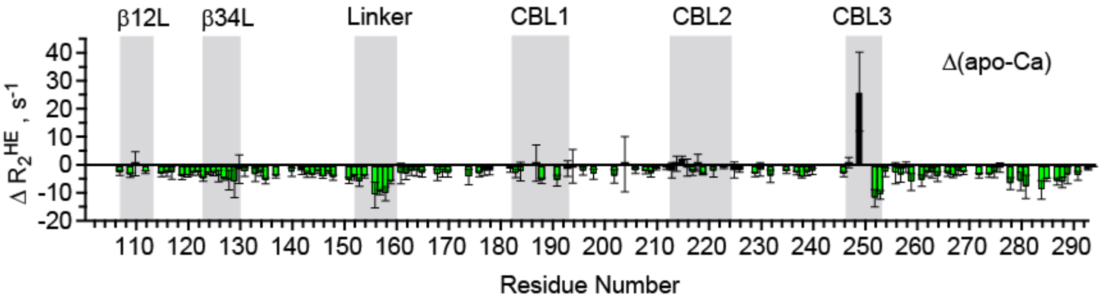

Figure 78. R_2^{HE} difference plot of rates between the Apo and Ca^{2+}-bound C1B-C2. The CIB β12L, β13L, linker, and C2 CBLs regions are highlighted in gray.

Discussion of results

The work presented in this chapter aims to overcome the biophysical challenges associated with probing multi-domain proteins arrangements; yet, it considered and exploited the valuable information gained from the study of the functional isolated domains. High resolution crystal structures have provided atomic-level details of ligand recognition sites and binding surfaces for high affinity complexes from which mechanistic information has been derived. However, crystal packing forces in multi-domain proteins have shown their ability to impose severe domain orientations and arrangements, that in most cases result in conformations that are not observed in solution.[228,229] Therefore, the functional characterization of multi-modular proteins ultimately requires the characterization of both, the structure and dynamic properties of its components in the free and complexed states. More importantly, it should also incorporate characterization of the conformational flexibility and involvement of the linker region connecting the functional domains.

In this chapter, a combination of the full atom description from X-ray crystallography and solution NMR techniques were implemented. This combination allowed for the characterization of intra-domain interactions, conformational flexibility, and arrangements induced by Ca^{2+} binding to the regulatory domain of PKCα without having to undertake a full *de novo* structure determination using NMR. This was carried out in the context of a two-domain construct comprised of the C1B and C2 domains, C1B-C2, connected by the native 9 amino acids linker. This construct will report on the interplay between the lipid recognition modules of PKCα upon Ca^{2+} binding during the first step of activation. The data presented corresponds to the characterization of the structure and dynamics of this construct. The understanding of these aspects are fundamental for the interpretation and subsequent determination of the solution orientations in the apo and Ca^{2+}-bound states, using NMR-PRE derived restraints.

First, the presence of significant chemical shift perturbation changes in the C1B-C2 construct with respect to the isolated domains revealed an important aspect of this multi-domain system, which is that these domains do not behave as fully independent modules in solution. Furthermore, the large changes detected for the linker region indicated the potential involvement of this segment in the domain rearrangement induced by Ca^{2+}-binding to the C2 region (Figure 73). These observations were further confirmed with ^{15}N spin-relaxation measurements. The R_1 and R_2 rates evaluation as a function of C1B-C2 primary sequence showed a noticeable transition between the C1B and C2 domains (Figure 75 and Figure 76). However, the rates corresponded to modules tumbling together as a significantly larger unit when compared to the rates observed for the isolated domains (for C1B refer to Stewart et al.[218] and for C2 see Chapter V). In fact, the correlation times estimated from the ratio (R_2/R_1) indicate that C1B and C2 domains tumble nearly together with an average τ_c in the apo and Ca^{2+}-bound states of ~ 11 ns (~18 kDa) and ~ 13 ns (~ 22.3 kDa), respectively in the C1B-C2 construct (22.3 kDa).

Furthermore, detailed contrast of C1B-C2 ^{15}N spin-relaxation rates in the apo and Ca^{2+}-bound states, showed the presence of significant contributions of chemical exchange in the μs-ms timescale associated with Ca^{2+}-binding to C2. These observations were confirmed with the use of Hahn-Echo relaxation experiments, in which R_2 rates were measured in the presence full dynamic contributions on this timescale. The difference between the apo and Ca^{2+}-bound R_2^{HE} rates indicated an increase for the C1B domain, the linker segment, and C2 C-terminal regions in the Ca^{2+}-

bound state (Figure 78). The latter two corresponded to the regions where a Ca^{2+}-dependent increase was also observed for the isolated C2 domain construct (Chapter V). Of particular interest is the C-terminal region, which has recently been implicated in intra-domain interactions with the upstream C1A domain.[40] Intriguingly, a molecular dynamics (MD) simulations study carried out in the isolated C2 domain from PKCβ also revealed substantial motions in this region and hydrogen bonding changes in this region associated with the binding of Ca^{2+} ions.[197] On the other hand, the dynamic changes observed in the linker region emphasized once more the potential role of this segment in communicating the Ca^{2+}-binding event to other regulatory domains within PKCα as well as potentially triggering the dissociation of intra-domain interactions in the first step of activation. Interestingly, the linker segment is conserved within cPKC isoforms and could represent another isoform-specific regulatory and communication element since in nPKCs the regulatory domain swap positions with the C2-like module as the first domain in the regulatory region (Figure 1). At this stage, full dynamic characterization on the μs-ms timescale is needed to quantitatively compare the potential interplay between C1B and C2 dynamics with respect to Ca^{2+}-binding and subsequent membrane binding. However, the divide and conquer approach taken in this study proved to be the best way to disentangle and identify the origins of conformational dynamics that are observed in the C1B-C2 construct.

The dependence of the ^{15}N relaxation rates measurement with respect to the diffusion tensor was further exploited to provide information of the relative domain orientation in solution. The analysis provided the orientations consistent with the NMR spin-relaxation data. The degeneracy of the diffusion tensor precludes the use of additional restraints (*vide infra*) for unambiguous domain orientation; however, the obtained orientation obtained in the apo differs from that observed in the Ca^{2+}-bound states. These provided the first physical evidence of domain rearrangement induced by Ca^{2+}-binding.

As described, the domain orientation derived from spin-relaxation data used the C1B-C2 in complex with Pb^{2+} structure as the initial orientation state (Figure 77). While potential crystal packing forces and Pb^{2+}-assisted interface between the C1B and C2 domains is very likely, this is yet to be confirmed using the PRE-NMR based restraints (*vide infra*). We previously showed that Pb^{2+} favors high coordination number spheres (Chapter II); thus the attachment of the two domains could be favored by this property of Pb^{2+} coordination chemistry. Nevertheless, the structure represents the highest resolution structure (1.24 Å) for a PKC C1 domain, and it could also represent the "poisoned" state of the domains in the presence of Pb^{2+}. Curiously, the observed domain orientation resembles the C1B and C2 orientation of a model proposed by Sutton et al.,[230] in which the C1B domain completes the coordination of the third Ca^{2+} ion in the PKCβ C2 domain.

In multi-modular proteins, selectivity is conferred by the collective contribution of each module membrane interaction mode in addition to domain shielding via intra-domain interactions that stabilize the inactive state by blocking the ligand binding sites. For this reason, the domain attachment effects in the enzyme Ca^{2+} requirements and membrane binding affinity will require further characterization. Biochemical data suggests that there is in fact an additive effect in membrane binding of the full-length enzyme when compared to the isolated domains.[38,73] If the domains are completely independent, the physical attachment should still induce a restricted local diffusion thereby generating a synergistic binding to the membrane as has been observed for other multi-modular proteins.[228,229] Therefore, we do expect a significant influence from the linker region. The short linker span, chemical shift perturbation and relatively restricted motions of this segment as judged by the moderately high NOE values supports this scenario (Figure 75C and Figure 76C).

The only other PKC structural information available regarding the interactions and relative orientation of the domains comes from the crystal structure of the full length PKCβII isoform.[72] However, in the captured conformation, the C2 is prominently involved in lattice stabilizing interactions with the catalytic domain at two different regions, one involving the catalytic domain from another PKC molecule. [72] In addition, the structure was solved in the presence of Ca^{2+}-bound C2, which altogether emerge into the arrest of an intermediate state in the activation pathway.[72] Moreover, there is missing density for the pseudosubstrate, C1A domain, and linker regions between C1B and C2 as well as the region between the C2 and catalytic domains (V3 linker segment). Small angle X-ray scattering (SAXS) used in combination with X-ray crystallography can generate accurate description of large and multi-modular complexes. However, the envelope generated by SAXS does not always account for the placement and fit of all present domains. This was the case for the full-length PKCβII structure: The envelope did not account for the position of all domains inside the envelope, yet it did show a lack of interaction between C2 and catalytic domains and it positioned the C2 domain in a conformation distant from the rest of the domains and readily available to interact with membranes.[72] Hence, the approach taken in this study, will represent the first attempt to characterize the domain rearrangement induced by Ca^{2+}-binding to the regulatory domain of PKCα, with a clean C2 metal-bound state.

The information about dynamics and domain orientation derived from the relaxation parameters forms the basis for further characterization of the C1B-C2. Specifically, this information will be used for the design, selection, and interpretation of the PRE-based orientation method that is currently being implemented. PRE provides long-range restraints (~15-35Å)[231], which are required for large multi-domains proteins and together with the C1B-C2 structure solved in this study, will avoid the need of NMR *de novo* structure determination. The existing data provides information about the potential interface between the domains, dynamic regions, and the top scored preferred orientation in solution, which will allow the strategic selection of the paramagnetic tag locations. The mutagenesis approach involves the incorporation of single cysteine mutants located at different regions throughout the C2 domain surface for subsequent modification with the 3-(2-Iodoacetamido)-PROXYL paramagnetic tag (Figure 79). The mutation sites were generated based on the thorough mutagenesis study carried out by Kohout et al.[56] These sites correspond to surface-exposed residues that were shown to have minimal effects on C2 Ca^{2+} affinity and membrane binding association.[56] As mentioned earlier, in multi-domain systems, the high specificity and affinity of the host enzyme functional interactions are not only dictated by the recognition mechanisms of each module but also the conformational flexibility. The data presented in this chapter along with the proposed ongoing work will provide insights into the functional interplay and flexibility of the regulatory domain of PKCα.

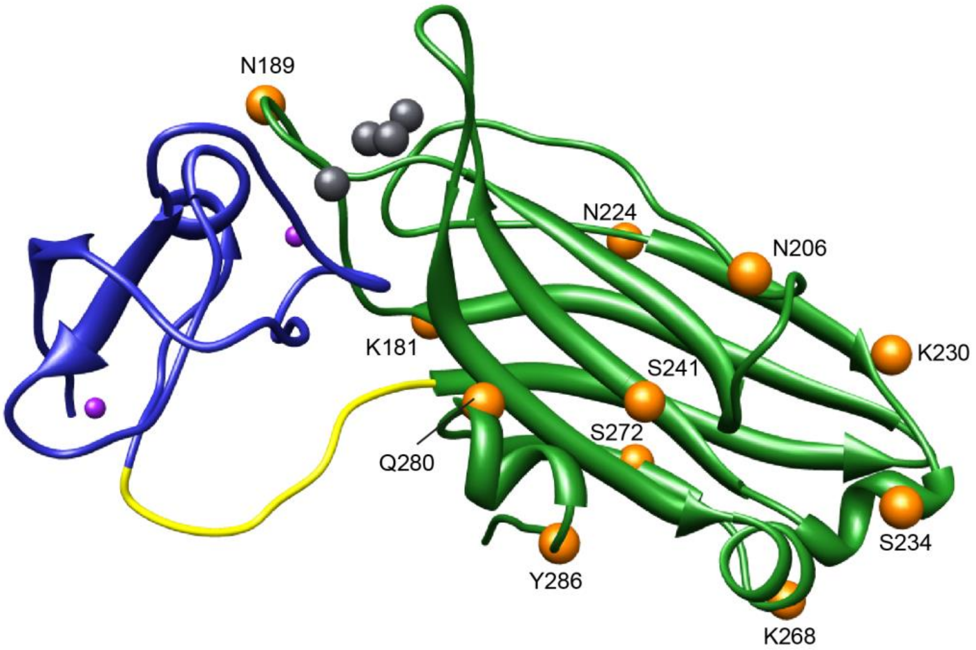

Figure 79. C1B-C2 cysteine mutagenesis strategy for paramagnetic PROXYL tag attachment.

CHAPTER VII

CONCLUSIONS AND FUTURE DIRECTIONS

The work conducted in this dissertation used C2α as a paradigm to understand the structural, functional and mechanistic role of metal ions in membrane-anchoring domains. The C2 domain is involved in the first step of cPKC isoforms activation. Therefore, the regulatory function of the C2 domain represents an important mechanistic step. Furthermore, PKCα has been identified as an important molecular target in Pb^{2+} poisoning. It was hypothesized that two out of three Pb^{2+} binding sites proposed in the full-length PKCα reside in its C2 domain (C2α).

The studies carried out in Chapters II and III focused on the characterization of Pb^{2+} effects on the structure and membrane-binding properties of C2α. These revealed different aspects that contribute to the potency of Pb^{2+} as Ca^{2+} surrogate. First, Pb^{2+} was shown to bind C2α with an affinity three orders of magnitude higher to the first metal-binding site within C2α (Pb1). This produced a 2,000-fold difference in affinity between the two Pb^{2+} sites (Pb1 and Pb2). Moreover, Pb^{2+} binding to the high affinity site dramatically modulated the binding of Ca^{2+} to the second metal-site by decreasing the affinity for Ca^{2+} ~ 50-fold. This highlights the potency of Pb^{2+} as a modulator of Ca^{2+}-dependent function since displacement and/or the formation of a Pb^{2+}/Ca^{2+} mixed species is very unlikely under physiological Ca^{2+} conditions.

Pb^{2+} was also able to drive C2α association with PtdSer-containing membranes nearly as efficient as Ca^{2+}, and it was capable of displacing Ca^{2+} from the C2α-Ca^{2+}-

membrane complex. Moreover, Pb^{2+} can significantly associate with PtdSer-containing membranes, consequently competing with C2α for PtdSer binding sites at the membrane even at low concentrations. These two aspects showed both the potency of Pb^{2+} to act as a Ca^{2+} surrogate and its indirect ability to affect C2α membrane-association.

In Chapter III,[69] it was demonstrated how the incorporation of PIP_2 component increased Pb^{2+} potency by influencing two aspects of C2α-Pb^{2+}-membrane interactions: the intrinsic affinity of C2α for Pb^{2+} and the competitive association of Pb^{2+} with the anionic sites on the membrane. This research defined the combined effect these factors have on the aberrant activation of PKCα, which contributes to the toxic effect of Pb^{2+}.

A comparison of the apo and Pb^{2+}-bound structures showed a lack of significant structural changes induced by metal-binding. However, the two Pb^{2+} ions adopted different coordination geometries, holodirected and hemidirected, in contrast to Ca^{2+} where both were holodirected. Interestingly, this geometry did not affect C2α-Pb^{2+} membrane interactions. The most striking difference was observed in C2α interactions with Cd^{2+}, described in Chapter IV. Cd^{2+} also binds C2α with higher affinity than Ca^{2+}. However, while Cd^{2+} adopts an identical coordination geometry to that observed for Ca^{2+}, it is unable to drive C2α to associate with PtdSer-containing membranes. This work, together with C2-Pb^{2+} interactions suggested a mechanism in which membrane association was coupled with an expansion of the metal coordination number. As demonstrated, this was dictated by the identity and ligand coordination capabilities of each metal ion.

Chapters II-IV provided the first direct evidence for the specific role of divalent metal ions in mediating protein-membrane interactions. This work also has important implications for biophysical metal substitution studies in proteins. This is critical for cases where the metal-ion plays a direct functional role other than a structural role. Lastly, this work illustrates how different toxic metal ions can generate opposite functional responses. C2 domains are independently folded Ca^{2+}-sensors ubiquitously found in many enzymes. Therefore, these results also stimulate the investigation of heavy metal-ions effects in other C2 domain-containing proteins that have been identified as important molecular targets of Pb^{2+} and Cd^{2+}.

Next, the lack of significant structural rearrangements associated with metal-binding to C2 domains has become more evident with the increased number of X-ray and NMR structures. The work carried out in Chapters II-IV showed no significant structural changes between C2α apo and metal-bound states. However, elevated B-factors are observed for the CBLs in the apo·C2α crystal structure. Moreover, C2α metal-binding induces chemical shift perturbations at the C-terminus, which is far in space from the CBLs region. This work stimulated the characterization of C2α metal-dependent conformational dynamics described in Chapter V. Chapter V represents the first full dynamic characterization of a Ca^{2+}-dependent C2 domain covering sub-nanosecond to millisecond timescales. Interestingly, metal-binding resulted in a concerted change of millisecond dynamics at C2α N- and C-terminal regions. These regions corresponded to the interface that was recently implicated in intra-domain interactions with the upstream C1A domain. Elimination of one hydrogen bond at the

N-terminal region by means of the C2α R159G mutation "uncoupled" the concerted change between the CBLs and the N- and C-terminal regions. Furthermore, the R159G mutant showed an increase in the rate of conformational exchange. Intriguingly, the rate of exchange also increased when the metal-sites are progressively occupied. Together, these findings suggest a possible mechanism for propagating the information about the metal-binding event to other domains of PKCα in which the C2α metal-saturation state "tunes" the response.

The observed conformational changes induced by the single high affinity Pb^{2+} site provides evidence that at low concentrations Pb^{2+} could induce changes in intra-domain interactions that will lead to higher enzyme activity. Additionally, the C2α Pb^{2+} saturated state can also be exploited to observe the CBLs dynamics changes when a hemidirected geometry and changes in bi-dentate ligands are imposed by Pb2 binding. The lack of full coordination could allow higher mobility particularly for CBL1 due to the absence of M186 coordination to Pb2. This could provide insight into the lower affinity of metal-ions for the second site.

The potential Ca^{2+} sensing capabilities "tuned" by conformational dynamics in C2 domains will need further exploration. However, this information establishes the foundation for future characterization and comparison of Ca^{2+}-affinity in the R159G C2α mutant versus wt C2α. In addition, the N-terminal region connects C2 to the preceding regulatory module C1B, in full-length PKC. Thus the C1B-C2 linker region could serve as a tuning and communication mechanism. These studies can also be extended to longer constructs including the addition, for example, of the C1A and C1B and C2 domains together.

Chapter VI reports the investigation of intra-domain rearrangement induced by Ca^{2+}-binding in the regulatory region of PKCα. This was carried out in the context of a two-domain construct C1B-C2, comprising the C1B and C2 domains. Preliminary structural and dynamical characterization showed that the C1B and C2 domains do not behave as individual independent domains in C1B-C2 construct and that an inter-domain rearrangement in the presence of Ca^{2+} is plausible. The next step involves the characterization of the inter-domain rearrangements induced by Ca^{2+} using NMR-derived PRE restraints. Furthermore, the success of these studies in solution will provide the foundation for the characterization of C1B-C2 geometry in the presence of a membrane-mimicking environment such as micelles or bicelles.

Direct domain-domain contacts or conformational dynamics of the linker region could also influence C2 affinity for Ca^{2+} and/or C1B affinity for membranes. Future experiments should also involve the characterization of C2 Ca^{2+}-affinity and membrane interactions in the context of the C1B-C2 construct. This may elucidate the influence of physical attachment effects in the membrane association event of C1B and C2. Noteworthy is the complexity of the system both in terms of function and the dynamic properties of each domain. Therefore, the “divide and conquer” approach promises to be the best way to build the full regulatory region and identify the origins of the metal-induced dynamics and of domain rearrangement in the C1B-C2 construct and larger constructs as well. Together, these findings contribute to the detailed molecular picture of cPKC activation that can be used to discover agents that can act as isoform specific-modulators for both research and clinical purposes. These findings can also be extrapolated to elucidate the specific role of metal-binding function in other C2 domain-containing proteins. Finally, this work delineates new mechanisms by which heavy metal ions interfere with the membrane interactions of metal-binding proteins.

REFERENCES

(1) Newton, A. C. *Am J Physiol Endocrinol Metab* **2010**, *298*, E395.

(2) Steinberg, S. F. *Physiol Rev* **2008**, *88*, 1341.

(3) Dempsey, E. C.; Newton, A. C.; Mochly-Rosen, D.; Fields, A. P.; Reyland, M. E.; Insel, P. A.; Messing, R. O. *Am J Physiol Lung Cell Mol Physiol* **2000**, *279*, L429.

(4) Castagna, M.; Takai, Y.; Kaibuchi, K.; Sano, K.; Kikkawa, U.; Nishizuka, Y. *J Biol Chem* **1982**, *257*, 7847.

(5) Blumberg, P. M.; Jaken, S.; Konig, B.; Sharkey, N. A.; Leach, K. L.; Jeng, A. Y.; Yeh, E. *Biochem Pharmacol* **1984**, *33*, 933.

(6) Battaini, F.; Mochly-Rosen, D. *Pharmacol Res* **2007**, *55*, 461.

(7) Mazzei, G. J.; Girard, P. R.; Kuo, J. F. *FEBS Lett* **1984**, *173*, 124.

(8) Speizer, L. A.; Watson, M. J.; Kanter, J. R.; Brunton, L. L. *J Biol Chem* **1989**, *264*, 5581.

(9) Tomsig, J. L.; Suszkiw, J. B. *J Neurochem* **1995**, *64*, 2667.

(10) Sun, X.; Tian, X.; Tomsig, J. L.; Suszkiw, J. B. *Toxicol Appl Pharmacol* **1999**, *156*, 40.

(11) Suszkiw, J. B. *Neurotoxicology* **2004**, *25*, 599.

(12) Ali, A. S.; Ali, S.; El-Rayes, B. F.; Philip, P. A.; Sarkar, F. H. *Cancer Treat Rev* **2009**, *35*, 1.

(13) Konopatskaya, O.; Poole, A. W. *Trends Pharmacol Sci* **2010**, *31*, 8.

(14) Reyland, M. E. *Front Biosci* **2009**, *14*, 2386.

(15) Nelson, T. J.; Sun, M. K.; Hongpaisan, J.; Alkon, D. L. *Eur J Pharmacol* **2008**, *585*, 76.

(16) Geraldes, P.; King, G. L. *Circ Res* **2010**, *106*, 1319.

(17) Palaniyandi, S. S.; Sun, L.; Ferreira, J. C.; Mochly-Rosen, D. *Cardiovasc Res* **2009**, *82*, 229.

(18) Ferreira, J. C.; Mochly-Rosen, D.; Boutjdir, M. *Front Biosci* **2012**, *4*, 532.

(19) de Barry, J.; Liegeois, C. M.; Janoshazi, A. *Exp Gerontol* **2010**, *45*, 64.

(20) Sun, M. K.; Alkon, D. L. *Pharmacol Ther* **2010**, *127*, 66.

(21) Zhang, D.; Anantharam, V.; Kanthasamy, A.; Kanthasamy, A. G. *J Pharmacol Exp Ther* **2007**, *322*, 913.

(22) Abrial, E.; Lucas, G.; Scarna, H.; Haddjeri, N.; Lambas-Senas, L. *Mol Neurobiol* **2011**, *44*, 407.

(23) Zarate, C. A.; Manji, H. K. *CNS Drugs* **2009**, *23*, 569.

(24) Irie, K.; Yanagita, R. C.; Nakagawa, Y. *Med Res Rev* **2012**, *32*, 518.

(25) Leskow, F. C.; Krasnapolski, M. A.; Urtreger, A. J. *Curr Pharm Biotechnol* **2011**, *12*, 1961.

(26) Mochly-Rosen, D.; Das, K.; Grimes, K. V. *Nat Rev Drug Discov* **2012**, *11*, 937.

(27) Agency for Toxic Substance and Disease Registry (ATSDR), **2011**. US Department of Health and Human Services, Public Health Service, Atlanta, GA, USA.

(28) Takai, Y.; Kishimoto, A.; Inoue, M.; Nishizuka, Y. *J Biol Chem* **1977**, *252*, 7603.

(29) Inoue, M.; Kishimoto, A.; Takai, Y.; Nishizuka, Y. *J Biol Chem* **1977**, *252*, 7610.

(30) Takai, Y.; Kishimoto, A.; Iwasa, Y.; Kawahara, Y.; Mori, T.; Nishizuka, Y. *J Biol Chem* **1979**, *254*, 3692.

(31) Parissenti, A. M.; Kirwan, A. F.; Kim, S. A.; Colantonio, C. M.; Schimmer, B. P. *J Biol Chem* **1998**, *273*, 8940.

(32) Lemmon, M. A. *Nat Rev Mol Cell Biol* **2008**, *9*, 99.

(33) Brodie, C.; Blumberg, P. M. *Apoptosis* **2003**, *8*, 19.

(34) Medkova, M.; Cho, W. *J Biol Chem* **1998**, *273*, 17544.

(35) Bolsover, S. R.; Gomez-Fernandez, J. C.; Corbalan-Garcia, S. *J Biol Chem* **2003**, *278*, 10282.

(36) Medkova, M.; Cho, W. *J Biol Chem* **1999**, *274*, 19852.

(37) Oancea, E.; Meyer, T. *Cell* **1998**, *95*, 307.

(38) Johnson, J. E.; Giorgione, J.; Newton, A. C. *Biochemistry* **2000**, *39*, 11360.

(39) Evans, J. H.; Murray, D.; Leslie, C. C.; Falke, J. J. *Mol Biol Cell* **2006**, *17*, 56.

(40) Stahelin, R. V.; Wang, J.; Blatner, N. R.; Rafter, J. D.; Murray, D.; Cho, W. *J Biol Chem* **2005**, *280*, 36452.

(41) Hurley, J. H.; Newton, A. C.; Parker, P. J.; Blumberg, P. M.; Nishizuka, Y. *Protein Science* **1997**, *6*, 477.

(42) Zhang, G.; Kazanietz, M. G.; Blumberg, P. M.; Hurley, J. H. *Cell* **1995**, *81*, 917.

(43) Cho, W.; Stahelin, R. V. *Biochim Biophys Acta* **2006**, *1761*, 838.

(44) Nalefski, E. A.; Falke, J. J. *Protein Science* **1996**, *5*, 2375.

(45) Nishizuka, Y. *Nature* **1988**, *334*, 661.

(46) Stahelin, R. V.; Digman, M. A.; Medkova, M.; Ananthanarayanan, B.; Melowic, H. R.; Rafter, J. D.; Cho, W. *J Biol Chem* **2005**, *280*, 19784.

(47) Chen, L.; Hahn, H.; Wu, G.; Chen, C. H.; Liron, T.; Schechtman, D.; Cavallaro, G.; Banci, L.; Guo, Y.; Bolli, R.; Dorn, G. W., 2nd; Mochly-Rosen, D. *Proc Natl Acad Sci U S A* **2001**, *98*, 11114.

(48) Morales, K. A.; Lasagna, M.; Gribenko, A. V.; Yoon, Y.; Reinhart, G. D.; Lee, J. C.; Cho, W.; Li, P.; Igumenova, T. I. *J Am Chem Soc* **2011**, *133*, 10599.

(49) Essen, L. O.; Perisic, O.; Katan, M.; Wu, Y.; Roberts, M. F.; Williams, R. L. *Biochemistry* **1997**, *36*, 1704.

(50) Murray, D.; Honig, B. *Mol Cell* **2002**, *9*, 145.

(51) Edwards, A. S.; Newton, A. C. *Biochemistry* **1997**, *36*, 15615.

(52) Verdaguer, N.; Corbalán-García, S.; Ochoa, W. F.; Fita, I.; Gómez-Fernández, J. C. *Embo Journal* **1999**, *18*, 6329.

(53) Stensman, H.; Larsson, C. *J Biol Chem* **2007**, *282*, 28627.

(54) Bittova, L.; Stahelin, R. V.; Cho, W. *J Biol Chem* **2001**, *276*, 4218.

(55) Slater, S. J.; Ho, C.; Kelly, M. B.; Larkin, J. D.; Taddeo, F. J.; Yeager, M. D.; Stubbs, C. D. *J Biol Chem* **1996**, *271*, 4627.

(56) Kohout, S. C.; Corbalán-García, S.; Gómez-Fernández, J. C.; Falke, J. J. *Biochemistry* **2003**, *42*, 1254.

(57) Shao, X.; Fernandez, I.; Südhof, T. C.; Rizo, J. *Biochemistry* **1998**, *37*, 16106.

(58) Torrecillas, A.; Laynez, J.; Menéndez , M.; Corbalán-García, S.; Gómez-Fernández , J. C. *Biochemistry* **2004**, *43*, 11727.

(59) Guerrero-Valero, M.; Ferrer-Orta, C.; Querol-Audi, J.; Marín-Vicente, C.; Fita, I.; Gómez-Fernández, J. C.; Verdaguer, N.; Corbalán-García, S. *Proc Natl Acad Sci U S A* **2009**, *106*, 6603.

(60) Nalefski, E. A.; Wisner, M. A.; Chen, J. Z.; Sprang, S. R.; Fukuda, M.; Mikoshiba, K.; Falke, J. J. *Biochemistry* **2001**, *40*, 3089.

(61) Kohout, S. C.; Corbalán-García, S.; Torrecillas, A.; Gómez-Fernández, J. C.; Falke, J. J. *Biochemistry* **2002**, *41*, 11411.

(62) Scott, A. M.; Antal, C. E.; Newton, A. C. *J Biol Chem* **2013**, *288*, 16905.

(63) Manna, D.; Bhardwaj, N.; Vora, M. S.; Stahelin, R. V.; Lu, H.; Cho, W. *J Biol Chem* **2008**, *283*, 26047.

(64) Guerrero-Valero, M.; Marín-Vicente, C.; Gómez-Fernández, J. C.; Corbalán-García, S. *J Mol Biol* **2007**, *371*, 608.

(65) Corbalán-García, S.; García-García, J.; Rodríguez-Alfaro, J. A.; Gómez-Fernández, J. C. *J Biol Chem* **2003**, *278*, 4972.

(66) Landgraf, K. E.; Malmberg, N. J.; Falke, J. J. *Biochemistry* **2008**, *47*, 8301.

(67) Lai, C. L.; Landgraf, K. E.; Voth, G. A.; Falke, J. J. *J Mol Biol* **2010**, *402*, 301.

(68) Corbin, J. A.; Evans, J. H.; Landgraf, K. E.; Falke, J. J. *Biochemistry* **2007**, *46*, 4322.

(69) Morales, K. A.; Igumenova, T. I. *Biochemistry* **2012**, *51*, 3349.

(70) Basu, A.; Pal, D. *Scientific World Journal* **2010**, *10*, 2272.

(71) Solodukhin, A. S.; Kretsinger, R. H.; Sando, J. J. *Cell Signal* **2007**, *19*, 2035.

(72) Leonard, T. A.; Różycki, B.; Saidi, L. F.; Hummer, G.; Hurley, J. H. *Cell* **2011**, *144*, 55.

(73) Newton, A. C. *Chem Rev* **2001**, *101*, 2353.

(74) Leonard, T. A.; Hurley, J. H. *Curr Opin Struct Biol* **2011**, *21*, 785.

(75) Beernink, P. T.; Segelke, B. W.; Hadi, M. Z.; Erzberger, J. P.; Wilson, D. M., 3rd; Rupp, B. *J Mol Biol* **2001**, *307*, 1023.

(76) Markovac, J.; Goldstein, G. W. *Nature* **1988**, *334*, 71.

(77) Long, G. J.; Rosen, J. F.; Schanne, F. A. *J Biol Chem* **1994**, *269*, 834.

(78) Warren, M. J.; Cooper, J. B.; Wood, S. P.; Shoolingin-Jordan, P. M. *Trends Biochem Sci* **1998**, *23*, 217.

(79) Erskine, P. T.; Duke, E. M.; Tickle, I. J.; Senior, N. M.; Warren, M. J.; Cooper, J. B. *Acta Crystallogr D Biol Crystallogr* **2000**, *56*, 421.

(80) Gourlaouen, C.; Parisel, O. *Angew Chem Int Ed Engl* **2007**, *46*, 553.

(81) Jaffe, E. K.; Martins, J.; Li, J.; Kervinen, J.; Dunbrack, R. L., Jr. *J Biol Chem* **2001**, *276*, 1531.

(82) Payne, J. C.; ter Horst, M. A.; Godwin, H. A. *J Am Chem Soc* **1999**, *121*, 6850.

(83) Magyar, J. S.; Weng, T. C.; Stern, C. M.; Dye, D. F.; Rous, B. W.; Payne, J. C.; Bridgewater, B. M.; Mijovilovich, A.; Parkin, G.; Zaleski, J. M.; Penner-Hahn, J. E.; Godwin, H. A. *J Am Chem Soc* **2005**, *127*, 9495.

(84) Neupane, K. P.; Pecoraro, V. L. *Angew Chem Int Ed Engl* **2010**, *49*, 8177.

(85) Wilson, M. A.; Brunger, A. T. *Acta Crystallogr D Biol Crystallogr* **2003**, *59*, 1782.

(86) Kursula, P.; Majava, V. *Acta Crystallogr Sect F Struct Biol Cryst Commun* **2007**, *63*, 653.

(87) Butt, T. R.; Edavettal, S. C.; Hall, J. P.; Mattern, M. R. *Protein Expr Purif* **2005**, *43*, 1.

(88) Marley, J.; Lu, M.; Bracken, C. *J Biomol NMR* **2001**, *20*, 71.

(89) Muhandiram, D. R.; Kay, L. E. *J Magn Reson Ser B* **1994**, *103*, 203.

(90) Montelione, G. T.; Lyons, B. A.; Emerson, S. D.; Tashiro, M. *J Am Chem Soc* **1992**, *114*, 10974.

(91) Yamazaki, T.; Lee, W.; Arrowsmith, C. H.; Muhandiram, D. R.; Kay, L. E. *J Am Chem Soc* **1994**, *116*, 11655.

(92) Delaglio, F.; Grzesiek, S.; Vuister, G. W.; Zhu, G.; Pfeifer, J.; Bax, A. *J Biomol NMR* **1995**, *6*, 277.

(93) Goddard, T. D; Kneller, D. G. **2003**. SPARKY 3 University of California: San Francisco, CA, USA.

(94) Wilcox, C. S. In *Frontiers in Supramolecular Organic Chemistry and Photochemistry.*; Schneider, H. J., Dürr, H., Eds.; Wiley-VCH: Weinheim, 1991, p 123.

(95) Montaville, P.; Coudevylle, N.; Radhakrishnan, A.; Leonov, A.; Zweckstetter, M.; Becker, S. *Protein Science* **2008**, *17*, 1025.

(96) Otwinowski, Z.; Minor, W. *Method Enzymol* **1997**, *276*, 307.

(97) Stahelin, R. V.; Cho, W. *Biochemistry* **2001**, *40*, 4672.

(98) Giorgione, J.; Newton, A. C. In *Protein Kinase C protocols*; Newton, A. C., Ed.; Methods in Molecular Biology: **2003**; Vol. 233, p 105.

(99) Barenholz, Y.; Amselem, S. *Liposome Technology*; 2nd edition; CRC Press: Boca Ratón, FL., **1993**; Vol. 1.

(100) Nalefski, E. A.; Falke, J. J. In *Methods in Molecular Biology*; Vogel, H. J., Ed.; Humana Press Inc.: **2002**; Vol. 172, p 295.

(101) Shao, X.; Davletov, B. A.; Sutton, R. B.; Südhof, T. C.; Rizo, J. *Science* **1996**, *273*, 248.

(102) Conesa-Zamora, P.; Lopez-Andreo, M. J.; Gómez-Fernández, J. C.; Corbalán-García, S. *Biochemistry* **2001**, *40*, 13898.

(103) Yamazaki, T.; Lee, W.; Revington, M.; Mattiello, D. L.; Dahlquist, F. W.; Arrowsmith, C. H.; Kay, L. E. *J Am Chem Soc* **1994**, *116*, 6464.

(104) Kirberger, M.; Yang, J. J. *J Inorg Biochem* **2008**, *102*, 1901.

(105) Claudio, E. S.; Godwin, H. A.; Magyar, J. S. *Prog Inorg Chem* **2003**, *51*, 1.

(106) Palmer, A. G., 3rd; Kroenke, C. D.; Loria, J. P. *Methods Enzymol* **2001**, *339*, 204.

(107) Ochoa, W. F.; Corbalán-García, S.; Eritja, R.; Rodríguez-Alfaro, J. A.; Gómez-Fernández, J. C.; Fita, I.; Verdaguer, N. *J Mol Biol* **2002**, *320*, 277.

(108) Cho, W.; Stahelin, R. V. *Biochimica et biophysica acta* **2006**, *1761*, 838.

(109) Johnson, E.; Bruschweiler-Li, L.; Showalter, S. A.; Vuister, G. W.; Zhang, F.; Bruschweiler, R. *J Mol Biol* **2008**, *377*, 945.

(110) Bouton, C. M.; Frelin, L. P.; Forde, C. E.; Arnold Godwin, H.; Pevsner, J. *J Neurochem* **2001**, *76*, 1724.

(111) Walters, J. D.; Johnson, J. D. *J Biol Chem* **1990**, *265*, 4223.

(112) Bitto, E.; Bingman, C. A.; Wesenberg, G. E.; McCoy, J. G.; Phillips, G. N., Jr. *J Biol Chem* **2006**, *281*, 20521.

(113) González, B.; Baños-Sanz , J. I.; Villate, M.; Brearley, C. A.; Sanz-Aparicio, J. *Proc Natl Acad Sci U S A* **2010**, *107*, 9608.

(114) Shumilin, I. A.; Kretsinger, R. H.; Bauerle, R. H. *Structure* **1999**, *7*, 865.

(115) Shimoni-Livny, L.; Carrell, H. L.; Wagner, T.; Kaufman Katz, A.; Afshar, C.; Mitchell, L. W.; Volin, M.; Jaffe, E. K.; Glusker, J. P. *Acta Crystallogr D Biol Crystallogr* **1998**, *54*, 438.

(116) Wilschut, J.; Papahadjopoulos, D. *Nature* **1979**, *281*, 690.

(117) Feigenson, G. W. *Biochemistry* **1986**, *25*, 5819.

(118) Coorssen, J. R.; Rand, R. P. *Biophys J* **1995**, *68*, 1009.

(119) Hoekstra, D. *Biochemistry* **1982**, *21*, 1055.

(120) Adonaylo, V. N.; Oteiza, P. I. *Toxicology* **1999**, *132*, 19.

(121) Godwin, H. A. *Curr Opin Chem Biol* **2001**, *5*, 223.

(122) Di Paolo, G.; De Camilli, P. *Nature* **2006**, *443*, 651.

(123) McLaughlin, S.; Murray, D. *Nature* **2005**, *438*, 605.

(124) Di Paolo, G.; Moskowitz, H. S.; Gipson, K.; Wenk, M. R.; Voronov, S.; Obayashi, M.; Flavell, R.; Fitzsimonds, R. M.; Ryan, T. A.; De Camilli, P. *Nature* **2004**, *431*, 415.

(125) Schiavo, G.; Gu, Q. M.; Prestwich, G. D.; Sollner, T. H.; Rothman, J. E. *Proc Natl Acad Sci U S A* **1996**, *93*, 13327.

(126) Bai, J.; Tucker, W. C.; Chapman, E. R. *Nat Struct Mol Biol* **2004**, *11*, 36.

(127) Coudevylle, N.; Montaville, P.; Leonov, A.; Zweckstetter, M.; Becker, S. *J Biol Chem* **2008**, *283*, 35918.

(128) Radhakrishnan, A.; Stein, A.; Jahn, R.; Fasshauer, D. *J Biol Chem* **2009**, *284*, 25749.

(129) Sánchez-Bautista, S.; Marín-Vicente, C.; Gómez-Fernández, J. C.; Corbalán-García, S. *J Mol Biol* **2006**, *362*, 901.

(130) Schumann, F. H.; Riepl, H.; Maurer, T.; Gronwald, W.; Neidig, K. P.; Kalbitzer, H. R. *J Biomol NMR* **2007**, *39*, 275.

(131) Baker, N. A.; Sept, D.; Joseph, S.; Holst, M. J.; McCammon, J. A. *Proc Natl Acad Sci U S A* **2001**, *98*, 10037.

(132) Humphrey, W.; Dalke, A.; Schulten, K. *J Mol Graph* **1996**, *14*, 33.

(133) Dolinsky, T. J.; Czodrowski, P.; Li, H.; Nielsen, J. E.; Jensen, J. H.; Klebe, G.; Baker, N. A. *Nucleic Acids Res* **2007**, *35*, W522.

(134) McLaughlin, S.; Wang, J.; Gambhir, A.; Murray, D. *Annu Rev Biophys Biomol Struct* **2002**, *31*, 151.

(135) Kazantsev, A. V.; Krivenko, A. A.; Pace, N. R. *RNA* **2009**, *15*, 266.

(136) Wang, C. Y.; Palmer, A. G. *Magn Reson Chem* **2003**, *41*, 866.

(137) Massi, F.; Grey, M. J.; Palmer, A. G., 3rd *Protein Science* **2005**, *14*, 735.

(138) Riley-Lovingshimer, M. R.; Reinhart, G. D. *Arch Biochem Biophys* **2005**, *436*, 178.

(139) Kuo, W.; Herrick, D. Z.; Cafiso, D. S. *Biochemistry* **2011**, *50*, 2633.

(140) Tucker, W. C.; Edwardson, J. M.; Bai, J.; Kim, H. J.; Martin, T. F.; Chapman, E. R. *J Cell Biol* **2003**, *162*, 199.

(141) Shao, X.; Li, C.; Fernandez, I.; Zhang, X.; Südhof, T. C.; Rizo, J. *Neuron* **1997**, *18*, 133.

(142) Rizo, J.; Sudhof, T. C. *J Biol Chem* **1998**, *273*, 15879.

(143) Zhang, X.; Rizo, J.; Sudhof, T. C. *Biochemistry* **1998**, *37*, 12395.

(144) Parekh, A. B. *Trends Biochem Sci* **2011**, *36*, 78.

(145) Gambhir, A.; Hangyas-Mihalyne, G.; Zaitseva, I.; Cafiso, D. S.; Wang, J.; Murray, D.; Pentyala, S. N.; Smith, S. O.; McLaughlin, S. *Biophys J* **2004**, *86*, 2188.

(146) Waisberg, M.; Joseph, P.; Hale, B.; Beyersmann, D. *Toxicology* **2003**, *192*, 95.

(147) Bridges, C. C.; Zalups, R. K. *Toxicol Appl Pharmacol* **2005**, *204*, 274.

(148) Swairjo, M. A.; Concha, N. O.; Kaetzel, M. A.; Dedman, J. R.; Seaton, B. A. *Nat Struct Biol* **1995**, *2*, 968.

(149) Thévenod, F.; Lee, W. K. *Met Ions Life Sci* **2013**, *11*, 415.

(150) Long, G. J. *Toxicol Appl Pharmacol* **1997**, *143*, 189.

(151) Long, G. J. *Toxicol Lett* **1997**, *91*, 91.

(152) Stohs, S. J.; Bagchi, D.; Hassoun, E.; Bagchi, M. *J Environ Pathol Toxicol Oncol* **2000**, *19*, 201.

(153) Lemire, J. A.; Harrison, J. J.; Turner, R. J. *Nat Rev Microbiol* **2013**, *11*, 371.

(154) Lawal, A. O.; Ellis, E. M. *Environ Toxicol Pharmacol* **2011**, *32*, 54.

(155) Ouelhadj, A.; Kuschk, P.; Humbeck, K. *The New phytologist* **2006**, *170*, 261.

(156) Martin, P.; Pognonec, P. *The FEBS journal* **2010**, *277*, 39.

(157) Souza, V.; Bucio, L.; Gutiérrez-Ruiz , M. C. *Toxicology* **1997**, *120*, 215.

(158) Rulíšek, L.; Vondrášek, J. *J Inorg Biochem* **1998**, *71*, 115.

(159) Morales, K. A.; Yang, Y.; Long, Z.; Li, P.; Taylor, A. B.; Hart, P. J.; Igumenova, T. I. *J Am Chem Soc* **2013**, *135*, 12980.

(160) Jensen, M. R.; Hansen, D. F.; Ayna, U.; Dagil, R.; Hass, M. A.; Christensen, H. E.; Led, J. J. *Magn Reson Chem : MRC* **2006**, *44*, 294.

(161) Monson, C. F.; Cong, X.; Robison, A. D.; Pace, H. P.; Liu, C.; Poyton, M. F.; Cremer, P. S. *J Am Chem Soc* **2012**, *134*, 7773.

(162) Gifford, J. L.; Walsh, M. P.; Vogel, H. J. *Biochem J* **2007**, *405*, 199.

(163) Berridge, M. J.; Lipp, P.; Bootman, M. D. *Nat Rev Mol Cell Biol* **2000**, *1*, 11.

(164) Berridge, M. J.; Bootman, M. D.; Lipp, P. *Nature* **1998**, *395*, 645.

(165) Carafoli, E.; Santella, L.; Branca, D.; Brini, M. *Crit Rev Biochem Mol Biol* **2001**, *36*, 107.

(166) Grabarek, Z. *J Mol Biol* **2006**, *359*, 509.

(167) Chazin, W. J. *Acc Chem Res* **2011**, *44*, 171.

(168) Stahelin, R. V.; Cho, W. *Biochem J* **2001**, *359*, 679.

(169) Xu, G. Y.; McDonagh, T.; Yu, H. A.; Nalefski, E. A.; Clark, J. D.; Cumming, D. A. *J Mol Biol* **1998**, *280*, 485.

(170) Hsu, Y. H.; Burke, J. E.; Stephens, D. L.; Deems, R. A.; Li, S.; Asmus, K. M.; Woods, V. L., Jr.; Dennis, E. A. *J Biol Chem* **2008**, *283*, 9820.

(171) Grobler, J. A.; Essen, L. O.; Williams, R. L.; Hurley, J. H. *Nat Struct Biol* **1996**, *3*, 788.

(172) Coudevylle, N.; Montaville, P.; Leonov, A.; Zweckstetter, M.; Becker, S. *J Biol Chem* **2008**, *283*, 35918.

(173) Contreras, M. A.; Ubach, J.; Millet, O.; Rizo, J.; Pons, M. *J Am Chem Soc* **1999**, *121*, 8947.

(174) Santamaria-Kisiel, L.; Rintala-Dempsey, A. C.; Shaw, G. S. *Biochem J* **2006**, *396*, 201.

(175) Nelson, M. R.; Chazin, W. J. *Protein Science* **1998**, *7*, 270.

(176) Zhang, M.; Tanaka, T.; Ikura, M. *Nat Struct Biol* **1995**, *2*, 758.

(177) Chazin, W. J. *Nat Struct Biol* **1995**, *2*, 707.

(178) Burgoyne, R. D.; Weiss, J. L. *Biochem J* **2001**, *353*, 1.

(179) Trave, G.; Lacombe, P. J.; Pfuhl, M.; Saraste, M.; Pastore, A. *EMBO J* **1995**, *14*, 4922.

(180) Yap, K. L.; Ames, J. B.; Swindells, M. B.; Ikura, M. *Proteins* **1999**, *37*, 499.

(181) Skelton, N. J.; Kordel, J.; Akke, M.; Forsen, S.; Chazin, W. J. *Nat Struct Biol* **1994**, *1*, 239.

(182) Akke, M.; Chazin, W. J. *Nat Struct Biol* **2001**, *8*, 910.

(183) Lee, A. L.; Kinnear, S. A.; Wand, A. J. *Nat Struct Biol* **2000**, *7*, 72.

(184) Tjandra, N.; Kuboniwa, H.; Ren, H.; Bax, A. *Eur J Biochem* **1995**, *230*, 1014.

(185) Johnson, E.; Chazin, W. J.; Rance, M. *J Mol Biol* **2006**, *357*, 1237.

(186) Kordel, J.; Skelton, N. J.; Akke, M.; Palmer, A. G., 3rd; Chazin, W. J. *Biochemistry* **1992**, *31*, 4856.

(187) Akke, M.; Forsen, S.; Chazin, W. J. *J Mol Biol* **1995**, *252*, 102.

(188) Malmendal, A.; Carlstrom, G.; Hambraeus, C.; Drakenberg, T.; Forsen, S.; Akke, M. *Biochemistry* **1998**, *37*, 2586.

(189) Wimberly, B.; Thulin, E.; Chazin, W. J. *Protein Science* **1995**, *4*, 1045.

(190) Akke, M.; Skelton, N. J.; Kordel, J.; Palmer, A. G., 3rd; Chazin, W. J. *Biochemistry* **1993**, *32*, 9832.

(191) Skelton, N. J.; Kordel, J.; Akke, M.; Chazin, W. J. *J Mol Biol* **1992**, *227*, 1100.

(192) Maler, L.; Blankenship, J.; Rance, M.; Chazin, W. J. *Nat Struct Biol* **2000**, *7*, 245.

(193) Mercier, P.; Spyracopoulos, L.; Sykes, B. D. *Biochemistry* **2001**, *40*, 10063.

(194) Gagne, S. M.; Tsuda, S.; Spyracopoulos, L.; Kay, L. E.; Sykes, B. D. *J Mol Biol* **1998**, *278*, 667.

(195) Venkitaramani, D. V.; Fulton, D. B.; Andreotti, A. H.; Johansen, K. M.; Johansen, J. *Protein Science* **2005**, *14*, 1894.

(196) Xu, X.; Ishima, R.; Ames, J. B. *Proteins* **2011**, *79*, 1910.

(197) Banci, L.; Cavallaro, G.; Kheifets, V.; Mochly-Rosen, D. *J Biol Chem* **2002**, *277*, 12988.

(198) Yamazaki, T.; Forman-Kay, J. D.; Kay, L. E. *J Am Chem Soc* **1993**, *115*, 11054.

(199) Farrow, N. A.; Muhandiram, R.; Singer, A. U.; Pascal, S. M.; Kay, C. M.; Gish, G.; Shoelson, S. E.; Pawson, T.; Forman-Kay, J. D.; Kay, L. E. *Biochemistry* **1994**, *33*, 5984.

(200) Lipari, G.; Szabo, A. *J Am Chem Soc* **1982**, *104*, 4546.

(201) Lipari, G.; Szabo, A. *J Am Chem Soc* **1982**, *104*, 4559.

(202) Clore, G. M.; Szabo, A.; Bax, A.; Kay, L. E.; Driscoll, P. C.; Gronenborn, A. M. *J Am Chem Soc* **1990**, *112*, 4989.

(203) García de la Torre, J.; Huertas, M. L.; Carrasco, B. *J Magn Reson* **2000**, *147*, 138.

(204) Verdaguer, N.; Corbalán-García, S.; Ochoa, W. F.; Fita, I.; Gómez-Fernández, J. C. *EMBO J* **1999**, *18*, 6329.

(205) Tjandra, N.; Feller, S. E.; Pastor, R. W.; Bax, A. *J Am Chem Soc* **1995**, *117*, 12562.

(206) Cross, T. A.; Frey, M. H.; Opella, S. J. *J Am Chem Soc* **1983**, *105*, 7471.

(207) Farrow, N. A.; Zhang, O.; Forman-Kay, J. D.; Kay, L. E. *Biochemistry* **1995**, *34*, 868.

(208) Farrow, N. A.; Zhang, O.; Szabo, A.; Torchia, D. A.; Kay, L. E. *J Biomol NMR* **1995**, *6*, 153.

(209) Peng, J. W.; Wagner, G. *Biochemistry* **1992**, *31*, 8571.

(210) Peng, J. W.; Wagner, G. *J Magn Reson* **1992**, *98*, 308.

(211) Loria, J. P.; Rance, M.; Palmer, A. G. *J Am Chem Soc* **1999**, *121*, 2331.

(212) O'Connor, C.; Kovrigin, E. L. *Biochemistry* **2008**, *47*, 10244.

(213) Millet, O.; Loria, J. P.; Kroenke, C. D.; Pons, M.; Palmer, A. G. *J Am Chem Soc* **2000**, *122*, 2867.

(214) Carver, J. P.; Richards, R. E. *J Magn Reson* **1972**, *6*, 89.

(215) Davis, D. G.; Perlman, M. E.; London, R. E. *J Magn Reson B* **1994**, *104*, 266.

(216) Slater, S. J.; Seiz, J. L.; Cook, A. C.; Buzas, C. J.; Malinowski, S. A.; Kershner, J. L.; Stagliano, B. A.; Stubbs, C. D. *J Biol Chem* **2002**, *277*, 15277.

(217) Kheifets, V.; Mochly-Rosen, D. *Pharmacol Res* **2007**, *55*, 467.

(218) Stewart, M. D.; Morgan, B.; Massi, F.; Igumenova, T. I. *J Mol Biol* **2011**, *408*, 949.

(219) Stewart, M. D.; Igumenova, T. I. *Biochemistry* **2012**, *51*, 7263.

(220) House, C.; Kemp, B. E. *Science* **1987**, *238*, 1726.

(221) Edwards, A. S.; Newton, A. C. *J Biol Chem* **1997**, *272*, 18382.

(222) Ananthanarayanan, B.; Stahelin, R. V.; Digman, M. A.; Cho, W. *The J Biol Chem* **2003**, *278*, 46886.

(223) Findeisen, M.; Brand, T.; Berger, S. *Magn Reson Chem* **2007**, *45*, 175.

(224) Stewart, M. D. Thesis, 2013. Texas A&M University, TX, USA.

(225) Walker, O.; Varadan, R.; Fushman, D. *J Magn Reson* **2004**, *168*, 336.

(226) Berlin, K.; O'Leary, D. P.; Fushman, D. *Proteins* **2011**, *79*, 2268.

(227) Tochio N., Saito K., Tomizawa T., Watanabe S., Harada T., Kigawa T., Yokoyama S.;*Structural Genomics Proteomics Initiative* **Ed. 2007**.

(228) Mackereth, C. D.; Sattler, M. *Curr Opin Struct Biol* **2012**, *22*, 287.

(229) Boehr, D. D.; Nussinov, R.; Wright, P. E. *Nat Chem Biol* **2009**, *5*, 789.

(230) Sutton, R. B.; Sprang, S. R. *Structure* **1998**, *6*, 1395.

(231) Iwahara, J.; Tang, C.; Marius Clore, G. *J Magn Reson* **2007**, *184*, 185.